

Mechanistic Study of Electrochemical Processes on A Porous Magnéli Phase Electrode

BY

YIN JING

B.S, Shenyang University of Chemical Technology, 2005

M.S, University of Dayton, 2010

THESIS

Submitted in partial fulfilment of the requirements

For the degree of Doctor of Philosophy in Chemical Engineering

in the Graduate College of the

University of Illinois at Chicago, 2017

Chicago, Illinois

Defense Committee:

Dr. Brian P. Chaplin, Chair and Advisor, Department of Chemical Engineering

Dr. Vikas Berry, Department of Chemical Engineering

Dr. Ludwig C. Nitsche, Department of Chemical Engineering

Dr. Sangil Kim, Department of Chemical Engineering

Dr. Robert J. LeSuer, Department of Chemistry, State University of New York

*This thesis work is dedicated to my wife, Songwei, who has always stood by me during the challenges of graduate school and life. This work is also dedicated to my parents, Shuze and Zelan, who has always showed me their unconditional loves and inspired me to work towards my goal.*

## ACKNOWLEDGEMENTS

I am very privileged to have the opportunity to pursue my Ph.D. degree at a university as friendly, diverse and collaborative as the University of Illinois at Chicago; Therefore, there are a number of people to appreciate for their parts in my success. Foremost, I would like to recognize my advisor, **Dr. Brian P. Chaplin**, for having me in his lab and his support over the years. I am very grateful for his guidance and the opportunities he has offered. Dr. Chaplin is an incredible organizer, a rigorous researcher, a great problem solver and a prompt email communicator, all these qualities were extremely helpful to move my project forward. Under his guidance, I have learned how to perform research as a real scientist and realized that I can always do better. I will remember these great moments with Dr. Chaplin in the lab.

I would also like to thank my thesis committee members, **Dr. Vikas Berry, Dr. Ludwig C. Nitsche, Dr. Sangil Kim, and Dr. Robert J. LeSuer**. Dr. Berry provided his insightful suggestions and scientific guidance in term of electronic properties of semiconducting materials, which are fundamental to my last project. Throughout all the projects, I used the numerical simulation methods learned from Dr. Nitsche's class, which are beneficial to a deep understanding of electrochemical processes. Dr. Kim's led me to solve the last piece of the membrane puzzle in his class, and helped me systematically understand the membrane processes. Dr. LeSuer opened the SECM world to me, and helped me grow to a SECM expert. A former preliminary exam committee member, **Dr. Yossef Elabd**, was instrumental to the initiation of my third paper. Through the collaboration with Dr. Elabd, we found the necessity to justify the hydroxyl radical probes used in the electrochemical systems.

I would like to thank the members of the Chaplin's lab who have all contributed to the progress I have achieved. Over the years, **Pralay Gayen** has given his time to discuss researches and contributed to the XPS measurement. **Lun Guo**, a true pioneer for the REM synthesis, deserves the thanks for synthesizing the REM which is the basis to my first two publications. I would like to thank **Meng-Hsuan Lin, Samuel Plunkett, Soroush Almassi, Saurabh Misal, and Sasmita Nayak** for challenging me with

## ACKNOWLEDGEMENTS (continued)

electrochemistry knowledges all the time. The Chaplin's lab members are a wonderful group of people who I have enjoyed working with and learning from.

I would like to express the sincere appreciation to my family. Mom and Dad have provided all their support and encouraged me to explore the uncharted. Thanks for the willingness and patience to listen to my problems and provide perspectives when I am confused. I would not be who I am today without you. I would like to thank my wife, **Songwei**. You have been continually and unconditionally supportive of my graduate study. Thank you for the happiness you bring to my life. Thank you for those weekends when you had to listen to my presentation rehearsals. I know you are there whenever I need you to just listen.

Finally, I would like to acknowledge the support from the National Science Foundation for funding my research projects and conference expenses.

YJ

## CONTRIBUTION OF AUTHORS

Chapter 1 represents an overview of my dissertation, which also includes the research objectives and sets up the outline of this dissertation. Chapter 2 is a literature review where the state of knowledge is presented, and the significance of my research questions is highlighted. Chapter 3 represents a published work (complete citation included) for which I was the first author and major contributor of the research. My research mentor, Dr. Brian P. Chaplin conceived the project, contributed to the manuscript revision and scientific discussion. Chapter 4 represents a published work (complete citation included) for which I was the first author and major contributor of the research. Lun Guo synthesized the membrane, performed the SEM and XRD measurements, and contributed to Figure 12 (a) – (d). Dr. Brian P. Chaplin conceived the project, and contributed to the manuscript revision and scientific discussion. Chapter 5 represents a published work (complete citation included) for which I was the first author and major contributor of the research. Dr. Brian P. Chaplin conceived the project, and contributed to writing part of the manuscript, the revision and scientific discussion. Chapter 6 represents a manuscript (include complete citation) for which I was the first author and major contributor of the research. Soroush Almassi synthesized the electrodes, and performed the TGA experiments and TGA data analysis. Dr. Robert J. LeSuer contributed to the manuscript revision and scientific discussion. Dr. Brian P. Chaplin conceived the project, and contributed to the manuscript revision and scientific discussion. Chapter 7 represents a concluding remark of the dissertation and the future directions of this field are also discussed.

## TABLE OF CONTENT

I.	INTRODUCTION .....	1
1.1	Background.....	1
1.2	Research objectives .....	3
1.3	Outlines of thesis .....	6
II.	STATE OF KNOWLEDGE .....	8
2.1.	Techniques of monitoring membrane fouling.....	8
2.1.1	Destructive method of monitoring membrane fouling .....	9
2.1.2	Non-destructive methods of monitoring membrane fouling.....	11
2.2.	Fouling control and membrane regeneration schemes on conductive membranes.....	13
2.3	Hydroxyl radical probes used in electrochemical systems .....	16
2.4	Surface passivation and reactivation of $Ti_nO_{2n-1}$ in electrochemical systems .....	17
III.	ELECTROCHEMICAL IMPEDANCE SPECTROSCOPY STUDY OF MEMBRANE FOULING CHARACTERIZATION AT A CONDUCTIVE SUB-STOICHIOMETRIC $TiO_2$ REACTIVE ELECTROCHEMICAL MEMBRANE: TRANSMISSION LINE MODEL DEVELOPMENT .....	19
3.1	Abstract.....	19
3.2	Introduction.....	19
3.3	Mathematical model .....	22
3.3.1	Theory.....	22
3.3.2	Mathematical interpretation of penetration depth ( $\lambda$ ) .....	29
3.3.3	Modeling approach.....	30
3.4	Results and discussion .....	31
3.4.1	Application of the transmission line model to membrane fouling.....	31
3.4.2	Monolayer adsorption and pore constriction .....	32
3.4.3	Fouling of outer membrane surface.....	41
3.4.4	Intermediate pore blockage .....	42
3.4.5	Calculation of $A_{electro}$ .....	44
3.5	Conclusions.....	44
3.6	Acknowledgements.....	44

TABLE OF CONTENT (continued)

IV. ELECTROCHEMICAL IMPEDANCE SPECTROSCOPY STUDY OF MEMBRANE FOULING AND ELECTROCHEMICAL REGENERATION AT A SUB-STOICHIOMETRIC TiO <sub>2</sub> REACTIVE ELECTROCHEMICAL MEMBRANE.....	45
4.1 Abstract.....	45
4.2 Introduction.....	45
4.3 Materials and methods.....	48
4.3.1 Reagents .....	48
4.3.2 Reactive electrochemical membrane .....	48
4.3.3 Filtration setup.....	49
4.3.4 Molecular weight cuutoff determination .....	50
4.3.5 Fouling experiments .....	50
4.3.6 Chemical free electrochemical regeneration (CFER) experiments .....	51
4.3.7 Electrochemical impedance spectroscopy measurements and transmission line model fitting .....	52
4.4 Results and discussion .....	54
4.4.1 Physical characterization .....	54
4.4.2 Humic acid membrane fouling and regeneration.....	57
4.4.2.1 Anodic chemical free electrochemical regeneration in forward wash mode .....	57
4.4.2.2 Anodic chemical free electrochemical regeneration in backwash mode .....	61
4.4.2.3 Multi-cycle test .....	68
4.4.3 Polystyrene microspheres membrane fouling and regeneration.....	69
4.4.3.1 Polystyrene microsphere fouling .....	70
4.4.3.2 Membrane regeneration .....	74
4.5 Conclusions.....	75
4.6 Acknowledgements.....	76
V. A MECHANISTIC STUDY OF THE VALIDITY OF USING HYDROXYL RADICAL PROBES TO CHARACTERIZE ELECTROCHEMICAL ADVANCED OXIDATION PROCESSES .....	77
5.1 Abstract.....	77
5.2 Introduction.....	77
5.3 Materials and method .....	80
5.3.1 Reagents .....	80
5.3.2 Electrochemical characterization.....	80
5.3.3 Bulk oxidation experiments.....	81
5.3.4 Mass transfer rates constants .....	81
5.3.5 Reaction rate constants and curve fitting.....	81

## TABLE OF CONTENT (continued)

5.3.6 Analytical methods .....	82
5.3.7 Quantum mechanical simulations.....	82
5.4 Results and discussion .....	83
5.4.1 Voltammetry results .....	83
5.4.2 Bulk oxidation experiments.....	87
5.4.3 Density functional theory modeling .....	90
5.5 Broader significance and environmental impacts .....	95
5.6 Acknowledgements.....	96
VI. MECHANISTIC STUDY OF SURFACE PASSIVATION AND REACTIVATION OF A SUBSTOICHIOMETRIC $\text{TiO}_2$ ELECTRODE.....	
6.1 Abstract.....	97
6.2 Introduction.....	97
6.3 Experimental section .....	100
6.3.1 Reagents .....	100
6.3.2 Preparation of $\text{Ti}_n\text{O}_{2n-1}$ electrode .....	101
6.3.3 Electrochemical methods.....	101
6.3.3.1 Scanning electrochemical microscope experiments.....	102
6.3.3.2 Electrochemical impedance spectroscopy (EIS) and Mott-Schottky analysis .....	102
6.3.3.4 Film resistivity .....	103
6.3.3.4 Topography mapping.....	103
6.3.4 Electrode Markers and surface profile.....	104
6.3.5 X-ray powder diffraction (XRD).....	104
6.3.6 X-ray photoelectron spectroscopy (XPS).....	104
6.3.7 Thermogravimetric analysis (TGA) .....	104
6.3.8 Kinetic analysis of different Magnéli phases for hydroxyl radical production .....	105
6.4 Results and discussion .....	106
6.4.1 Examination of crystalline structure and electronic properties during electrolysis.....	106
6.4.2 Variation in localized and bulk charge transfer kinetics during electrolysis.....	109
6.4.3 Implication of surface passivation and reactivation in energy technologies .....	113
6.4.4 Implication of surface passivation and regeneration in water treatment .....	113
6.4.5 Mechanism of loss and regeneration of electrochemical activity in various electrolyte .....	115
6.5 Conclusion .....	118
6.6 Acknowledgements.....	118

TABLE OF CONTENT (continued)

VII. CONCLUDING REMARKS ..... 120

APPENDICES ..... 120

    APPENDIX A..... 124

    APPENDIX B..... 128

    APPENDIX C..... 146

    APPENDIX D..... 161

    APPENDIX E ..... 189

CITED LITERATURE ..... 192

VITA.....213

## LIST OF TABLES

Table I DETERMINATION OF FOULING MECHANISMS BY FILTRATION MODEL.....	12
Table II PENETRATION DEPTH OF $\Delta E$ SIGNAL AT AN ASYMMETRIC MEMBRANE .....	30
Table III MODEL PARAMETERS FOR DIFFERENT MODES OF FOULING SIMULATION (UNIT: R (OHM), Y ( $F \cdot S^{A-1}$ ), $C_{DL}$ (FARAD), A ( $CM^2$ )).....	35
Table IV MODEL PARAMETERS, CALCULATED DOUBLE LAYER CAPACITANCES AND ELECTRO-ACTIVE SURFACE AREAS OF BACKGROUND, 150 MG L <sup>-1</sup> HA FOULING AND ANODIC CFER IN FORWARD FLUSH MODE (UNIT: X <sub>1</sub> (OHM), R (OHM), Y ( $F \cdot S^{A-1}$ ), $C_{DL}$ (FARAD), A ( $CM^2$ )).....	63
Table V MODEL PARAMETERS, CALCULATED DOUBLE LAYER CAPACITANCES AND ELECTRO-ACTIVE SURFACE AREAS OF BACKGROUND, 150 MG L <sup>-1</sup> HA FOULING AND ANODIC CFER IN BACKWASH MODE (UNIT: X <sub>1</sub> (OHM), R (OHM), Y ( $F \cdot S^{A-1}$ ), $C_{DL}$ (FARAD), A ( $CM^2$ )).....	65
Table VI MODEL PARAMETERS, CALCULATED DOUBLE LAYER CAPACITANCES AND ELECTRO-ACTIVE SURFACE AREAS OF BACKGROUND, 150 MG L <sup>-1</sup> HA FOULING AND THE 2 <sup>ND</sup> BACKWASH OPERATION (UNIT: X <sub>1</sub> (OHM), R (OHM), Y ( $F \cdot S^{A-1}$ ), $C_{DL}$ (FARAD), A ( $CM^2$ )) ..	67
Table VII MODEL PARAMETER AND CALCULATED DOUBLE LAYER CAPACITANCES OF BACKGROUND, 1.58 $\mu$ M POLYSTYRENE FOULING AND CATHODIC/ANODIC CFER IN BACKWASH MODE (UNIT: X <sub>1</sub> (OHM), R (OHM), Y ( $F \cdot S^{A-1}$ ), $C_{DL}$ (FARAD), A ( $CM^2$ )). RESULTS FOR REPLICATE EXPERIMENTS ARE INCLUDED IN THE APPENDIX.....	73
Table VIII THEORETICAL PARAMETERS DETERMINED FOR THE REACTION OF PROBE MOLECULES BY THE FORRESTER-HEPBURN MECHANISM. ....	92
Table IX MOLECULAR WEIGHT CUTOFF DETERMINATION OF PRISTINE TIO <sub>2</sub> MEMBRANE AND REM .....	128
Table X FLUX RECORD ON 1.58 $\mu$ M POLYSTYRENE FOULING BEFORE ANODIC CFER IN BACKWASH MODE AND FILTRATION MODEL CALCULATION (EXP 1).....	130
Table XI FLUX RECORD ON 1.58 $\mu$ M POLYSTYRENE FOULING BEFORE ANODIC CFER IN BACKWASH MODE AND FILTRATION MODEL CALCULATION (EXP 2).....	131
Table XII FLUX RECORD ON 1.58 $\mu$ M POLYSTYRENE FOULING BEFORE CATHODIC CFER IN BACKWASH MODE AND FILTRATION MODEL CALCULATION (EXP 1).....	132
Table XIII FLUX RECORD ON 1.58 $\mu$ M POLYSTYRENE FOULING BEFORE CATHODIC CFER IN BACKWASH MODE AND FILTRATION MODEL CALCULATION (EXP 2).....	133

LIST OF TABLES (continued)

Table XIV COMPLEMENTARY FITTING PARAMETERS TO TABLE XI IN THE MAIN MANUSCRIPT.....	135
Table XV COMPLEMENTARY FITTING PARAMETERS TO TABLE XII IN THE MAIN MANUSCRIPT.....	135
Table XVI COMPLEMENTARY FITTING PARAMETERS TO TABLE XIII IN THE MAIN MANUSCRIPT.....	135
Table XVII COMPLEMENTARY FITTING PARAMETERS TO TABLE XIV IN THE MAIN MANUSCRIPT.....	135
Table XVIII COMPLEMENTARY FITTING PARAMETERS TO TABLE XIV IN THE MAIN MANUSCRIPT.....	136
Table XIX MODEL PARAMETERS, CALCULATED DOUBLE LAYER CAPACITANCES AND ELECTRO-ACTIVE SURFACE AREAS UNDER BACKGROUND, 150MG L <sup>-1</sup> HA FOULING AND ANODIC CFER IN BACKWASH MODE IN LONGEVITY TEST (UNIT: R, R <sub>s</sub> , X <sub>1</sub> , X <sub>2</sub> AND Z <sub>B</sub> (OHM), Y (F S <sup>A-1</sup> ), CDL (F), A (CM <sup>2</sup> )) .....	142
Table XX LITERATURE SUMMARY OF HYDROXYL RADICAL PROBES USED IN THE ELECTROCHEMICAL OXIDATION PROCESS.....	146
Table XXI LITERATURE SUMMARY OF HYDROXYL RADICAL PROBES USED IN THE ELECTROCHEMICAL FENTON PROCESS.....	147
Table XXII LITERATURE SUMMARY OF HYDROXYL RADICAL PROBES USED IN THE FENTON PROCESS .....	147
Table XXIII LITERATURE SUMMARY OF HYDROXYL RADICAL PROBES USED IN THE PHOTOCATALYTIC PROCESS .....	148
Table XXIV ANODIC PEAK POTENTIALS FOR SELECTED COMPOUNDS.....	149
Table XXV DIFFUSION COEFFICIENTS AND MASS TRANSFER RATE CONSTANTS OF COU, TA, AND P-BQ AT 25 °C.....	151
Table XXVI REACTION RATE CONSTANTS (K <sub>S</sub> ) AND MASS TRANSFER RATE CONSTANTS (K <sub>M</sub> ) FOR BULK OXIDATION OF COU, TA, AND P-BQ AT DIFFERENT TEMPERATURES AND 3.0 V/SHE.....	155
Table XXVII THEORETICAL VALUES DETERMINED BY DFT METHODS AND USED TO DETERMINE E <sub>A</sub> VERSUS POTENTIAL PROFILES.....	159
Table XXVIII THEORETICAL PARAMETERS DETERMINED FOR THE REACTION OF PROBE MOLECULES BY THE FORRESTER-HEPBURN MECHANISM. ....	159
Table XXIX SUMMARY OF CHARGE CARRIER DENSITY (N <sub>D</sub> ) OF Ti <sub>N</sub> O <sub>2N-1</sub> AT DIFFERENT STATES. ERRORS REPRESENT 95% CONFIDENCE INTERVAL. ....	169

LIST OF TABLES (continued)

Table XXX SUMMARY OF FLAT BAND POTENTIAL ( $E_{FB}$ ) OF  $Ti_NO_{2N-1}$  AT DIFFERENT STATES. ERRORS REPRESENT 95% CONFIDENCE INTERVAL..... 169

Table XXXI SUMMARY OF FILM RESISTIVITIES OF  $Ti_NO_{2N-1}$  AT DIFFERENT STATES. ERRORS REPRESENT 95% CONFIDENCE INTERVAL..... 171

Table XXXII SUMMARY OF CHARGE TRANSFER RESISTANCES ( $R_{CT}$ ) OF  $Ti_NO_{2N-1}$  AT DIFFERENT STATES. ERRORS REPRESENT 95% CONFIDENCE INTERVAL..... 174

Table XXXIII SUMMARY OF NORMALIZED FIRST ORDER KINETIC CONSTANTS OF  $Ti_NO_{2N-1}$  TREATED IN 1 M  $H_2SO_4$  ELECTROLYTE..... 183

Table XXXIV SUMMARY OF NORMALIZED FIRST ORDER KINETIC CONSTANTS OF  $Ti_NO_{2N-1}$  TREATED IN 2 M  $HClO_4$  ELECTROLYTE ..... 184

Table XXXV SUMMARY OF NORMALIZED FIRST ORDER KINETIC CONSTANTS OF  $Ti_NO_{2N-1}$  TREATED IN 2 M  $HCl$  ELECTROLYTE ..... 185

Table XXXVI ATOMIC CONCENTRATION OF SURFACE COMPOSITION ON  $Ti_NO_{2N-1}$  TREATED WITH AND WITHOUT APPLIED POTENTIAL IN 1 M  $H_2SO_4$  ELECTROLYTE FOR 30 MIN..... 188

## LIST OF FIGURES

Figure 1 Mechanisms for fouling in membrane filtration: (a) pore blockage, (b) pore constriction, and (c) cake layer formation .....	9
Figure 2 Modified transmission line model for a reactive electrochemical membrane with an asymmetric structure. ....	25
Figure 3 Schematic diagrams of various fouling mechanisms, (a) monolayer adsorption and (b) pore constriction at the active layer, (c) monolayer adsorption at the support layer, (d) outer surface fouling and (e) intermediate pore blockage.....	33
Figure 4 Illustration of penetration depth on outer surface (red, square), active (blue, circle) and support (green, triangle) layers in a simulated EIS (a) overall and (b) zoomed-in Nyquist EIS spectra, and (c) Bode phase plot of a clean REM. Solid triangles represent the characteristic frequencies of 10 mHz, 2 Hz, and 1 kHz.....	34
Figure 5 Variation of averaged pore dielectric constant and normalized ion concentration inside the pore. Hollow points are at 5 nm in pore radius. ....	37
Figure 6 Simulated Nyquist plot from TLM in the case of monolayer adsorption at active layer over (a) all frequencies and (b) high and mid frequencies, and (c) Bode phase plot. Unfilled symbols represent characteristic frequencies at 10 mHz, 2 Hz and 1 kHz. ....	38
Figure 7 Simulated Nyquist plot from TLM in the case of pore constriction at active layer over (a) all frequencies and (b) high and mid frequencies, and (c) Bode phase plot. Unfilled symbols represent characteristic frequencies at 10 mHz, 2 Hz and 1 kHz. ....	39
Figure 8 Simulated results from TLM in the case of membrane fouling at support layer over (a) all frequencies and (b) high and mid frequencies, and (c) Bode phase plot. Unfilled symbols represent characteristic frequency at 10 mHz, 2 Hz and 1 kHz.....	41
Figure 9 Simulated results from TLM in the case of membrane fouling at outer surface over (a) all frequencies and (b) high and mid frequencies, and (c) Bode phase plot. Unfilled symbols represent characteristic frequencies at 10 mHz, 2 Hz and 1 kHz. ....	42
Figure 10 Simulated (a) Nyquist and (b) Bode plots from TLM in the case of intermediate pore blockage. Unfilled symbols represent characteristic frequency at 10 mHz, 2 Hz and 1 kHz. ....	43
Figure 11 (a) System sketch of filtration (fouling) experiment, EIS measurement setup and (b) setup for CFER in backwash mode. Inset image shows a three-electrode placement sketch inside the REM. Dead end mode is realized by completely cutting off Line 1 (cross flow) in Setup (a).....	49
Figure 12 SEM of REM, (a) overall SEM image, (b) active layer, (c) support layer; (d) XRD of substoichiometric TiO <sub>2</sub> membrane with red (solid) and green (dash) arrows representing standard characteristic peaks of Ti <sub>4</sub> O <sub>7</sub> and Ti <sub>6</sub> O <sub>11</sub> , respectively; results of Hg intrusion porosimetry analysis of (e) cumulative pore area, and (f) log differential intrusion pore volume. ....	56
Figure 13 (a) Normalized permeate flux $J$ of REM at different operational condition for treatment of 150 mg L <sup>-1</sup> humic acid feed solution in forward wash mode; initial membrane flux $J_0 = 1499$ LMH bar <sup>-1</sup> ; (b1) simulated potential drop along membrane pore and (b2) active layer. ....	58

LIST OF FIGURES (continued)

Figure 14 (a) Normalized permeate flux  $J$  under different operational conditions for the anodic CFER in forward wash mode of  $150 \text{ mg L}^{-1}$  HA fouled REM; (b) EIS spectra in complete frequency range; (c) zoomed-in EIS spectra in high and mid frequency range; and (d) Bode phase plot; initial membrane flux  $J_0 = 1499.0 \text{ LMH bar}^{-1}$ . (Solid lines represent TLM fit, unfilled symbols represent characteristic frequency at 10 mHz, 1.0 Hz and 30 kHz and layers of the REM are differentiated through various shades.) ..... 59

Figure 15 (a) Normalized permeate flux  $J$  under different operational conditions for the anodic CFER in backwash mode of  $150 \text{ mg L}^{-1}$  HA fouled REM; (b) EIS spectra in complete frequency range; (c) zoomed-in EIS spectra in high and mid frequency range; (d) Bode phase plot; initial membrane flux  $J_0 = 1592 \text{ LMH bar}^{-1}$ . (Solid lines represent TLM fit, unfilled symbols represent characteristic frequency at 10 mHz, 1.0 Hz and 30 kHz and layers of the REM are differentiated through various shades.)..... 62

Figure 16 (a) Normalized permeate flux  $J$  under different operation conditions for backwash regeneration of  $150 \text{ mg L}^{-1}$  HA fouled REM; (Backwash conditions: DI water and 40 mbar vacuum); (b) EIS spectra in complete frequency range; (c) zoomed-in EIS spectra in high and low frequency range; (d) Bode phase plot; initial membrane flux  $J_0 = 1405.0 \text{ LMH bar}^{-1}$ . (Solid lines represent TLM fit, unfilled symbols represent characteristic frequency at 10 mHz, 1.0 Hz, and 30 kHz and layers of the REM are differentiated through various shades.)..... 66

Figure 17 Normalized permeate flux  $J$  under different operational conditions for the anodic CFER in backwash mode of  $150 \text{ mg L}^{-1}$  HA fouled REM in long term experiment; BG: background, F: fouling, R: anodic CFER; initial membrane flux  $J_0 = 1480 \text{ LMH bar}^{-1}$ ; Duration of anodic CFER in backwash mode: 0.5 hour ..... 68

Figure 18 (a) Normalized permeate flux  $J$  under different operational conditions for regenerations of 0.001 wt% polystyrene fouled REM, initial membrane flux  $J_0 = 2286.0 \text{ LMH}$ ; (b) filtration law (Equation 9) fit of permeate flux, fit equation:  $y = a*x + b$ ,  $R^2$  after the exponential fit Line 1:0.995, Line 2: 0.926..... 71

Figure 19 EIS spectra (a) and Bode phase plot (b) in cathodic CFER of polystyrene fouled membrane in backwash mode; EIS spectra (c) and Bode phase plot (d) in anodic CFER of polystyrene fouled membrane in backwash mode. (Solid lines represent TLM fit, unfilled symbols represent characteristic frequency at 10 mHz, 1.0 Hz, and 30 kHz and layers of the REM are differentiated through various shades.) ..... 72

Figure 20 LSV of (a) COU and (c)  $p$ -CBA (background subtracted) with different concentrations, and relationship between peak currents and concentrations with linear regression fit of the data for (b) COU and (d)  $p$ -CBA. In panel (c), hollow symbols and solid lines represent experimental and simulation data, respectively. Temperature:  $25^\circ\text{C}$  and electrolyte:  $1.0 \text{ M KH}_2\text{PO}_4$  (pH 5.8). ..... 86

Figure 21 LSV scans of  $5 \text{ mM COU}$  (background subtracted) under different scan rates and solution pH values, (a) pH 2.16, (b) pH 5.80 and (c) pH 11.95 (d) Relationship between peak current and square-root of scan rate in different pH solutions. In panel (b), hollow symbols and solid lines represent experimental and simulation data, respectively. Temperature:  $25^\circ\text{C}$  and electrolyte:  $1.0 \text{ M KH}_2\text{PO}_4$  (see each panel for pH). ..... 87

LIST OF FIGURES (continued)

Figure 22 Bulk oxidation of 1 mM COU at 2.0 V/SHE and a temperature of (a) 15 °C, (b) 25 °C, and (c) 35 °C, respectively. (d) Arrhenius plot for the oxidation of COU at 2.0 V/SHE. ● and ■ represent reactant (COU) and product (7-OH COU), respectively. Experiments were performed in duplicate, and the 1<sup>st</sup> order reaction rate model was fitted to both data sets simultaneously (dashed line). Electrolyte: 100 mM KH<sub>2</sub>PO<sub>4</sub> (pH 4.5)..... 89

Figure 23 DFT determined E<sub>a</sub> versus electrode potential profiles. Profile for OH<sup>•</sup> taken from Chaplin *et al.* [256] Squares represent experimental values determined for COU oxidation in RDE experiments..... 92

Figure 24 Free energy diagram of COU oxidation by ECE mechanism..... 95

Figure 25 XRD patterns of the Ti<sub>n</sub>O<sub>2n-1</sub> samples at pristine state and after anodic and cathodic polarizations in (A) 1 M H<sub>2</sub>SO<sub>4</sub>, (B) 2 M HClO<sub>4</sub>, and (C) 2 M HCl solutions. Characteristic peak of Ti<sub>4</sub>O<sub>7</sub> is shown as the dashed pink line (2θ = 20.78), and 2θ angle position at 22.80° is shown as green vertical line. AP and CP stand for anodic polarization and cathodic polarization, respectively. .... 107

Figure 26 Surface images collected in the same area at (A) pristine, (B) post anodic polarization in H<sub>2</sub>SO<sub>4</sub> electrolyte, and (C) post cathodic polarization states in H<sub>2</sub>SO<sub>4</sub> electrolyte. (D) Topographic mapping of this area. (Dashed circles represent the actual size of UME tip.) ..... 111

Figure 27 Averaged kinetic change in 1 M H<sub>2</sub>SO<sub>4</sub> (▲), 2 M HClO<sub>4</sub> (●) and 2 M HCl (■) electrolyte at post (A) anodic and (B) cathodic polarizations. Error bars represent 95% confidence interval. .... 112

Figure 28 (A) XRD patterns of different Magnéli phase mixtures, and (B) steady state surface hydroxyl radical concentration on different samples in a dead-end flow-through setup at room temperature. The number on top of each data point in (B) represents the n in Ti<sub>n</sub>O<sub>2n-1</sub>. Solution: 0.1 mM terephthalic acid in 1 M KH<sub>2</sub>PO<sub>4</sub> (pH 5.8). The solution resistance corrected electric potentials on Sample 1 to 5 are 3.32, 3.29, 3.35, 3.38 and 3.40 V, respectively. Permeate flux on Sample 1 to 5 (LMH): 780, 840, 900, 720, 1080. Transmembrane pressure: 1.03 bar. .... 115

Figure 29 XPS spectra of Ti<sub>n</sub>O<sub>2n-1</sub> electrode after 30 mins' anodic polarization in 1 M H<sub>2</sub>SO<sub>4</sub> electrolyte at 20 mA cm<sup>-2</sup>. (A) Full spectrum, (B) S 2p doublet regions, and (C) Ti 2p doublet regions. .... 117

Figure 30 Normalized concentration of oxidant in the pore at various convection velocities under (a) 100 mV overpotential and (b) 10 mV overpotential. Green dashed line represents the boundary between active and support layers. .... 126

Figure 31 Normalized overpotential decay in the pore at various convection velocities under (a) 100 mV overpotential and (b) 10 mV overpotential. Green dashed line represents the boundary between active and support layers. .... 126

Figure 32 Molecular weight cutoff determination of a pristine TiO<sub>2</sub> membrane and REM ..... 128

Figure 33 Reproducibility of polystyrene microspheres fouling and regeneration on REM under anodic CFER in backwash mode, initial flux J<sub>0</sub> (Exp 1) = 2285.6 LMH; J<sub>0</sub> (Exp 2) = 2374.7 LMH..... 129

LIST OF FIGURES (continued)

Figure 34 EIS spectra in repeated anodic CFER in backwash mode of polystyrene fouled membrane (Exp 2). ..... 130

Figure 35 Reproducibility of polystyrene microspheres fouling and regeneration on REM under cathodic CFER in backwash mode, initial flux  $J_0$  (Exp 1) = 2291.7 LMH;  $J_0$  (Exp 2) = 2390.1 LMH..... 131

Figure 36 EIS spectra in repeated cathodic CFER in backwash mode of polystyrene fouled membrane (Exp 2) ..... 132

Figure 37 Concentrations of redox active species during filtration process ..... 134

Figure 38 Tafel plot and its linear fit; Fit equation:  $\log(i) = 2.43\eta - 5.78$ ; R-square = 0.9956 ..... 140

Figure 39 EIS spectra in multi-cycle test of anodic regeneration of humic acid fouled REM in backwash mode, and (a)- (e) represent Cycle 1 - 5. .... 141

Figure 40 zeta-potential of polystyrene microspheres in pH range 1 to 11 ..... 143

Figure 41 Change in polystyrene concentration in feed solution during fouling experiment; A: the fouling experiment before cathodic CFER with backwash; B: the fouling experiment before anodic CFER with backwash; fit equation:  $C_A = C_{A0} \cdot \exp(k \cdot t)$ ;  $R^2$  after the exponential fit A:0.99765, B: 0.99591 ..... 144

Figure 42 Normalized permeate flux  $J$  under different operation conditions for backwash regeneration of 150 mg L<sup>-1</sup> HA fouled REM; (Backwash conditions: 100 mM NaClO<sub>4</sub> and 40 mbar vacuum); initial membrane flux  $J_0 = 1295.1$  LMH bar<sup>-1</sup>. ..... 145

Figure 43 System schematic for voltammetry and bulk oxidation experiments. ① working electrode, ② counter electrode, ③ reference electrode, and ④ Nafion membrane. .... 150

Figure 44. LSV on BDD of (a) TA and (b) *p*-BQ with different concentrations. Temperature: 25°C and electrolyte: 1.0 M KH<sub>2</sub>PO<sub>4</sub> (pH adjusted to 6.37 with NaOH for TA LSV, and pH 5.8 for BQ LSV)..... 152

Figure 45 LSV on Pt of (a) COU (background subtracted), (b) *p*-CBA, and (c) TA with different concentrations on a platinum disk electrode (surface area 0.03 cm<sup>2</sup>). Temperature: 25°C. Electrolyte: 1 M KH<sub>2</sub>PO<sub>4</sub> (pH 5.8) for COU LSV, 0.1 M HClO<sub>4</sub> (pH 1.0) for *p*-CBA LSV, and 1 M KH<sub>2</sub>PO<sub>4</sub> (pH adjusted to 6.37 with NaOH) for TA LSV. .... 153

Figure 46 CV on BDD of 5 mM COU (red dashed line) in 1.0 M K<sub>2</sub>HPO<sub>4</sub> electrolyte (background, black solid line). Temperature: 25°C and electrolyte: 1.0 M KH<sub>2</sub>PO<sub>4</sub> (pH 5.8). ..... 154

Figure 47 Bulk oxidation on BDD of 1 mM COU at 1.7 V/SHE and a temperature of (a) 15 °C, (b) 25 °C, and (c) 35 °C, respectively. (d) Arrhenius plot for the oxidation of COU at 1.7 V/SHE. ● and ■ represent reactant (COU) and product (7-OH COU), respectively. Experiments were performed in duplicate, and the 1<sup>st</sup> order reaction rate was fitted to both data sets simultaneously (dashed line). Electrolyte: 100 mM KH<sub>2</sub>PO<sub>4</sub> (pH 4.5). ..... 156

LIST OF FIGURES (continued)

Figure 48 Bulk oxidation on BDD of 0.1 mM TA at 3.0 V/SHE and a temperature of (a) 15 °C, (b) 25 °C, and (c) 35 °C, respectively. ● and ■ represent reactant (TA) and product (2-OH TA), respectively. Experiments were performed in duplicate, and the 1<sup>st</sup> order reaction rate was fitted to both data sets simultaneously (dashed line). Electrolyte: 100 mM KH<sub>2</sub>PO<sub>4</sub> (pH 4.5)..... 157

Figure 49 Bulk oxidation on BDD of 1 mM *p*-BQ at 3.0 V/SHE and a temperature of (a) 25 °C, (b) 35 °C, (c) 35 °C, and (d) 45 °C, respectively in a H-cell jacketed glass reactor. Experiments were performed in duplicate, and the 1<sup>st</sup> order reaction rate was fitted to both data sets simultaneously (dashed line). Electrolyte: 100 mM KH<sub>2</sub>PO<sub>4</sub> (pH 4.5)..... 158

Figure 50 Transition state structures for nucleophilic attack of OH<sup>-</sup> on: a) COU; b) TA; c) *p*-BQ; d) *p*-CBA. .... 160

Figure 51 Laser marking pattern sketch..... 161

Figure 52 Cyclic voltammetry on UME in 5 mM Ru(NH<sub>3</sub>)<sub>6</sub>Cl<sub>3</sub> and 100 mM KCl ..... 166

Figure 53 CV of Ti<sub>n</sub>O<sub>2n-1</sub> electrode in 1 M NaClO<sub>4</sub> aerated solution (solid blank line) and argon purged solution (dashed orange line) ..... 167

Figure 54 Summary of Mott Schottky results of Ti<sub>n</sub>O<sub>2n-1</sub> at different states in (A)-(C) 1 M H<sub>2</sub>SO<sub>4</sub>, (D)-(F) 2 M HClO<sub>4</sub>, and (G)-(I) 2 M HCl electrolytes. Hollow symbols and solid lines represent experimental and simulation data, respectively..... 168

Figure 55 Summary of film resistivities of Ti<sub>n</sub>O<sub>2n-1</sub> at different states in (A)-(C) 1 M H<sub>2</sub>SO<sub>4</sub>, (D)-(F) 2 M HClO<sub>4</sub>, and (G)-(I) 2 M HCl electrolytes Hollow symbols and solid lines represent experimental and simulation data, respectively..... 170

Figure 56 XRD patterns of control samples at open circuit potential in (A) 1 M H<sub>2</sub>SO<sub>4</sub>, (B) 2 M HClO<sub>4</sub>, and (C) 2 M HCl..... 172

Figure 57 Electrochemical impedance spectroscopy of Ti<sub>n</sub>O<sub>2n-1</sub> at different states in (A) 1 M H<sub>2</sub>SO<sub>4</sub>, (B) 2 M HClO<sub>4</sub>, and (C) 2 M HCl. Hollow symbols and solid lines represent experimental and simulation data, respectively. .... 173

Figure 58 Laser marked patterns shown in (A) overview by profilometer, (B) single view by profilometer, (C) overview by SECM (Ru(NH<sub>3</sub>)<sub>6</sub>Cl<sub>3</sub> redox reaction), (D) single view by SECM (oxygen reduction reaction) ..... 175

Figure 59 SECM Images of Ti<sub>n</sub>O<sub>2n-1</sub> at different states in 1 M H<sub>2</sub>SO<sub>4</sub> electrolyte at (A)-(C) area 1, (D)-(F) area 2, (G)-(I) area 3, (J)-(L) area 4, and (M)-(O) area 5..... 176

Figure 60 SECM Images of Ti<sub>n</sub>O<sub>2n-1</sub> at different states in 2 M HClO<sub>4</sub> electrolyte at (A)-(C) area 1, (D)-(F) area 2, (G)-(I) area 3, (J)-(L) area 4, and (M)-(O) area 5..... 177

LIST OF FIGURES (continued)

Figure 61 SECM Images of  $Ti_nO_{2n-1}$  at different states in 2 M HCl electrolyte at (A)-(C) area 1, (D)-(F) area 2, (G)-(I) area 3, (J)-(L) area 4, and (M)-(O) area 5. .... 178

Figure 62 (A) Image collected in 5 mM  $Ru(NH_3)_6Cl_3$  in 100 mM KCl by SECM, and (B) probe approach curve collected at point 1 at pristine, post anodic and cathodic polarizations. Solid lines and hollow points represent experimental data and simulation, respectively..... 183

Figure 63 Topographic images collected by oxygen reduction reaction in SECM for  $Ti_nO_{2n-1}$  samples studied in (A)  $H_2SO_4$ , (B)  $HClO_4$ , and (C) HCl cases..... 186

Figure 64 Thermogravimetric analysis results of  $Ti_nO_{2n-1}$  in air at different temperature ramps..... 187

Figure 65 Activation energy required for the conversion from  $Ti_4O_7$  to  $Ti_nO_{2n-1}$  ( $n > 4$ ) ..... 187

## LIST OF ABBREVIATIONS

AFM	Atomic Force Microscopy
AOPs	Advanced Oxidation Processes
BDD	Boron Doped Diamond
CFER	Chemical Free Electrochemical Regeneration
CLSM	Confocal Laser Scanning Microscopy
CNT	Carbon Nanotube
CV	Cyclic Voltammetry
DFT	Density Functional Theory
EAOPs	Electrochemical Advanced Oxidation Processes
EIS	Electrochemical Impedance Spectroscopy
ESR	Electron Spin Resonance
LSV	Linear Sweep Voltammetry
MWCO	Molecular Weight Cutoff
NOM	Natural Organic Matter
OCP	Open Circuit Potential
OH <sup>•</sup>	Hydroxyl Radical
QRE	Quasi-Reference Electrode
REM	Reactive Electrochemical Membrane
SECM	Scanning Electrochemical Microscopy
SHE	Standard Hydrogen Electrode
TGA	Thermogravimetric Analysis
TLM	Transmission Line Model
TMP	Transmembrane Pressure
UF	Ultrafiltration
UME	Ultramicroelectrode
UTDR	Ultrasonic Time-Domain Reflectometry
XPS	X-ray Photoelectron Spectroscopy
XRD	X-ray Powder Diffraction

## SUMMARY

This dissertation focused on developing a mechanistic understanding of electrochemical processes that occur on a substoichiometric  $\text{TiO}_2$  ( $\text{Ti}_n\text{O}_{2n-1}$ ) electrode. Specific goals of this work were to 1) understand the effectiveness of electrochemical regeneration of  $\text{Ti}_n\text{O}_{2n-1}$  based reactive electrochemical membranes (REMs) that were fouled by organic compounds and particles and develop efficient membrane regeneration protocols, 2) determine appropriate hydroxyl radical ( $\text{OH}^\bullet$ ) probes that can be used to characterize electrochemical advanced oxidation processes (EAOPs), and 3) investigate passivation and reactivation mechanisms on  $\text{Ti}_n\text{O}_{2n-1}$  electrodes. These goals were accomplished by the development of a comprehensive methodology that utilized advanced experimental and theoretical techniques. Experimental techniques included bulk oxidation experiments, scanning electrochemical microscopy (SECM), electrochemical impedance spectroscopy (EIS), and a variety of other electrochemical methods. The experimental data was interpreted by theoretical techniques, which included density functional theory (DFT) simulations, transmission line modeling (TLM), and linear sweep voltammetry (LSV) modeling. The combination of these methods allowed for a greater understanding of the processes that occurred at  $\text{Ti}_n\text{O}_{2n-1}$  electrodes.

The main achievements of this work were 1) development of a TLM to interpret membrane fouling on an asymmetric REM, 2) development of a chemical free electrochemical regeneration (CFER) scheme to recover the flux at REMs fouled by organic compounds and particles, 3) determination of appropriate  $\text{OH}^\bullet$  probes to characterize electrochemical systems, and 4) identification of surface passivation and reactivation mechanisms on  $\text{Ti}_n\text{O}_{2n-1}$ , which are discussed in more detail in the following paragraphs.

A non-invasive EIS method was successfully used to spatially characterize membrane fouling during multiple membrane fouling and regeneration events, and a TLM was developed to interpret the EIS spectra collected from an asymmetric REM. Based on the fouling mechanisms found using EIS characterizations, a CFER method was established, which utilized electrochemical regeneration in a backwash mode. Compared to current methods for membrane regeneration, such as offline chemical

## SUMMARY (continued)

cleaning, the advantages of CFER method include 1) complete recovery of membrane flux, 2) cost effectiveness, and 3) minimal operating time, which minimizes membrane downtime.

The formation of OH<sup>•</sup> is the key to the successful operation of EAOPs, and therefore detection and quantification of OH<sup>•</sup> are necessary to characterize the performance of electrode materials. Improper selection of OH<sup>•</sup> probes in electrochemical systems exists due to neglect of possible direct electron transfer reactions of these probes, leading to a false positive detection of OH<sup>•</sup>. Results from bulk oxidation experimental and LSV were compared to DFT simulation to determine the validity of OH<sup>•</sup> probes used in electrochemical processes. Results from this work indicated that among the commonly used probes, terephthalic acid is the most selective OH<sup>•</sup> probe, due to its high resistance to direct electron transfer and stability against reduction and nucleophilic attack.

Although Ti<sub>n</sub>O<sub>2n-1</sub> has been considered as a promising electrode material for EAOPs, its electronic conductivity and electrochemical activity suffer from gradual deterioration during extended anodic polarization. The mechanisms responsible for these observations are under debate. In our study, we determined that decreases in electronic conductivity and electrochemical reactivity were related to a depletion of H-doping after anodic polarization, which was largely recovered after cathodic treatments. However, the formation of a passivation film occurred when Ti<sub>n</sub>O<sub>2n-1</sub> was electrolyzed in H<sub>2</sub>SO<sub>4</sub> electrolytes, which was related to sulfate adsorption at the electrode surface. This study also revealed the relation between the kinetics for OH<sup>•</sup> formation and the Ti<sub>n</sub>O<sub>2n-1</sub> phase. Results indicated a decrease in the kinetics of OH<sup>•</sup> formation with increasing  $n$  in Ti<sub>n</sub>O<sub>2n-1</sub>. Therefore, to maintain the best performance, the Ti<sub>4</sub>O<sub>7</sub> phase should be maintained and frequent cathodic polarizations should be implemented to maintain optimal conductivity and electrochemical activity.

## I. INTRODUCTION

### *1.1 Background*

A considerable fraction of the world's population has inadequate access to clean drinking water due to climate change and increasing water usage for domestic, agricultural, and industrial applications [1]. Use of contaminated water containing pathogens, toxins, and suspensions leads to acute and chronic illness, and is considered as a main reason of death in many developing countries [2]. In recent decades, many governments have started to introduce strict regulations that limit the discharge of pollutants, due to the increased public awareness of these environmental problems, which has led to a prominent increase in research concerned with water quality.

A grand challenge in developing an effective environmental remediation strategy is the ability to implement technologies that are technically efficient, economically viable, sustainable and capable to treat a broad range of water contaminants. Treatment methods can be classified into two categories, physical separation and chemical oxidation [3]. Separation processes, such as coagulation, flocculation, sedimentation, ion exchange, and membrane filtration, are based on the physical interaction between contaminants and treatment modules [4–7]. Several disadvantages are related to the physical removal, for example, in coagulation and flocculation, pH adjustment is needed before and after the treatment, both processes are sensitive to temperature changes, higher dosages of coagulants and clarifying agents are required due to insufficient charge neutralization, and excessive sludges are produced [8]. Membrane filtration suffers from membrane fouling, and periodic physical and chemical cleanings are needed to maintain its performance [9–12]. Chemical oxidation processes include chlorination, ozonation, UV disinfection, and Fenton processes, and the removal of contaminants are realized through the reaction with the strong oxidizing chemicals [3]. Studies on water treatment using chlorination produce chlorinated byproducts, such as chloroform and chlorinated organics, which lead to cancer in humans [13]. In advanced oxidation processes, reactive oxygen species are produced through the decomposition of ozone and water,

and can react with a broad range of contaminants at diffusion limited rates. However, high dosages of ozone and high intensity UV lamps related high costs, treatment of Fenton slurries, as well as the recycle of photocatalyst from the treated water are major challenges to operate both processes effectively [14–18].

In recent years, electrochemical advanced oxidation processes (EAOPs) have received greater attention for drinking water and wastewater treatment [19–26]. EAOPs offer numerous advantages for water treatment, which include a low operational cost, high energy efficiency, high reactivity, and chemical addition is not needed [19,23]. During EAOPs, hydroxyl radicals ( $\text{OH}^\bullet$ ) are produced at the anode surface from water oxidation and these radicals react with contaminants in water. EAOPs have been limited by their low active surface areas and reactor configurations that lead to low mass transfer rates. Recent work with REMs have addressed these problems, as REMs have high electroactive surface area and are operated in a flow-through mode, which greatly enhances mass transport [27–29]. However, there are many challenges associated with REM for use in drinking water and wastewater treatment.

REM suffers from membrane fouling by organics and particulates. Conventional methods for membrane regeneration are ineffective, for example, physical cleaning cannot completely recover membrane flux, and chemical cleaning requires massive investment in chemical synthesis and disposal. Therefore, electrochemical processes should be explored on REM to develop a cost effective and highly efficient membrane regeneration scheme without chemicals addition.

Appropriate identifying and quantifying  $\text{OH}^\bullet$  formation kinetics are essential to characterize the performance of REM in EAOPs. Characterization methods in electrochemical systems are realized through the interaction of either spin traps or probe molecules with  $\text{OH}^\bullet$ . However, the stabilities of spin traps and probe molecules have never been examined in the electrochemical systems, which could lead to a false positive detection of  $\text{OH}^\bullet$ .

As one of most promising electrode materials for use in EAOPs, energy devices and photocatalysis, substoichiometric  $\text{TiO}_2$  ( $\text{Ti}_n\text{O}_{2n-1}$ ) has received a great amount of attention due to its environmental

compatibility and low cost. However, the primary concerns are associated with the longevity of  $\text{Ti}_n\text{O}_{2n-1}$  electrodes when used upon extended anodic polarization in the presence of different electrolytes, and the effect of deteriorated conductivity and electrochemical activity on its performance in many applications.

## ***1.2 Research objectives***

The overall goal of this research was to develop a mechanistic understanding of electrochemical processes that occur on a porous  $\text{Ti}_n\text{O}_{2n-1}$  electrode. Specially, REM fouling and regeneration were studied using EIS, and a TLM was developed to interpret the experimental EIS data. The validity of  $\text{OH}^*$  probes used in the electrochemical processes was examined using both experimental and theoretical methods to appropriately identify  $\text{OH}^*$  produced in EAOPs. A gradual loss of conductivity and electrochemical activity during anodic polarizations was found on  $\text{Ti}_n\text{O}_{2n-1}$  based REMs, the mechanism of such observation and the reactivation strategy was studied and evaluated in three different electrolytes (HCl,  $\text{HClO}_4$ , and  $\text{H}_2\text{SO}_4$ ). The specific objectives of this research were as follows:

### *1) Theoretical study of reactive electrochemical membrane fouling mechanisms using a transmission line model*

Membrane fouling deteriorates membrane filtration performance, as it leads to greater power consumption and reduced membrane life, which brings up serious economic and operational challenges [30–34]. Understanding fouling mechanisms, early fouling detection, and efficient, cost effective and sustainable regeneration methods are extremely necessary to optimize the membrane module design, improve the membrane filtration performance, and extend membrane lifetime. Traditional membrane fouling detection methods include monitoring the change in transmembrane pressure or permeate flux, visual methods such as scanning electron microscopy and confocal laser scanning microscopy, and ultrasonic time-domain reflectometry. The limitations associated with these methods include a restriction to bench-scale, unable to identify multiple simultaneous fouling mechanism, destructive, and short penetration depth.

This work utilized an EIS method for membrane fouling detection, and a TLM was developed to interpret the EIS spectrum. Several membrane fouling mechanisms, such as monolayer adsorption, pore constriction, and intermediate pore blockage, were simulated using TLMs, and the simulated EIS spectra showed distinctive signatures of different fouling mechanisms, which allowed it to be used to spatially characterize membrane fouling and regeneration at an asymmetric REM.

## *2) Development of a chemical free electrochemical regeneration method on reactive electrochemical membranes*

Traditional membrane regeneration methods include physical and chemical protocols, however neither method is effective from a performance, cost or environmental ramification stand point. Physical cleaning, which is often referred to high flow backwash, is able to partially regenerate membrane flux by removing the cake layer and a portion of the porous matrix foulants. Chemical cleaning, such as use of high concentration of acid or base, requires substantial investment in chemical synthesis, shipment, storage, and waste disposal. The use of REMs can directly address these disadvantages by using electrochemical regeneration protocols. The polarization of the REM as either an anode or cathode can remove foulants by a combination of electrochemical reactions between the electrode and adsorbed foulants and the formation of hydroxyl radicals, O<sub>2</sub>, or H<sub>2</sub> from water electrolysis. The only two reagents required in these methods are water and electrons, which eliminate the need for chemical addition.

In this work, EIS was used to study the membrane fouling mechanisms on the REM, since understanding the fouling mechanisms is the key to develop effective membrane regeneration strategies. The performances of electrochemical regeneration in both forward and backward wash modes were compared, and a multiple-cycle regeneration test was conducted to evaluate the long-term performance of this method on a humic acid fouled REM. Membrane fouling with polystyrene microsphere, a model foulant with well-defined particle size and shape, was identified as causing intermediate pore blockage and used to justify the validity of the TLM developed in *research objective 1*.

### 3) Examination of the validity of hydroxyl radical probes used in electrochemical systems

The OH<sup>•</sup> is a strong oxidant, and reacts with many organic compounds with diffusion-limited rate constants to produce innocuous end products. Quantification of OH<sup>•</sup> production and understanding its formation mechanisms are goals in many scientific areas. However, in electrochemical systems, such as EAOPs, photocatalysis, and energy conversion/storage, due to the neglect of alternative reaction mechanisms, such as direct electron transfer and the Forrester-Hepburn mechanism, many inappropriate OH<sup>•</sup> probes have been used for characterization purposes.

This work studied the suitability of four commonly used OH<sup>•</sup> probes, i.e., coumarin, *p*-chlorobenzoic acid, terephthalic acid, and *p*-benzoquinone, for use in EAOPs. Experimental methods included linear sweep voltammetry to resolve the oxidation potential required for the direct electron transfer reaction, and bulk oxidation experiments to quantify the OH<sup>•</sup> formation and probe molecule removal kinetic rate constants. Simulations using density functional theory was used to determine redox potentials for probe compounds and if non-OH<sup>•</sup> mediated pathways were feasible for the probe compounds.

### 4) Investigation of surface passivation and reactivation on a $Ti_nO_{2n-1}$ reactive electrochemical membrane

The key to operating EAOPs is the formation of OH<sup>•</sup> *via* electrochemical oxidation of water. It is reported that  $Ti_nO_{2n-1}$  suffers from a gradual loss of conductivity and electrochemical activity in the electrochemical oxidation in the presence of sulfate and sulfide ions, however, the mechanisms are still under debate.

In this work, the mechanisms of surface passivation and reactivation were studied in sulfate, perchlorate, and chloride electrolytes. Electronic conductivity and electrochemical activity were monitored at the pristine state and after anodic and cathodic polarizations using Mott-Schottky analysis, two-point probe method, EIS, and scanning electrochemical microscopy (SECM). We also developed the methodology of using SECM to interrogate the localized kinetic variations among the three states at precise locations at the electrode surface. A statistical analysis of these local kinetic measurements by SECM were

compared with bulk kinetics, which was determined by EIS analysis. The results of this study were discussed in a broader context, such as the implication of surface passivation and reactivation on energy technology, and the effect of different phases of  $Ti_nO_{2n-1}$  on the  $OH^\bullet$  production used for water treatment.

### **1.3 Outlines of thesis**

The current state of knowledge in the field regarding membrane fouling detection methods, fouling control and regeneration schemes on conductive membranes, common  $OH^\bullet$  probes used to characterize EAOPs, and studies of  $Ti_nO_{2n-1}$  surface passivation and reactivation is presented in **Chapter 2**. **Chapter 3** comprises the work that was published in Journal of Membrane Science in 2016 entitled “*Electrochemical impedance spectroscopy study of membrane fouling characterization at a conductive sub-stoichiometric  $TiO_2$  reactive electrochemical membrane: Transmission line model development*” with co-author Brian P. Chaplin. This paper addresses *research objective 1* and is a comprehensive study of TLM development and various membrane fouling mechanism simulations. **Chapter 4** comprises the work that was published in Journal of Membrane Science in 2016 entitled “*Electrochemical impedance spectroscopy study of membrane fouling and electrochemical regeneration at a sub-stoichiometric  $TiO_2$  reactive electrochemical membrane*” with co-author Lun Guo and Brian P. Chaplin. This paper addresses *research objective 2*, uses the TLM model developed in *research objective 1* to understand the EIS spectra collected on a humic acid fouled REM and establishes a chemical free electrochemical regeneration scheme, and validates the TLM with an intermediate pore blockage membrane fouling mechanism produced by polystyrene microspheres. **Chapter 5** comprises the work that was published in Environmental Science & Technology in 2017 entitled “*A mechanistic study of the validity of using hydroxyl radical probes to characterize electrochemical advanced oxidation processes*” with co-author Brian P. Chaplin. This paper addresses *research objective 3*, and uses both experimental and theoretical methods to justify the validity of commonly used  $OH^\bullet$  probes in electrochemical systems. **Chapter 6** comprises a paper in preparation for submission to Journal of the American Chemical Society with co-author Soroush Almassi, Robert J. LeSuer, and Brian P. Chaplin. This paper addresses *research objective 4*, and uses advanced electrochemical methods, as well as X-ray based

diffractometry and photoelectron spectroscopy to investigate the mechanism of surface passivation and reactivation of  $Ti_nO_{2n-1}$  in three different electrolytes:  $H_2SO_4$ ,  $HClO_4$  and  $HCl$ . In **Chapter 7**, concluding remarks and future research direction are discussed.

## II. STATE OF KNOWLEDGE

### ***2.1. Techniques of monitoring membrane fouling***

An accumulation of solutes, such as physical, chemical and biological substances, on the membrane surface or in the membrane matrix, causes membrane fouling during water filtration [35]. Although membrane fouling is considered as a complicated phenomenon due to the variety of foulants and their complex physical and chemical interactions with membrane surfaces, it is generally accepted that the rapid buildup of solutes at the membrane surface, which is also known as concentration polarization, leads to the initial membrane permeate flux decline, and the long-term decline is attributed to the fouling in the membrane matrix [36–38]. It is important to understand the type of foulants and fouling mechanisms before an effective fouling mitigation or membrane regeneration scheme can be implemented [39]. Membrane fouling can be classified as reversible and irreversible, and the distinction between these two entirely depends on the membrane operation and cleaning protocol [12,40]. Reversible fouling refers to deposition of retained solutes on the membrane surface, leading to the formation of a cake layer and can be completely removed by the backwash flow, and irreversible fouling refers to the retained solutes within the membrane matrix after the backwash [40]. Membrane fouling can be generalized as occurring through three classical mechanisms – pore blockage, pore constriction, and cake layer formation, as shown in Figure 1 [41]. Pore blockage (Figure 1A) takes place when the entrance to a pore is completely closed by a particle. Pore constriction (Figure 1B) is the reduction of the pore channel within a membrane due to foulant adsorption. Cake layer formation (Figure 1C) occurs when particles are too large to enter the pores and thus collect on the membrane surface.

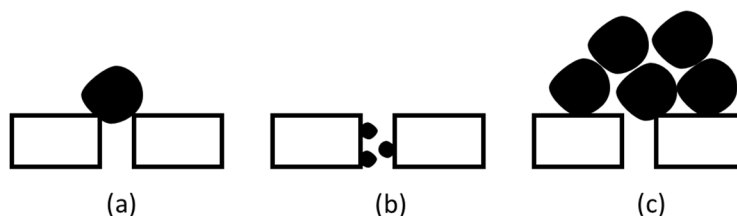


**Figure 1** Mechanisms for fouling in membrane filtration: (a) pore blockage, (b) pore constriction, and (c) cake layer formation

Fouling behavior is significantly affected by different chemical and physical properties of the foulants, such as molecular size and structure, functional groups, and surface charge [35]. Natural organic matter (NOM) is the most commonly found foulant in natural waters, which possesses various functional groups including, phenolic, hydroxyl, carbonyl, amine, sulfide, and carboxylic groups and a wide range of molecular weights [42]. Humic substances, as one type of NOM, has been identified as a major foulant in membrane filtration and causes more fouling than any other NOM compound, due to its high adsorptive capacity on the membrane surface [43–46]. To maintain the economic viability of a membrane process, membrane fouling must be limited. It will be beneficial to understand the mechanisms responsible for membrane fouling in order to regenerate the fouled membrane efficiently and cost-effectively using appropriate regeneration methods, and thus techniques for monitoring fouling phenomena in membrane filtration are needed [42].

Techniques of monitoring membrane fouling are classified as destructive or non-destructive. Use of destructive methods requires the destruction of membrane in order to prepare the specimen, whereas the non-destructive method can be directly applied to an intact membrane module.

### *2.1.1 Destructive method of monitoring membrane fouling*

Generally, the membrane fouling morphology can be characterized using scanning electron microscopy (SEM), confocal laser scanning microscopy (CLSM) and atomic force microscopy (AFM).

These methods are considered as destructive, since the preparation of specimen requires the destruction of the original membrane structure.

SEM can provide visualization of membrane fouling, especially in high resolution images of fouling layer structures, the origins of foulants, and the size and shape of foulants, and therefore is able to aid in elucidation of fouling mechanisms. This method was used to study the membrane fouling through surface morphology and internal microstructure in membrane filtration of various aqueous sources [11,47–49]. However, the pretreatment of SEM specimen including sample dehydration and gold sputtering would inevitably destroy the original structure of membrane and fouling layer.

In CLSM observation, a laser beam is focused on the sample by the microscope objective, and then fluorescence is excited. The detector only allows the fluorescence light from the in-focus spot to pass through, and produces an image. The construction of a 3D image is possible when a number of optical images in the xy plane with different depths are taken. The advantage of using CLSM is that it can differentiate the foulants by using fluorescent probes, and the 3D images can offer more useful information about the structure of fouling layer. These advantages allow CLSM to be used extensively in understanding membrane fouling in membrane bioreactors [48,50].

AFM has been considered as a powerful tool for visualizing membrane fouling, since it can provide 3D images with atomic resolution and quantification of cake morphology from the analysis software. Another advantage of AFM is the mapping of force profile and adhesive force between two interacting surfaces, which are extremely important in understanding the membrane fouling behavior. As indicated by Bowen *et al.*, the adhesive force measurement by AFM allows one to compare the membrane to foulant, foulant to foulant, and foulant to cleaning agent interactions at a molecular level, consequently it offers fundamental information for understanding the fouling mechanism and determining effective cleaning strategies [10,49,51,52].

The disadvantage of using these destructive methods to monitor membrane fouling is the poor resolution achievable without using high beam energies which may lead to sample damage [36]. Besides, they offer little information on the progressive accumulation and buildup of fouling layers on the membranes due to the complicated surface.

### 2.1.2 Non-destructive methods of monitoring membrane fouling

In order to retain membrane structure and provide dynamic formation of membrane fouling, non-destructive methods are often used. As a straightforward observation method, direct pressure measurements (constant flux operation) or direct flux measurements (constant transmembrane pressure (TMP) operation) can be used to monitor membrane fouling. The relation between TMP and permeate flux can be interpreted using a resistance in series model [53–55]. This model in the simplest form, as shown in Equation 2-1, indicates that the permeate flux is proportional to the driving force (TMP) and inversely proportional to the cake layer, irreversible fouling, and membrane resistances.

$$J = \frac{\Delta P_r}{\mu(R_m + R_f + R_c)} \quad 2-1$$

where  $J$  ( $\text{m s}^{-1}$ ) is water flux,  $\Delta P_r$  is the TMP (Pa),  $\mu$  is the viscosity of permeate ( $\text{kg m}^{-1} \text{s}^{-1}$ ), and  $R_m$ ,  $R_f$ , and  $R_c$  are the resistances of membrane, irreversible fouling, and cake layer, respectively ( $\text{m}^{-1}$ ). Variations of this model exist by considering more resistance terms in Equation 2-1, such as pore adsorption, pore plugging, reversible fouling, and concentration polarization [53,54]. The limitation of the resistance in series model is that each of the experimentally obtained resistances are influenced by experiment methods, therefore resistances measured from different experimental sets are not comparable.

Many mathematical models have also been proposed to understand the membrane fouling mechanisms based on flux data under constant TMP [43,44,56,57]. The model at its basic form proposed by Hermia, as shown in Equation 2-2, is commonly used by calculating the change of filtrate volume at a certain time interval [56]. Although this method is easy to perform, it cannot distinguish the pore

constriction or plugging at two different layers in an asymmetric membrane and is unable to detect the extent of membrane fouling.

$$\frac{d^2t}{dV^2} = k\left(\frac{dt}{dV}\right)^n \quad 2-2$$

where  $t$  ( $s^{-1}$ ) is the filtration time,  $V$  ( $m^3$ ) is total filtered volume,  $k$  is the blocking law filtration coefficient, and  $n$  indicates the fouling mechanism. The fouling mechanisms determined by the model are summarized in Table I.

**Table I** DETERMINATION OF FOULING MECHANISMS BY FILTRATION MODEL

<b>Fouling Mechanism</b>	<b>N</b>
cake layer formation	0
intermediate blocking	1
pore constriction	1.5
complete pore blocking	2

Ultrasonic time-domain reflectometry (UTDR) is a technique, which uses sound waves to measure the location of an interface and is able to provide insight into the physical characteristics of the media where the sound waves travel. A reflected wave will occur when the ultrasonic waves encounter an interface between two media. The time interval between the initial injection of the waves and the detection of the reflective waves can be used to measure the distance between interfaces. UTDR was used to study membrane fouling and successfully detected the cake layer formation from the microfiltration of paper mill effluent [58,59]. However, the ultrasonic wave is not able to effectively penetrate the porous matrix and thus cannot detect fouling mechanisms related to pore constriction or plugging [36].

Electrochemical impedance spectroscopy (EIS) can be used as a non-invasive and non-destructive *in situ* membrane fouling characterization technique. EIS is a frequency domain method where a small-amplitude alternating potential is superimposed onto a constant applied potential on the working electrode.

Its high sensitivity towards interfacial processes, such as conductance and capacitance, and surface geometry makes EIS an ideal tool to evaluate membrane fouling [60]. Previous studies showed EIS measurements were able to characterize the skin layer conductances and capacitances of a multi-layer ultrafiltration polysulphone membrane, and to investigate the conductivity and dielectric permittivity dispersion of membrane before and after fouling [61–63]. However, the limitation of this work is that a Pt coating was added to the membrane to make it conductive, which does not represent the real morphology of the membrane, and Pt particles may block some of the membrane pores, leading to a change of the membrane morphology [36]. EIS measurements has also been implemented without changing the membrane morphology on reverse osmosis, forward osmosis and nanofiltration flat sheet membranes [64–66]. Bannwarth *et al.* placed a hollow fiber membrane between two electrodes, and the impedance can be measured in the 2-electrode method in a radial electric field [67,68]. To interpret the impedance spectrum, equivalent circuit model is used, which must provide a fit to the experimental data and represent the physical and electric processes in the system. The impedance of the ionic double layer at the electrode-electrolyte interface is added to the total impedance of the membrane when 2-electrode method is used, and therefore special attention is needed to construct the equivalent electric circuit.

## **2.2. Fouling control and membrane regeneration schemes on conductive membranes**

On conventional membranes, methods used for the fouling control and regeneration include pretreatment of the feed water to minimize fouling and membrane surface modification, which is usually performed on polymeric membranes. However, fouling control cannot permanently eradicate membrane fouling, since a suitable pretreatment can only effectively remove particulates, and part of bacteria and organics, and therefore a periodic membrane regeneration is still needed [69]. Membrane regeneration methods are comprised of physical and chemical cleaning. Physical cleaning, such as periodic backwash, can partially regenerate the membrane by physical shear forces [70]. Chemical cleaning is necessary to recover all the membrane flux, where acids, bases, chelatants, and surfactants are the commonly used agents. [10]. A higher concentration of chemical cleaning agents is usually required to increase the driving force

for the mass transport and achieve satisfying results. In addition, repeated chemical cleaning gradually degrades the lifetime of polymeric membranes, which leads to decreased water flux and rejection performance [69]. The cost of chemical synthesis, shipment, storage, disposal, and their consequence on the environment make chemical cleaning undesirable from both the environmental and economic standpoints.

Due to their conductive nature, conductive membranes introduce new ideas in fouling control and membrane regeneration, which include electrostatic repulsion and electrochemical regeneration. Foulants such as polysaccharides, oily emulsions, and humic substances, commonly found in natural waters and wastewaters, possess negative charges, which allow the rejection by a negatively charged membrane surface *via* electrostatic forces [71]. This method is realized on the polymeric membranes by grafting negatively charged polymers on the membrane surface [72,73], and can be readily implemented on the conductive membranes by a non-faradic charging process. Extensive studies have been carried out on carbon nanotube (CNT) based conductive membranes [71,74,75]. Lower fouling rates were found while treating Suwanee River fulvic acid and alginic acid solutions on an electro-negatively charged CNT conductive membrane, compared to the same membrane without an applied potential [71,75]. Theoretically, an electrostatic force could act as a fouling inhibitor, making the membrane surface impermeable to fouling agents, preventing foulants of the same charge from interacting with the surface, and resulting in reduced fouling rates. Electrostatic repulsion is achieved in a low ionic strength electrolyte (less than 1 mM) and increased ionic strength lowers the fouling control performance, as the non-faradaic process no longer dominates [75]. In addition to electrostatic repulsion on CNT membranes, electrochemical reduction of oxygen to hydrogen peroxide ( $\text{H}_2\text{O}_2$ ) can also occur on CNT cathodes, as shown in Equation 2-2, and the CNT with surface carboxylate groups is able to strongly chelate  $\text{Fe}^{2+}$  that can further reduce  $\text{H}_2\text{O}_2$  to hydroxyl radical ( $\text{OH}^\cdot$ ), as shown in Equation 2-3, through the Fenton process. The produced  $\text{Fe}^{3+}$  is able to be reduced by  $\text{H}_2\text{O}_2$  to recover the  $\text{Fe}^{2+}$  and yield  $\text{HO}_2^\cdot$  (Equation 2-4), which regenerates  $\text{Fe}^{2+}$ . This combined electrochemical Fenton process is reported to remove 4 times more total organic carbon than the single Fenton process or

electrochemical oxidation [74]. The organic removal *via* electrochemical oxidation was also reported on the CNT filter as anode, a study showed that the oxidation of the antibiotic tetracycline is mainly through direct electron transfer reaction, whereby dimethylamino group is oxidized [76].



Electrostatic repulsion can be considered as a method for fouling control, because it is only able to reject foulants of the same charge through physical interaction. Electrochemical oxidation can be deemed as a viable option for membrane regeneration, as it can remove the organic foulants by either direct electron transfer or strong oxidants produced *via* electrochemical oxidation reactions. The goal of electrochemical oxidation is to mineralize the contaminants to carbon dioxide, water, and inorganic compounds, or at least a less harmful product. Electrochemical oxidation can be divided into two categories: (1) direct oxidation at the anode surface *via* direct electron transfer, and (2) indirect oxidation using anodically formed oxidants *via*, for example, electrochemical advanced oxidation processes (EAOPs). Similar to the advanced oxidation process, the key oxidizing product is  $OH^\bullet$  in EAOP, a reactive oxygen species, which can react unselectively with most organic molecules with rate constants usually on the order of  $10^6$ - $10^9$   $M^{-1} s^{-1}$  [7]. The  $OH^\bullet$  in EAOP is produced *via* the oxidation of water on the anode surface, as shown in Equation 2-5, at a potential greater than 2.5 V vs a standard hydrogen electrode (SHE).



The inherent advantage of EAOP is its environmental compatibility and cost-effectiveness, since the main reagents, the electron and water, are not only clean, but also abundant in amount. Studies show that  $OH^\bullet$  can only be produced on the surfaces of anode materials, such as BDD [77–80], substoichiometric  $TiO_2$  ( $Ti_nO_{2n-1}$ ) and Nb-doped  $TiO_2$  [27,28,81],  $PbO_2$  [82,83], and doped- $SnO_2$  [84,85], however direct evidence does not exist on the generation of  $OH^\bullet$  from polymeric and carbon based conductive materials

(e.g., CNTs). Conductive membranes based on BDD,  $\text{Ti}_n\text{O}_{2n-1}$ , Nb-doped  $\text{TiO}_2$ ,  $\text{PbO}_2$ , and doped- $\text{SnO}_2$  are able to realize membrane regeneration through EAOPs, but comprehensive considerations are needed in membrane synthesis including cost, synthesis technique, and environmental compatibility.

### **2.3 Hydroxyl radical probes used in electrochemical systems**

As stated in the above section,  $\text{OH}^\bullet$ , as a reactive oxygen species, is the key to operate the EAOPs, and thereby enables the membrane regeneration strategy. Therefore, quantifying  $\text{OH}^\bullet$  production and understanding its formation mechanisms are important to characterize the performance of EAOPs based conductive membranes.

The short lifetime of  $\text{OH}^\bullet$  and high reactivity make its detection extremely difficult, and thus indirect methods are used. The first method involves electron spin resonance (ESR) spectroscopy in the presence of a spin trap, a compound that can selectively reacts with  $\text{OH}^\bullet$  to produce an adduct species which has an adequate lifetime to be detected in ESR. The most common spin traps for  $\text{OH}^\bullet$  detection are substituted nitrones, and 5,5-dimethyl-1-pyrroline N-oxide is commonly used due to its high selectivity for  $\text{OH}^\bullet$ , which has been widely used in many systems, such as photocatalysis [86–88], electrochemical oxidation [89–91], and Fenton-based oxidation processes [92–95]. Other spin traps, such as dimethyl sulphoxide [96–98], as well as tetramethyl-piperidine-1-oxyl and N-tert-butyl nitron derivatives [87,99], are also common  $\text{OH}^\bullet$  probes used in these aforementioned processes.

The other method is the use of probe molecules that selectively react with  $\text{OH}^\bullet$ , and often produce adduct species which can be detected analytically by chromatographic techniques. A number of compounds have been used, including coumarin [28,81,100–107], benzoic acid [108–111], salicylic acid [25,82,90,112], terephthalic acid [28,103,113–122], *p*-benzoquinone [27,100,123–125], *p*-chlorobenzoic acid [51,126–133], *p*-nitrosodimethylaniline [123,134–137], luminol [101], 3-carboxyproxyl [138], 1,4-dioxane [139], 1-propanol [110], and methylene blue dye [140]. The detection of  $\text{OH}^\bullet$  using probe molecules depends on either the removal of probe molecules or the appearance of an adduct product.

#### **2.4 Surface passivation and reactivation of $Ti_nO_{2n-1}$ in electrochemical systems**

The oxygen vacancy, as an intrinsic and shallow donor, is considered as the key to modifying the electronic and optical properties of  $TiO_2$  [141–143]. To minimize rutile  $TiO_2$ 's limitations, such as its fast electron-hole recombination and wide band gap energy ( $E_g = 3.0$  eV),  $Ti_nO_{2n-1}$ , with a smaller band gap and larger charge carrier density is becoming attractive [132,142,144]. These oxygen deficient materials are known collectively as Magnéli phases, with a general formula of  $Ti_nO_{2n-1}$  ( $4 \leq n \leq 10$ ) [145].

In spite of its great potential as material for memresistive and thermoelectric devices, and electrodes for EAOPs, visible light photocatalytic processes, and energy storage devices [27–29,146–151], it is reported that  $Ti_nO_{2n-1}$  is subjected to a gradual loss of electronic conductivity especially when used as an electrode during electrolysis with the presence of sulfate or sulfide ion [123,151–153]. Kao *et al.* claimed that the surface passivation can occur in both anodic and cathodic polarizations, and attributed the mechanisms to phase change from  $Ti_4O_7$  to  $Ti_6O_{11}$  in anodic polarization, and formation of titanium hydrate in cathodic polarization [151]. Chen *et al.* compared the electrochemical stability between a  $Ti_nO_{2n-1}$  and Nb-doped  $TiO_2$  by the EIS method, and the distinction between these two materials is the crystal structure, where Nb-doped  $TiO_2$  retains the rutile structure after the introduction of Nb dopant, whereas  $Ti_nO_{2n-1}$  is oxygen deficient due to the presence of crystallographic shear plane [152]. Their results showed loss of electrochemical activity on both crystals, and furthermore, the loss on  $Ti_nO_{2n-1}$  in sulfate electrolyte was irreversible due to the formation of more thermodynamic stable  $TiO_2$ , while that on Nb-doped  $TiO_2$  was reversible due to the conversion between  $Ti^{3+}$  and  $Ti^{4+}$  taking place in the same rutile phase. El-Sherif *et al.* studied the electrochemical activity of  $Ti_nO_{2n-1}$  through monitoring the electrochemical kinetics in removing sulfide, and found the same observation after the anodic polarization, however on the contrary to Chen *et al.*, they asserted that this loss of electrochemical activity can be reversed by periodic polarity reversal [153]. The same observation has been reported by Bejan *et al.* by monitoring the kinetics of removing *p*-benzoquinone in 100 mM  $NaClO_4$  with 40 mA applied current [123].

The disagreements in the literature regarding the passivation mechanism of  $\text{Ti}_n\text{O}_{2n-1}$  are not clear, and may be attributed to the presence of different Magnéli phases in the tested samples. More comprehensive studies on the passivation and reactivation of  $\text{Ti}_n\text{O}_{2n-1}$  are required, since the formation of Magnéli phases from  $\text{TiO}_2$  is only achievable in a thermo-reduction process.

### III. ELECTROCHEMICAL IMPEDANCE SPECTROSCOPY STUDY OF MEMBRANE FOULING CHARACTERIZATION AT A CONDUCTIVE SUB-STOICHIOMETRIC TiO<sub>2</sub> REACTIVE ELECTROCHEMICAL MEMBRANE: TRANSMISSION LINE MODEL DEVELOPMENT

REPRINTED WITH PERMISSION FROM Y. JING, B.P. CHAPLIN, ELECTROCHEMICAL IMPEDANCE SPECTROSCOPY STUDY OF MEMBRANE FOULING CHARACTERIZATION AT A CONDUCTIVE SUB-STOICHIOMETRIC TiO<sub>2</sub> REACTIVE ELECTROCHEMICAL MEMBRANE: TRANSMISSION LINE MODEL DEVELOPMENT, J. MEMB. SCI. 511 (2016) 238–249.

#### ***3.1 Abstract***

This work presents a non-invasive and non-destructive electrochemical impedance spectroscopy (EIS) method for studying membrane fouling at a sub-stoichiometric TiO<sub>2</sub> reactive electrochemical membrane (REM). An asymmetric, ceramic, ultrafiltration REM is studied through EIS simulations, that are based on a mathematical transmission line model (TLM). The TLM is developed to interpret EIS data and is shown to be sensitive to fouling at multiple interfaces of the REM (outer surface, active and support layers). Mathematical interpretation of penetration depth of the alternating voltage signal allows a determination of the characteristic frequencies, associated with different layers of the membrane. The simulation results of membrane fouling mechanisms, such as monolayer adsorption and pore constriction at either active or support layer, and intermediate pore blockage at the outer surface produce distinguishable EIS spectra. Simulation results suggest that interpreting EIS spectra by the TLM is a useful technique for spatially characterizing membrane fouling and determining prevalent fouling mechanisms at a conductive membrane surface.

#### ***3.2 Introduction***

Membrane filtration utilizing microfiltration or ultrafiltration membranes is a well-recognized technology that is used in a variety of industries (e.g. food processing [154–156], biotechnologies [157–159], wastewater treatment [42,160,161], and pharmaceutical industries [162–164]). Membrane

technologies are able to provide high quality product water, have a small footprint, and require relatively easy maintenance [35]. However, membrane fouling is a common problem, that leads to increased power consumption and reduced membrane life, and causes serious operational and economical challenges for industries utilizing membrane separations (e.g., water and wastewater treatment plants, food and beverage industry, pharmaceutical industry) [30–34]. Early detection of membrane fouling and efficient and sustainable membrane regeneration strategies are necessary in order to optimize operational design, improve the filtration performance, and extend membrane life.

In pressure driven membrane process, permeate flux and transmembrane pressure (TMP) are the most straightforward indicators of membrane fouling. Under constant TMP operation, permeate flux decreases due to membrane fouling. Conversely, TMP increases in order to maintain a constant permeate throughput. Membrane fouling can be directly observed using *ex situ* destructive visual methods and *in situ* permeate flux or TMP measurements, but the investigation of the mechanisms associated with membrane fouling is still challenging.

Current methods for studying the mechanisms of membrane fouling have well known limitations. Studying membrane fouling mechanisms by fitting filtration law models to the TMP or permeate flux profile with time during the filtration process is commonly used but is limited to bench-scale testing and cannot be used to identify multiple simultaneous fouling mechanisms [7]. Scanning electron microscopy (SEM) is able to provide visual evidence of fouling, but preparation of an SEM specimen requires destruction of the membrane [36]. Li *et al.* used the ultrasonic time-domain reflectometry method to study membrane fouling and successfully detected cake layer formation, however the ultrasonic wave is unable to penetrate the porous membrane matrix and thus cannot detect fouling mechanisms associated with internal membrane fouling (e.g., pore constriction or plugging mechanisms).

The development and application of a non-invasive and non-destructive characterization technique to study membrane fouling mechanisms would enable the effectiveness of fouling remediation and cleaning strategies, which is possible by using electrochemical impedance spectroscopy (EIS). Potentiostatic EIS is

a frequency domain method where a small-amplitude alternating potential is superimposed onto a constant applied potential between the working and reference electrodes. Its high sensitivity towards interfacial processes and surface geometry makes EIS an ideal tool to evaluate membrane fouling and regeneration [60]. EIS measurements have been made across non-conductive membranes, mostly polymeric reverse osmosis membranes, in order to study membrane fouling. Coster *et al.* [61,62] employed EIS to characterize the skin layer conductances and capacitances of different layers on an ultrafiltration polysulphone membrane. Chilcott *et al.* [63] proposed an EIS mathematical model applied to membranes to investigate the conductivity and dielectric permittivity dispersion of the membrane before and after fouling and found that fouling along the surface of the membrane was more easily detectable than inside the pore. Gaedt *et al.* [63] adopted the method of Chilcott *et al.* [63] to a polymeric ultrafiltration membrane that was made conductive by sputtering platinum particles to the membrane surface. The Pt-coated membrane was modeled by the Maxwell–Wagner equation, which characterizes the capacitance and conductance as a function of the sinusoidal voltage wave [63]. However, the limitation of this work is that the Pt coating on the membrane is not able to represent the true morphology of the membrane, and Pt particles may occlude some of the membrane pores and thus change the membrane morphology [36]. The four-electrode EIS measurement technique has also been applied to membrane fouling studies on reverse osmosis [64], forward osmosis [65] and nanofiltration [66] flat sheet membrane without sputtering a conductive coating. It is found that the layers of asymmetric membrane can be spatially resolved by using EIS and the measured dielectric constants are sensitive to condition changes.

Recently, a reactive electrochemical membrane (REM), made from a substoichiometric  $\text{TiO}_2$  tubular membrane consisting primarily of the  $\text{Ti}_4\text{O}_7$  Magnéli phase was developed, and was shown to function as both a membrane and a reactive substrate that could oxidize organic compounds by a combined process of direct electron transfer and interaction with hydroxyl radicals ( $\text{OH}^*$ ) formed *via* water oxidation [27,28,165]. Since REMs are conductive, EIS measurements can be directly implemented without changing the

membrane morphology, and therefore can act as a powerful characterization tool for accessing membrane fouling and providing informative suggestions to optimize electrochemical regeneration protocols.

In this study, a transmission line model (TLM) was developed that simulates EIS spectra collected on an asymmetric Magnéli phase, ultrafiltration (UF) REM. The UF REM consists of a thin active filtration layer overlaying a thick porous support layer. The model is used to simulate EIS spectra for the REM as a function of membrane fouling. Common fouling mechanisms are simulated (i.e., pore constriction, monolayer adsorption, and intermediate pore blocking), and changes in the EIS spectra are shown to be unique, indicating the diagnostic power of the technique. Experimental verification of this model is investigated in a separate study [166].

### 3.3 Mathematical model

#### 3.3.1 Theory

EIS is a powerful characterization technique that can provide detailed information about the electrode-electrolyte interface of an electrochemical system [167]. Potentiostatic EIS is the most common variant of this technique, where a small amplitude sinusoidal potential signal ( $e$ ) at a given frequency is superimposed onto a constant potential ( $E_c$ ). The relation for the total potential ( $E$ ) of the interface under investigation is shown in Equation 3-1.

$$E = E_c + e = E_c + \Delta E \cdot \sin(\omega t) \quad 3-1$$

where  $\Delta E$  (V) is the amplitude of the potential perturbation,  $\omega$  ( $s^{-1}$ ) is the angular frequency ( $2\pi f$ ), and  $f$  (Hz) is the alternating voltage frequency. EIS data is usually measured against the open circuit potential (OCP), and therefore for convenience  $E_c$  is set to zero.

$$E = \Delta E \cdot \sin(\omega t) \quad 3-2$$

The alternating current (ac) response ( $i$ ) of the electrochemical system is usually out of phase with the potential signal due to the existence of non-faradaic processes (e.g., double layer capacitance) and reaction

of adsorbed species, which act as capacitors and inductors, respectively [167]. The ac response is given by Equation 3-3, assuming that  $E_c$  is at the open circuit potential.

$$i = \Delta I \cdot \sin(\omega t + \varphi) \quad 3-3$$

where  $\varphi$  represents the phase angle shift between  $i$  and  $E$ , and  $\Delta I$  is the amplitude of  $i$ .

In the absence of mass transfer limitations and a significant concentration of adsorbed reactive species, the impedance of an electrode-electrolyte interface can be modeled by a resistor ( $R$ ) and capacitor ( $C$ ) in parallel, which represent the simultaneous processes of charge transfer and double layer charging, respectively. The total impedance ( $Z_{total}$ ) of the resistor and capacitor in parallel is given by Equation 3-4:

$$Z_{total} = \left( \frac{1}{Z_{resistor}} + \frac{1}{Z_{capacitor}} \right)^{-1} = \frac{R}{1 + j\omega RC} \quad 3-4$$

where  $Z_{resistor}$  and  $Z_{capacitor}$  are the impedances of the resistor and capacitor, respectively, and  $j$  is the imaginary unit of the complex number. The product of  $RC$  represents the characteristic time constant for the system. Impedance is represented as a complex number, where the real component ( $Z_{real}$ ) is the impedance due to resistance and the imaginary component ( $Z_{imag}$ ) is the impedance due to capacitance (and inductance if present). Therefore,  $\varphi$  can be calculated from Equation 3-5:

$$\varphi = \tan^{-1} \frac{Z_{imag}}{Z_{real}} \quad 3-5$$

During EIS measurements,  $Z_{total}$  is measured as a function of  $f$  and the resulting data is often represented on a Nyquist plot ( $-Z_{imag}$  versus  $Z_{real}$ ) or Bode phase plot ( $\varphi$  versus  $f$ ). When applying EIS to a porous conductive membrane in the presence of a redox active couple in solution, the impedance comes from several simultaneous processes: [168] (1) resistance to electron transport in the conductive membrane, (2) charge transfer resistance between the redox couple and the conductive membrane surface, and (3) the

charging of capacitive elements in the high surface area porous structure. Each process has a different  $RC$  time constant, which can be determined by interpreting EIS data collected at different values of  $f$  [169].

Analyzing EIS data by appropriate mathematical models allows for decoupling of the resistance and capacitance at distinct physical locations of the REM. Therefore, in principle EIS measurements should provide spatial characterization data of electrode fouling. For example, the adsorption of foulants at different locations of the REM (e.g., outer surface versus inner pore) will result in an increase in the resistance to charge transfer ( $R_{ct}$ ) between the redox couple and electrode, and a decrease of the double layer capacitance ( $C_{dl}$ ) due to the decreased active surface area of the REM. If the electrode surface is homogeneous and foulants are electrochemically inert, then fouling of a portion of the surface area will not change the  $RC$  time constant due to the inverse relationship that exists between  $R$  and  $C$ .

In this study, the REM of interest is an asymmetric, ceramic, ultrafiltration membrane, with a thin active layer overlying a thick, porous support layer, as shown in Figure 2. The morphology of asymmetric membranes varies with respect to the thickness of the layers. The active layer, where filtration takes place, generates significant resistance to flow due to small pores and therefore the thickness is usually  $< 100 \mu\text{m}$ . The support layer provides mechanical support to the thin active layer and is usually of mm-scale thickness [7].

Mathematical models for EIS data interpretation must provide a fit to experimental data and represent the physical and electrochemical processes taking place in the electrochemical system under investigation. Park and Macdonald first adopted a TLM to study the dynamic formation of a porous magnetite film on carbon steel during a corrosion process [170]. In their model, a collection of identical cylindrical pores of uniform cross section and finite length is used to represent the overall porous structure, and the total impedance of the system is comprised of ionic, electronic, and interfacial electrochemical impedances. Bisquert *et al.* applied the TLM to study the electrochemical process on a nanoporous  $\text{TiO}_2$  photoelectrode, whose reference point is based on the assumptions that the pore geometry is cylindrical and ion transport is only driven by the alternating voltage [168,171].

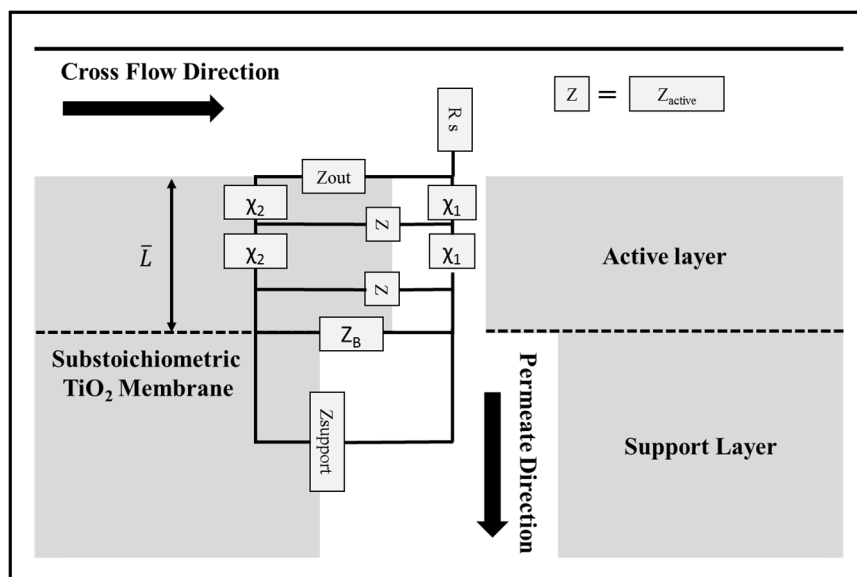


**Figure 2** Modified transmission line model for a reactive electrochemical membrane with an asymmetric structure.

Applying an EIS model to the REM requires transformation of the three-dimensional porous geometry into one dimension by assuming the REM contains a collection of cylindrical homogeneous pores of uniform radius. In our model, we are characterizing the impedance of fluid transport pores, and therefore we define the pore radius as an effective radius ( $r$ ), which can be determined by interpreting Hg porosimetry or measured flux data as a function of pressure using a Poiseuille flow model. Studies have also developed correlations between membrane pore size and molecular weight cutoff (MWCO) capacities for membranes, which were based on Poiseuille flow models [172–174]. Any of these methods are appropriate for obtaining  $r$  for impedance modeling.

As shown in Figure 2, the porous interface is then divided into three distinct regions (outer surface, active layer, and support layer) and the resistances of the solid phase (electronic) and solution phase (ionic) are placed in the direction of current flow, with the interfacial impedances distributed in between. The impedance at each of the three interfaces includes a  $R_{ct}$  and constant phase element (CPE) connected in parallel. CPEs are used instead of ideal capacitors in order to account for the inhomogeneity of the double

layers. Double layer inhomogeneity is attributed to ion adsorption, surface roughness of the membrane, and coupling of the solution resistance with the double-layer capacitance; all of which cause a capacitance dispersion at the interfacial region [167]. The impedance of a CPE ( $Z_{CPE}$ ) can be expressed as:

$$Z_{CPE} = \frac{1}{(j\omega)^\alpha Y_0} \quad 3-6$$

where  $Y_0$  is a constant ( $F s^{\alpha-1}$ );  $\alpha$  is an exponential factor that describes the rotation angle of a capacitive line on the complex plane plots (dimensionless). The non-ideal behavior of the CPE depends on the  $\alpha$  value. The CPE represents a pure capacitor when  $\alpha = 1$  and a pure resistor when  $\alpha = 0$ . A rough electrode surface is implied when  $0.5 < \alpha < 1.0$  [175].

The model for the total impedance is formulated by considering the potential and current distributions in both electronic and ionic phases, which are obtained by integrating the electronic and ionic currents along the pore depth with suitable boundary conditions. Prior work has shown that the application of a TLM to EIS data collected on a symmetric substoichiometric  $TiO_2$  REM could accurately match experimental data and was used to extract the electroactive surface area of the REM [27]. As for the asymmetric ultrafiltration REM considered in this study, the morphology has been discussed above and shown in Figure 2. The pore size of the active layer is much smaller than that of the support layer and the overall active layer has two interfaces experiencing electrochemical reaction and charging processes, which are the outer surface and active layer pore walls, as illustrated in Figure 2. Meanwhile the support layer has only one interface, which exists at the pore walls. Due to the existence of another porous layer (support layer) with a different pore size distribution, previously developed TLMs need to be modified accordingly. The support layer can be assumed as a planar electrode as it possesses more void space compared to the active layer, and this assumption is justified through calculation of the penetration depth ( $\lambda$ ) of the ac signal (see *Section 3.3.2*). The modification of the TLM was achieved by adding a Randles circuit in series to account for the support layer. The adoption of a serial circuit structure is based on the assumption that the boundary between these two layers can be considered an equipotential plane [176]. The modified TLM is illustrated in Figure 2,

with a rail-like transmission line circuit to simulate the active layer, followed by a Randles circuit to simulate the support layer.

Based on the description above, the mathematical formulation of the total impedance of the membrane ( $Z_m$ ) is expressed as:

$$Z_m = R_s + Z_{al} + Z_{sup} \quad 3-7$$

where  $Z_{al}$  and  $Z_{sup}$  are the impedances of the active layer and support layer, respectively, and  $R_s$  is the bulk solution resistance. The following TLM is used for  $Z_{al}$ : [171]

$$\begin{aligned} Z_{al} = & \frac{1}{\chi_1 + \chi_2} \left[ \lambda_{al} (\chi_1 + \chi_2) S_\lambda + (Z_{out} + Z_B) C_\lambda + \frac{1}{Z_{active} (\chi_1 + \chi_2)} Z_{out} Z_B S_\lambda \right]^{-1} \\ & \times \left\{ \bar{L} \lambda_{al} \chi_1 \chi_2 (\chi_1 + \chi_2) S_\lambda + \chi_1 [\lambda_{al} \chi_1 S_\lambda + \bar{L} \chi_2 C_\lambda] Z_{out} \right. \\ & + \chi_2 [\lambda_{al} \chi_2 S_\lambda + \bar{L} \chi_1 C_\lambda] Z_B \\ & \left. + \frac{1}{\chi_1 + \chi_2} \times \left[ 2\chi_1 \chi_2 + (\chi_1^2 + \chi_2^2) C_\lambda + \frac{\bar{L}}{\lambda_{al}} \chi_1 \chi_2 S_\lambda \right] Z_{out} Z_B \right\} \end{aligned} \quad 3-8$$

where  $C_\lambda = \cosh(\bar{L} / \lambda_{al})$ ;  $S_\lambda = \sinh(\bar{L} / \lambda_{al})$ ;  $\lambda_{al}$ ;  $\chi_1$  (ohm) is the ionic resistance;  $\chi_2$  (ohm) is the electronic resistance;  $Z_B$  (ohm) is the boundary impedance, which in this case represents the electronic plane connecting the active and support layers and is set to a low value (e.g.,  $1 \times 10^{-7}$  ohm) in the simulation due to sufficient electrical contact between the two layers;  $\bar{L}$  is the dimensionless thickness of the electrode active layer; and  $Z_{out}$  (ohm) and  $Z_{active}$  (ohm) represent the interfacial impedances at the outer surface and active layer, respectively. Each interfacial impedance contains a time constant characterizing the interfacial response to a variable frequency  $\Delta E$  signal, as shown in Equations 3-9 and 3-10.

$$Z_{out} = \frac{R_{ct,out}}{1 + (j\omega)^\alpha Y_{0,out} R_{ct,out}} \quad 3-9$$

$$Z_{\text{active}} = \frac{R_{\text{ct,active}}}{1 + (j\omega)^\alpha Y_{0,\text{active}} R_{\text{ct,active}}} \quad 3-10$$

The expression for  $Z_{\text{sup}}$  is given by a Randles circuit model, as follows:

$$Z_{\text{sup}} = \frac{R_{\text{ct,sup}}}{1 + (j\omega)^\alpha Y_{0,\text{sup}} R_{\text{ct,sup}}} \quad 3-11$$

where  $R_{\text{ct},m}$  (ohm) is the charge transfer resistance at interface  $m$  ( $m = \text{out}, \text{active}, \text{or sup}$ ).

As shown in Equations 3-9 to 3-11, there is a unique time constant  $(Y_0 R_{\text{ct}})^{\frac{1}{\alpha}}$  for each of the three representative interfaces (outer surface, active layer, and support layer). By conducting the EIS measurements over a range of frequencies, each of these time constants is assessed and the specific location of membrane fouling can be characterized. More specifically, fouling is characterized by evaluating the measured electro-active surface area of the REM at each interface, which is determined from the average double layer capacitance ( $C_{\text{dl},m}$ ) of each interface. Therefore the change in the average  $C_{\text{dl},m}$  can be used as a measure of membrane fouling. The average  $C_{\text{dl},m}$  at a specific interface is determined by the following equation [177]:

$$C_{\text{dl},m} = \left( \frac{Y_{0,m}}{[R_s^{-1} + R_{\text{ct},m}^{-1}]^{1-\alpha}} \right)^{1/\alpha} \quad 3-12$$

A surface area normalized  $\bar{C}_{\text{dl}}$  value of  $60 \mu\text{F cm}^{-2}$  is assumed to be representative for a metal oxide electrode [178], and  $C_{\text{dl},m}$  is divided by this value to calculate the electro-active surface area ( $A_{\text{electro}}$ ) of the REM. Although this is a well-accepted value for  $\bar{C}_{\text{dl}}$ , some variation may occur since the original study calculated this value for a dielectric and not an electrolyte-electrode interface [178].

In order to avoid the complications of electrode polarization effects and drifting of the OCP, an active redox couple is used during EIS measurements, and a small  $\Delta E$  is superimposed on the OCP of the redox couple. In order to avoid mass transport effects on the EIS measurements, spectra should be collected during

convective flow of the solution through the REM pores. To determine if concentration gradients will develop in the REM pores, an analysis of reactive mass transport of the redox species under dc conditions is necessary [179]. A detailed analysis of the redox couple concentration profile and potential distribution with depth into the REM is provided in the Appendix A. Results indicate that a concentration gradient of the active redox couple does not develop when  $\Delta E$  is restricted to small values ( $\leq 10$  mV). The potential decay with depth into the pore is ubiquitous under various operational conditions due to the existence of the solution resistance, but not to the extent that affects the EIS measurement.

### 3.3.2 Mathematical interpretation of penetration depth ( $\lambda$ )

The prior analysis indicates that a potential drop will occur with depth into the REM pores, which is caused by the solution resistance within the pore and hindered access of ions to the surface [60]. This potential drop affects the  $\lambda$  of the  $\Delta E$  signal, which is proportional to the inverse of  $\omega$ . Mathematically the relationship between  $\lambda$  and  $\omega$  is given by Equation 3-13 [180].

$$\lambda = \sqrt{\frac{Z}{R}} = \sqrt{\frac{\pi r^2}{2\pi r \rho \omega \bar{C}_{dl}}} = \sqrt{\frac{r}{2\rho \bar{C}_{dl} \omega}} \quad 3-13$$

In the calculation,  $\rho = 0.08 \Omega \text{ m}$  was used to represent a 100 mM ionic strength solution for a symmetric electrolyte. The REM membrane used for measurements is an asymmetric UF membrane with an active layer thickness of  $\sim 60.0 \mu\text{m}$  and support layer thickness of 2.19 mm. The effective pore radii of these two layers, determined by MWCO studies and Hg porosimetry, are 5.0 nm in the active layer and 1.5  $\mu\text{m}$  in the support layer [166]. These values will be used in Equation 3-13 to calculate  $\lambda$ . Values for  $\lambda$  were calculated at 4 different characteristic frequencies and the results are shown in Table II.

**Table II** PENETRATION DEPTH OF  $\Delta E$  SIGNAL AT AN ASYMMETRIC MEMBRANE

Characteristic Frequencies (Hz)	$\lambda$ ( $\mu\text{m}$ )
10,000 (r = 5.0 nm)	0.910
1000 (r = 5.0 nm)	2.88
2 (r = 5.0 nm)	64.4
2 (r = 1.5 $\mu\text{m}$ )	1120
0.01 (r = 1.5 $\mu\text{m}$ )	15800

As shown in the Table II, the  $\Delta E$  signal in the high frequency range (10,000 Hz to 1000 Hz) is able to penetrate to a depth of 2.88  $\mu\text{m}$ , which accounts for the whole outer surface region. The 60  $\mu\text{m}$  thick active layer is fully penetrated at a frequency of 2 Hz. The  $\Delta E$  signal in the low frequency range (2 Hz to 0.01 Hz) is able to reach a theoretical depth of 15.8 mm, which is much greater than the thickness of the support layer (2.19 mm). Therefore, at sufficiently low frequencies (0.01 Hz), the electrode surface at the support layer appears to be quasi-planar [181], and the assumption of using a Randles circuit to represent the support layer is justified.

### 3.3.3 *Modeling approach*

TLMs have been extensively used in studying corrosion of porous structures [182–184] and electrochemical processes in batteries [185–187]. However, this study is the first to utilize EIS interpreted by a TLM to study membrane fouling at a novel asymmetric REM. A main advantage of the TLM developed in our work, is that it can accurately detect changes in the impedances at the three physical interfaces (outer membrane surface, active and support layers), and therefore is capable of detecting the dominant fouling mechanism (e.g., adsorption at outer, active and support layers, and pore blockage at the outer membrane surface).

In order to illustrate the diagnostic power of the TLM for membrane fouling, EIS simulations were performed on the fouling mechanisms shown in Figure 3. By changing the  $R_{ct}$  and  $Y_0$  at one specific interface

and holding all other parameters constant at the other two interfaces, the EIS simulations can represent different fouling modes. The  $R_{ct}$  and  $Y_0$  are changed by an inverse factor, which results in a constant value for  $(Y_0 R_{ct})^{\frac{1}{\alpha}}$ , which assumes a homogenous REM surface. The impedance is calculated as a function of frequency, and both Nyquist and Bode phase plots are presented. In the Bode phase plot,  $\varphi$  is presented on a logarithmic scale of frequency to reveal the important behavior seen over a range of frequencies [176].

### **3.4 Results and discussion**

#### **3.4.1 Application of the transmission line model to membrane fouling**

EIS Simulations were conducted to represent (1) fouling at either the active or support layers, (2) fouling of the outer membrane surface, and (3) intermediate pore blockage. Simulation parameter values for each of these fouling modes along with that of a clean membrane (background) are summarized in Table III. The background EIS spectra were obtained from experimental data, and values for  $\alpha$  were set to 1.0 for simplicity, although values between 0.8-1.0 are often observed experimentally [166].

Model simulations were conducted over a frequency range of 10 mHz to 10 kHz, where the high frequency range is defined between 1000 Hz and 10 kHz ( $\lambda = 0.910$  to  $2.88 \mu\text{m}$ ), mid frequency range between 2 and 1000 Hz ( $\lambda = 64.4 \mu\text{m}$ ), and low frequency range between 10 mHz and 2 Hz ( $\lambda > 64.4 \mu\text{m}$ ). Figure 4 shows a simulated EIS spectrum, where data from each distinct membrane layer is delineated. The outer REM surface is characterized at frequencies between 1000 and 10000 Hz ( $\lambda < 3 \mu\text{m}$ ), which is shown in red. The active layer is characterized at frequencies between 2 and 1000 Hz ( $\lambda \sim 3$  to  $60 \mu\text{m}$ ), which is shown in blue. The support layer is characterized at frequencies  $< 2\text{Hz}$  ( $\lambda > 60 \mu\text{m}$ ), which is shown in green.

Values of  $R_{ct,m}$  and  $Y_{0,m}$  were varied while maintaining a constant  $RC$  value, and other parameters were held constant:  $\bar{L} \sim 1.0$ ,  $\chi_1 \sim 10.0$  ohm,  $\chi_2 \sim 0.5$  ohm,  $R_s \sim 0.5$  ohm,  $\alpha \sim 1.0$ , and  $Z_B \sim 1 \times 10^{-7}$  ohm. In the simulated EIS spectrum, three features are taken into consideration during membrane fouling: (1) the

increase of  $Z_{real}$  over the mid frequency range (active layer), (2) the change in the semi-circle over the low frequency range (support layer), and (3) the change of the  $\phi$ , which is defined by Equation 3-5.

### 3.4.2 Monolayer adsorption and pore constriction

Membrane fouling mechanisms at the active layer consist of monolayer adsorption and pore constriction. In monolayer adsorption, it is assumed that foulants only adsorb to the pore walls and do not accumulate as multi-layers (Figure 3a). Pore constriction allows for the formation of multi-layers of the foulants that can result in a decrease in the pore diameter (Figure 3b).

The variation of the pore size can affect the solution conductivity by excluding the electrolyte and redox couple ions. The variation of the average pore dielectric constant (Equation 3-14) and normalized ion concentration (Equations 3-15 and 3-16) are calculated by the methods of Bowen and Welfoot [188].

$$\varepsilon_p = 80 - 2(80 - \varepsilon^*) \left(\frac{d}{r}\right) + (80 - \varepsilon^*) \left(\frac{d}{r}\right)^2 \quad 3-14$$

$$\frac{C_{ion}}{C^*} = \beta \exp\left(\frac{-zF}{RT} \Delta\psi_D\right) \exp\left(\frac{-\Delta W}{kT}\right) \quad 3-15$$

where  $\varepsilon_p$  (dimensionless) is the pore dielectric constant,  $\varepsilon^*$  (dimensionless) is the dielectric constant of an oriented water layer adsorbed at the pore walls,  $d$  (m) is the thickness of the oriented solvent layer,  $C_{ion}$  (M) is the concentration of ions within the pore,  $C^*$  (M) is the concentration of ions in the bulk solution,  $z$  (1, dimensionless) is the valence of the ion,  $R$  ( $\text{J mol}^{-1} \text{K}^{-1}$ ) is the universal gas constant,  $T$  (298 K) is the absolute temperature,  $\Delta\psi_D$  (V) is the Donnan potential,  $k$  ( $\text{J K}^{-1}$ ) is the Boltzmann constant, and  $\beta$  (dimensionless) is the steric partition coefficient of the ion and can be calculated by Equation 3-16.

$$\beta = (1 - \tau)^2 \quad 3-16$$

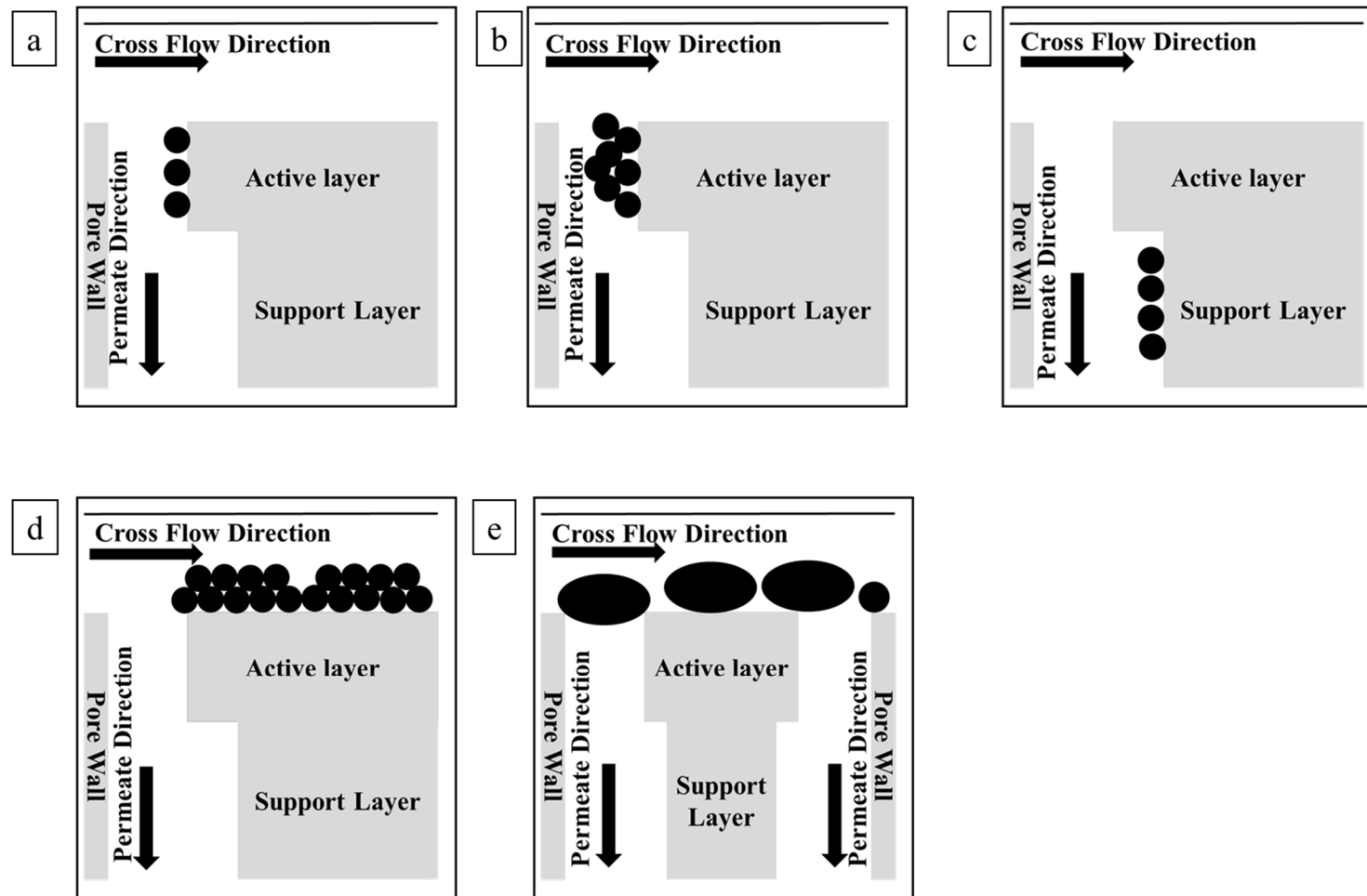


**Figure 3** Schematic diagrams of various fouling mechanisms, (a) monolayer adsorption and (b) pore constriction at the active layer, (c) monolayer adsorption at the support layer, (d) outer surface fouling and (e) intermediate pore blockage.

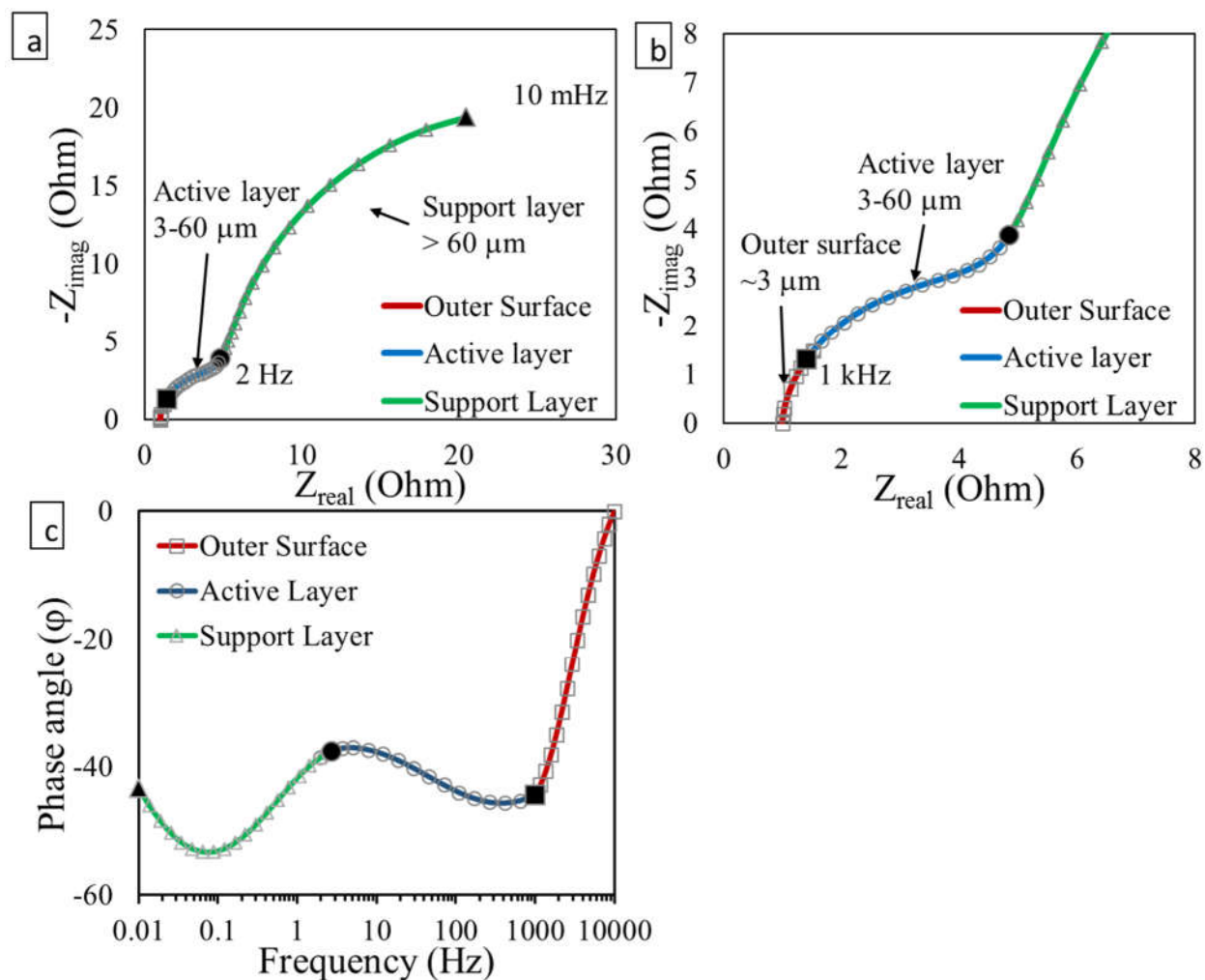


**Figure 4** Illustration of penetration depth on outer surface (red, square), active (blue, circle) and support (green, triangle) layers in a simulated EIS (a) overall and (b) zoomed-in Nyquist EIS spectra, and (c) Bode phase plot of a clean REM. Solid triangles represent the characteristic frequencies of 10 mHz, 2 Hz, and 1 kHz.

**Table III** MODEL PARAMETERS FOR DIFFERENT MODES OF FOULING SIMULATION (UNIT: R (OHM), Y (F·S<sup>A-1</sup>), C<sub>DL</sub> (FARAD), A (CM<sup>2</sup>))

Parameter		Background	Outer Surface Fouling			Active Layer Fouling		Support Layer Fouling		Intermediate Pore Blockage
Fouling Factor		0x	5x	10x	5x	10x	5x	10x		
Ionic Resistance	$\chi_1$	$1.00 \times 10^1$	$5.00 \times 10^2$							
	$R_{ct,out}$	$1.00 \times 10^1$	$5.00 \times 10^1$	$1.00 \times 10^2$	$1.00 \times 10^1$	$1.00 \times 10^1$	$1.00 \times 10^1$	$1.00 \times 10^1$	$1.00 \times 10^3$	
Outer Surface	$Y_{0,out}$	$1.00 \times 10^{-2}$	$2.00 \times 10^{-3}$	$1.00 \times 10^{-3}$	$1.00 \times 10^{-2}$	$1.00 \times 10^{-2}$	$1.00 \times 10^{-2}$	$1.00 \times 10^{-2}$	$1.00 \times 10^{-4}$	
	$R_{ct,active}$	$1.00 \times 10^1$	$1.00 \times 10^1$	$1.00 \times 10^1$	$5.00 \times 10^1$	$1.00 \times 10^2$	$1.00 \times 10^1$	$1.00 \times 10^1$	$1.00 \times 10^2$	
Active Layer	$Y_{0,active}$	$2.00 \times 10^{-2}$	$2.00 \times 10^{-2}$	$2.00 \times 10^{-2}$	$4.00 \times 10^{-3}$	$2.00 \times 10^{-3}$	$2.00 \times 10^{-2}$	$2.00 \times 10^{-2}$	$2.00 \times 10^{-3}$	
	$R_{ct,sup}$	$4.00 \times 10^1$	$2.00 \times 10^2$	$4.00 \times 10^2$	$4.00 \times 10^2$					
Support Layer	$Y_{0,sup}$	$5.00 \times 10^{-1}$	$1.00 \times 10^{-1}$	$5.00 \times 10^{-2}$	$5.00 \times 10^{-2}$					
Location		Background	Outer Surface Fouling			Active Layer Fouling		Support Layer Fouling		Intermediate Pore Blockage
Outer Surface	$C_{dl,out}$	$1.00 \times 10^{-2}$	$2.00 \times 10^{-3}$	$1.00 \times 10^{-3}$	$1.00 \times 10^{-2}$	$1.00 \times 10^{-2}$	$1.00 \times 10^{-2}$	$1.00 \times 10^{-2}$	$1.00 \times 10^{-4}$	
	$A_{out}$	$1.67 \times 10^2$	$3.34 \times 10^1$	$1.67 \times 10^1$	$1.67 \times 10^2$	$1.67 \times 10^2$	$1.67 \times 10^2$	$1.67 \times 10^2$	$1.67 \times 10^0$	
Active Layer	$C_{dl,active}$	$2.00 \times 10^{-2}$	$2.00 \times 10^{-2}$	$2.00 \times 10^{-2}$	$4.00 \times 10^{-3}$	$2.00 \times 10^{-3}$	$2.00 \times 10^{-2}$	$2.00 \times 10^{-2}$	$2.00 \times 10^{-3}$	
	$A_{active}$	$3.33 \times 10^2$	$3.33 \times 10^2$	$3.33 \times 10^2$	$6.66 \times 10^1$	$3.33 \times 10^1$	$3.33 \times 10^2$	$3.33 \times 10^2$	$3.33 \times 10^1$	
Support Layer	$C_{dl,sup}$	$5.00 \times 10^{-1}$	$1.00 \times 10^{-1}$	$5.00 \times 10^{-2}$	$5.00 \times 10^{-2}$					
	$A_{sup}$	$8.33 \times 10^3$	$1.67 \times 10^2$	$8.33 \times 10^2$	$8.33 \times 10^2$					

where  $\tau$  is the dimensionless ratio of the Stokes radius of the ion to membrane pore radius, and  $\Delta W$  (J) is the Born solvation energy barrier and is defined as:

$$\Delta W = \frac{z^2 e^2}{8\pi\epsilon_0 a_s} \left( \frac{1}{\epsilon_p} - \frac{1}{\epsilon_b} \right) \quad (17)$$

where  $e$  (C) is the electronic charge,  $a_s$  ( $2.4 \times 10^{-10}$  for perchlorate ion, m) is the Stokes radius of the ion,  $\epsilon_b$  (dimensionless) is the bulk dielectric constant of water, and  $\epsilon_0$  ( $J^{-1} C^2 m^{-1}$ ) is the permittivity of free space.

The Debye length  $\kappa^{-1}$  of the electric double layer inside the pore is obtained by Equation 3-18 and is equal to 1.0 nm for the pores with 5.0 nm radius ( $\epsilon_p = 71.94$ ) and 100 mM bulk ionic strength condition (decreased to 77.0 mM in pores with  $r = 5.0$  nm as shown in Figure 5), which indicates the electric double layer does not overlap within the pore, and thus ion exclusion is due to the increase of ion solvation energy and the Donnan effect is neglected ( $\Delta\psi_D = 0$ ).

$$\kappa^{-1} = \sqrt{\frac{\epsilon_p \epsilon_0 kT}{2000 N_A e^2 C_{ion}}} \quad 3-18$$

where  $N_A$  ( $\text{mol}^{-1}$ ) is the Avogadro constant.

The calculated results for the perchlorate ion ( $ClO_4^-$ ) using Equations 3-14 and 3-15 are shown in Figure 5. The values of  $\epsilon_p$  and  $C_{ion}$  are similar to the bulk solution values when  $r > 30$  nm, which indicates the pores in the support layer ( $r = 1.5 \mu\text{m}$ ) do not affect ion transport. The pore dielectric constant and ion concentration inside the pore change significantly when the pore radius is smaller than 10 nm (hollow points). The 5 nm pore radius at the active layer is able to cause ion exclusion and reduces the ion concentration and dielectric constant inside the pores to 77% and 72% of the bulk solution values, respectively, which affects the ion movement inside the pore and causes  $\chi_l$  to be higher than  $R_s$  [189]. Since the pore size of the support layer is much greater than the active layer, the ionic resistance in the support layer is equal to that of the active layer. At the active layer, fouling modes, such as pore constriction and pore blockage, are able to change the pore size due to the adsorption of foulants on the pore wall or

deposition of foulants at the pore orifice, which result in an ionic resistance increase due to the decrease in pore dielectric constant and ion concentration inside the pores.

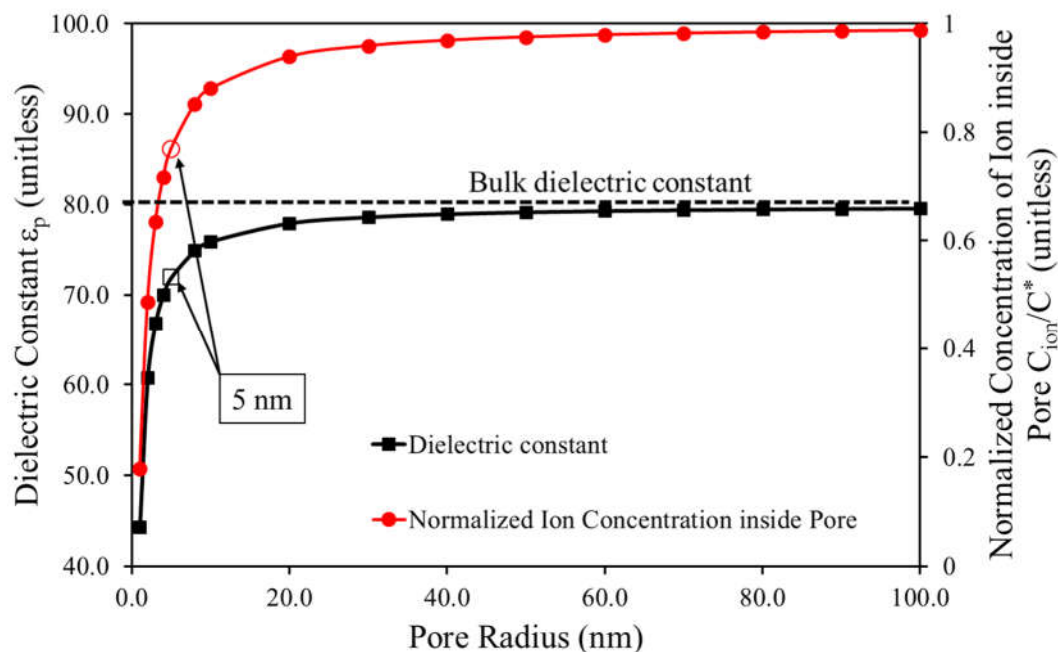


**Figure 5** Variation of averaged pore dielectric constant and normalized ion concentration inside the pore. Hollow points are at 5 nm in pore radius.

The simulation of monolayer adsorption at the active layer is conducted by increasing  $R_{ct,active}$  by 5 and 10 times and decreasing  $Y_0$  by 5 and 10 times of background values, in order to maintain a constant  $RC$  time constant (Table III). The simulated EIS spectra are represented as Nyquist plots in Figure 6a for the overall frequency range and 6b for the high and mid frequency data. Figure 6c shows the effect of  $f$  on  $\phi$  (Bode phase plot). The characteristic features associated with monolayer adsorption at the active layer are an increase of  $Z_{real}$  in the mid frequency data points (2 – 1000 Hz) (Figure 5a and 5b), and a shift in  $\phi$  at mid and low frequencies (Figure 6c). The values for  $\phi$  are shifted to more negative values at frequencies characteristic of the active layer and less negative values at frequencies characteristic of the support layer (Figure 6c). Changes to  $\phi$  at the active layer are attributed to fouling of this region, and changes to  $\phi$  at the support layer are due to the increase in  $Z_{real}$  from superposition of active layer fouling. The  $\phi$  value

approaches zero at the high frequency limit due to the influence of the solution resistance  $R_s$ . The  $\varphi$  at high frequencies (Figure 6c) and the magnitude of semi-circle over the low frequencies do not change (Figure 6a).

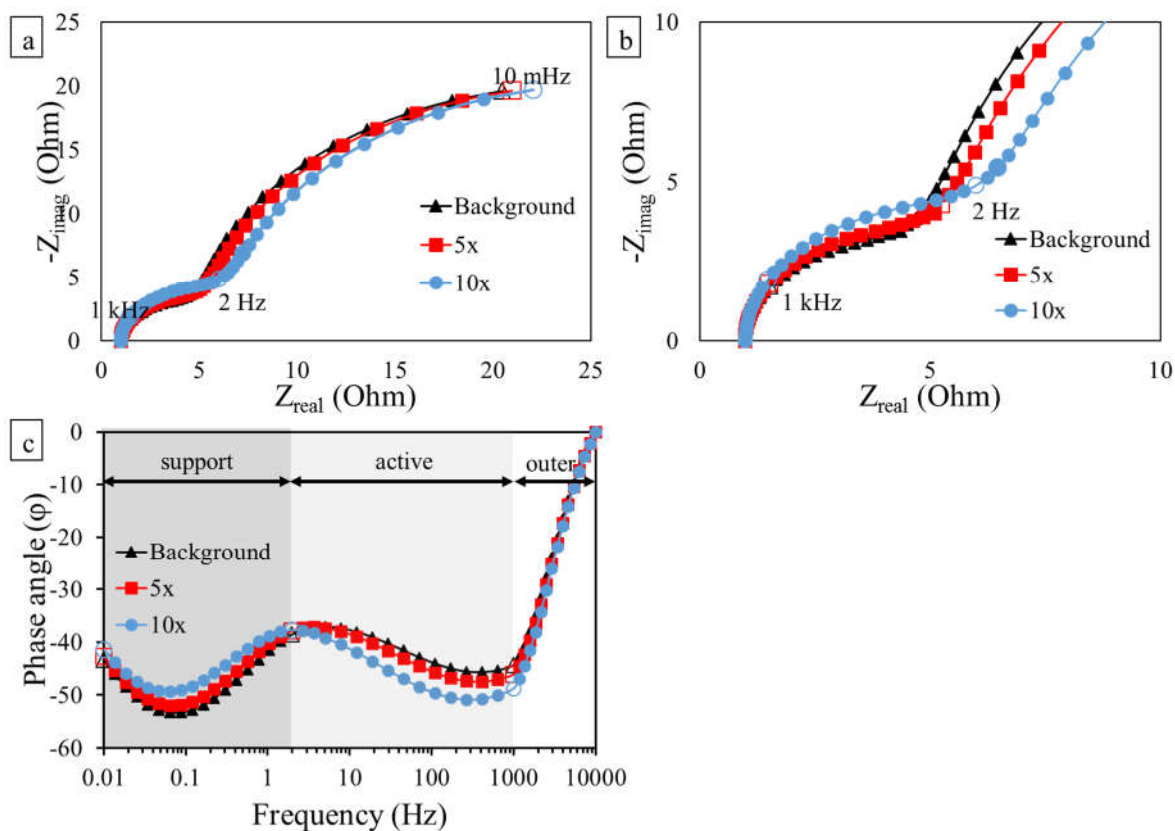


**Figure 6** Simulated Nyquist plot from TLM in the case of monolayer adsorption at active layer over (a) all frequencies and (b) high and mid frequencies, and (c) Bode phase plot. Unfilled symbols represent characteristic frequencies at 10 mHz, 2 Hz and 1 kHz.

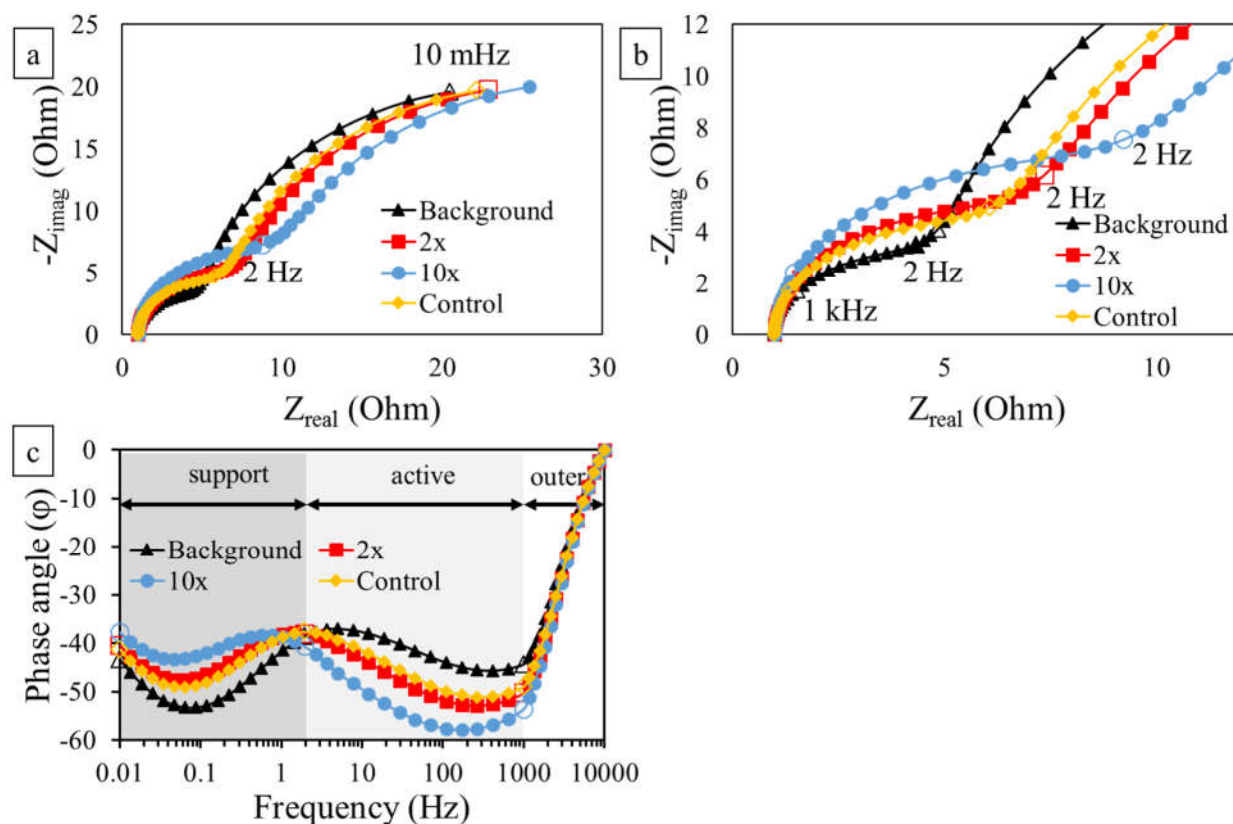


**Figure 7** Simulated Nyquist plot from TLM in the case of pore constriction at active layer over (a) all frequencies and (b) high and mid frequencies, and (c) Bode phase plot. Unfilled symbols represent characteristic frequencies at 10 mHz, 2 Hz and 1 kHz.

The simulation of pore constriction at the active layer is achieved by increasing  $R_{ct,active}$  and decreasing  $Y_{0,active}$  100-fold and increasing the ionic resistance 2-fold and 10-fold. Figure 3b shows a schematic for pore constriction of the active layer. The simulated EIS spectra are shown in Figure 7a for the overall frequency range and Figure 7b contains only the high and mid frequency data. A control simulation, which accounts for only monolayer fouling (100-fold) at the active layer, without changing the ionic resistance is shown in yellow in Figure 7. Pore constriction at the active layer causes an increase of  $Z_{real}$  in the mid frequency data points (2 — 1000 Hz) compared to the background spectrum (Figure 7a and 7b). Due to the pore size shrinkage, the dielectric constant within the pore decreases which also decreases ion solvation and leads to a lower concentration of both the background electrolyte and redox couple in the pore. This

process increases  $Z_{al}$  significantly and results in a shift in  $\varphi$  to more negative values at the active layer. According to Equation 3-5, the negative shift in  $\varphi$  indicates  $Z_{imag}$  is affected to a greater extent than  $Z_{real}$  (Figure 7c). Comparing results in Figures 6 and 7, indicate  $Z_{al}$  is more sensitive to changes in  $\chi_l$  than changes to  $R_{ct,active}$  and  $Y_{0,active}$ . Therefore, pore constriction and monolayer adsorption at the active layer have unique EIS spectra and should be distinguishable using the TLM. Furthermore, pore constriction at the active layer shifts  $\varphi$  to less negative values at the support region, due to an increase in  $Z_{real}$  from superposition of active layer fouling. Neither  $\varphi$  values at high frequencies (Figure 7c), nor the magnitude of the semi-circle at low frequencies (Figure 7a) change significantly as a result of pore constriction fouling at the active layer.

Similarly, the simulation of membrane fouling at the support layer is achieved by increasing  $R_{ct, sup}$  5 and 10 times and decreasing  $Y_0$  accordingly under a constant  $RC$  (Table III). Membrane fouling at the support layer does not affect the ionic resistance because of the large pore size. Figure 3c shows a schematic for fouling of the support layer pores, which results in a significant growth of the semi-circle at low frequencies ( $< 2$  Hz) (Figure 8a). As shown in Figure 8a, the Nyquist plot primarily shows one large semi-circle and hides the characteristics of the other two time constants. Figure 8c also shows that pore constriction of the support layer results in a shift of  $\varphi$  to more negative value in the whole frequency range, which is a direct result of the superposition of the large semi-circle shown in the Nyquist plot on other features of the EIS spectra.

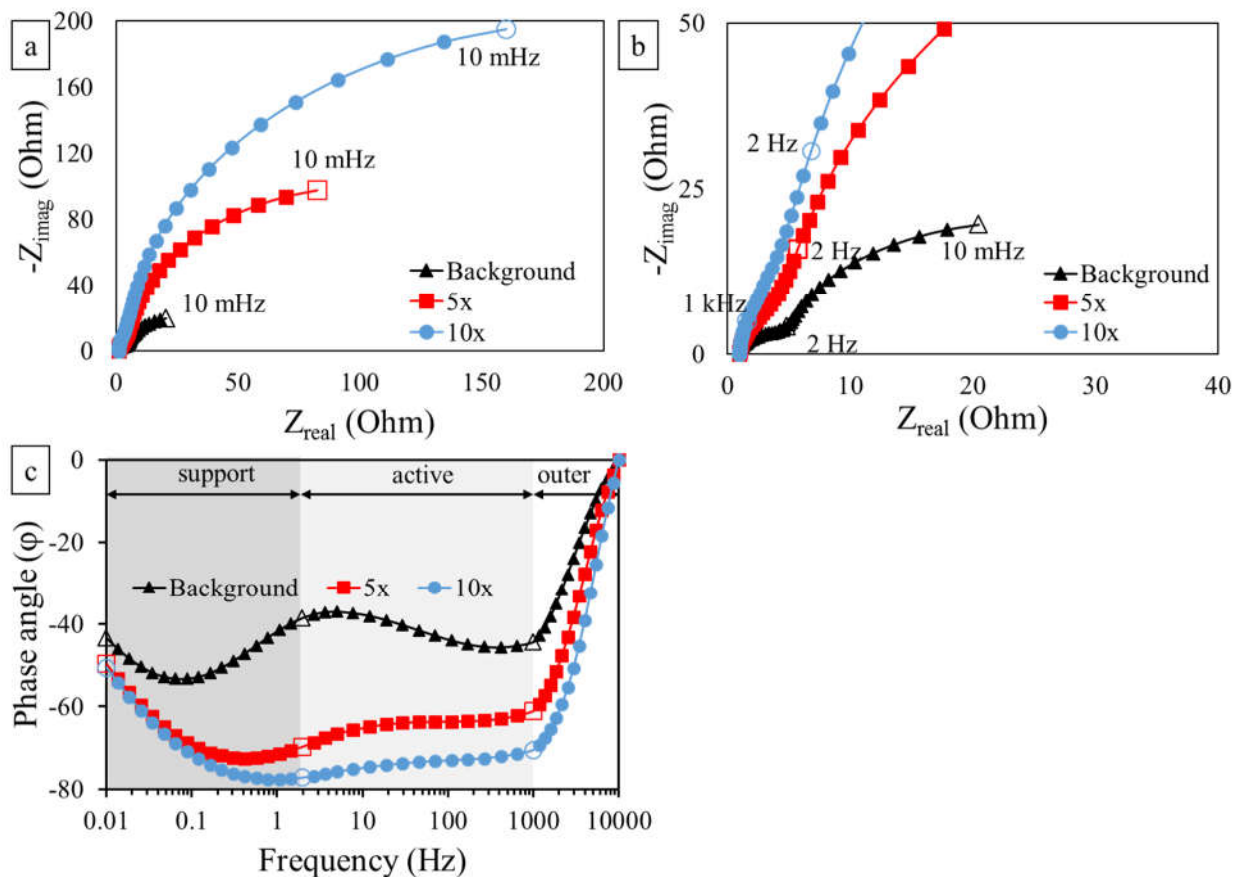


**Figure 8** Simulated results from TLM in the case of membrane fouling at support layer over (a) all frequencies and (b) high and mid frequencies, and (c) Bode phase plot. Unfilled symbols represent characteristic frequency at 10 mHz, 2 Hz and 1 kHz.

### 3.4.3 Fouling of outer membrane surface

Adsorption of foulants at the outer membrane surface was simulated using the parameters shown in Table III. Figure 3d shows a schematic for membrane fouling at the outer surface, which leads to an increase in  $Z_{real}$  at the mid frequency data (2 Hz to 1000 Hz) (Figures 9a and 9b), and a unique shift of  $\phi$  as a function of  $f$  (Figure 9c). A shift of  $\phi$  to more negative values at high frequencies is associated with an increased fouling at the outer surface. The fouling of the outer surface masks the characteristic  $\phi$  profile of the active layer, such that only two time constants are evident. Meanwhile the magnitude of the semi-circle at low

frequencies does not change in the Nyquist plot (Figure 9a), but the shift of  $\varphi$  to less negative values in this frequency range is due to the superposition of the outer surface fouling at the support (Figure 9c).

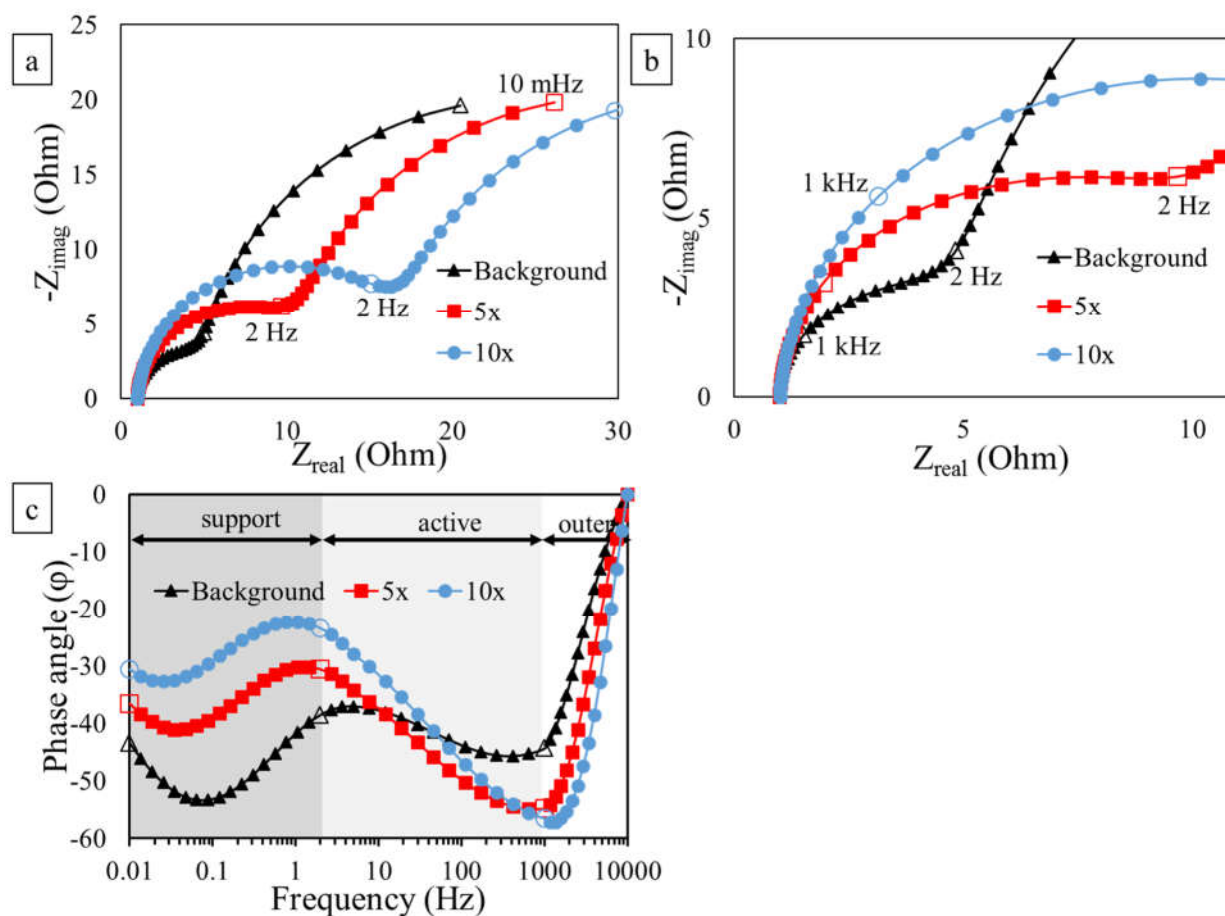


**Figure 9** Simulated results from TLM in the case of membrane fouling at outer surface over (a) all frequencies and (b) high and mid frequencies, and (c) Bode phase plot. Unfilled symbols represent characteristic frequencies at 10 mHz, 2 Hz and 1 kHz.

### 3.4.4 *Intermediate pore blockage*

Fouling at the outer surface represents the initial stage of membrane flux decline [43] during the filtration of large aggregates and particles. In this stage, the outer electro-active surface area is reduced, but the membrane is still permeable to fluid flow. As the membrane surface becomes more densely fouled, some aggregates deposit as multi-layers while other aggregates block the membrane pore, which leads to

membrane permeability decrease. This fouling mode is defined as intermediate pore blockage [190]. Intermediate pore blockage requires a dense fouling layer at the outer surface, and results in a reduction of the ionic current due to reduced accessibility to ionic solutions (i.e. the resistance for ions entering the pore will increase). To simulate this fouling mode the EIS simulation,  $R_{ct, out}$  was increased from 10 to 1,000 ohm,  $Y_{0, out}$  was decreased from 0.1 to 0.001 F, and  $\chi_l$  was increased from 10 to 500 ohm. Due to reduced accessibility to ion solutions, 10x fouling is set to both active and support layers. Figure 3e shows a schematic for pore blockage at the outer surface, which results in the formation of an additional semi-circle at high to mid frequencies (Figure 10a). The semi-circle spanning the high and mid frequency ranges represents the outer surface, which tends to be planar compared to the porous structure due to pore blockage, and the semi-circle at the lower frequencies represents the quasi-planar support layer. The intermediate pore blockage increases the  $Z_{real}$  at all three representative areas of the REM, which leads to a shift in  $\varphi$  to less negative values over nearly the entire frequency range (Figure 10b).

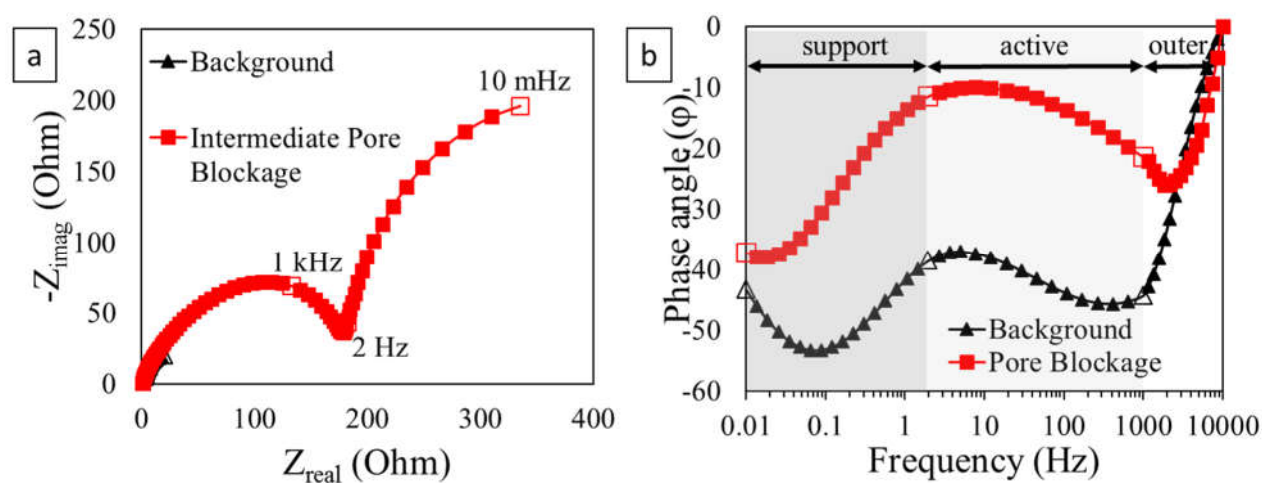


**Figure 10** Simulated (a) Nyquist and (b) Bode plots from TLM in the case of intermediate pore blockage. Unfilled symbols represent characteristic frequency at 10 mHz, 2 Hz and 1 kHz.

### 3.4.5 Calculation of $A_{electro}$

Table III also contains values for  $A_{electro}$  before and after fouling at each specific location (*outer surface, active layer, and support layer*), which was calculated from the double layer capacitance (Equation 3-12). This estimate assumes that the fouling layer is not redox active, and thus the  $A_{electro}$  value decreases in response to membrane fouling, and can be used as a surrogate of membrane fouling in experimental studies.

### 3.5 Conclusions

This study has established the fundamentals of a TLM, which can be used to spatially characterize membrane fouling and regeneration at an asymmetric REM. Different areas of the asymmetric REM (outer surface, active layer, support layer) can be assessed at different characteristic frequencies, which is due to the relationship between the penetration depth of the sinusoidal voltage wave and voltage frequency. Membrane fouling mechanisms, such as monolayer adsorption, pore constriction, and intermediate pore blockage are studied through Nyquist and Bode phase plots based on TLM simulations. The EIS simulations developed here show that the EIS data produces distinct signatures of membrane fouling at different locations on the membrane surface, and will be used in future studies to characterize REM fouling after experimental fouling and regeneration treatments [166].

### 3.6 Acknowledgements

Funding for this work was provided by the National Science Foundation (CBET-1159764). We acknowledge the valuable suggestions from the anonymous reviewers.

#### IV. ELECTROCHEMICAL IMPEDANCE SPECTROSCOPY STUDY OF MEMBRANE FOULING AND ELECTROCHEMICAL REGENERATION AT A SUB-STOICHIOMETRIC TiO<sub>2</sub> REACTIVE ELECTROCHEMICAL MEMBRANE

REPRINTED WITH PERMISSION FROM Y. JING, L. GUO, B.P. CHAPLIN, ELECTROCHEMICAL IMPEDANCE SPECTROSCOPY STUDY OF MEMBRANE FOULING AND ELECTROCHEMICAL REGENERATION AT A SUB-STOICHIOMETRIC TiO<sub>2</sub> REACTIVE ELECTROCHEMICAL MEMBRANE, J. MEMB. SCI. 510 (2016) 510–523.

##### ***4.1 Abstract***

In this study, a novel substoichiometric TiO<sub>2</sub> ultrafiltration reactive electrochemical membrane (REM) was synthesized and used for electrochemical regeneration of membranes fouled by humic acid (HA) and polystyrene beads (PS). A non-invasive and non-destructive electrochemical impedance spectroscopy (EIS) characterization technique was used to spatially characterize fouling at the REM and data were successfully interpreted by a Transmission Line Model. Based on these analyses, a chemical free electrochemical regeneration (CFER) scheme in backwash mode was developed. The CFER in anodic treatment mode recovered the flux of a HA fouled REM from 3.0% to between 76% and 99% of the initial flux over 5 continuous fouling/regeneration cycles. Full flux recovery of a PS fouled REM (fouling 31% to 38%) was achieved when using either cathodic or anodic CFER. By contrast, regeneration without an applied potential showed only partial flux recovery of 66% and 62% on HA fouled and PS fouled membranes, respectively. The operating cost of CFER was \$0.04 m<sup>2</sup> to \$0.06 m<sup>2</sup> per regeneration cycle, which is only 1.3% the cost of NaOH cleaning. Results suggest that the REM can provide an efficient and cost-effective regeneration scheme that allows it to function in a diverse set of water treatment applications.

##### ***4.2 Introduction***

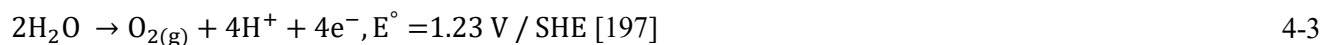
Membrane fouling significantly affects membrane filtration processes, as it leads to increased power consumption, reduced membrane life, and causes serious economic and operational challenges [30–34]. In order to recover fouled membranes, traditional membrane regeneration methods utilize physical and chemical cleaning protocols. Physical cleaning, such as periodic backwash, is able to partially regenerate the membrane

using physical shear forces [70]. However, backwash treatments do not recover all of the membrane flux, and therefore chemical cleaning procedures are needed. The effectiveness of chemical cleaning is primarily hindered by mass transfer of the chemical reagents to the fouled membrane pores, which requires high concentrations of reagents (e.g., 0.5 M NaOH) in order to increase the driving force for mass transport [9]. In addition, the cost of chemical synthesis, shipment, storage, and disposal, and the environmental ramifications of the above make chemical cleaning methods undesirable from both the economic and environmental perspectives [191,192]. In order to address the challenges associated with membrane fouling and regeneration, we herein report on the synthesis of a novel ceramic, asymmetric, ultrafiltration (UF), reactive electrochemical membrane (REM) and the use of this REM to overcome membrane fouling through a chemical free electrochemical regeneration (CFER) method.

Electrochemical advanced oxidation processes (EAOPs) have emerged as a clean, cost effective, and promising technology for the destruction of recalcitrant organic compounds [22,24–26,193,194], and therefore this method should be amenable as an alternative to chemical cleaning methods for membrane regeneration. The only reagents needed during EAOPs are electrons, which eliminate the need for chemical addition. Organic foulants can be removed by hydroxyl radicals ( $\text{OH}^\bullet$ ) produced from water oxidation on the anode surface (reaction 4-1), or oxidized through direct electron transfer reactions (reaction 4-2), where  $R$  is an organic compound [19].



In addition, membrane foulants can potentially be physically removed by electrostatic forces [71,75] and interaction with oxygen or hydrogen gas bubbles produced during water electrolysis reactions [196].



The integration of membrane filtration and EAOP into a single technology can provide efficient separations, oxidation of contaminants, and self-cleaning function. This combined process was recently realized through the development of a substoichiometric TiO<sub>2</sub> REM, which was applied to organic compound oxidation [27,165]. Substoichiometric TiO<sub>2</sub> is an ideal material for REM development, due to its long-term stability under both anodic and cathodic polarization [199,200], chemical inertness [201], and its high reactivity towards both inorganic [202] and organic [27,165] contaminants in wastewater streams. Substoichiometric TiO<sub>2</sub>, known as Magnéli phases, has a general formula of Ti<sub>n</sub>O<sub>2n-1</sub> ( $3 \leq n \leq 20$ ). The conversion of TiO<sub>2</sub> to Magnéli phases is achieved at temperatures above 1000 °C and in the presence of a reducing environment.[201] Magnéli phase materials are usually produced containing a mixture of compounds, with n typically between 4 and 6 [203]. The water treatment potential of the substoichiometric TiO<sub>2</sub> REM is immense, although few papers have investigated its potential [27,28,165], and therefore to our knowledge published studies have not been conducted that have documented fouling regeneration using a REM.

In this study, a substoichiometric TiO<sub>2</sub> UF membrane was developed and used as a REM in filtration mode. The objectives of this study were to (1) synthesize a durable and highly conductive substoichiometric TiO<sub>2</sub> membrane, (2) use a non-invasive EIS method to characterize membrane fouling after various membrane fouling and regeneration events, and (3) establish a CFER method. The composition, porosity, and structure of the substoichiometric TiO<sub>2</sub> membrane were characterized using X-ray diffraction (XRD), Hg porosimetry, and scanning electron microscopy (SEM). The membrane fouling was induced by using model humic acid and polystyrene microspheres foulants. In order to understand the fouling modes, EIS spectra were interpreted by fitting a transmission line model (TLM) developed in a previous study to experimental EIS data [204]. The TLM parameter values were assessed in order to gain an understanding of the dominant fouling mechanisms present on the REM as a function of both membrane fouling and regeneration.

### **4.3 Materials and methods**

#### **4.3.1 Reagents**

Chemicals were reagent-grade and obtained from Sigma-Aldrich and Bangs Lab (Fishers, IN). All chemicals were used as received. All solutions used in this study were made using purified deionized water obtained from a NANOPure water purification system (Barnstead) with resistivity greater than 18.2 M $\Omega$  cm (25° C), referred to as DI water.

#### **4.3.2 Reactive electrochemical membrane**

The REM used in this study was synthesized from an asymmetric TiO<sub>2</sub> UF tubular membrane with a molecular weight cut-off (MWCO) of 50 kDa (TAMI Industries, Les Laurons, France). The TiO<sub>2</sub> membrane was converted to conductive Magnéli phases (Ti<sub>n</sub>O<sub>2n-1</sub>) in a tube furnace (OTF-1200X, MTI) under a H<sub>2</sub> atmosphere and at a temperature of 1050 °C for 30 hours. The outer and inner diameters of the membrane are 10 mm and 5.5 mm, respectively, with a length of 100 mm. The total thickness of the REM is 2.25 mm, the REM active layer thickness is ~ 60.0  $\mu$ m and the support layer thickness is 2.19 mm. The REM was characterized by X-ray diffraction (XRD), scanning electron microscopy (SEM), and Hg porosimetry. Porosimetry analysis was carried out by Micrometric Analytical Services (Norcross, GA) using the method ISO 15901-1 [205]. SEM was performed by a Hitachi S-3000N to study the morphology and surface pore size on REM. XRD analysis was conducted on a Siemens D5000 X-ray diffractometer.

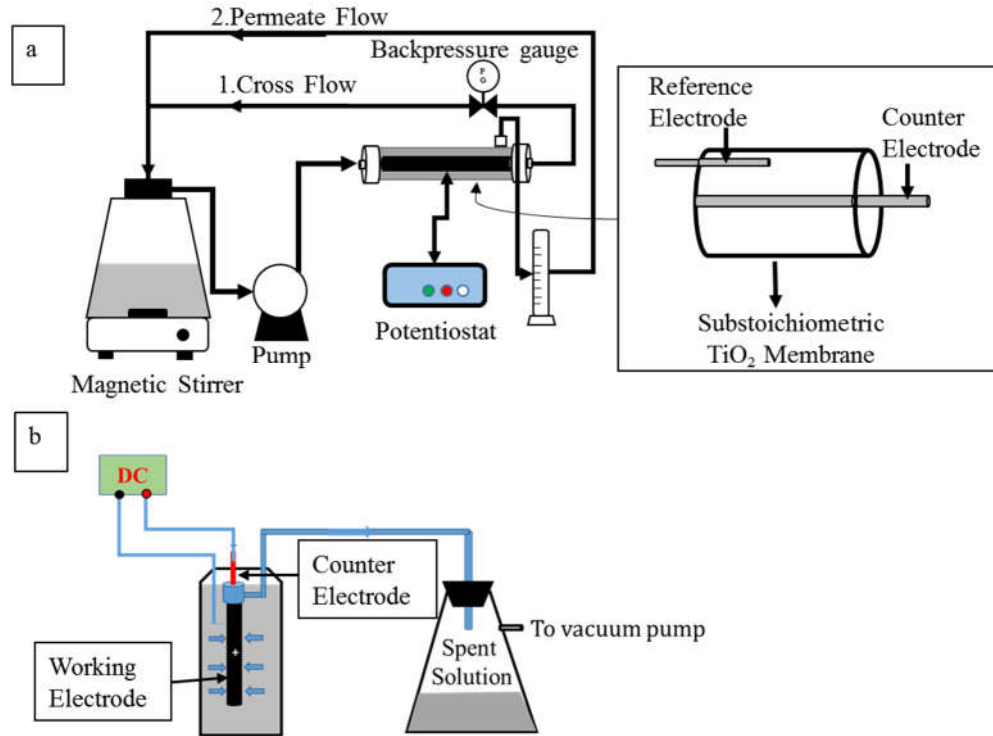


**Figure 11** (a) System sketch of filtration (fouling) experiment, EIS measurement setup and (b) setup for CFER in backwash mode. Inset image shows a three-electrode placement sketch inside the REM. Dead end mode is realized by completely cutting off Line 1 (cross flow) in Setup (a).

#### 4.3.3 Filtration setup

Figure 11a shows a schematic representation of the cross-flow UF experimental system combined with a potentiostat to control electrode potential and current. This setup is adapted from our previous work [27]. The feed solution was fed into the system at a constant cross-flow rate ( $Q = 30.6 \text{ L h}^{-1}$ ), using a bench analog drive gear pump (Cole Parmer) and a trans-membrane pressure of 1.0 bar was maintained using a pressure regulator. In every membrane filtration experiment, the feed was continuously stirred in the feed tank. The permeate flux was measured volumetrically per unit time and normalized by the outer geometric surface area and trans-membrane pressure, which is defined as the membrane permeability ( $J$ ). Both the retentate and permeate streams were 100% recycled to the feed tank. Each experiment started by recirculating a 100 mM  $\text{NaClO}_4$  (pH 5.95) supporting electrolyte through the filtration system at 1.0 bar trans-membrane pressure until a steady-state initial

permeate flux was achieved ( $J_0$ ). An initial EIS measurement was also recorded, which together with  $J_0$  represent the initial conditions of the membrane. The normalized permeate flux  $\bar{J}$  is defined as  $\frac{J}{J_0}$ .

#### 4.3.4 Molecular weight cuotoff determination

All MWCO experiments on the pristine TiO<sub>2</sub> membrane and REM were performed in the setup shown in Figure 11a in a dead-end filtration mode. Prior to a MWCO experiment, DI water was circulated in the system until steady state  $J$  was achieved and permeate flux  $J_0$  was used to indicate the state of the membrane. The feed was replaced with a 0.1 – 2.5 g L<sup>-1</sup> dextran standard solution (MW of 6, 10, 20, 40, or 70 kDa), the concentrations of permeate were analyzed using UV-spectroscopy (Shimadzu UV-1800) after a steady state  $J$  was reached during the filtration process. The rejection of the dextran solution was calculated based on:  $R = (C_f - C_p) / C_p$ , where  $C_p$  and  $C_f$  are the concentrations in permeate and feed solutions, respectively. Details of MWCO experimental methods and results are summarized in Appendix B.1.

The pore radius of the active filtration layer was estimated from MWCO results and using Equation 4-5:[172]

$$r = 0.33 \times (\text{MWCO})^{0.46} \quad 4-5$$

where  $r$  (Å) is the mean radius of the pore and  $\text{MWCO}$  (Da) is the molecular weight cutoff.

#### 4.3.5 Fouling experiments

Fouling experiments consisted of humic acid and polystyrene microsphere fouling as model natural organic matter (NOM) and particulate foulants, respectively. Synthetic humic acid was chosen as a model NOM foulant because it has a similar structure to NOM found in drinking water sources. It, however, is recognized that this type of humic acid is known to be much larger in size, higher content in aromatic structure, and lower content in acidic functional groups compared to the commonly used Suwannee river humic acid [32], but was deemed to be appropriate to accomplish the goals of our work (i.e, studying the feasibility of fouling/regeneration at the REM surface). All humic acid solutions were freshly made less than 24 hours prior to each experiment. Humic acid (150 mg L<sup>-1</sup>) was injected into the feed supporting electrolyte solution and pumped through the membrane in the cross-flow mode with 100% recycle for 120 minutes in order to achieve significant and rapid fouling and

compact the fouling layer under the trans-membrane pressure. The open circuit potential (OCP) monitored during this step was 0.37 V vs. the standard hydrogen electrode (SHE). Prior to the regeneration step, 2 L of DI water was pumped through the fouled membrane in order to remove loosely sorbed organic compounds, which is termed as the “DI Water Rinse” step. The reproducibility of humic acid fouling on the REM was examined in different regeneration experiments and during a *Multi-Cycle Test* (Section 4.4.2.3).

Polystyrene microsphere solutions, 1 L of 0.001 wt% polystyrene microsphere (Bangs Laboratory) with a mean diameter of 1.58  $\mu\text{m}$ , were made the same day of the experiment in a 10 mM  $\text{NaClO}_4$  supporting electrolyte in order to provide ionic strength similar to natural water conditions. The polystyrene microsphere fouling experiments were performed in dead end inside-out filtration mode, with 100% recycle for 90 minutes. The concentration of 1.58  $\mu\text{m}$  polystyrene microspheres in the feed and permeate solutions were monitored by UV-Vis spectroscopy at a wavelength of 312 nm. The reproducibility of the polystyrene microsphere fouling on REM was assessed through the comparison of duplicate fouling experiments before different regeneration experiments.

#### 4.3.6 Chemical free electrochemical regeneration (CFER) experiments

Membrane regeneration consisted of CFER in either forward wash or backwash mode at 25 °C. Constant current was applied to both regeneration modes by a direct current power supply (Protek P6035). The electrochemical regeneration in forward wash mode was conducted in the same setup as used in fouling experiments (Figure 11a), with the REM as the anode, and a stainless-steel rod with a diameter of 1.52 mm placed at the tubular center of the REM working as the cathode. The two electrodes were 1.95 mm apart. The electric conductivity measurement was made using an EIS method discussed by Guo *et al.*[28], and the conductivity of the REM was  $15.06 \pm 2.11 \text{ S cm}^{-1}$ . Electrical contact to the REM was made using a titanium wire wrapped around the outer diameter of the membrane. The concentric placement of the electrodes insures a uniform potential on the REM surface with respect to REM length and curvature. The 100 mM  $\text{NaClO}_4$  supporting electrolyte was pumped through the membrane in the cross-flow mode with 100% recycle for 180 min.

The CFER in backwash mode was conducted as shown in Figure 11b. The backwash suction was achieved by applying 40 mbar vacuum using a vacuum pump (KNF Laboport). The CFER was accomplished using the REM as either the anode or cathode and the stainless-steel rod as the counter electrode. The electrode placement is the same as discussed above. Constant direct current was supplied to the cell using a power supply during the filtration of a 1 L 100 mM NaClO<sub>4</sub> electrolyte. For polystyrene microsphere fouled membranes the concentration of microspheres in the regenerant solution was determined by UV spectroscopy. The reproducibility of the regeneration of the humic acid fouled REM was examined during the *Multi-Cycle Test* (Section 4.4.2.3) and that of the polystyrene microsphere fouled REM was performed in duplicate and results are shown in Appendix B.2.

The backwash control experiments were performed twice in the setup shown in Figure 11b without an applied current. The first backwash control experiment used 1 L of DI water (30 minutes) accounting for the solution volume effect brought upon by 1 L NaClO<sub>4</sub> electrolyte pumped through the membrane during anodic regeneration in backwash mode. The second backwash control experiment consisted of pumping DI water continuously through the membrane for 1-hour accounting for the total time spent in pumping 1 L NaClO<sub>4</sub> electrolyte during anodic regeneration in backwash mode.

#### 4.3.7 Electrochemical impedance spectroscopy measurements and transmission line model fitting

EIS measurements were conducted on the REM, as shown in Figure 11a using a three-electrode setup, with REM as working electrode, stainless-steel rod as counter electrode, and silver wire (diameter = 0.50 mm) as quasi-reference electrode (QRE). Potentials and currents were controlled and measured using a Gamry Potentiostat (Interface 1000). The electrode placement was the same as described above and the QRE was located 1.0 mm from the REM surface. Before each EIS measurement, the QRE was polished to remove the passivation layer and calibrated against a saturated Ag/AgCl reference electrode (1.0 mm from the REM surface). The QRE was used for EIS measurements because the Ag/AgCl reference electrode had high impedance, which interfered with the measurements. EIS measurements were made at the OCP in an electrolyte solution containing 5 mM K<sub>4</sub>Fe(CN)<sub>6</sub> and 5 mM K<sub>3</sub>Fe(CN)<sub>6</sub> with an amplitude of 4 mV in the sinusoid perturbation and over a frequency range of 30 kHz to 10 mHz.

The presence of the redox active species is not expected to have a large effect on the impedance elements. However, there is a possibility of adsorption of the redox active species to the REM surface, which would affect the impedance measurements by changing the interfacial polarization processes. Due to this concern, the EIS measurements were conducted over a short time-scale (*i.e.*, ~15 min) and the REM was thoroughly rinsed afterwards to minimize adsorption of the redox active species. The concentrations of the redox active species were found the same in both the feed and permeate during the filtration process with and without the alternating potential, as shown in Figure 37, Appendix B, and thus indicates a discernable concentration gradient of the redox active species did not exist.

Lissajous curves were also monitored as a real-time assessment of the quality of impedance measurements and thus to ensure good performance of the QRE. The EIS data were also examined by Kramers-Kronig relations to insure the validity of the data and confirm that the measurements were not corrupted by instrument artifacts or transient behavior [176]. The EIS data were fit by a TLM developed by our research group [204]. The TLM decouples the impedances from different layers of the UF REM, and thus has the ability to spatially characterize membrane fouling. The fitting of the TLM to EIS data is realized by a minimization of the sum of the square of the residuals, the model results are also reported along with error estimates calculated at the 95% confidence interval. The double layer capacitance ( $C_{dl}$ ) and electro-active surface area ( $A_{electro}$ ) of the UF REM can be determined by EIS and calculated through Equation 4-6 and 4-7, respectively.

$$C_{dl,m} = \left( \frac{Y_{0,m}}{[R_s^{-1} + R_{ct,m}^{-1}]^{1-\alpha}} \right)^{1/\alpha} \quad 4-6$$

$$A_{electro,m} = \frac{C_{dl,m}}{\bar{C}_{dl}} \quad 4-7$$

where  $Y_{0,m}$  ( $F s^{\alpha-1}$ ) is the capacitance constant at interface  $m$ ,  $\alpha$  is the exponential factor,  $R_{ct,m}$  (ohm) is the charge transfer resistance of interface  $m$ ,  $R_s$  (ohm) is the solution resistance,  $\bar{C}_{dl}$  ( $\mu F cm^{-2}$ ) is the surface normalized double layer capacitance ( $m = outer, active or sup$ ).

Fitted parameters including  $R_{ct,m}$ ,  $Y_{0,m}$ ,  $\alpha$  and ionic resistance  $\chi_l$ , are reported here for the analysis, while the other parameters are tabulated in Appendix B.4. Details of EIS spectra fit and error estimate calculations are presented in Appendix B.5.

Analysis of the penetration depth ( $\lambda$ ) of the alternating voltage signal during EIS measurements on an asymmetric UF REM of identical geometry allow for defining characteristic frequency ranges for each representative surface of the REM: high frequencies of 1 to 30 kHz ( $\lambda = 0.53 - 2.88 \mu\text{m}$ ) accounts for the outer surface, mid frequencies of 2 Hz to 1 kHz ( $\lambda = 2.88 - 64.4 \mu\text{m}$ ) accounts for the active layer, and frequencies  $< 2$  Hz accounts for the support layer [204]. It is noted that overlapping of outer surface and active layer may exist, since the surface roughness and the boundary between these two layers are not well defined. All experiments, including filtration, fouling, CFER and EIS measurement, were carried out at room temperature (25 °C).

## **4.4 Results and discussion**

### **4.4.1 Physical characterization**

The dual pore structure of the UF REM is shown in SEM images presented in Figure 12a - c. The thickness of the active layer is  $\sim 60 \mu\text{m}$  (Figure 12a). The support layer has a pore diameter that is much larger than the active layer and makes up the remainder of the membrane. Both active and support layers were converted to substoichiometric  $\text{TiO}_2$  Magnéli phases, as determined by XRD (Figure 12d). The characteristic peaks for  $\text{Ti}_4\text{O}_7$  and  $\text{Ti}_6\text{O}_{11}$  are located at 2 theta angles of  $20.78^\circ$  and  $22.84^\circ$ , respectively [203]. The existence of peaks at these two positions indicates that the REM consists primarily of  $\text{Ti}_4\text{O}_7$  and  $\text{Ti}_6\text{O}_{11}$ . Peaks characteristic of  $\text{TiO}_2$  were not present, which indicates a full conversion from  $\text{TiO}_2$  to the Magnéli phases was accomplished.

The MWCO experiments were conducted on the  $\text{TiO}_2$  membrane and REM. The MWCO of the  $\text{TiO}_2$  membrane was 50 kDa and increased to 60 kDa for the REM, which was a result of particle sintering leading to pore size enlargement during the high temperature reduction process (Figure 32, Appendix B). Estimates of the pore size according to Equation 4-5 yielded mean pore diameters of 9.6 and 10.4 nm for the  $\text{TiO}_2$  membrane and REM, respectively.

The REM's pore structure was further characterized by Hg porosimetry, which is shown in Figure 12e and 12f. The REM shows a bimodal pore size distribution, and a surface area of  $0.12 \text{ m}^2 \text{ g}^{-1}$  is associated with the support layer (pores  $> 1.0 \text{ }\mu\text{m}$ ) and a surface area of  $0.79 \text{ m}^2 \text{ g}^{-1}$  is associated with the active layer and the surface roughness of the REM (pores  $< 8 \text{ nm}$ ) (Figure 12e). Nearly the entire pore volume is dominated by the support layer, which contains pores in the range of  $1.0$  to  $3.8 \text{ }\mu\text{m}$  diameter (Figure 12f). Porosimetry results determined a porosity of 28.2%, specific surface area of  $0.94 \text{ m}^2 \text{ g}^{-1}$ , and median pore diameter of  $3.27 \text{ }\mu\text{m}$  (based on pore volume data), which represents the pore size in the support layer. The total porous surface area of the REM determined by Hg porosimetry was  $16.90 \text{ m}^2$ .

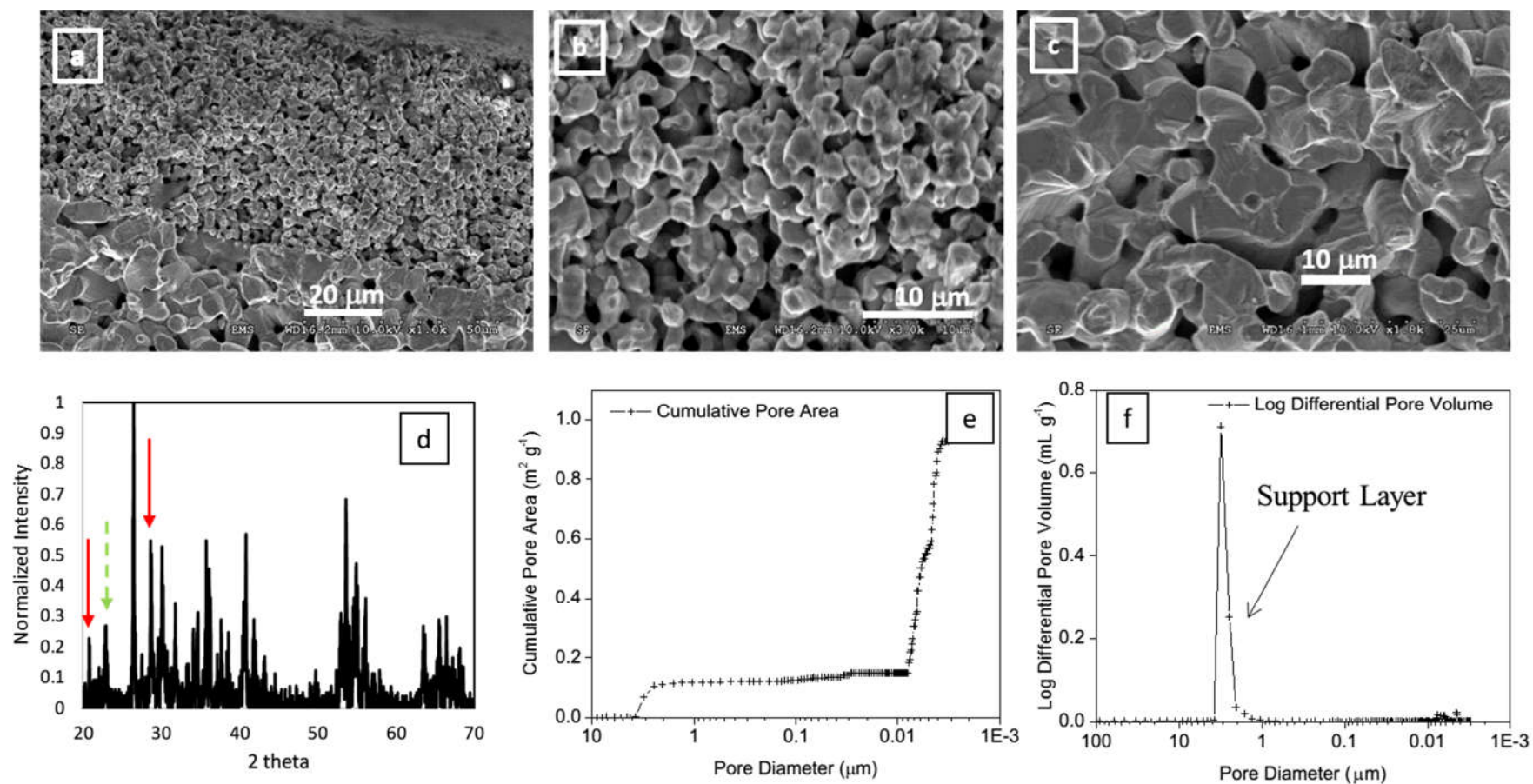


**Figure 12** SEM of REM, (a) overall SEM image, (b) active layer, (c) support layer; (d) XRD of substoichiometric  $\text{TiO}_2$  membrane with red (solid) and green (dash) arrows representing standard characteristic peaks of  $\text{Ti}_4\text{O}_7$  and  $\text{Ti}_6\text{O}_{11}$ , respectively; results of Hg intrusion porosimetry analysis of (e) cumulative pore area, and (f) log differential intrusion pore volume.

The total  $A_{electro}$  determined by EIS was  $1.9 \pm 0.06 \text{ m}^2$ , which indicates that only about 11.4% of the surface area determined by Hg porosimetry was electroactive. The distribution of the electroactive surface area was  $4.74 \pm 0.368\%$  outer surface,  $18.4 \pm 1.05\%$  active layer, and  $78.9 \pm 1.58\%$  support layer. Using the  $17.20 \text{ cm}^2$  nominal geometric inside surface area of the REM, the average roughness factor, which is the ratio of electrochemically active surface area to the geometric surface area of the REM, was  $1122 \pm 34.9$ , indicating a high surface area was available for electrochemical reactions.

#### 4.4.2 Humic acid membrane fouling and regeneration

In the following sections, EIS was used to understand REM fouling by humic acid and the CFER scheme was optimized in order to achieve a complete permeate flux recovery. As a model foulant, humic acid is present in most natural waters and is a major foulant during membrane operation [44,45]. Humic acid is usually negatively charged at neutral to high pH due to the deprotonation of the carboxylic and phenolic groups [206], therefore the negatively charged humic acid causes more fouling on a positively charged membrane [207]. Aggregation of humic acid can also occur by a combination of intermolecular hydrophobic interaction involving the aromatic or aliphatic regions of the humic acid,  $\pi$  bonding between aromatic groups, and hydrogen bonding between polar groups [44,208].

##### 4.4.2.1 Anodic chemical free electrochemical regeneration in forward wash mode

Figure 13a shows results for UF of a  $150 \text{ mg L}^{-1}$  humic acid feed solution, which caused a severe decline in  $\bar{J}$  with respect to time ( $3.80 \pm 0.71\%$  of initial  $1499 \text{ LMH bar}^{-1}$ ). After the fouling experiment, a DI water rinse increased  $\bar{J}$  from  $3.80 \pm 0.71$  to  $20.0 \pm 1.1\%$  (Figure 13a). In an attempt to oxidize the adsorbed humic acid from the membrane surface, an anodic CFER of the REM was performed. A constant current of 800 mA (cell potential = 8.2 V; anode potential = 4.9 V) was applied to the electrochemical cell for 180 minutes during inside-out cross-flow operation. Permeate flux was monitored during the CFER (150 to 320 min.) and  $\bar{J}$  was  $35.0 \pm 0.40\%$  at the end of regeneration (Figure 13a). After which, the permeate flux was again tested (320 to 360 min), and  $\bar{J}$  was

$37.0 \pm 1.7\%$  (Figure 13a). The CFER in forward wash mode was not able to completely regenerate the humic acid fouled REM, which was hypothesized to be due to an electrode potential drop with depth into the REM pores.

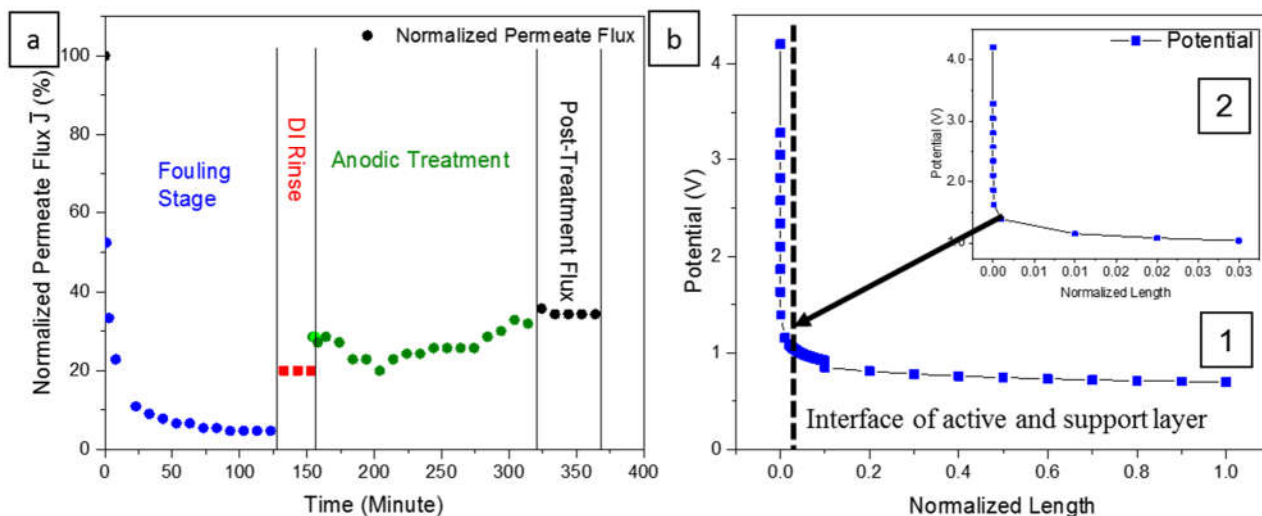


**Figure 13** (a) Normalized permeate flux  $\bar{J}$  of REM at different operational condition for treatment of  $150 \text{ mg L}^{-1}$  humic acid feed solution in forward wash mode; initial membrane flux  $J_0 = 1499 \text{ LMH bar}^{-1}$ ; (b1) simulated potential drop along membrane pore and (b2) active layer.

The potential distribution in porous electrodes has been rigorously treated, and an analytical solution has been developed by Lasia [60] (see Appendix B.6). The calculated potential profile on the REM in a  $100 \text{ mM NaClO}_4$  supporting electrolyte is shown in Figure 13b. Results indicate that the potential drops drastically with depth into the porous membrane and the depth at which the potential is able to drive  $\text{OH}^\bullet$  production is only approximately  $0.023 \text{ }\mu\text{m}$ . This calculation is dependent on several parameters (e.g., pore radius, exchange current density, specific solution resistance, and overpotential) and therefore should be taken as a first-order approximation. Nevertheless, this approximation indicates that the majority of the interior porosity of the REM would have a potential much lower than that needed for  $\text{OH}^\bullet$  production, and is likely the reason that anodic CFER in forward wash mode did not fully regenerate the REM. Humic acid has been shown to react readily with  $\text{OH}^\bullet$  ( $k = 2.28 \times 10^8 \text{ M}^{-1}\text{s}^{-1}$  [209]), and thus during anodic CFER polyphenolic compounds are likely removed from the outer

membrane surface. However, due to potential drop with distance within the membrane only direct electron transfer reactions can occur that prevent efficient ring cleavage and removal of the adsorbed humic acid/phenolic intermediates present within the active layer and membrane support regions. This mechanism would explain the lack of complete flux recovery in the forward wash mode.

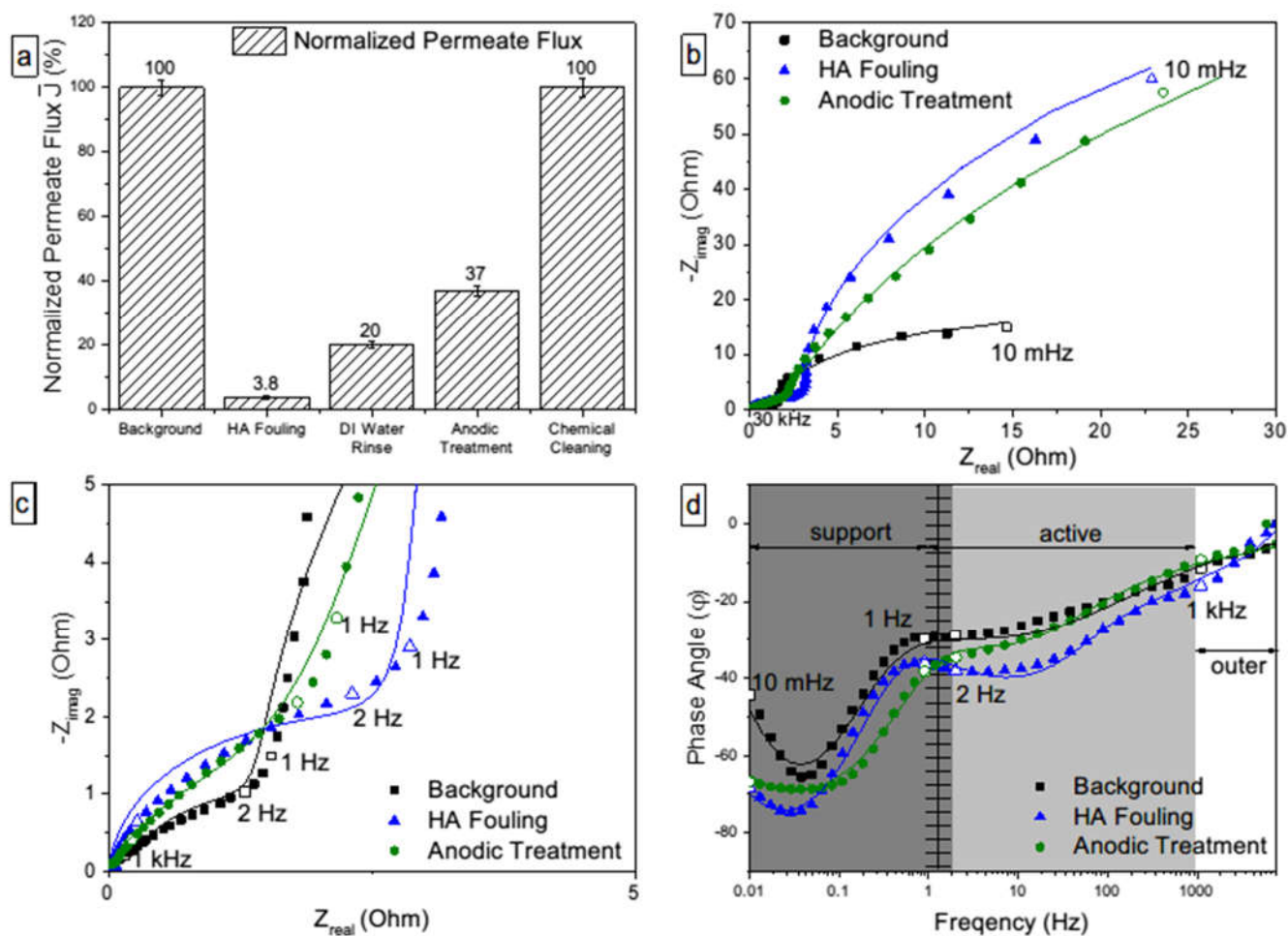


**Figure 14** (a) Normalized permeate flux  $\bar{J}$  under different operational conditions for the anodic CFER in forward wash mode of 150 mg L<sup>-1</sup> HA fouled REM; (b) EIS spectra in complete frequency range; (c) zoomed-in EIS spectra in high and mid frequency range; and (d) Bode phase plot; initial membrane flux  $J_0 = 1499.0$  LMH bar<sup>-1</sup>. (Solid lines represent TLM fit, unfilled symbols represent characteristic frequency at 10 mHz, 1.0 Hz and 30 kHz and layers of the REM are differentiated through various shades.)

EIS was used to characterize the REM under conditions of fouling and regeneration. It is noted that, in Figure 14d, the characteristic frequency differentiating the active and support layer boundary shifts to a lower frequency

from the theoretical determined 2 Hz, which can be explained by the choice of the  $\bar{C}_{dl}$  ( $60 \mu\text{F}\cdot\text{cm}^{-2}$  in the theoretical calculation) and the variation of specific solution resistance  $\rho$  in the sub-micron pore. The value of  $\lambda$  is dependent on  $\bar{C}_{dl}$  and  $\rho$  [204]. The range of typical  $\bar{C}_{dl}$  is commonly on the order of 10-100  $\mu\text{F}\cdot\text{cm}^{-2}$  [210]. The value of  $\rho$  increases to  $0.089 \Omega \text{ m}$  from  $0.080$  due to the decrease of dielectric constant from 80 in the bulk solution to 71.94 in the pores with 5 nm radius [204]. When  $\bar{C}_{dl}$  is taken as  $100 \mu\text{F cm}^{-2}$ ,  $\rho$  as  $0.089 \Omega \text{ m}$  and  $\lambda$  is kept constant ( $64.4 \mu\text{m}$ ), the characteristic frequency at the active and support layer boundary decreases to 1 Hz. In Figure 14d, the mesh marks the range of characteristic frequencies that describe the boundary between the active and support layers (1 to 2 Hz). The characteristic frequency of 1 Hz matches the observed time constants in Figure 14d and thus will be used in the analysis henceforth.

The permeate flux change is summarized in Figure 14a, and EIS data and model fits are provided as Nyquist (Figure 14b and 14c) and Bode phase plots (Figure 14d). The parameters of the best-fit TLM to the EIS spectra are provided in Table IV. The adsorption of humic acid leads to a decrease in pore size, and pore constriction at the active layer will increase  $\chi_l$ , as shown in Table IV, due to the decrease in dielectric constant [204]. Additionally, humic acid fouling leads to an increase in  $R_{ct}$  (22-fold increase at the outer surface, 224-fold increase at the active layer, and 7-fold increase at support layer compared to the background), indicating that the adsorption of humic acid decreases the rate of charge transfer. The  $R_{ct}$  decrease at both the outer surface (1.3-fold of background) and active layer (5.5-fold of background) after anodic CFER in forward wash mode, suggests partial removal of adsorbed humic acid at these two areas. However,  $R_{ct,sup}$  further increases (2.6-fold), indicating the support layer experienced additional fouling during the regeneration process. This interpretation of membrane fouling and regeneration is also supported by  $A_{electro}$  calculations. Membrane fouling causes a decrease in  $A_{electro}$  by  $\sim 50\%$  at all three areas. The anodic CFER recovered most ( $\sim 77\%$  of the initial) of the  $A_{outer}$  and  $A_{active}$  and decreased  $A_{sup}$  to 23% of the initial value. The change in  $A_{electro}$  does not follow an inverse relationship with  $R_{ct,sm}$ , which is due to the inhomogeneity of the REM surface [204].

The Bode phase plot shows a similar trend as the Nyquist plots, but allows for a clearer visualization of fouling at each layer (Figure 14d). The  $\varphi$  at all three areas is shifted to more negative values after fouling, which is

consistent with results from a theoretical interpretation of REM fouling using a TLM [204]. The  $\varphi$  were restored to near background values after CFER, except at the support (low frequency range) (Figure 14d).

It is concluded from the interpretation of the EIS data by the TLM that humic acid fouling takes place at all three representative areas (outer surface, active layer, and support layer), and after anodic CFER the partial regeneration of active layer pores and the outer membrane surface were achieved. However, after regeneration the EIS data suggests further fouling of the support layer, likely due to the polymerization of organic fragments removed from the active layer and flushed into the support during anodic CFER. The low pH generated by reaction (1) likely does not promote humic acid desorption because prior studies suggest that humic acid adsorption is enhanced on  $\text{TiO}_2$  at acidic pH [211].

Sodium hydroxide has been shown to promote the dissolution of weakly acidic organic matter with carboxylate functional groups [212], and therefore is used to clean the REM. Therefore, the membrane was soaked in 2.5 wt% sodium hydroxide for 10 hours at room temperature to achieve complete recovery of permeate flux, as shown in Figure 14a, termed as “chemical cleaning”.

#### 4.4.2.2 Anodic chemical free electrochemical regeneration in backwash mode

Analysis showed that only a fraction of the active layer is active for  $\text{OH}^\bullet$  production. Therefore, it is hypothesized that conducting anodic CFER in the backwash mode would be more efficient because: (1) desorbed foulants and intermediates during the regeneration process will be physically transported in the direction of higher electrode potential where  $\text{OH}^\bullet$  production exists, (2) the dissociation of foulants from the interfaces due to the shear force by the backwash flow, and (3) the enhanced shear force by electrochemically generated gas bubbles and bubble collapse with a release of energy [196,213,214]. While cathodic regeneration would generate basic conditions and should help to desorb humic acid, preliminary results show that it was not effective (data not shown).

Figure 15a shows that  $\bar{J}$  decreased to  $5.00 \pm 0.30\%$  after the humic acid fouling step, and increased to approximately  $34.0 \pm 2.3\%$  after the DI water rinse. Application of the anodic CFER in backwash mode was able to completely recover the membrane flux ( $\bar{J} = 118 \pm 8.1\%$ ). The EIS spectra shown in Figures 15b and 15c and

fitted TLM parameter values in Table V show a similar response to fouling than those presented in Figures 14b and 14c and Table IV, confirming the reproducibility of the fouling mechanism by humic acid on this REM. After regeneration, both the  $R_{ct}$  and  $A_{electro}$  at the outer surface and support layer are restored approximately to their background values (Table V), and the value of  $\chi_l$  is also brought back to its background value, indicating a restoration of the pore size at the active layer. The recovery of both the active and support layers is directed responsible for the  $> 100\%$  recovery of  $\bar{j}$ . The  $R_{ct,active}$  and  $A_{active}$  were not fully recovered after CFER in backwash mode, but was not a factor in affecting permeate flux, indicating that some residual monolayer fouling may have persisted in this area.

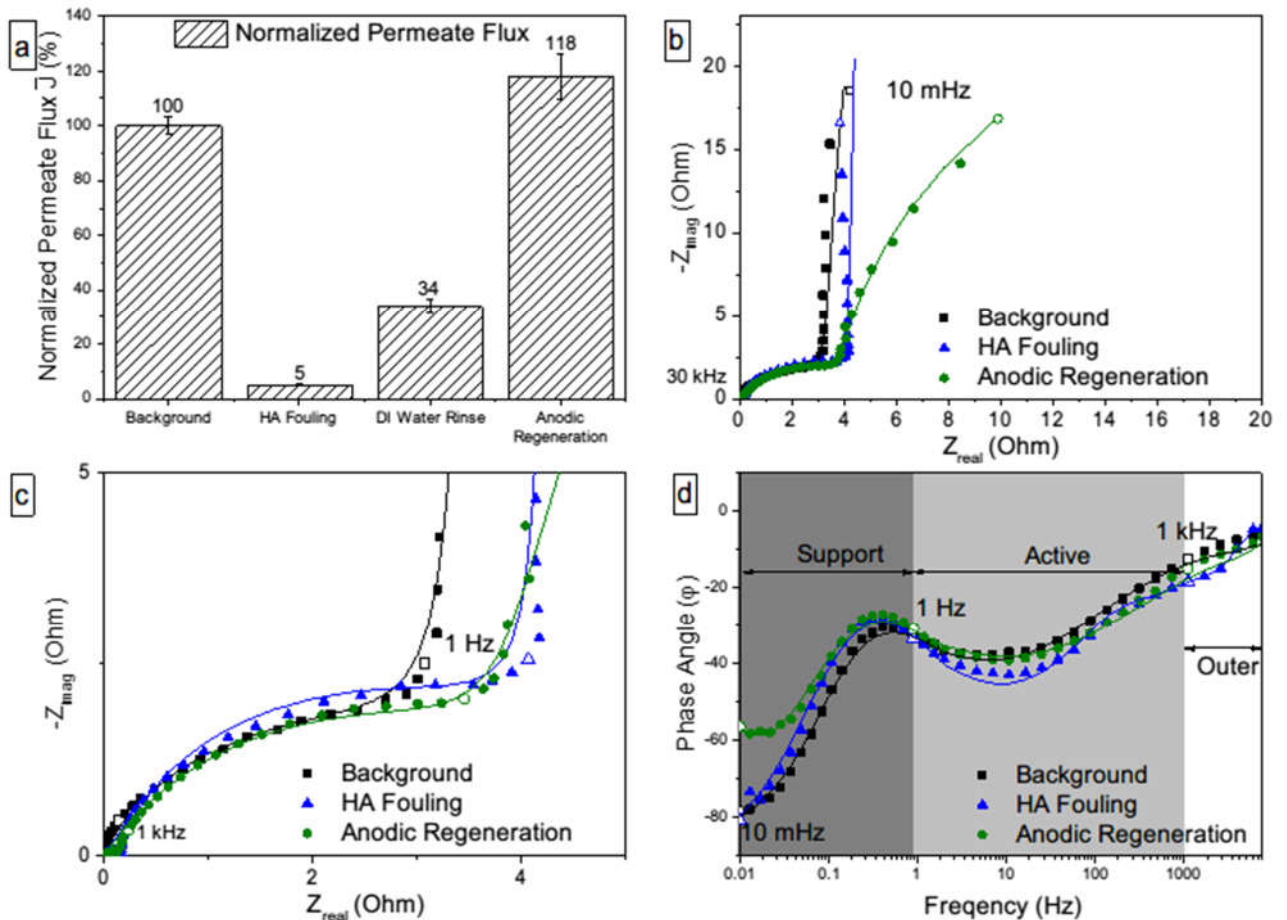


**Figure 15** (a) Normalized permeate flux  $\bar{j}$  under different operational conditions for the anodic CFER in backwash mode of  $150 \text{ mg L}^{-1}$  HA fouled REM; (b) EIS spectra in complete frequency range; (c) zoomed-in EIS spectra in high and mid frequency range; (d) Bode phase plot; initial membrane flux  $J_0 = 1592 \text{ LMH bar}^{-1}$ . (Solid lines represent TLM fit, unfilled symbols represent characteristic frequency at 10 mHz, 1.0 Hz and 30 kHz and layers of the REM are differentiated through various shades.)

**Table IV** MODEL PARAMETERS, CALCULATED DOUBLE LAYER CAPACITANCES AND ELECTRO-ACTIVE SURFACE AREAS OF BACKGROUND, 150 MG L<sup>-1</sup> HA FOULING AND ANODIC CFER IN FORWARD FLUSH MODE (UNIT: X<sub>1</sub> (OHM), R (OHM), Y (F·S<sup>A-1</sup>), C<sub>DL</sub> (FARAD), A (CM<sup>2</sup>))

Parameter	Background	Error (±)	HA Fouled	Error (±)	Anodic CFER	Error (±)	
$\chi_l$	$4.30 \times 10^0$	$2.27 \times 10^{-2}$	$6.23 \times 10^0$	$1.88 \times 10^{-2}$	$4.50 \times 10^0$	$1.32 \times 10^{-2}$	
Outer Surface	R <sub>ct,out</sub>	$4.52 \times 10^0$	$3.65 \times 10^{-1}$	$1.01 \times 10^2$	$1.20 \times 10^1$	$5.89 \times 10^0$	$1.67 \times 10^{-1}$
	Y <sub>0,out</sub>	$1.00 \times 10^{-1}$	$1.13 \times 10^{-3}$	$3.04 \times 10^{-2}$	$6.22 \times 10^{-4}$	$8.02 \times 10^{-2}$	$1.14 \times 10^{-3}$
	$\alpha$	$7.00 \times 10^{-1}$	$2.31 \times 10^{-2}$	$9.23 \times 10^{-1}$	$5.33 \times 10^{-3}$	$7.00 \times 10^{-1}$	$8.34 \times 10^{-4}$
Active Layer	R <sub>ct,active</sub>	$4.45 \times 10^0$	$6.66 \times 10^{-1}$	$1.00 \times 10^3$	$9.21 \times 10^1$	$2.45 \times 10^1$	$2.16 \times 10^0$
	Y <sub>0,active</sub>	$1.16 \times 10^{-1}$	$5.70 \times 10^{-3}$	$8.70 \times 10^{-2}$	$1.82 \times 10^{-3}$	$1.01 \times 10^{-1}$	$6.70 \times 10^{-3}$
	$\alpha$	$9.60 \times 10^{-1}$	$6.98 \times 10^{-3}$	$7.13 \times 10^{-1}$	$5.89 \times 10^{-3}$	$8.55 \times 10^{-1}$	$5.19 \times 10^{-3}$
Support Layer	R <sub>ct,sup</sub>	$3.16 \times 10^1$	$2.09 \times 10^0$	$2.21 \times 10^2$	$4.36 \times 10^1$	$5.68 \times 10^2$	$8.20 \times 10^1$
	Y <sub>0,sup</sub>	$7.00 \times 10^{-1}$	$5.94 \times 10^{-2}$	$3.01 \times 10^{-1}$	$4.52 \times 10^{-2}$	$1.70 \times 10^{-1}$	$2.88 \times 10^{-3}$
	$\alpha$	$1.00 \times 10^0$	$2.68 \times 10^{-2}$	$1.00 \times 10^0$	$4.64 \times 10^{-2}$	$8.49 \times 10^{-1}$	$2.86 \times 10^{-3}$
Location	Background	Error (±)	HA Fouled	Error (±)	Anodic CFER	Error (±)	
Outer Surface	C <sub>dl,out</sub>	$5.23 \times 10^{-2}$	$5.45 \times 10^{-3}$	$2.64 \times 10^{-2}$	$9.10 \times 10^{-4}$	$4.06 \times 10^{-2}$	$1.13 \times 10^{-3}$
	A <sub>out</sub>	$8.72 \times 10^2$	$9.08 \times 10^1$	$4.40 \times 10^2$	$1.52 \times 10^1$	$6.77 \times 10^2$	$1.88 \times 10^1$
Active Layer	C <sub>dl,active</sub>	$1.09 \times 10^{-1}$	$6.91 \times 10^{-3}$	$6.77 \times 10^{-2}$	$2.30 \times 10^{-3}$	$8.56 \times 10^{-2}$	$7.33 \times 10^{-3}$
	A <sub>active</sub>	$1.83 \times 10^3$	$1.15 \times 10^2$	$1.12 \times 10^3$	$3.83 \times 10^1$	$1.43 \times 10^3$	$1.22 \times 10^2$
Support Layer	C <sub>dl,sup</sub>	$7.00 \times 10^{-1}$	$7.43 \times 10^{-2}$	$3.01 \times 10^{-1}$	$4.60 \times 10^{-2}$	$1.60 \times 10^{-1}$	$3.26 \times 10^{-3}$
	A <sub>sup</sub>	$1.17 \times 10^4$	$1.24 \times 10^3$	$5.02 \times 10^3$	$7.67 \times 10^2$	$2.67 \times 10^3$	$5.43 \times 10^1$

The Bode phase plot shows a shift of  $\varphi$  to more negative values in the high and mid frequency ranges after fouling, and a return to background  $\varphi$  values after the CFER (Figure 15d). The  $\varphi$  values in the low frequency range (support layer) do not change significantly due to fouling, but a significant shift to less negative values is observed after the anodic CFER treatment. The  $\varphi$  values at high frequencies after CFER in backwash mode (Figure 15d) are more comparable to background values shown in Figure 14d, suggesting a more thorough cleaning of the REM than by NaOH chemical cleaning.

Although the anodic CFER in backwash mode is able to fully regenerate  $\bar{J}$  of the fouled membrane, it is unclear whether regeneration is due to anodic CFER or the shear force of the backwash itself. Therefore, a control experiment was conducted where the fouled membrane was backwashed twice in the absence of an applied potential. Figure 16a shows  $\bar{J}$  was recovered to  $57.0 \pm 1.7\%$  after the 1<sup>st</sup> backwash and  $66.0 \pm 2.8\%$  after the 2<sup>nd</sup> backwash, which suggests that backwash alone cannot fully recover the fouled membrane.

The EIS spectra after the 2<sup>nd</sup> backwash (Figures 16b and 16c) and best-fit TLM parameter values (Table VI) show that only the active layer experiences a decrease in  $R_{ct}$  and increase in  $A_{\text{electro}}$ . The value of  $\chi_l$ , however, is only partially restored to the background value, indicating that backwash cleaning alone is not able to fully remove pore constriction at the active layer [204], compared to a full recovery of  $\chi_l$  after CFER in backwash mode, which justifies the effectiveness of this regeneration scheme. The outer surface experiences a significant increase in  $R_{ct}$  by 1.6-fold after the backwash, due to adsorption of foulants removed from the active layer and support. An increase in  $R_{ct,sup}$  was also observed after backwash, which was attributed to a redistribution of the foulant. However, only  $A_{out}$  experienced a decrease after backwash (17.7% of the background  $A_{out}$ ) and  $A_{sup}$  remained unchanged. This result is likely due to the fact that a small portion of regeneration is not statistically significant in the support layer due to the high value for  $A_{sup}$  (56.0% of the total). The Bode phase plot shows a similar behavior as prior humic acid fouling (Figure 16d), which is a shift of  $\varphi$  to more negative values at the fouled regions (i.e., support and active layer).

**Table V** MODEL PARAMETERS, CALCULATED DOUBLE LAYER CAPACITANCES AND ELECTRO-ACTIVE SURFACE AREAS OF BACKGROUND, 150 MG L<sup>-1</sup> HA FOULING AND ANODIC CFER IN BACKWASH MODE (UNIT: X<sub>1</sub> (OHM), R (OHM), Y (F·S<sup>A-1</sup>), C<sub>DL</sub> (FARAD), A (CM<sup>2</sup>))

Parameter		Background	Error (±)	HA Fouled	Error (±)	Anodic CFER w/ Backwash	Error (±)
$\chi_I$		$8.74 \times 10^0$	$1.11 \times 10^{-2}$	$1.18 \times 10^1$	$3.02 \times 10^{-1}$	$8.50 \times 10^0$	$5.79 \times 10^{-2}$
Outer Surface	R <sub>ct,out</sub>	$1.66 \times 10^2$	$4.38 \times 10^1$	$2.32 \times 10^3$	$6.16 \times 10^1$	$1.23 \times 10^2$	$5.95 \times 10^0$
	Y <sub>0,out</sub>	$5.58 \times 10^{-2}$	$1.11 \times 10^{-2}$	$2.96 \times 10^{-2}$	$1.20 \times 10^{-3}$	$6.16 \times 10^{-2}$	$1.20 \times 10^{-3}$
	$\alpha$	$1.00 \times 10^0$	$2.99 \times 10^{-1}$	$8.36 \times 10^{-1}$	$1.70 \times 10^{-2}$	$7.55 \times 10^{-1}$	$7.61 \times 10^{-2}$
Active Layer	R <sub>ct,active</sub>	$1.46 \times 10^0$	$1.27 \times 10^0$	$5.06 \times 10^2$	$2.01 \times 10^1$	$1.69 \times 10^0$	$2.85 \times 10^{-1}$
	Y <sub>0,active</sub>	$2.33 \times 10^{-1}$	$7.65 \times 10^{-2}$	$6.60 \times 10^{-2}$	$9.71 \times 10^{-3}$	$9.51 \times 10^{-2}$	$1.13 \times 10^{-3}$
	$\alpha$	$9.22 \times 10^{-1}$	$5.31 \times 10^{-2}$	$9.79 \times 10^{-1}$	$2.84 \times 10^{-2}$	$9.51 \times 10^{-1}$	$3.61 \times 10^{-2}$
Support Layer	R <sub>ct,sup</sub>	$5.32 \times 10^2$	$1.17 \times 10^2$	$2.14 \times 10^4$	$1.10 \times 10^3$	$5.58 \times 10^1$	$5.38 \times 10^0$
	Y <sub>0,sup</sub>	$7.57 \times 10^{-1}$	$3.73 \times 10^{-2}$	$6.44 \times 10^{-1}$	$9.15 \times 10^{-3}$	$8.83 \times 10^{-1}$	$1.20 \times 10^{-2}$
	$\alpha$	$9.98 \times 10^{-1}$	$2.85 \times 10^{-3}$	$9.94 \times 10^{-1}$	$4.57 \times 10^{-3}$	$9.94 \times 10^{-1}$	$4.57 \times 10^{-3}$
Location		Background	Error (±)	HA Fouled	Error (±)	Anodic CFER w/ Backwash	Error (±)
Outer Surface	C <sub>dl,out</sub>	$5.58 \times 10^{-2}$	$2.37 \times 10^{-2}$	$2.40 \times 10^{-2}$	$1.92 \times 10^{-3}$	$4.88 \times 10^{-2}$	$4.39 \times 10^{-3}$
	A <sub>out</sub>	$9.31 \times 10^2$	$3.95 \times 10^2$	$4.00 \times 10^2$	$3.20 \times 10^1$	$8.14 \times 10^2$	$7.31 \times 10^1$
Active Layer	C <sub>dl,active</sub>	$2.10 \times 10^{-1}$	$1.01 \times 10^{-1}$	$6.56 \times 10^{-2}$	$1.15 \times 10^{-2}$	$8.73 \times 10^{-2}$	$7.12 \times 10^{-3}$
	A <sub>active</sub>	$3.50 \times 10^3$	$1.69 \times 10^2$	$1.09 \times 10^3$	$1.91 \times 10^2$	$1.45 \times 10^3$	$1.19 \times 10^2$
Support Layer	C <sub>dl,sup</sub>	$7.58 \times 10^{-1}$	$3.94 \times 10^{-2}$	$6.48 \times 10^{-1}$	$1.24 \times 10^{-2}$	$8.94 \times 10^{-1}$	$2.05 \times 10^{-2}$
	A <sub>sup</sub>	$1.26 \times 10^4$	$6.56 \times 10^2$	$1.08 \times 10^4$	$2.07 \times 10^2$	$1.49 \times 10^4$	$3.42 \times 10^2$

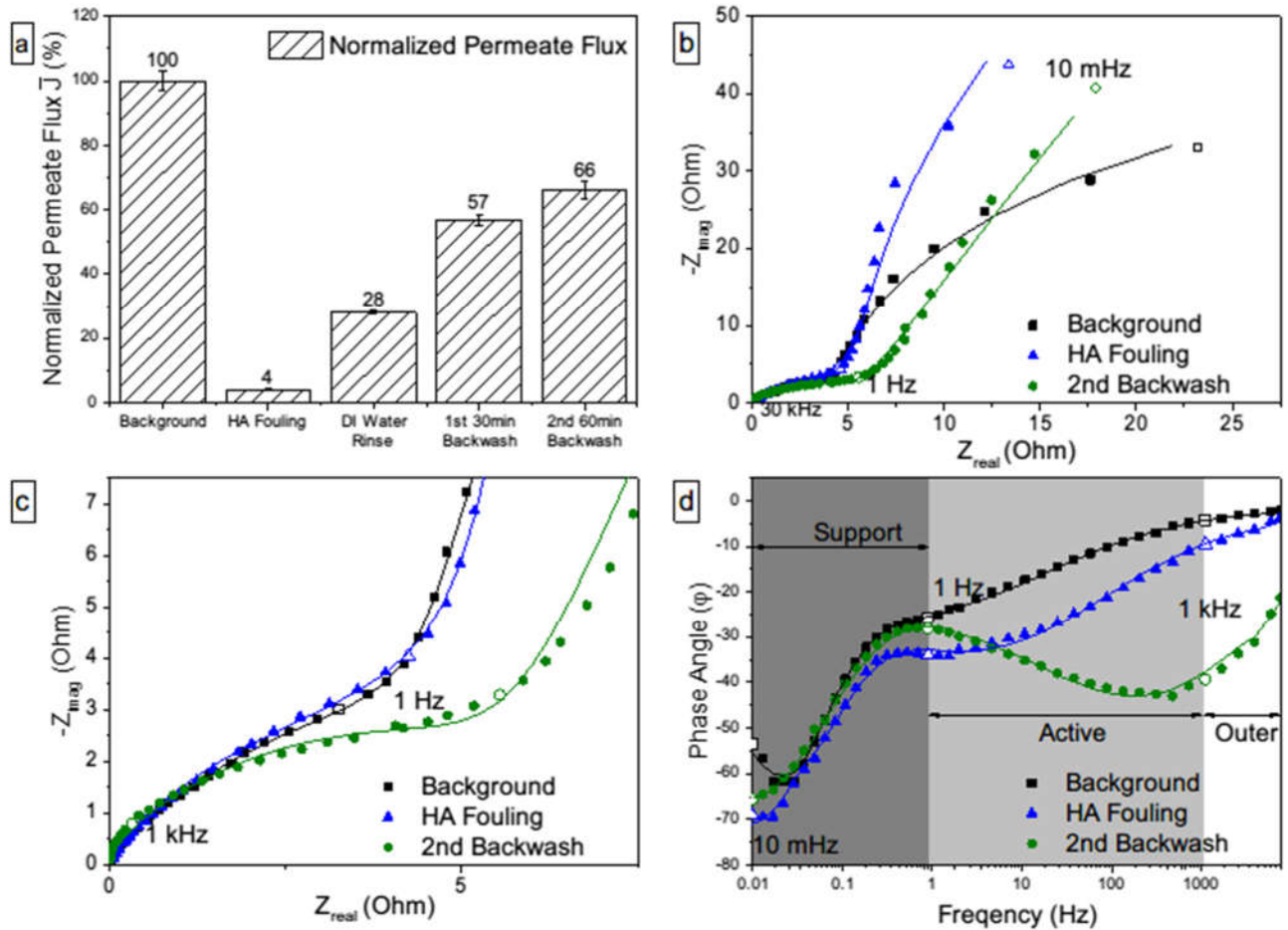


**Figure 16** (a) Normalized permeate flux  $\bar{J}$  under different operation conditions for backwash regeneration of  $150 \text{ mg L}^{-1}$  HA fouled REM; (Backwash conditions: DI water and 40 mbar vacuum); (b) EIS spectra in complete frequency range; (c) zoomed-in EIS spectra in high and low frequency range; (d) Bode phase plot; initial membrane flux  $J_0 = 1405.0 \text{ LMH bar}^{-1}$ . (Solid lines represent TLM fit, unfilled symbols represent characteristic frequency at 10 mHz, 1.0 Hz, and 30 kHz and layers of the REM are differentiated through various shades.)

**Table VI** MODEL PARAMETERS, CALCULATED DOUBLE LAYER CAPACITANCES AND ELECTRO-ACTIVE SURFACE AREAS OF BACKGROUND, 150 MG L<sup>-1</sup> HA FOULING AND THE 2<sup>ND</sup> BACKWASH OPERATION (UNIT: X<sub>i</sub> (OHM), R (OHM), Y (F·S<sup>A-1</sup>), C<sub>DL</sub> (FARAD), A (CM<sup>2</sup>))

Parameter	Background	Error (±)	HA Fouled	Error (±)	2 <sup>nd</sup> Backwash	Error (±)	
$\chi_l$	$8.28 \times 10^0$	$2.51 \times 10^{-2}$	$1.01 \times 10^1$	$9.88 \times 10^{-2}$	$9.50 \times 10^0$	$3.26 \times 10^{-2}$	
Outer Surface	$R_{ct,out}$	$7.68 \times 10^1$	$4.92 \times 10^0$	$8.00 \times 10^1$	$3.15 \times 10^0$	$1.22 \times 10^2$	$5.63 \times 10^0$
	$Y_{0,out}$	$4.05 \times 10^{-2}$	$2.59 \times 10^{-3}$	$4.04 \times 10^{-2}$	$1.99 \times 10^{-3}$	$4.86 \times 10^{-3}$	$9.26 \times 10^{-5}$
	$\alpha$	$7.55 \times 10^{-1}$	$5.38 \times 10^{-2}$	$7.93 \times 10^{-1}$	$2.01 \times 10^{-2}$	$1.00 \times 10^0$	$2.26 \times 10^{-2}$
Active Layer	$R_{ct,active}$	$7.51 \times 10^0$	$5.80 \times 10^{-1}$	$2.43 \times 10^2$	$1.90 \times 10^1$	$3.00 \times 10^0$	$1.39 \times 10^{-1}$
	$Y_{0,active}$	$8.17 \times 10^{-2}$	$4.86 \times 10^{-3}$	$4.00 \times 10^{-2}$	$9.22 \times 10^{-4}$	$8.57 \times 10^{-2}$	$2.04 \times 10^{-3}$
	$\alpha$	$9.05 \times 10^{-1}$	$2.90 \times 10^{-2}$	$8.71 \times 10^{-1}$	$2.26 \times 10^{-2}$	$8.31 \times 10^{-1}$	$5.70 \times 10^{-3}$
Support Layer	$R_{ct,sup}$	$8.16 \times 10^1$	$3.54 \times 10^0$	$1.05 \times 10^3$	$1.78 \times 10^2$	$2.00 \times 10^3$	$3.72 \times 10^2$
	$Y_{0,sup}$	$4.01 \times 10^{-1}$	$1.13 \times 10^{-3}$	$3.17 \times 10^{-1}$	$5.22 \times 10^{-3}$	$2.60 \times 10^{-1}$	$1.18 \times 10^{-2}$
	$\alpha$	$1.00 \times 10^0$	$3.64 \times 10^{-3}$	$9.31 \times 10^{-1}$	$6.25 \times 10^{-3}$	$8.22 \times 10^{-1}$	$1.86 \times 10^{-2}$
Location	Background	Error (±)	HA Fouled	Error (±)	2 <sup>nd</sup> Backwash	Error (±)	
Outer Surface	$C_{dl,out}$	$2.76 \times 10^{-2}$	$5.46 \times 10^{-3}$	$2.76 \times 10^{-2}$	$3.03 \times 10^{-3}$	$4.85 \times 10^{-3}$	$4.15 \times 10^{-4}$
	$A_{out}$	$4.59 \times 10^2$	$9.10 \times 10^1$	$4.59 \times 10^2$	$5.04 \times 10^1$	$8.09 \times 10^1$	$6.92 \times 10^0$
Active Layer	$C_{dl,active}$	$7.35 \times 10^{-2}$	$7.54 \times 10^{-3}$	$3.48 \times 10^{-2}$	$2.09 \times 10^{-3}$	$6.15 \times 10^{-2}$	$2.96 \times 10^{-3}$
	$A_{active}$	$1.22 \times 10^3$	$1.26 \times 10^2$	$5.79 \times 10^2$	$3.48 \times 10^1$	$1.03 \times 10^3$	$4.93 \times 10^1$
Support Layer	$C_{dl,sup}$	$4.01 \times 10^{-1}$	$2.68 \times 10^{-3}$	$3.48 \times 10^{-1}$	$7.14 \times 10^{-3}$	$3.33 \times 10^{-1}$	$2.78 \times 10^{-2}$
	$A_{sup}$	$6.68 \times 10^3$	$4.46 \times 10^1$	$5.54 \times 10^3$	$1.19 \times 10^2$	$5.54 \times 10^3$	$4.63 \times 10^2$

#### 4.4.2.3 Multi-cycle test

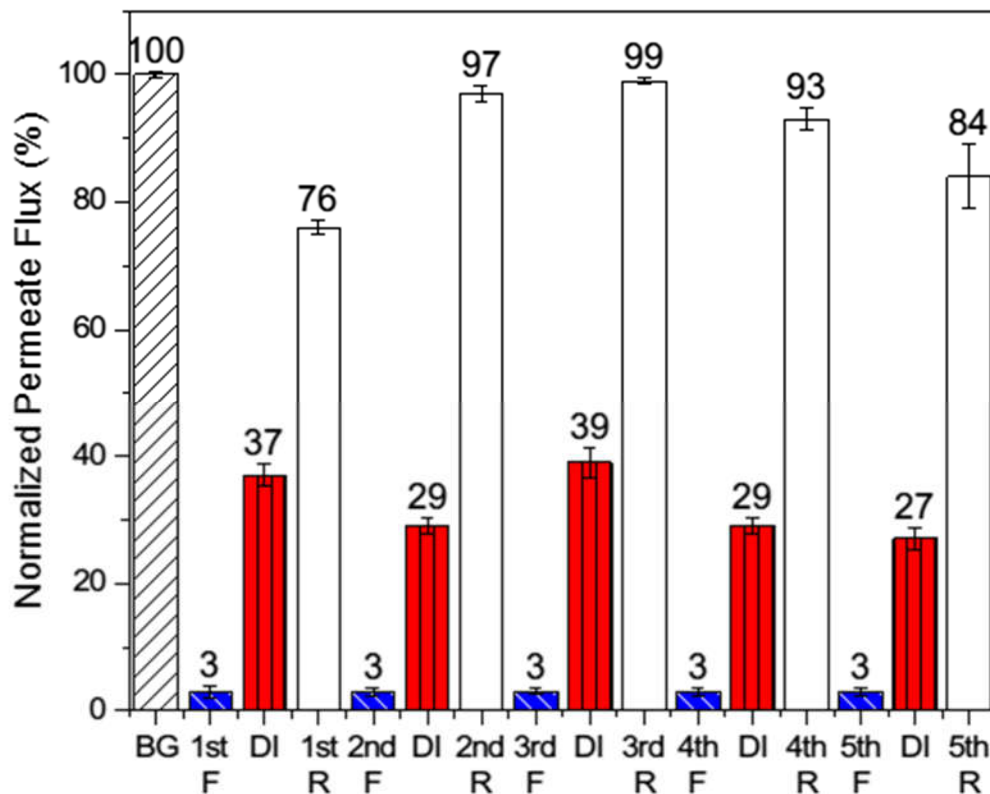


**Figure 17** Normalized permeate flux  $\bar{J}$  under different operational conditions for the anodic CFER in backwash mode of  $150\text{mg L}^{-1}$  HA fouled REM in long term experiment; BG: background, F: fouling, R: anodic CFER; initial membrane flux  $J_0 = 1480\text{ LMH bar}^{-1}$ ; Duration of anodic CFER in backwash mode: 0.5 hour

The effectiveness of the anodic CFER in backwash mode was assessed using a multi-cycle fouling and regeneration experiment. A combination of humic acid fouling and the anodic CFER in backwash mode was conducted for 5 continuous cycles of fouling and regeneration (i.e., the regenerated membrane in one cycle would be directly fouled in the following cycle). Figure 17 shows values for  $\bar{J}$  under different operating conditions in the long-term experiment. The  $\bar{J}$  during all 5 fouling cycles was  $\sim 3.00 \pm 1.0\%$ . After the DI rinse step  $\bar{J}$  was recovered to between  $27.0 \pm 1.7$  and  $37.0 \pm 1.7\%$ , and the anodic CFER in backwash mode was able to recover  $\bar{J}$  to between  $76.0 \pm 1.1$  and  $99.0 \pm 0.57\%$  during the 5 cycles. These results indicate that the anodic

CFER in backwash mode can be used as an effective off-line cleaning method for a near complete recovery of  $\bar{J}$  after humic acid fouling. EIS spectra collected during the Multi-Cycle Test are presented in Appendix B.7 and results show that the active layer is not fully recovered in cycles 1, 3 and 4, and the values of  $\chi_l$  are 1.18, 1.23 and 1.21-fold greater than that of the background, respectively, which indicates residual fouling at the active layer. The permeate recoveries in these three cycles were 76%, 99%, and 93%, suggesting that full active layer regeneration is not needed to obtain full flux recovery, since significant pressure drop takes place across the thick support layer.

#### 4.4.3 Polystyrene microspheres membrane fouling and regeneration

Polystyrene microspheres are often used as a model particulate foulant [41] and result in pore blockage and cake layer formation fouling mechanisms. In this study, a 0.001 wt% polystyrene microsphere solution with a mean diameter of 1.58  $\mu\text{m}$  was prepared in 10 mM  $\text{NaClO}_4$  supporting electrolyte. In the regeneration experiment, both cathodic CFER in backwash mode and anodic CFER in backwash mode were conducted separately in order to test if electrostatic interactions between the polystyrene microspheres and the REM surface have an effect on regeneration. The zeta potentials (-10.8 – 15.7 mV) of polystyrene microspheres in pH 2.0 to 12 solutions were all negatively charged (Figure 40, Appendix B). Therefore, better membrane flux recovery under cathodic CFER was expected, since negatively charged microspheres can be electrostatically repelled from a cathodic polarized membrane surface. In the fouling experiments, 1.58  $\mu\text{m}$  polystyrene microspheres were filtered through the REM, and are completely rejected by the membrane active layer, causing only external membrane fouling. The concentration decay of polystyrene microspheres in the recycled feed solution during the 90-minute filtration experiment is shown in Figure 41, Appendix B. The concentrations of polystyrene microspheres in the permeate solutions were below the detection limit ( $2.0 \text{ mg L}^{-1}$ ), which indicates substantial rejection.

#### 4.4.3.1 *Polystyrene microsphere fouling*

The fouling of the REM with 1.58  $\mu\text{m}$  polystyrene microspheres caused  $\bar{J}$  to decrease to between  $31.0 \pm 2.5\%$  and  $45.0 \pm 3.6\%$  during the three fouling experiments (Figure 18a). It was also observed that the  $\bar{J}$  of the fouled membrane was not completely recovered ( $62.0 \pm 4.3\%$ ) by a single backwash treatment. To gain insight into the fouling mechanism, the common filtration law model [56] was fitted to the permeate flux data. The filtration law model has the following form:

$$\frac{d^2t}{dV^2} = \beta \left( \frac{dt}{dV} \right)^\phi \quad 4-9$$

where  $t$  (min) is the operational time,  $V$  (mL) is accumulated permeate volume at time  $t$ ,  $\beta$  is the blocking law filtration coefficient and the units depend on the value of  $\phi$  (the dimensionless blocking law filtration exponent). Different  $\phi$  values represent different fouling modes. As shown in Figure 18b,  $\phi$  values are 0.89 in the anodic CFER experiment and 0.70 in the cathodic CFER experiment, which are between 0 and 1. The  $\phi$  values suggest that the fouling mechanism is intermediate pore blocking, which assumes the particles reaching the membrane surface obstruct pores and also deposit in multilayers or as a cake layer, or a combination of the two fouling mechanisms [7]. Both the permeate flux data after REM fouling and fouling mechanism extracted from the filtration law confirm the reproducibility of polystyrene microspheres fouling on the REM. Replicate experiments are shown in Appendix B.2.

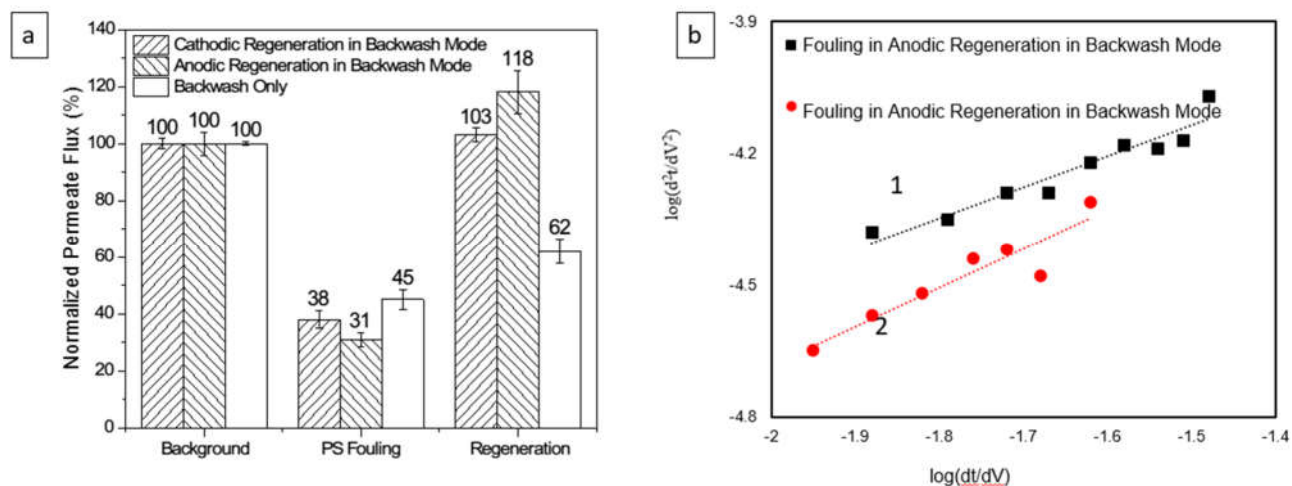


**Figure 18** (a) Normalized permeate flux  $\bar{J}$  under different operational conditions for regenerations of 0.001 wt% polystyrene fouled REM, initial membrane flux  $J_0 = 2286.0$  LMH; (b) filtration law (Equation 9) fit of permeate flux, fit equation:  $y = a \cdot x + b$ ,  $R^2$  after the exponential fit Line 1: 0.995, Line 2: 0.926.

As shown in both Figures 19a and 19c and Table VII, compared to the background EIS spectra, the EIS data after membrane fouling shows an increase of  $R_{ct}$  and decrease of  $A_{electro}$  at all three representative areas. The rejection of microspheres by the active layer should only cause fouling at the outer surface. The membrane “fouling” observed at the active and support layers is due to the fact that pore blockage by the microspheres restricts access of the redox couple and thus increases values for  $R_{ct,active}$  and  $R_{ct,sup}$  at these locations. The hypothesis of intermediate pore blockage is supported by the EIS simulations that show the emergence of two distinct semi-circles over the investigated frequency range and also a significant increase of  $\chi_1$  after fouling [204]. Membrane fouling in the cathodic CFER experiments was greater than that in anodic CFER experiments, which reflects the variability of fouling that is inherent in cake layer fouling. This variability may be due to an uneven pressure drop that develops across the membrane during cake layer formation and back diffusion of the PS. Consequently the fouled membrane in cathodic CFER has much less  $A_{out}$  (24-fold decrease) and produces a more distinct semi-circle at mid frequencies (Figure 19a and 19b), which resembles the EIS simulation results of intermediate pore blockage [204]. The experimental Bode phase plots are also consistent with TLM simulation [204]. Figure 19b and 19d show that the  $\phi$  at the high frequency range shifts to more negative values and at the low frequency range shifts to less negative values.

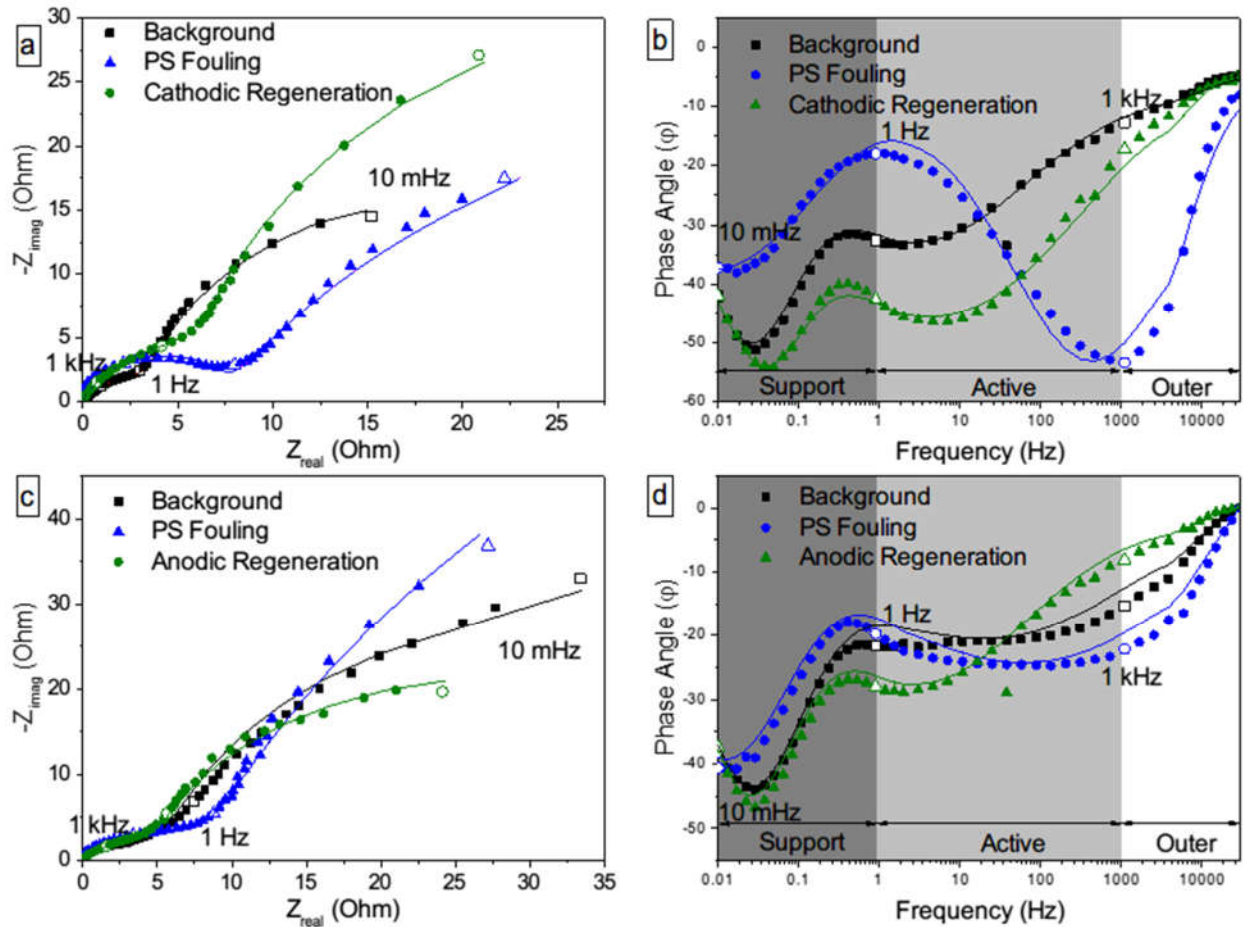


**Figure 19** EIS spectra (a) and Bode phase plot (b) in cathodic CFER of polystyrene fouled membrane in backwash mode; EIS spectra (c) and Bode phase plot (d) in anodic CFER of polystyrene fouled membrane in backwash mode. (Solid lines represent TLM fit, unfilled symbols represent characteristic frequency at 10 mHz, 1.0 Hz, and 30 kHz and layers of the REM are differentiated through various shades.)

**Table VII** MODEL PARAMETER AND CALCULATED DOUBLE LAYER CAPACITANCES OF BACKGROUND, 1.58  $\mu\text{M}$  POLYSTYRENE FOULING AND CATHODIC/ANODIC CFER IN BACKWASH MODE (UNIT:  $X_1$  (OHM), R (OHM), Y ( $\text{F}\cdot\text{S}^{\text{A}-1}$ ),  $C_{\text{DL}}$  (FARAD), A ( $\text{CM}^2$ )). RESULTS FOR REPLICATE EXPERIMENTS ARE INCLUDED IN THE APPENDIX.

a. Cathodic CFER in Backwash Mode							b. Anodic CFER in Backwash Mode								
Parameter	Background	Error ( $\pm$ )	PS Fouled	Error ( $\pm$ )	Regeneration	Error ( $\pm$ )	Parameter	Background	Error ( $\pm$ )	PS Fouled	Error ( $\pm$ )	Regeneration	Error ( $\pm$ )		
$\chi I$	$7.13 \times 10^0$	$4.23 \times 10^{-2}$	$8.19 \times 10^1$	$2.27 \times 10^{-2}$	$1.01 \times 10^1$	$1.83 \times 10^{-2}$	$\chi I$	$1.56 \times 10^1$	$9.38 \times 10^{-2}$	$5.99 \times 10^1$	$7.77 \times 10^{-2}$	$1.99 \times 10^1$	$3.24 \times 10^{-2}$		
Outer Surface	$R_{\text{ct,out}}$	$3.89 \times 10^1$	$2.03 \times 10^0$	$2.92 \times 10^4$	$5.03 \times 10^2$	$3.89 \times 10^1$	$3.13 \times 10^0$	Outer Surface	$R_{\text{ct,out}}$	$2.18 \times 10^1$	$5.08 \times 10^0$	$1.11 \times 10^2$	$1.59 \times 10^1$	$9.74 \times 10^0$	$4.54 \times 10^{-1}$
	$Y_{0,\text{out}}$	$4.03 \times 10^{-2}$	$1.09 \times 10^{-3}$	$9.87 \times 10^{-4}$	$1.64 \times 10^{-5}$	$1.47 \times 10^{-2}$	$9.05 \times 10^{-4}$		$Y_{0,\text{out}}$	$6.54 \times 10^{-3}$	$3.46 \times 10^{-4}$	$1.54 \times 10^{-3}$	$5.21 \times 10^{-4}$	$1.29 \times 10^{-2}$	$5.10 \times 10^{-3}$
	$\alpha$	$7.03 \times 10^{-1}$	$2.46 \times 10^{-2}$	$1.00 \times 10^0$	$1.31 \times 10^{-1}$	$1.00 \times 10^0$	$7.07 \times 10^{-2}$		$\alpha$	$9.88 \times 10^{-1}$	$1.30 \times 10^{-2}$	$1.00 \times 10^0$	$1.01 \times 10^{-1}$	$9.09 \times 10^{-1}$	$3.45 \times 10^{-2}$
Active Layer	$R_{\text{ct,active}}$	$4.26 \times 10^0$	$1.20 \times 10^{-1}$	$1.85 \times 10^4$	$3.46 \times 10^2$	$6.00 \times 10^0$	$3.85 \times 10^{-1}$	Active Layer	$R_{\text{ct,active}}$	$7.73 \times 10^0$	$2.83 \times 10^{-1}$	$3.64 \times 10^1$	$5.66 \times 10^0$	$8.78 \times 10^0$	$3.99 \times 10^{-1}$
	$Y_{0,\text{active}}$	$1.22 \times 10^{-1}$	$1.04 \times 10^{-2}$	$9.12 \times 10^{-3}$	$2.05 \times 10^{-4}$	$1.11 \times 10^{-1}$	$1.36 \times 10^{-2}$		$Y_{0,\text{active}}$	$1.64 \times 10^{-1}$	$2.92 \times 10^{-2}$	$2.95 \times 10^{-2}$	$6.91 \times 10^{-4}$	$1.63 \times 10^{-1}$	$2.83 \times 10^{-2}$
	$\alpha$	$9.60 \times 10^{-1}$	$6.43 \times 10^{-3}$	$1.00 \times 10^0$	$8.84 \times 10^{-2}$	$9.94 \times 10^{-1}$	$3.01 \times 10^{-2}$		$\alpha$	$7.00 \times 10^{-1}$	$2.21 \times 10^{-2}$	$9.11 \times 10^{-1}$	$3.98 \times 10^{-2}$	$9.21 \times 10^{-1}$	$2.55 \times 10^{-2}$
Support Layer	$R_{\text{ct,sup}}$	$3.67 \times 10^1$	$2.88 \times 10^0$	$7.72 \times 10^1$	$6.47 \times 10^0$	$8.29 \times 10^1$	$3.02 \times 10^0$	Support Layer	$R_{\text{ct,sup}}$	$6.49 \times 10^1$	$3.46 \times 10^0$	$4.95 \times 10^2$	$6.49 \times 10^1$	$4.81 \times 10^1$	$5.66 \times 10^0$
	$Y_{0,\text{sup}}$	$5.69 \times 10^{-1}$	$3.95 \times 10^{-3}$	$2.36 \times 10^{-1}$	$2.36 \times 10^{-3}$	$2.01 \times 10^{-1}$	$1.50 \times 10^{-3}$		$Y_{0,\text{sup}}$	$2.93 \times 10^{-1}$	$2.65 \times 10^{-3}$	$1.94 \times 10^{-1}$	$1.84 \times 10^{-2}$	$3.52 \times 10^{-1}$	$8.01 \times 10^{-2}$
	$\alpha$	$9.32 \times 10^{-1}$	$1.73 \times 10^{-3}$	$7.03 \times 10^{-1}$	$3.33 \times 10^{-3}$	$9.05 \times 10^{-1}$	$5.70 \times 10^{-3}$		$\alpha$	$9.44 \times 10^{-1}$	$3.64 \times 10^{-3}$	$7.55 \times 10^{-1}$	$3.46 \times 10^{-3}$	$9.24 \times 10^{-1}$	$3.64 \times 10^{-3}$
Location	Background	Error ( $\pm$ )	PS Fouled	Error ( $\pm$ )	Regeneration	Error ( $\pm$ )	Location	Background	Error ( $\pm$ )	PS Fouled	Error ( $\pm$ )	Regeneration	Error ( $\pm$ )		
Outer Surface	$C_{\text{dl,out}}$	$2.65 \times 10^{-2}$	$2.46 \times 10^{-3}$	$1.08 \times 10^{-3}$	$5.87 \times 10^{-4}$	$1.47 \times 10^{-2}$	$2.98 \times 10^{-3}$	Outer Surface	$C_{\text{dl,out}}$	$6.31 \times 10^{-3}$	$5.96 \times 10^{-4}$	$1.54 \times 10^{-3}$	$1.15 \times 10^{-3}$	$1.03 \times 10^{-2}$	$5.37 \times 10^{-3}$
	$A_{\text{out}}$	$4.41 \times 10^2$	$4.10 \times 10^1$	$1.81 \times 10^1$	$9.78 \times 10^0$	$2.46 \times 10^2$	$4.96 \times 10^1$		$A_{\text{out}}$	$1.05 \times 10^2$	$9.94 \times 10^0$	$2.57 \times 10^1$	$1.92 \times 10^1$	$1.72 \times 10^2$	$8.95 \times 10^1$
Active Layer	$C_{\text{dl,active}}$	$1.18 \times 10^{-1}$	$1.11 \times 10^{-2}$	$7.96 \times 10^{-3}$	$1.57 \times 10^{-3}$	$1.09 \times 10^{-1}$	$1.60 \times 10^{-2}$	Active Layer	$C_{\text{dl,active}}$	$1.48 \times 10^{-1}$	$4.00 \times 10^{-2}$	$2.83 \times 10^{-2}$	$2.22 \times 10^{-3}$	$1.60 \times 10^{-1}$	$3.13 \times 10^{-2}$
	$A_{\text{active}}$	$1.96 \times 10^3$	$1.86 \times 10^2$	$1.33 \times 10^2$	$2.62 \times 10^1$	$1.82 \times 10^3$	$2.67 \times 10^2$		$A_{\text{active}}$	$2.46 \times 10^3$	$6.67 \times 10^2$	$4.72 \times 10^2$	$3.71 \times 10^1$	$2.67 \times 10^3$	$5.22 \times 10^2$
Support Layer	$C_{\text{dl,sup}}$	$6.41 \times 10^{-1}$	$7.50 \times 10^{-3}$	$3.44 \times 10^{-1}$	$8.34 \times 10^{-3}$	$2.17 \times 10^{-1}$	$2.92 \times 10^{-3}$	Support Layer	$C_{\text{dl,sup}}$	$3.12 \times 10^{-1}$	$4.36 \times 10^{-3}$	$2.52 \times 10^{-1}$	$3.14 \times 10^{-2}$	$3.85 \times 10^{-1}$	$9.28 \times 10^{-2}$
	$A_{\text{sup}}$	$1.07 \times 10^4$	$1.25 \times 10^2$	$5.74 \times 10^3$	$1.39 \times 10^2$	$3.62 \times 10^3$	$4.86 \times 10^1$		$A_{\text{sup}}$	$5.21 \times 10^3$	$7.26 \times 10^1$	$4.20 \times 10^3$	$5.23 \times 10^2$	$6.42 \times 10^3$	$1.55 \times 10^3$

#### 4.4.3.2 Membrane regeneration

After the application of either a cathodic or an anodic CFER to the REM in backwash mode, the  $\bar{J}$  values were completely recovered (Figure 18a). The flux was not completely restored for the backwash treatment without an applied electrode potential, which showed  $\bar{J}$  of  $62.0 \pm 4.3\%$  (Figure 18a). These results suggest that electrochemical reactions also had an influence on the regeneration process. In the spent backwash solution, the normalized concentrations of polystyrene microsphere washed out of the REM for anodic and cathodic CFER were 78.0% and 82.0%, respectively.

From the fitted model parameters shown in Table VII, the decrease in  $R_{ct}$  over all three interfaces indicates restoration of the membrane and decrease in  $\chi_l$  indicates that the pores at the active layer are accessible to the active redox couple after the regeneration. However, the regeneration is only due to the removal of the fouling layer at the outer REM surface, which allows the redox couple to regain access to the active and support layers. These observations also support the calculated  $A_{electro}$  values in Table VII, which show near complete recovery. Figure 18a shows that both anodic and cathodic CFER in backwash mode produced a higher permeate flux ( $103 \pm 2.4\%$  after cathodic CFER and  $118 \pm 7.4\%$  after anodic CFER) than that in backwash only operation ( $62 \pm 4\%$ ). The Bode phase plots show that a shift to less negative  $\varphi$  in the high frequencies after the CFER, which justifies the recovery of the outer surface. Although  $\bar{J}$  was completely restored after regeneration (Figure 18a), the EIS spectra were not identical to background conditions. This result indicates that either surface passivation or other changes to the REM may have occurred. Further work is needed to investigate the dimensional stability of the REM during fouling and regeneration cycling.

The zeta potentials of the microspheres were negatively charged at all pH values, most likely due to residual sulfonate groups leftover during the polystyrene microsphere synthesis process. Since both anodic and cathodic CFER were equally effective, the electrostatic interactions between the microspheres and the REM do not appear to be an important mechanism for regeneration. However, the fact that both anodic and cathodic CFER in backwash mode were able to completely recover the fouled membrane and backwash

alone was not, indicates that an electrochemical potential is a necessary step during membrane regeneration. Therefore, the possible reasons for better flux recovery during electrochemical regeneration is likely related to the interaction of electrochemically produced gas bubbles with microspheres. However, the mechanism for regeneration needs further study.

#### **4.5 Conclusions**

A substoichiometric TiO<sub>2</sub> REM was successfully synthesized from a TiO<sub>2</sub> UF tubular membrane and the main composition was Ti<sub>4</sub>O<sub>7</sub> and Ti<sub>6</sub>O<sub>11</sub>. Two model foulants, humic acid and polystyrene microspheres, were used for the investigation of REM fouling. An EIS technique was used to spatially characterize membrane fouling. Based on the information obtained from EIS characterization, a new CFER scheme was developed that utilized electrochemical regeneration in backwash mode, and was able to fully recover a fouled membrane without chemical reagent addition. The REM also proved to be durable and stable in a multi-cycle experiment consisting of 5 consecutive fouling/regeneration cycles. The use of a redox active species for EIS measurements does not allow this method to be used for *in situ* measurements. Future studies should explore using EIS measurements in the oxygen evolution region so that the addition of a redox active species can be avoided. The power consumption during the non-optimized membrane regeneration procedure was low, at only 0.61 kWh m<sup>-2</sup> (geometric surface area) for anodic CFER of both humic acid fouled and polystyrene microsphere fouled REMs with backwash (5.36 V average cell potential and 0.70 A current for 30 min) and 0.39 kWh m<sup>-2</sup> for cathodic CFER of polystyrene microsphere fouled REM with backwash (3.43 V average cell potential and 0.70 A current for 30 min). Using an estimated price of electricity of \$0.10 kWh<sup>-1</sup>, the additional operating cost of applying electrical current to the REM would be between \$0.06 m<sup>-2</sup> and \$0.04 m<sup>-2</sup> per regeneration cycle for anodic and cathodic CFER, respectively. In this study, a 100 mM salt solution was used to provide sufficient ionic strength, and would add additional cost to the process. The cost of refined salt used in the chemical industry is \$150 ton<sup>-1</sup>, preparing a 100 mM salt solution adds an additional \$0.28 m<sup>-2</sup> per regeneration cycle. Therefore, the use of the onsite water sources should be investigated.

The chemical costs for chemical regeneration in a 2.0 wt% NaOH solution are \$3.86 m<sup>-2</sup> per regeneration cycle without including shipping costs. The cost of NaOH is \$0.27 lb<sup>-1</sup> [215], and increases to \$2.72 lb<sup>-1</sup> [216] if shipping is considered, indicating chemical cleaning could be as high as \$38.60 m<sup>-2</sup>. The advantage of an electrochemical regeneration scheme is the elimination of traditional membrane cleaning using chemical reagents, which is not only cost effective and time efficient, but also environmentally friendly. This study has not addressed CFER performance in a water source of low conductivity nor using EIS as a real time on-line monitoring tool, which are topics for further study. However, results of this study are promising and suggest that our novel REM can function effectively in various water treatment applications.

#### **4.6 Acknowledgements**

Funding for this work was provided by the National Science Foundation (CBET-1159764). We thank Dr. Wen Zhang and his research group for performing zeta-potential measurement. We acknowledge the valuable suggestions from the anonymous reviewers.

## V. A MECHANISTIC STUDY OF THE VALIDITY OF USING HYDROXYL RADICAL PROBES TO CHARACTERIZE ELECTROCHEMICAL ADVANCED OXIDATION PROCESSES

REPRINTED WITH PERMISSION FROM Y. JING, B.P. CHAPLIN, A MECHANISTIC STUDY OF THE VALIDITY OF USING HYDROXYL RADICAL PROBES TO CHARACTERIZE ELECTROCHEMICAL ADVANCED OXIDATION PROCESSES, ENVIRON. SCI. TECHNOL. 51 (2017) 2355–2365. COPYRIGHT 2017 AMERICAN CHEMICAL SOCIETY

### 5.1 Abstract

The detection of hydroxyl radicals ( $\text{OH}^\bullet$ ) is typically accomplished by using reactive probe molecules, but prior studies have not thoroughly investigated the suitability of these probes for use in electrochemical advanced oxidation processes (EAOPs), due to the neglect of alternative reaction mechanisms. In this study, we investigated the suitability of four  $\text{OH}^\bullet$  probes (coumarin, *p*-chlorobenzoic acid, terephthalic acid, and *p*-benzoquinone) for use in EAOPs. Experimental results indicated that both coumarin and *p*-chlorobenzoic acid are oxidized *via* direct electron transfer reactions, while *p*-benzoquinone and terephthalic acid are not. Coumarin oxidation to form the  $\text{OH}^\bullet$  adduct product 7-hydroxycoumarin was found at anodic potentials lower than that necessary for  $\text{OH}^\bullet$  formation. Density functional theory (DFT) simulations found a thermodynamically favorable and non- $\text{OH}^\bullet$  mediated pathway for 7-hydroxycoumarin formation, which is activationless at anodic potentials  $> 2.10$  V/SHE. DFT simulations also provided estimates of  $E^\circ$  values for a series of  $\text{OH}^\bullet$  probe compounds, which agreed with voltammetry results. Results from this study indicate that terephthalic acid is the most appropriate  $\text{OH}^\bullet$  probe compound for the characterization of electrochemical and catalytic systems.

### 5.2 Introduction

The hydroxyl radical ( $\text{OH}^\bullet$ ) is a highly reactive oxidant species, which is produced *via* autoxidation in biological systems, advanced oxidation processes (AOPs), and electrochemical advanced oxidation processes (EAOPs) [19,22,25,27,28,81,82,89,90,92,100,112,115,121,123,126,217–220]. Its ability to react

with organic compounds, often with diffusion limited rate constants, and its rapid decay to an innocuous end product of water, has led to an increased interest in using technologies that generate OH<sup>•</sup> for toxic pollutant degradation [101,122,220–223]. The formation of OH<sup>•</sup> at the solid-electrolyte interface is key to the operation of photocatalytic and EAOP technologies, and it is an unwanted side product in several energy technologies (e.g., polymer electrolyte membrane fuel cells; secondary batteries; redox flow batteries) [224–233]. Therefore, quantifying OH<sup>•</sup> production and understanding formation mechanisms are goals across numerous scientific fields.

The short lifetime of OH<sup>•</sup> (~10<sup>-9</sup> s in biological cells [101,102,222,223,234], and 10<sup>-6</sup> to 10<sup>-3</sup> s in water [235–237]) and high reactivity complicate its analytical determination. Therefore, two indirect methods are primarily employed for their detection. The first method is using electron spin resonance (ESR) spectroscopy in the presence of a spin trap, which is a compound that selectively reacts with a radical to form an adduct species that has a sufficient lifetime to allow ESR detection. The second method uses probe compounds that selectively react with OH<sup>•</sup> and often form adduct species that are detected analytically by conventional chromatographic techniques.

The most common spin traps for OH<sup>•</sup> determination are substituted nitrones, where 5,5-Dimethyl-1-pyrroline *N*-oxide (DMPO) is commonly used due to its high selectivity for OH<sup>•</sup> [86–88,91,95,238–242]. However, spin traps can result in the false positive detection of OH<sup>•</sup>, which is documented in the biochemical and toxicology fields [243–248]. False positive detection of OH<sup>•</sup> has been attributed to inverted spin trapping [244–246,249] or the Forrester-Hepburn mechanism [243,247,248]. Inverted spin trapping involves a direct electron transfer oxidation reaction of the spin trap (R) followed by nucleophilic attack by water (Reaction 5-1).



The Forrester-Hepburn mechanism is the reverse of this process, which involves nucleophilic attack of the spin trap by water followed by direct electron transfer oxidation (Reaction 5-2).



Both methods form a radical adduct (R-OH) which is identical to that formed by OH<sup>•</sup> attack on the original spin trap. Cyclic voltammetry experiments have shown that spin trap compounds used for OH<sup>•</sup> detection have peak potentials ( $E_p$ ) of 1.47 to 2.17 V/SHE on a Pt electrode in nonaqueous solvents (e.g., DMPO,  $E_p = 1.87$  V/SHE) [123,250], and thus they are not suitable for OH<sup>•</sup> detection during photocatalytic and EAOP studies. Studies have also shown that metal ions (e.g., Cu(II), Fe(III), Cr(V)) can catalyze the nucleophilic addition step of the Forrester-Hepburn mechanism [240,251], which greatly decreases the redox potential necessary for the subsequent direct electron transfer oxidation step [245]. Ebersson showed that the DMPO-OH<sup>•</sup> product of nucleophilic addition was oxidized to the DMPO-OH adduct by compounds with low redox potentials (-0.26 to 0.74 V/SHE) [245]. While these mechanisms are well reported in the biochemistry literature [243–247], this knowledge has not been adequately transferred to catalytic and electrochemical fields, and thus spin traps have been used to quantify OH<sup>•</sup> production during numerous photocatalytic [87,88,96,99,138], electrochemical oxidation [86,89–91,135], and Fenton-based oxidation studies [92–98,240].

The alternative approach of using probe molecules to detect OH<sup>•</sup> production has also been widely used in a large number of processes, for example, photocatalytic [101–104,113–119,138], electrochemical [25,27,28,81,82,90,100,105–108,123,126,134,135,137], Fenton [109,110,112,122,140], and electrochemical Fenton studies [120,121,139]. Several compounds have been used, including coumarin (COU) [28,81,100–107], salicylic acid [25,82,90,112], benzoic acid (BA) [108–111], terephthalic acid (TA) [28,103,113–122,252], 1,4-benzoquinone (*p*-BQ) [27,100,123,124,253,254], *p*-chlorobenzoic acid (*p*-CBA) [51,126–133,255], *p*-nitrosodimethylaniline (RNO) [123,134,135,137], luminol [113], 3-carboxyproxyl [138], 1,4-dioxane [139], 1-propanol [110], and methylene blue dye [140]. A summary of commonly used OH<sup>•</sup> probes used in various processes are included in the Appendix C.1, and oxidation potentials of select molecules are summarized in the Table XXIV, Appendix C. The most commonly used OH<sup>•</sup> probes are COU, TA, BA, *p*-CBA, and *p*-BQ. The use of probe molecules relies on either the detection of the adduct product,

or the disappearance of the probe molecule. Both direct electron transfer and Forrester-Hepburn mechanisms are also possible with probe molecules, and thus could lead to the false positive detection of  $\text{OH}^\bullet$ . These mechanisms are largely missing from the catalytic and electrochemical literature.

In principle, an appropriate  $\text{OH}^\bullet$  probe should 1) react with  $\text{OH}^\bullet$  at diffusion-limited rates; 2) be resistant to direct electron transfer oxidation reactions at solid/electrolyte interfaces and with soluble redox species; 3) have sufficient solubility in aqueous solutions; and 4) yield a stable product that is detectable by conventional analytical techniques. In this study, we experimentally investigated the suitability of four common probes (i.e., COU, *p*-CBA, TA, and *p*-BQ) for  $\text{OH}^\bullet$  detection at a boron-doped diamond (BDD) electrode using electrochemical methods. Density functional theory simulations were conducted to interpret the experimental data and determine mechanisms for probe compound oxidation. The primary objectives of this study were to determine a stable, selective, and sensitive probe for the detection of  $\text{OH}^\bullet$  produced during EAOPs, and determine the oxidation mechanisms for their removal. Results are discussed in a broader context related to catalytic and photocatalytic systems.

### **5.3 Materials and method**

#### **5.3.1 Reagents**

Chemicals were reagent-grade and used as received (Sigma-Aldrich). Solution pH was adjusted with  $\text{H}_3\text{PO}_4$  or NaOH. All solutions were made with deionized water obtained from a NANOPure water purification system (Barnstead) with resistivity greater than  $18.2 \text{ M}\Omega \text{ cm}$  ( $25^\circ \text{C}$ ).

#### **5.3.2 Electrochemical characterization**

Linear sweep voltammetry (LSV) and cyclic voltammetry (CV) experiments were performed using a Gamry Reference 600 potentiostat (Warminster, PA). A three-electrode setup was used, with BDD as the working electrode ( $0.35 \text{ cm}^2$ ), a 10 cm long, 0.3 mm diameter Pt wire as counter, and a single-junction saturated Ag/AgCl electrode as reference (Pine Research Instruments, Grove City, Pennsylvania).

Experiments used a 50 mL, 1.0 M  $\text{KH}_2\text{PO}_4$  background electrolyte ( $\text{pH} = 5.8$ ) at 25 °C. Potentials were reported versus the standard hydrogen electrode (SHE) by subtracting 0.197 V from the potential measured versus the reference. Prior to the experiment, the BDD electrode was cleaned in the 100 mM  $\text{KH}_2\text{PO}_4$  electrolyte solution at 20  $\text{mA cm}^{-2}$  for 10 min, followed by a cathodic current density of 20  $\text{mA cm}^{-2}$  for another 10 min. The preconditioning step was used to remove adsorbed organic contaminants from the electrode surface. LSV simulations were performed in Matlab 2015b, and details can be found in the Appendix C.3.

### 5.3.3 *Bulk oxidation experiments*

Experiments were performed using a rotating disk electrode (RDE) setup at 5000 rpm using a Pine Research Instruments (Grove City, Pennsylvania) rotator assembly (Model: AFMSRCE). Solution temperatures (15, 25, 35 and 45° C) were maintained in a divided and jacketed glass reactor (H-cell) using a re-circulating water bath (Thermo Scientific Neslab RTE 7). A Nafion N115 membrane separator (Ion Power Inc., New Castle, Delaware) was used in the H-cell to isolate anodic/cathodic reactions. A schematic of the reactor setup is shown in Figure 43, Appendix C.

### 5.3.4 *Mass transfer rates constants*

The mass transfer rate constant ( $k_m$ ) was determined by methods described by Donaghue and Chaplin [256]. Briefly, the limiting current technique was used to estimate the limiting current density and  $k_m$  to the electrode surface at a given rotation speed. The  $k_m$  values at 25 °C are listed in the Table XXV, Appendix C. The diffusion coefficient was calculated by the Stokes-Einstein equation, and the temperature dependent viscosity was calculated using the equation proposed by Al-Shemmeri [257].

### 5.3.5 *Reaction rate constants and curve fitting*

The reaction rate constants were determined by simultaneous regression of duplicate experimental data sets, and the fitting results are reported with 95% confidence intervals. The specific, surface area

normalized reaction rate constant ( $k_s$  ( $\text{m s}^{-1}$ )) was obtained by dividing the first order rate constant by the specific surface area ( $0.7 \text{ m}^{-1}$ ).

### 5.3.6 *Analytical methods*

Liquid chromatography (LC) (Shimadzu, LC-20AD) used a SPD-M30A variable wavelength UV-Visible detector set at 254 nm and a reverse-phase C18 column (Phenomenex,  $4.6 \times 250 \text{ mm}$ ,  $5 \mu\text{m}$ ). Methanol:water (40:60, v/v for COU and 50:50 for *p*-BQ) and methanol:water with 0.1% (v/v) formic acid (60:40 v/v for TA) were used as mobile phases at a total flow rate of  $1.0 \text{ mL} \cdot \text{min}^{-1}$ . The injection volume was programmed at  $5 \mu\text{L}$  (COU or *p*-BQ) or  $10 \mu\text{L}$  (TA). LC with a fluorescent detector (TF-20A, Shimadzu) was used for 7-hydroxycoumarin (7-OH COU) ( $\lambda_{\text{ex}}=332 \text{ nm}$  and  $\lambda_{\text{em}} = 471 \text{ nm}$ ) and 2-hydroxyterephthalic acid (2-OH TA) ( $\lambda_{\text{ex}} = 315 \text{ nm}$  and  $\lambda_{\text{em}} = 435 \text{ nm}$ ) quantification. Analysis was performed in duplicate and evaluated using LabSolutions Lite Version 5.63 software.

### 5.3.7 *Quantum mechanical simulations*

Density functional theory (DFT) simulations were performed using Gaussian 09 software [258]. Unrestricted spin, all-electron calculations were performed using the 6-31G+(d) basis set for geometry optimization and frequency calculations and the 6-311G+(3df, 2p) basis set for energy calculations. Scale factors of 0.9806 and 0.989 were used to correct for known systematic errors in frequency and thermal energies, respectively [259]. Frequency calculations allowed for adjustment of the Gibbs free energies of the reactants and products to standard state conditions ( $\Delta G^\circ$ ). The gradient corrected Becke, three-parameter, Lee–Yang–Parr (B3LYP) functional was used for exchange and correlation. Implicit water solvation was incorporated using the SMD model [260].

The standard reduction potential of the direct electron transfer reaction ( $E^\circ$ ) was calculated according to Equation 5-3.

$$E^\circ = -\frac{\Delta_r G^\circ}{nF} - E_{\text{abs}}^\circ(\text{SHE}) \quad 5-3$$

where  $\Delta_r G^\circ$  is the free energy of the reduction reaction,  $n$  is the number of electrons transferred,  $F$  is the

Faraday constant, and  $E_{abs}^0$ (SHE) is a reference value for the absolute standard reduction potential of the SHE ( $E_{abs}^0$ (SHE) = 4.28 eV) [261–263]. Values for  $\Delta_r G^o$  were calculated from the  $\Delta G^o$  values determined from the geometrically optimized reactant and product structures.

Gibbs free energy of activation ( $E_a$ ) versus electrode potential profiles for direct electron transfer oxidation reactions were determined using Marcus theory according to Equation 5-4 [198].

$$E_a = \frac{\lambda_f}{4} \left( 1 - \frac{96.5(E-E^o)}{\lambda_f} \right)^2 \quad 5-4$$

where  $E$  is the electrode potential (V/SHE) and  $\lambda_f$  is the total reorganization energy for the forward reaction (oxidation reaction). The reorganization energy represents the energy needed to transform the geometric structure of the reactant and solvent to those of the product. Values for  $\lambda_f$  were calculated by subtracting  $\Delta G^o$  of the reactant from that of a compound with an identical geometry of the product, but with the same charge as the reactant. Ionic effects of the supporting electrolyte on  $\lambda_f$  were not calculated, as previous work has shown the effect is minimal in polar solvents with high dielectric constants [264]. Transition state structures were determined using the synchronous transit-guided quasi-newton (STQN) method [265,266] using the QST3 scheme in the Gaussian 09 software. When this method did not converge, the pseudo reaction coordinate method was used. Transition state structures were verified by confirming that frequency calculations yielded a single negative frequency corresponding to the normal mode along the reaction coordinate. Previous work indicates that errors in the calculation of the reaction energies by DFT methods may be up to  $\sim 16$  kJ mol<sup>-1</sup> [267].

## **5.4 Results and discussion**

### **5.4.1 Voltammetry results**

In order to determine if COU, TA, *p*-CBA, and *p*-BQ underwent direct electron transfer reactions at the BDD surface, LSV experiments were conducted with various concentrations of these compounds. Results from LSV experiments indicated that only COU (Figure 20a) and *p*-CBA (Figure 20c) exhibited an increased current with respect to the background electrolyte at approximately 1.7 and 2.0 V/SHE,

respectively, while TA and *p*-BQ did not (Figure 44, Appendix C). The absence of a current response for TA and *p*-BQ in this potential range suggested that these compounds did not undergo direct electron transfer reactions. By contrast, linear relationships between the peak currents and concentrations were observed for both COU and *p*-CBA (Figures 20b and 20d), suggesting they were oxidized by direct electron transfer reactions at the BDD surface. Additionally, LSV study of COU, *p*-CBA, and TA on a Pt electrode showed that oxidation peaks associated with direct electron transfer were found for both COU and *p*-CBA at 1.3 and 1.4 V/SHE, respectively (Figure 45, Appendix C). Evidence for a direct electron transfer reaction for TA was not found (Figure 45, Appendix C). Therefore, it is concluded that the findings of this study are not exclusive to BDD.

Figures 21a and 21b show the background subtracted LSV scans of 5 mM COU at different scan rates and solution pH values. The reversal scans are not shown, since corresponding cathodic peaks were not observed in the CV scans (Figure 46, Appendix C), indicating either a fast chemical reaction removed the direct electron transfer oxidation product or the product itself was not electrochemically active. The anodic peaks for COU oxidation shifted to less positive potentials with increasing solution pH, indicating OH<sup>-</sup> participated in the reaction [268]. For example, at a scan rate of 300 mV s<sup>-1</sup> the peak potentials for COU oxidation at pH 2.16, 5.80 and 11.95 were 2.45, 2.38 and 2.12 V/SHE, respectively. The slope between the anodic peak potential and pH at a scan rate of 20 mV s<sup>-1</sup> was  $-22.5 \pm 3.40$  mV per pH unit. Figure 21c shows that the peak current plotted against the square-root of scan rate follows a linear relationship, indicating a diffusion controlled process and therefore interaction with the electrode surface was not significantly affecting the electron transfer reaction [198].

The kinetic parameters governing the electrochemical reaction kinetics were determined by fitting a mathematical model to the experimental LSV data. The LSV model fits for COU (root-mean-square error (rms) = 0.072) and *p*-CBA (rms = 0.058) are shown in Figures 21b and 20c. The simulation results provided  $E^0$  values for COU and *p*-CBA oxidation of 1.95 and 2.34 V/SHE, respectively. The oxidation kinetics of *p*-CBA were more facile than COU, as the first order heterogeneous kinetic rate constant  $k^0$  for *p*-CBA

oxidation ( $1.46 \times 10^{-3} \text{ m s}^{-1}$ ) was approximately 3 orders of magnitude higher than COU ( $6.00 \times 10^{-6} \text{ m s}^{-1}$ ). The values for transfer coefficient  $\alpha$  were determined as 0.7 and 0.6 for COU and *p*-CBA oxidation, respectively, which agree with reported values [198].

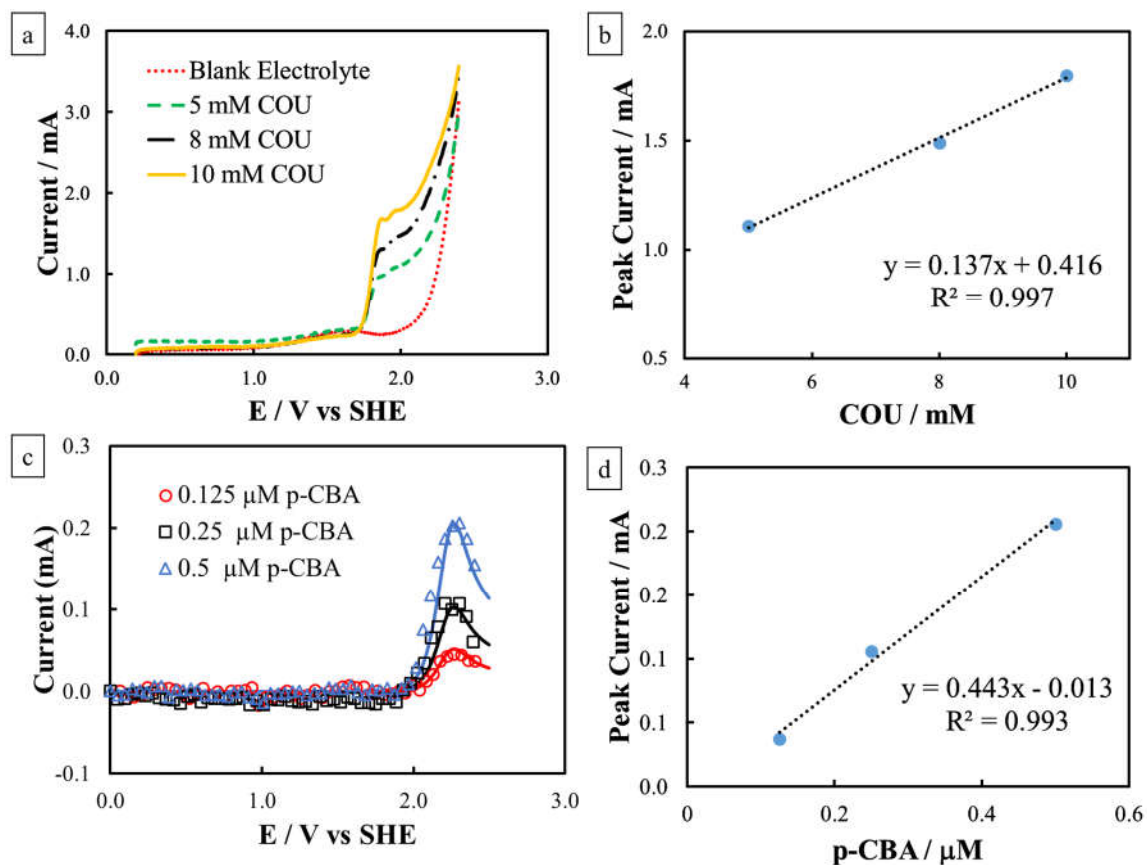


**Figure 20** LSV of (a) COU and (c) *p*-CBA (background subtracted) with different concentrations, and relationship between peak currents and concentrations with linear regression fit of the data for (b) COU and (d) *p*-CBA. In panel (c), hollow symbols and solid lines represent experimental and simulation data, respectively. Temperature: 25°C and electrolyte: 1.0 M  $\text{KH}_2\text{PO}_4$  (pH 5.8).

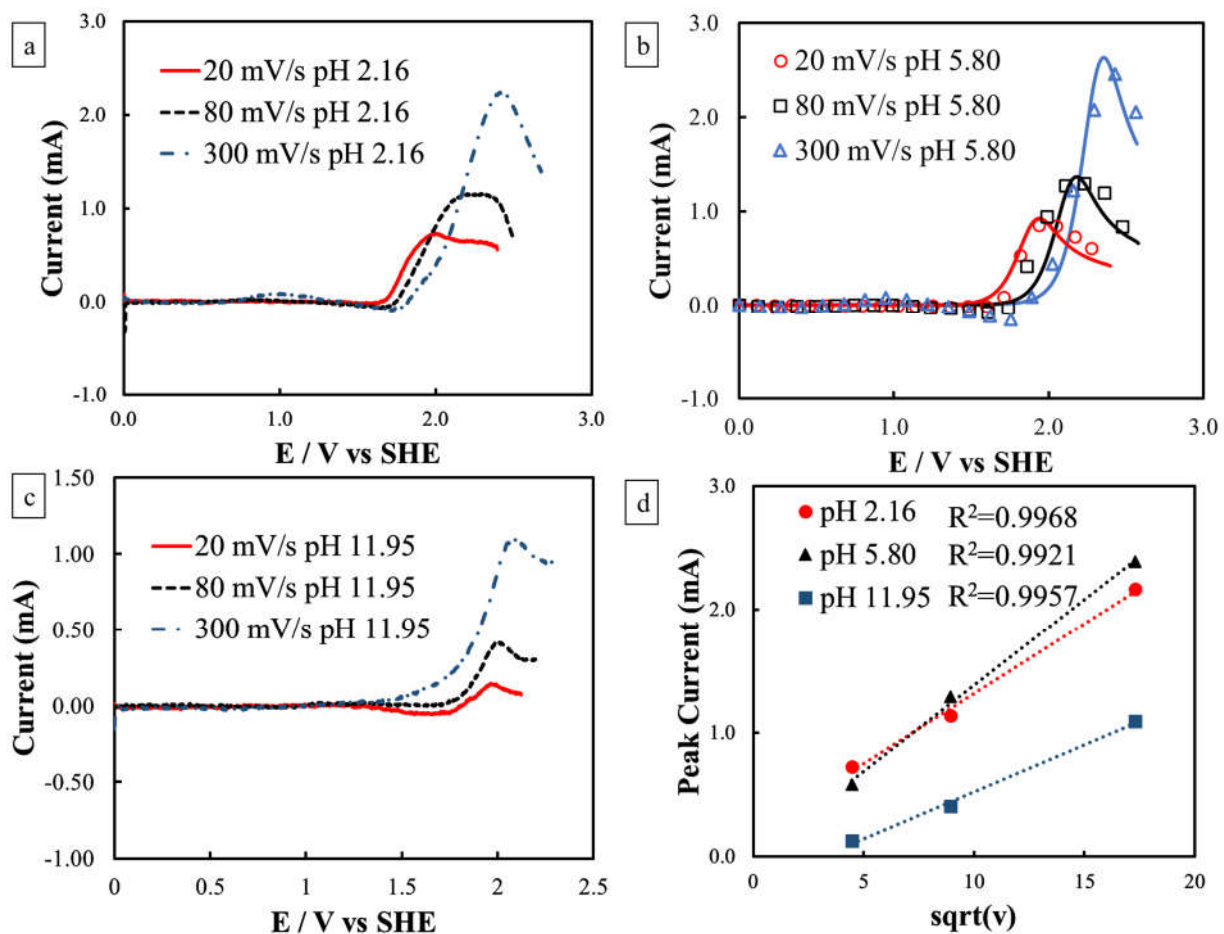


**Figure 21** LSV scans of 5 mM COU (background subtracted) under different scan rates and solution pH values, (a) pH 2.16, (b) pH 5.80 and (c) pH 11.95 (d) Relationship between peak current and square-root of scan rate in different pH solutions. In panel (b), hollow symbols and solid lines represent experimental and simulation data, respectively. Temperature: 25°C and electrolyte: 1.0 M  $\text{KH}_2\text{PO}_4$  (see each panel for pH).

#### 5.4.2 Bulk oxidation experiments

Results from LSV scans indicated that COU reacted *via* a direct electron transfer reaction at potentials  $> 1.7$  V/SHE (Figure 20a), and therefore bulk oxidation of 1 mM COU was performed at anodic potentials of 1.7 and 2.0 V/SHE to determine the  $E_a$  for COU oxidation. The solution was also monitored for the presence of the 7-OH COU product, which is generally considered to be an adduct compound that is formed by  $\text{OH}^-$  addition (Figure 22). Pseudo first-order reaction rate constants were fit to the concentration versus time profiles measured during COU oxidation, and results are summarized in the Table XXVI, Appendix C. The

calculated  $k_m$  for COU was nearly one order of magnitude higher than  $k_s$  values determined for COU oxidation at both potentials, and therefore the oxidation of COU was assumed to be kinetically limited. The Arrhenius plots yielded  $E_a$  values of  $45.2 \pm 2.75$  (Figure 47, Appendix C) and  $16.8 \pm 3.63$  kJ mol<sup>-1</sup> (Figure 22d) at 1.7 and 2.0 V/SHE, respectively. Significant concentrations of the fluorescent 7-OH COU product were detected during the bulk oxidation of COU (Figure 22). At the conclusion of the oxidation experiments  $2.12 \times 10^{-5}$  and  $4.36 \times 10^{-4}$  mM of 7-OH COU was observed at 1.7 and 2.0 V/SHE, respectively, corresponding to average percent yields of 0.03% and 0.22%, respectively. However, OH<sup>•</sup> production should be negligible at the anodic potentials of the experiments (1.7 and 2.0 V/SHE), due to the high redox potential for OH<sup>•</sup> formation ( $E^0 = 2.80$  V/SHE [269]). Negligible OH<sup>•</sup> production is also supported by the low background current (i.e., 0.29 - 0.31 mA) observed in LSV scans of the blank electrolyte (Figure 20a). Therefore, it was assumed that the production of 7-OH COU at anodic potentials of both 1.7 and 2.0 V/SHE was by an alternative reaction mechanism.

Sweep voltammetry results indicate that TA and *p*-BQ were resistant to direct electron transfer oxidation, and thus the oxidation of both compounds at a potential greater than that necessary for OH<sup>•</sup> formation was attributed solely to OH<sup>•</sup> oxidation. An anodic potential of 3.0 V/SHE, which was sufficient to produce OH<sup>•</sup> at the BDD electrode [80], was chosen for the oxidation of both compounds. Results from the bulk oxidation of TA and *p*-BQ at various temperatures are shown in the Figure 48 and 49, Appendix C. The values of  $k_s$  obtained for the concentration profiles of both compounds are summarized in the Table XXVI, Appendix C. A significant concentration ( $4.63 \times 10^{-4}$  mM and average percent yield of 0.11%) of the fluorescent 2-OH TA product from the bulk oxidation of TA was detected at the conclusion of the experiment (Figure 47, Appendix C). Meanwhile, there were not any products detected by either the UV-vis or fluorescent detectors from *p*-BQ oxidation, indicating that ring cleavage of *p*-BQ occurred, which is consistent with previous studies [124,165,253]. The  $k_s$  values for both TA and *p*-BQ oxidation were comparable to the  $k_m$  values (Table XXVI, Appendix C), indicating the bulk oxidation of both TA and *p*-BQ at 3.0 V/SHE were mass transfer controlled. Mass transfer controlled oxidation of *p*-BQ and TA was

attributed to the fast reaction with  $\text{OH}^\bullet$  ( $k_{\text{OH}^\bullet, p\text{-BQ}} = 1.2 \times 10^9 \text{ M}^{-1}\text{s}^{-1}$  [221] and  $k_{\text{OH}^\bullet, \text{TA}} = 4.4 \times 10^9 \text{ M}^{-1}\text{s}^{-1}$  [252]). There is not a signature product from  $p\text{-BQ}$  oxidation that is indicative of  $\text{OH}^\bullet$  formation, and therefore the disappearance of  $p\text{-BQ}$  during anodic oxidation experiments was used to assess  $\text{OH}^\bullet$  formation. However,  $p\text{-BQ}$  is easily reduced to hydroquinone ( $E^0 = 0.28 \text{ V/SHE}$  [270]), and therefore  $p\text{-BQ}$  is only a useful  $\text{OH}^\bullet$  probe in a divided cell, where the anode and cathode are separated by a selective membrane (e.g., Nafion membrane). Therefore,  $p\text{-BQ}$  is also not a useful probe in photocatalytic systems where the catalyst possesses both oxidative and reductive active sites.

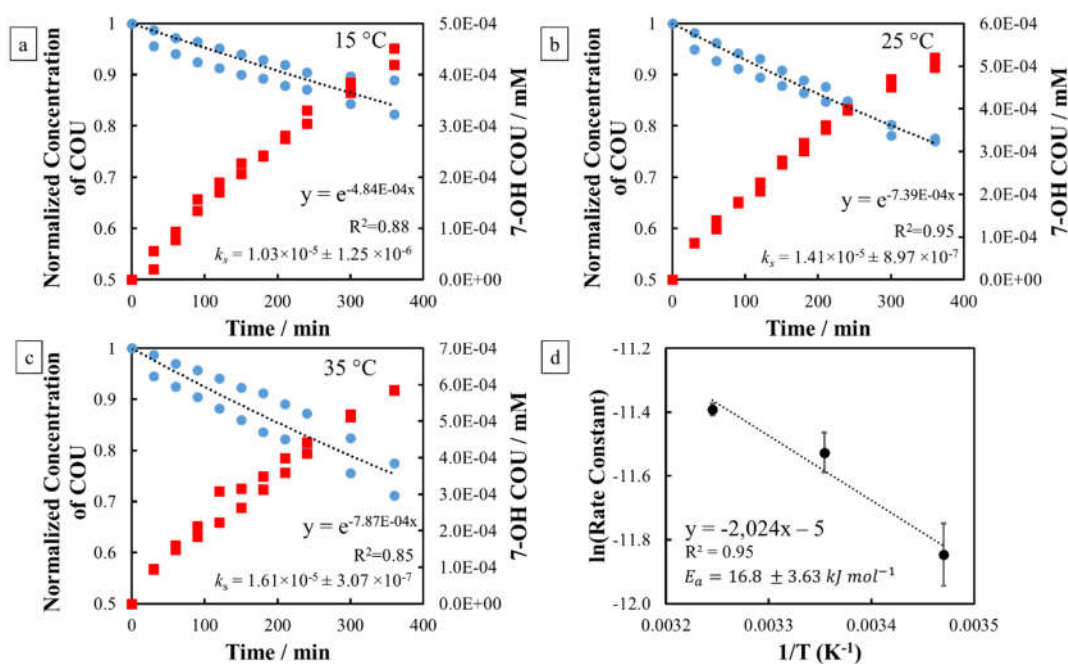


**Figure 22** Bulk oxidation of 1 mM COU at 2.0 V/SHE and a temperature of (a) 15 °C, (b) 25 °C, and (c) 35 °C, respectively. (d) Arrhenius plot for the oxidation of COU at 2.0 V/SHE. ● and ■ represent reactant (COU) and product (7-OH COU), respectively. Experiments were performed in duplicate, and the 1<sup>st</sup> order reaction rate model was fitted to both data sets simultaneously (dashed line). Electrolyte: 100 mM  $\text{KH}_2\text{PO}_4$  (pH 4.5).

### 5.4.3 Density functional theory modeling

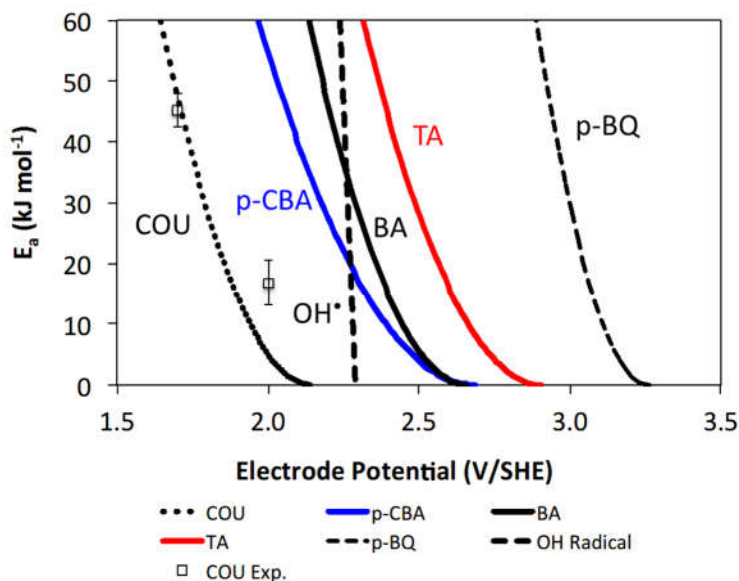
DFT modeling was used to determine  $E^\circ$  and  $\lambda_f$  values for the direct electron transfer reaction (Reaction 5-1) of each of the OH $\cdot$  probe compounds investigated experimentally (COU, *p*-BQ, TA, *p*-CBA). These values were used in Equation 23 to determine  $E_a$  profiles as a function of electrode potential. Some additional common OH $\cdot$  probe compounds were also investigated theoretically, including BA and RNO. Results are shown in Figure 23, and  $E^\circ$  and  $\lambda_f$  values are reported in the Table XXVII, Appendix C. The  $E^\circ$  values of 0.84, 2.04, 2.48, 2.55, 2.76, and 3.21 V/SHE were determined for RNO, COU, *p*-CBA, BA, TA, and *p*-BQ, respectively. These results were consistent with values determined by model fits of the LSV scans for COU and *p*-CBA, which yielded  $E^\circ$  values of 2.34 V/SHE (Figure 20c) and 1.95 V/SHE (Figure 21b), respectively. A comparison between experimental and DFT determined  $E_a$  values for COU also showed close agreement (Figure 23). Experimentally measured  $E_a$  values for COU were  $45.2 \pm 2.75$  kJ mol $^{-1}$  at 1.7 V/SHE and  $16.8 \pm 3.63$  kJ mol $^{-1}$  at 2.0 V/SHE, which were within  $-1.2$  kJ mol $^{-1}$  and  $12.1$  kJ mol $^{-1}$  of DFT determined values, respectively (Figure 23). The close agreement between experimental and theoretical  $E_a$  values at 1.7 V/SHE shows the robustness of the theoretical method. The difference between experimental and theoretical  $E_a$  values at 2.0 V/SHE is largely a result of unactivated processes influencing the experimental  $E_a$  measurement. For example, temperature effects on molecular diffusion, adsorption, or the structure of the double layer can cause errors in accurately measuring  $E_a$  values in this range [271].

Figure 23 also contains the  $E_a$  versus potential profile for OH $\cdot$  formation at an oxidized BDD surface, taken from Chaplin *et al.*[272] Results indicated that the direct electron transfer reaction for RNO and COU proceeded at potentials much less than that for OH $\cdot$  formation, and thus neither RNO nor COU are useful OH $\cdot$  probes. The  $E_a$  versus potential profiles for *p*-CBA and BA in Figure 23 are intersected by the profile for OH $\cdot$ , indicating direct electron transfer reactions were likely dominant at potentials  $< 2.3$  V/SHE, and that both direct electron transfer and OH $\cdot$  oxidation likely occurred at potentials  $> 2.3$  V/SHE for these compounds. The results from LSV experiments showed the direct electron transfer oxidation of *p*-CBA occurred at potentials  $> 2.0$  V/SHE (Figure 20c). By contrast, direct electron transfer reactions for TA and

*p*-BQ were predicted to occur after OH<sup>•</sup> formation. At anodic potentials > 2.3 V/SHE the water oxidation reaction dominated the measured current and therefore LSV scans were not able to provide evidence for direct electron transfer reactions involving *p*-BQ and TA. In addition, these compounds have fast reaction rate constants with OH<sup>•</sup> (i.e.,  $k_{\text{OH}^{\bullet}, \text{BQ}} = 1.2 \times 10^9 \text{ M}^{-1} \text{ s}^{-1}$ ;  $k_{\text{OH}^{\bullet}, \text{COU}} = 2.0 \times 10^9 \text{ M}^{-1} \text{ s}^{-1}$ ) [221,252]. and at high anodic potentials reactions became mass transfer limited (as noted in Table XXVI, Appendix C). Past studies have concluded that under mass transfer limited conditions the indirect oxidation with OH<sup>•</sup> was the dominant oxidation mechanism, because the substrates were depleted *via* reaction with OH<sup>•</sup> in the diffusion boundary layer and did not reach the electrode surface [256]. The results above suggest that *p*-BQ and TA are resistant to direct electron transfer reactions and therefore should be appropriate OH<sup>•</sup> probes, while other probe compounds investigated are not, and their use in electrochemical and heterogeneous catalytic systems should be revisited.

An additional requirement for the OH<sup>•</sup> probes is that they are nonreactive by the Forrester-Hepburn mechanism. Reactivity by this mechanism was assessed by determining  $E_a$  and  $\Delta_r G^o$  values for the nucleophilic addition of OH<sup>-</sup> to each of the compounds, followed by calculation of  $E^o$  and  $\lambda_f$  values for the subsequent direct electron transfer reaction (Table VIII). Transition state structures for the nucleophilic reactions are provided in the Figures 50, Appendix C. Simulations were conducted for OH<sup>-</sup> attack on the C7 and C2 atoms for COU and TA, respectively, as these were the fluorescent adduct probes used to assess OH<sup>•</sup> production in this and other studies [28,81,100–105,107,113–122,252,273]. Simulations determined that nucleophilic addition of OH<sup>-</sup> to COU yielded  $E_a = 130 \text{ kJ mol}^{-1}$  and  $\Delta_r G^o = 118 \text{ kJ mol}^{-1}$ , and addition of OH<sup>-</sup> to TA yielded  $E_a = 123 \text{ kJ mol}^{-1}$  and  $\Delta_r G^o = 111 \text{ kJ mol}^{-1}$  (Table VIII). The relatively high  $E_a$  values and positive  $\Delta_r G^o$  values suggested that these reactions were unlikely to be significant at room temperature. Experimental results supported these theoretical calculations, as removal of COU and TA were not observed under alkaline conditions (pH = 12.4, T = 25 °C). However, catalytic nucleophilic addition has been reported to occur by metal ions in solution (e.g., Fe, Cu, Cr) [240,251]. Therefore, this reaction may be catalyzed by Fenton type reactions and therefore warrants further study. The  $E^o$  values for the

corresponding direct electron transfer reactions are -0.23 and -0.05 V/SHE for COU and TA (Table VIII), respectively; indicating that these reactions would proceed at anodic potentials provided the nucleophilic addition reactions occurred.



**Figure 23** DFT determined  $E_a$  versus electrode potential profiles. Profile for  $\text{OH}^\cdot$  taken from Chaplin *et al.*[256] Squares represent experimental values determined for COU oxidation in RDE experiments.

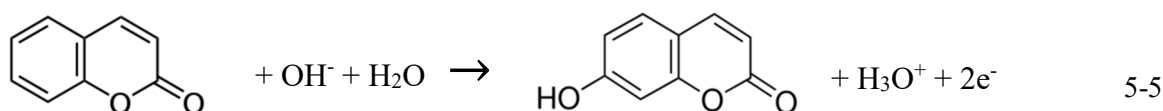
**Table VIII** THEORETICAL PARAMETERS DETERMINED FOR THE REACTION OF PROBE MOLECULES BY THE FORRESTER-HEPBURN MECHANISM.

Reaction	$\Delta_r G^\circ$	$E_a$	$E^\circ$	$\lambda_r$
	( $\text{kJ mol}^{-1}$ )	( $\text{kJ mol}^{-1}$ )	(V/SHE)	( $\text{kJ mol}^{-1}$ )
$\text{COU} + \text{OH}^\cdot \rightarrow \text{COU-OH}^\cdot$	118	130	--	--
$\text{COU-OH}^\cdot \rightarrow \text{COU-OH} + e^-$	--	--	-0.23	13.4
$\text{TA} + \text{OH}^\cdot \rightarrow \text{TA-OH}^\cdot$	111	123	--	--
$\text{TA-OH}^\cdot \rightarrow \text{TA-OH} + e^-$	--	--	-0.05	11.9
$\text{p-BQ} + \text{OH}^\cdot \rightarrow \text{p-BQ-OH}^\cdot$	14.9	42.1	--	--
$\text{p-BQ-OH}^\cdot \rightarrow \text{p-BQ-OH} + e^-$	--	--	1.22	14.9
$\text{p-CBA} + \text{OH}^\cdot \rightarrow \text{p-HBA} + \text{Cl}^-$	-146	125	--	--

The nucleophilic addition of  $\text{OH}^-$  to *p*-BQ was investigated at both the C1 and C2 positions. Due to the symmetry of the molecule, these were the only two unique positions for  $\text{OH}^-$  attack. The  $\Delta_r G^\circ$  for nucleophilic addition of  $\text{OH}^-$  at the C1 and C2 positions of *p*-BQ were 14.9 and 289  $\text{kJ mol}^{-1}$ , respectively (Table VIII). These results indicated that attack at the C1 position was thermodynamically favorable and the calculated  $E_a$  of 42.1  $\text{kJ mol}^{-1}$  indicated that the reaction was feasible at room temperature (Table VIII) [274]. The corresponding direct electron transfer reaction has a calculated  $E^\circ = 1.22 \text{ V/SHE}$ , and thus this reaction would readily occur at anodic potentials used in EAOPs and during photocatalysis.

The nucleophilic addition of  $\text{OH}^-$  to *p*-CBA was studied at the C4 position, and resulted in a substitution reaction that formed *p*-hydroxybenzoic acid (*p*-HBA), with  $\text{Cl}^-$  as the leaving group (Table VIII). The calculated  $E_a$  and  $\Delta_r G^\circ$  values for the nucleophilic substitution reaction were 125 and -146  $\text{kJ mol}^{-1}$ , respectively (Table VIII), indicating the reaction was thermodynamically favorable but likely not significant at room temperature. Since *p*-HBA is a stable product and *p*-CBA is usually used as a  $\text{OH}^\bullet$  probe based on its disappearance, the direct electron transfer reaction was not studied. These results indicated that *p*-BQ has the potential to react *via* the Forrester-Hepburn mechanism, and therefore reactions should not be conducted in alkaline conditions. Results for other compounds are consistent with studies of nucleophilic attack on aromatic derivatives, which indicated that high temperatures are needed for significant reaction rates to proceed [275–277].

Experimental results showed that the anodic oxidation of COU produced the 7-OH COU product at anodic potentials lower than that necessary to produce  $\text{OH}^\bullet$  (i.e., 1.7 and 2.0 V/SHE), which suggested that this product was not exclusively formed by reaction with  $\text{OH}^\bullet$ . Therefore, DFT simulations were conducted to determine a thermodynamically favorable mechanism for its formation. The overall anodic reaction of COU to form 7-OH COU is given by Reaction 5-5.



This reaction involves  $2e^-$  oxidation, which may occur by either direct electron transfer or indirect oxidation with  $\text{OH}^\bullet$ . Results in Figure 23 show that the direct electron transfer oxidation was activationless at potentials  $> 2.1$  V/SHE, which was likely the initial step responsible for conversion to 7-OH COU *via* a non- $\text{OH}^\bullet$  radical mechanism. A possible reaction mechanism that does not involve  $\text{OH}^\bullet$  oxidation is given in Figure 24, where  $\Delta_r G^o$  values were calculated at an electrode potential of  $E = 2.044$  V/SHE ( $E_a = 2.44$   $\text{kJ mol}^{-1}$  (Figure 23)). The mechanism involves three steps, one single electron transfer electrochemical (E) step, followed by one chemical (C) step and another single electron transfer (E) step, and the overall  $\Delta_r G^o = -390$   $\text{kJ mol}^{-1}$  at  $E = 2.044$  V/SHE. The mechanism was defined as an ECE mechanism. At an electrode potential of 2.044 V/SHE, the first electrochemical step (E1) had  $\Delta_r G^o = 0$   $\text{kJ mol}^{-1}$ , and values for  $E_a$  versus electrode potential are given in Figure 23. All subsequent steps were exothermic. The first chemical step (C1) involved nucleophilic attack by  $\text{OH}^-$ , which was activationless and  $\Delta_r G^o = -152$   $\text{kJ mol}^{-1}$ . The second electrochemical step (E2) involved a coupled  $\text{H}^+$  and  $e^-$  transfer to form 7-OH COU. This reaction had a calculated  $E^o = -0.43$  V/SHE, and thus was activationless at an electrode potential of 2.044 V/SHE ( $\Delta_r G^o = -239$   $\text{kJ mol}^{-1}$ ). The participation of  $\text{OH}^-$  in the reaction mechanism was consistent with LSV experimental results that showed  $\text{OH}^-$  dependence on the measured peak potential for COU (Figure 21). The stepwise  $e^-$  and  $\text{H}^+$  transfer reactions were also investigated, which yielded  $E^o = 0.81$  V/SHE for the  $e^-$  transfer step and the  $\text{H}^+$  transfer to  $\text{H}_2\text{O}$  was activationless.

The results above provided an activationless and exothermic pathway for the formation of 7-OH COU from COU oxidation at an applied anodic potential of  $E > 2.1$  V/SHE, indicating that COU was not a useful  $\text{OH}^\bullet$  probe. Since the initial direct electron transfer reaction was rate limiting, the  $E_a$  versus  $E$  profile given in Figure 23 should accurately describe the energy barrier for 7-OH COU formation as a function of potential for the non- $\text{OH}^\bullet$  pathway.

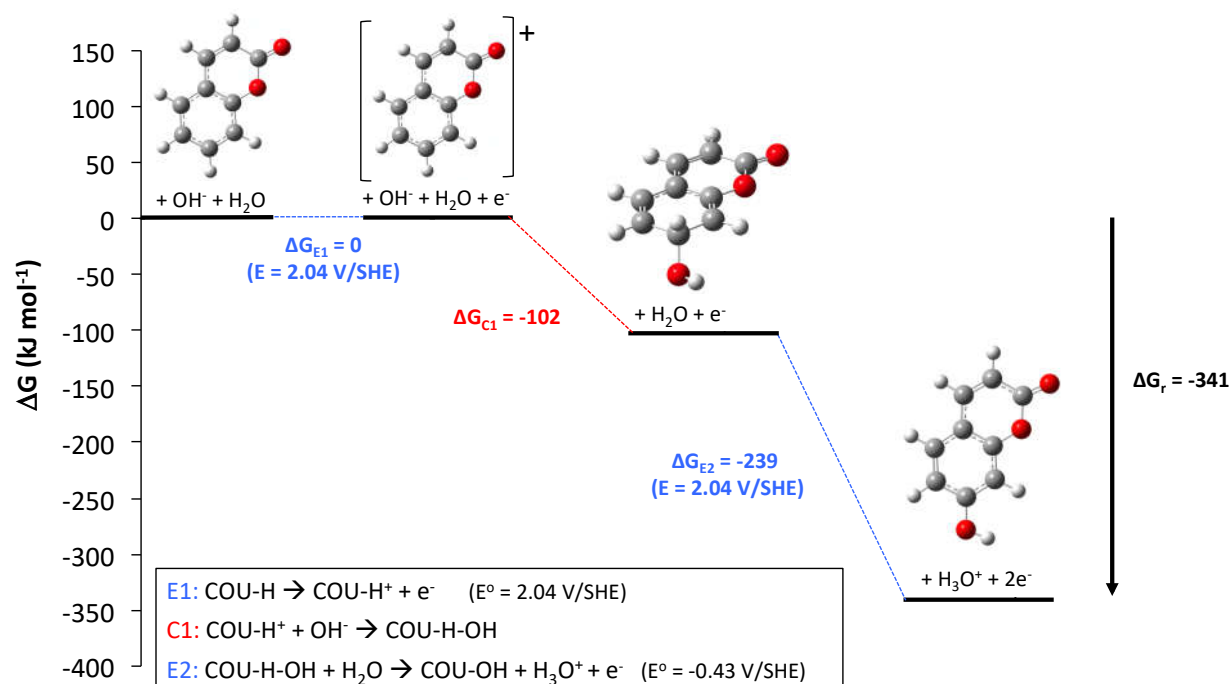


**Figure 24** Free energy diagram of COU oxidation by ECE mechanism

### 5.5 Broader significance and environmental impacts

Although this study was focused on selecting appropriate  $\text{OH}^\bullet$  probes for EAOPs, our findings have broader impacts that extend to other processes involving electron transfer, such as photocatalysis and energy storage/conversion technologies. In photocatalysis, the formation of  $\text{OH}^\bullet$  occurs through a direct electron transfer reaction from  $\text{H}_2\text{O}$  to the UV light excited holes in the valence band of the photocatalyst. This same type of direct electron transfer reaction mechanism can occur for  $\text{OH}^\bullet$  probe compounds, and thus may be falsely interpreted as an indication of  $\text{OH}^\bullet$  formation. Often the direct electron transfer reaction mechanism was assessed in photocatalysis by adding a  $\text{OH}^\bullet$  scavenging compound and assessing its effect on a given substrate [101–104,113,115–119,129,130]. This method does not provide definitive proof for or against a direct electron transfer mechanism, since the  $\text{OH}^\bullet$  scavenger can block direct electron transfer reaction sites and thus slow the reaction of the substrate. In energy storage/conversion technologies,  $\text{OH}^\bullet$  can be formed

from H<sub>2</sub>O<sub>2</sub>, which is a product of the oxygen reduction reaction at the cathode surface. The formation of OH<sup>•</sup> is also possible during the charging process in aqueous electrolytes. Therefore, the use of appropriate probe compounds to characterize OH<sup>•</sup> formation during the charging/discharging process at the electrodes or during fuel cell operation is necessary to prevent false positive detection of OH<sup>•</sup>.

A detailed literature review of OH<sup>•</sup> probes used in various processes is provided in Table XX to XXIII, Appendix C, and electrochemical oxidation potentials of select molecules are summarized in the Table XXIV, Appendix C. Table XXIV, Appendix C indicates that OH<sup>•</sup> probes, such as salicylic acid, luminol, 1-propanol and methylene blue, are susceptible to direct electron transfer reaction, since their reported oxidation potentials are lower than 2.3 V/SHE (Figure 23), however, 1,4-dioxane, with the oxidation potential at 2.4 V, may be an appropriate OH<sup>•</sup> probe in electrochemical and catalytic systems, but requires further investigation.

Many prior studies have used EAOPs and photocatalysis for the oxidation of contaminants in water, and therefore the correct identification and quantification of OH<sup>•</sup> is necessary in order to understand and optimize these processes for environmental remediation. Careful attention should be given when selecting the appropriate probes to detect the formation of OH<sup>•</sup> in these processes. Spin trap compounds, RNO, COU, and *p*-CBA can react by direct electron transfer and Forrester-Hepburn mechanisms, and therefore are not appropriate probes. The results of this study indicated that TA is the most selective OH<sup>•</sup> probe investigated, since it has a high redox potential ( $E^{\circ} = 2.76$  V/SHE), is resistant to the Forrester-Hepburn mechanism, and is not easily reducible.

## **5.6 Acknowledgements**

Funding for this work was provided by the National Science Foundation (CBET-1159764 and CBET-1453081 (CAREER)).

## VI. MECHANISTIC STUDY OF SURFACE PASSIVATION AND REACTIVATION OF A SUBSTOICHIOMETRIC TiO<sub>2</sub> ELECTRODE

### 6.1 Abstract

Substoichiometric TiO<sub>2</sub> has been deemed as one of the most promising and cost-effective electrode materials being investigated for use in many applications, such as information storage, energy conversion and storage, and water treatment. Upon extended anodic polarization, it reportedly suffers from gradual loss in conductivity and electrochemical reactivity, which is also known as surface passivation. However, the mechanism of surface passivation is under debate. In this study, a novel substoichiometric TiO<sub>2</sub> monolithic electrode was synthesized by a thermal reduction process, and the surface passivation and reactivation were examined in three different electrolyte solutions (i.e., H<sub>2</sub>SO<sub>4</sub>, HClO<sub>4</sub>, HCl). The intrinsic electronic properties were evaluated using two-point probe and Mott-Schottky analysis. The charge transfer kinetics of soluble redox couples were studied using scanning electrochemical microscopy and electrochemical impedance spectroscopy, and the crystalline structure and surface composition were examined by X-ray powder diffraction and X-ray photoelectron spectroscopy, respectively. Results showed that reversible surface passivation only occurred in the H<sub>2</sub>SO<sub>4</sub> electrolyte, which was attributed to the formation of TiOSO<sub>4</sub> and not related to a change in the Magnéli phases. The changes in conductivity and electrochemical activity in the presence of HClO<sub>4</sub> and HCl electrolytes were only associated with variations of charge carriers, such as hydrogen doping level and Ti<sup>3+</sup> sites. It was also determined that the Ti<sub>n</sub>O<sub>2n-1</sub> phase was directly related to the hydroxyl radical formation rate, with the highest rate observed for Ti<sub>4</sub>O<sub>7</sub>. Results of this study provided a greater understanding of the surface passivation and reactivation mechanisms on Ti<sub>n</sub>O<sub>2n-1</sub>, which are fundamental to developing electrode materials with long term stability.

### 6.2 Introduction

The creation of oxygen vacancies, which act as intrinsic defects and shallow donors, is an important method that can be used to modify the electronic and optical properties of most transition metal oxide based

semiconductors [141–143]. Among these metal oxides, titanium oxide ( $\text{TiO}_2$ ) generally exhibits higher environmental compatibility, lower cost, and greater chemical stability [278]. To overcome the wide band gap energy of  $\text{TiO}_2$  ( $E_g = 3.0 \text{ eV}$ ) [144], the synthesis of substoichiometric  $\text{TiO}_2$ , by creating oxygen vacancies in the lattice structure of  $\text{TiO}_2$ , is an active area of research [132,142]. As the prevalent defects, oxygen deficiencies are created in the lattice structure of  $\text{TiO}_2$  due to edge sharing of  $\text{TiO}_6$  octahedra in crystallographic shear planes, resulting in dramatic changes in the crystal structure and to the electronic, charge transport, and surface chemical properties, such as adsorptive capacity, polarity, and surface reactivity [152,279]. Depending on the extent of oxygen deficiencies, a series of substoichiometric  $\text{TiO}_2$  phases can be obtained, which are known as Magnéli phases with a general formula of  $\text{Ti}_n\text{O}_{2n-1}$  ( $4 \leq n \leq 10$ ). The oxidation state of Ti atoms are altered as a result of these oxygen vacancies. The Ti atoms in a defect free  $\text{TiO}_2$  surface, are in the  $4+$  oxidation state, the removal of a bridging oxygen atom, which is more energetically favorable compared to in-plane oxygen atom removal, leaves two subsurface  $\text{Ti}^{3+}$  sites exposed [280]. The average electronic charge of a single Magnéli phase is determined by the ratio of  $\text{Ti}^{3+}$  to  $\text{Ti}^{4+}$  that forms a shear structure by electron sharing [281]. Among the Magnéli phases,  $\text{Ti}_4\text{O}_7$  ( $\text{Ti}^{3.5+}$ ) consists of an equal proportion of  $\text{Ti}^{3+}$  and  $\text{Ti}^{4+}$  atoms, where the d band electrons are fully delocalized, and therefore possesses the optimum conductivity [282]. The Magnéli phases can undergo metal-insulator transition under the control of external stimuli, such as temperature, light, and pressure, and thus can be readily used as memristive material for memory and switching devices, or thermoelectric material in electric power generation by waste heat and in cooling systems [146–149]. The superior electronic properties also make Magnéli phases an ideal material for electrodes in electrochemical advanced oxidation processes (EAOPs) [27–29,81,123,283], visible light photocatalysis [150,284], and energy storage [151,278,285–288] and conversion [289–292].

Despite the great potential of  $\text{Ti}_n\text{O}_{2n-1}$  discussed above, it is reported that  $\text{Ti}_n\text{O}_{2n-1}$  suffers from a gradual loss of conductivity during anodic polarization, especially when polarized in a sulfate electrolyte [123,151–153]. The presence of a passivation layer will decrease the electronic conductivity of  $\text{Ti}_n\text{O}_{2n-1}$ ,

which leads to capacity loss from ohmic drop and less stable cycling in energy storage and conversion devices [293], and a decrease in hydroxyl radical production, which are key to the operation of EAOPs and photocatalytic processes [19]. Several authors have studied the gradual loss of electrode activity by monitoring the oxidation kinetics of model compound removal [123,153], X-ray powder diffraction (XRD) measurements [151], and electrochemical impedance spectroscopy (EIS) [152], but the mechanism of surface passivation is still unclear. Among the studies of  $Ti_nO_{2n-1}$  passivation in 0.5 M  $H_2SO_4$ , Chen *et al* claimed the loss of  $Ti_nO_{2n-1}$  activity was due to the irreversible conversion from  $Ti^{3+}$  to a more thermodynamically stable  $Ti^{4+}$  after a 7-hour anodic polarization at  $7 \text{ mA cm}^{-2}$ , meanwhile the phase change from  $Ti_4O_7$  to  $Ti_6O_{11}$ , as confirmed by XRD, after the anodic polarization was observed by Kao *et al* when the electrode was cycled between 1.68 V and 2.58 V vs a Ag/AgCl reference electrode, who also claimed the passivation can occur during cathodic polarization due to the formation of titanium hydride [151].

All previous studies of surface passivation of  $Ti_nO_{2n-1}$  have focused on the use of bulk electrochemical characterization techniques to elucidate the overall change in interfacial electron-transfer properties of this material. However, the resultant charge transfer resistances ( $R_{ct}$ ) and kinetic rate constants generally represent an average for the entire surface. To resolve the surface heterogeneity and local reactivity, studies employed scanning electrochemical microscopy (SECM) to provide spatial resolution of intrinsic charge transfer kinetics at the electrolyte/electrode interface [294–297]. The kinetic heterogeneity is originated from the rate of tunneling of electrons/holes to the redox active species in solution, and therefore slow kinetics occur when either the charge carriers are deep inside the material and slow to migrate to the surface, or charge carrier density is low [296]. The operation of SECM is based on the measurement of the current through a redox reaction by an ultramicroelectrode (UME) tip with a radius on the order of a few nanometers to tens of microns, when it is held constant or moved near the electrode interface [298]. The perturbation in current response of the UME tip in the presence of the electrode provides information about the nature and properties of the electrode with tip size resolution, such as conductivity, electron transfer reaction kinetics, and electrode topography. Local kinetics can be resolved using approach curve

method, which determines the dependence of UME tip current and travelling distance to the substrate, in the feedback mode, where only tip current is monitored. The approach curve method has been used extensively to study the heterogenous charge transfer at an interface [294,296,299,300].

In this study, we investigated the oxygen vacancy stability of  $\text{Ti}_n\text{O}_{2n-1}$  in three supporting electrolytes (HCl,  $\text{HClO}_4$ , and  $\text{H}_2\text{SO}_4$ ), discussed the implication of surface passivation and reactivation on energy technologies, and examined the effect of different Magnéli phases on the hydroxyl radical. We developed the methodology to study changes in charge transfer kinetics at specific locations on a  $\text{Ti}_n\text{O}_{2n-1}$  electrode as a function of anodic and cathodic applied charges. The crystalline structure was monitored by XRD, the variations in the electronic conductivity were evaluated in terms of charge carrier density ( $N_D$ ) by Mott-Schottky analysis and film resistivity ( $\rho_f$ ) by two-point probe method. The changes of local and bulk charge transfer kinetics were investigated using SECM and EIS, respectively. Findings from this work will provide a greater understanding on the oxygen vacancy stability of  $\text{Ti}_n\text{O}_{2n-1}$  at the electrode/electrolyte interface that is an important factor for the successful operation of water treatment and energy storage and conversion technologies, and will also offer insights for improving material manufacture and operational strategies.

### **6.3 Experimental section**

#### **6.3.1 Reagents**

Chemicals were reagent-grade and obtained from Sigma-Aldrich. All chemicals were used as received. All solutions used in this study were made with deionized (DI) water obtained from a NANOPure water purification system (Barnstead Nanopure, Thermo Scientific, Waltham, MA) with resistivity greater than  $18.2 \text{ M}\Omega \text{ cm}$  ( $25^\circ \text{ C}$ ).

### 6.3.2 Preparation of $Ti_nO_{2n-1}$ electrode

Rutile  $TiO_2$  powder was reduced to  $Ti_nO_{2n-1}$  in a tube furnace (OTF-1200X, MTI) at a temperature of 1050 °C and 1.0 atm flowing  $H_2$  environment for 6 hours. The monolith electrode was prepared by mixing 0.78 g of  $Ti_nO_{2n-1}$  powder with 0.12 g of paraffin oil as binder, and the mixture was then pressed to a pellet form through an industrial hydraulic press (RAMCO) under a 17.2 bar uniaxial pressure in a 1.12 cm diameter die, which produced a pellet thickness of ~3.4 mm. Finally, the paraffin oil binder was removed in the furnace at temperature of 1050 °C and flowing argon environment for 6 hours to produce a binder-free  $Ti_nO_{2n-1}$  pellet.

The binder-free  $Ti_nO_{2n-1}$  pellet was then mounted in a rotating disk electrode holder and attached to a rotator (Pine Research Instruments; MSR rotator; Durham, NC), and polished with grade 800 sandpaper (3M, St. Paul, AK), followed by alumina/DI water slurries (alumina particle diameters: 1.0, 0.3 and 0.05  $\mu m$ ) under a rotation speed of 900 rpm (rounds per minute) for 5, 10, and 15 mins with each particle size. The  $Ti_nO_{2n-1}$  pellet was sonicated in DI water in a sonicator (Cole-Parmer, Vernon Hills, Illinois) for 5 min, and then rinsed with ethanol to remove any residual alumina, and followed by DI water to remove the residual ethanol.

### 6.3.3 Electrochemical methods

SECM experiment was carried out with a CH instrument model 920d (CH instrument, Austin, Texas), the electrochemical cell was made of Teflon and placed on a stainless-steel stage in a sandwich structure with the  $Ti_nO_{2n-1}$  electrode and an underlying glass slide mounted in between as the substrate. Electrochemical impedance spectroscopy, Mott-Schottky analysis, anodic and cathodic polarizations were performed using a Gamry Interface 1000 potentiostat (Gamry, Warminster, PA). All potentials were reported against the saturated Ag/AgCl reference electrode (0.197 V vs a standard hydrogen electrode).

### 6.3.3.1 Scanning electrochemical microscope experiments

A platinum (Pt) UME (CHI116, CH instrument) was used for all SECM measurements. The structure of the UME was discussed elsewhere [299], briefly, the tip of UME was made of 10-micron diameter Pt disk, enclosed by insulating glass. The ratio of glass radius to disk radius (RG) was determined 2.98 by fitting a probe approach curve into the negative feedback equation developed by Lefrou and Cornut [301], as a fresh UME approached to a glass substrate at -0.3 V tip potential in 5 mM Ru(NH<sub>3</sub>)<sub>6</sub>Cl<sub>3</sub> and 100 mM KCl. The value of RG was recorded every time after polishing with 0.05-micron alumina powders and substantial variations were not observed (2.97-3.01). The distance between the UME tip and substrate was controlled coarsely and accurately by monitoring the current using a stepper motor and piezoelectric nanopositioning system, respectively. The resolution limits of the stepper motor and piezo nanopositioner were 8 nm and 1.6 nm, respectively, and in our experiment 4 μm s<sup>-1</sup> and 1 μm s<sup>-1</sup> were used for controlling stepper motor and piezo nanopositioner, respectively. SECM measurements were performed using a four-electrode setup, Pt UME and the substrate electrode were both working electrodes and controlled separately by a bipotentiostat (920d, CH Instrument), while the UME and the substrate shared a Pt wire counter electrode and saturated Ag/AgCl reference electrode. The local reactivity measurements were performed in a solution of 5 mM Ru(NH<sub>3</sub>)<sub>6</sub>Cl<sub>3</sub> and 100 mM KCl, while a tip potential was held at -0.3 V to reach the steady state current for Ru(NH<sub>3</sub>)<sub>3</sub><sup>3+</sup> reduction (See Figure 52, Appendix D). All SECM measurements were made at room temperature (22 °C ± 1 °C).

### 6.3.3.2 Electrochemical impedance spectroscopy (EIS) and Mott-Schottky analysis

The potentiostatic EIS and Mott-Schottky analyses used a three-electrode setup with the Ti<sub>n</sub>O<sub>2n-1</sub> electrode as working electrode, Pt wire with a 0.51 mm diameter as counter electrode, and saturated Ag/AgCl as reference electrode. EIS measurements were made at the open circuit potential (OCP) in an electrolyte containing 5 mM Ru(NH<sub>3</sub>)<sub>6</sub>Cl<sub>3</sub> and 100 mM KCl with an amplitude of 4 mV in the sinusoid perturbation and over a frequency range of 30 kHz to 100 mHz. Mott-Schottky measurements were made at ± 1 V of the OCP and at a frequency of 30 kHz with a voltage step of 0.05 V and an amplitude of 4 mV

perturbation in a 100 mM NaClO<sub>4</sub> electrolyte. A constant temperature was maintained in both measurements at 25 °C using a glass, jacketed reactor and a recirculating water bath (Neslab RTE 7, Thermo Scientific).

#### 6.3.3.3 Anodic aging and cathodic reversal experiments

Anodic aging and cathodic reversal were carried out in 1 M H<sub>2</sub>SO<sub>4</sub>, 2 M HClO<sub>4</sub> and 2 M HCl electrolytes for 30 minutes at an applied 20 mA cm<sup>-2</sup> and -20 mA cm<sup>-2</sup> constant currents, respectively at a constant temperature of 25 °C. The corresponding averaged anodic potentials in H<sub>2</sub>SO<sub>4</sub>, HClO<sub>4</sub>, and HCl were 2.81, 2.67 and 2.58 V, respectively. The corresponding averaged cathodic potentials in H<sub>2</sub>SO<sub>4</sub>, HClO<sub>4</sub>, and HCl were -0.727, -0.766, and -0.782 V, respectively. Control experiments were performed in the electrolyte of same concentration, but without an applied current.

#### 6.3.3.4 Film resistivity

The film resistivity was measured through a source meter (Keithley 2615) using a two-point probe method.

#### 6.3.3.4 Topography mapping

The topography on a specific area of the Ti<sub>n</sub>O<sub>2n-1</sub> electrode was determined by measuring the oxygen reduction current at the UME tip at an applied potential of -0.7 V in a 100 mM NaClO<sub>4</sub> electrolyte, while Ti<sub>n</sub>O<sub>2n-1</sub> was left at the OCP (0.12 V). The justification of this method was detailed in the Appendix D.4.

The amperometric mapping of the oxygen reduction current over a specific area was converted to a topographic map by using the equations developed by Lefrou and Cornut [301]. Briefly, the negative feedback equation described the relationship between the tip current and the relative distance between the tip and substrate, and a Matlab script was used to solve the relative distance by taking the current at each point from the amperometric map.

#### 6.3.4 Electrode Markers and surface profile

In order to characterize charge transfer kinetics at specific locations during SECM measurements, accurate electrode markers were made on the  $\text{Ti}_n\text{O}_{2n-1}$  electrode using a TYKMA electrox laser marking system (EMS300, Chillicothe, OH) with 30% laser power, 15 repeated times and  $200.0 \text{ mm s}^{-1}$  traveling speed. These markers allowed for a triangulation method to be used to resample the same spots on the electrode. A pattern containing three anchor points, as shown in Figure 51, Appendix D, was created on the electrode using the laser marking system. Details of laser marking, pattern examination, and a Matlab script for implementing the triangulation procedure can be found in the Appendix (Sections D-1 and D-2).

The marked pattern was examined by using a nano-contour GT-K optical profilometer (Bruker, Billerica, Massachusetts).

#### 6.3.5 X-ray powder diffraction (XRD)

The crystalline structures of  $\text{Ti}_n\text{O}_{2n-1}$  were examined by XRD (Siemens D-5000) with a Cu X-ray tube (40 kV and 25 mA), and scans were collected with DataScan software (MDI, v. 4.3.355, 2005) at a  $0.02^\circ$  step size and a 0.6 s dwell time, XRD patterns were examined in MDI Jade Plus v 6.5.26.

#### 6.3.6 X-ray photoelectron spectroscopy (XPS)

The surface elemental composition of  $\text{Ti}_n\text{O}_{2n-1}$  was examined by XPS (Kratos Axis-165). XPS peak fitting was implemented on XPS Peak Software V4.1.

#### 6.3.7 Thermogravimetric analysis (TGA)

Sample weight was normalized to the initial weight. In order to calculate the activation energy required to convert to a certain higher oxidation state phase from  $\text{Ti}_4\text{O}_7$ , four ramp rates at 5, 10, 20 and  $40^\circ\text{C}/\text{min}$  were chosen, and the equation used for calculating the activation energy ( $E_a$ ) was shown as Equation 6-1.

$$Ea = -R \frac{d \ln \beta}{d \frac{1}{T}} \quad 6-1$$

where  $\beta$  is the heating rate ( $^{\circ}\text{C min}^{-1}$ ),  $T$  is the temperature at which the weight ratio in the TGA plot matches with the molecular weight ratio of the phase of interest to  $\text{Ti}_4\text{O}_7$  ( $^{\circ}\text{K}$ ), and  $R$  is the gas constant ( $8.314 \text{ J K}^{-1} \text{ mol}^{-1}$ )

### 6.3.8 Kinetic analysis of different Magnéli phases for hydroxyl radical production

The hydroxyl radical production rate was determined as the removal rate of 0.1 mM terephthalic acid in 1 M  $\text{KH}_2\text{PO}_4$  from the permeate, and the removal rate was calculated using the equation described by Zaky and Chaplin [27], in a dead-end filtration setup at an applied anodic potential of 3.5 V. The lower bound estimates on the surface concentration of hydroxyl radicals at steady state ( $[\text{OH}^{\bullet}]_s$ ) was calculated using Equation 6-2.

$$[\text{OH}^{\bullet}]_s = \frac{k_{TA}}{k_{TA, \text{OH}^{\bullet}}} \quad 6-2$$

where  $k_{TA, \text{OH}^{\bullet}} = 4.0 \times 10^6 \text{ m}^3 \text{ mole}^{-1} \text{ s}^{-1}$  [221], and  $k_{TA}$  is the nominal surface area normalized observed rate constant for terephthalic acid oxidation determined from the experiment.

$\text{Ti}_n\text{O}_{2n-1}$  samples of different phases were prepared as follows. First, 5 pristine samples were prepared as described in *Section 6.3.2*. According to the TGA analysis (Appendix D.15), Sample 2 to 5 were heated in the furnace in the presence of air to 466.4, 483.7, 494.5 and 501.3  $^{\circ}\text{C}$  from room temperature at a heating ramp of  $5 \text{ }^{\circ}\text{C min}^{-1}$ , while Sample 1 was left untreated.

The solution resistances were measured using EIS and determined as 11.6, 17.2, 15.2, 14.7 and 16.4 ohm for the experiments performed on Sample 1-5, and therefore the solution resistance corrected anodic potentials were calculated 3.32, 3.29, 3.35, 3.38 and 3.40 V, respectively. The analytical method used for terephthalic acid and 2-hydroxyterephthalic acid quantification was described by Jing and Chaplin [302].

## **6.4 Results and discussion**

### **6.4.1 Examination of Crystalline Structure and Electronic Properties during Electrolysis**

Figure 25 shows the XRD patterns of  $Ti_nO_{2n-1}$  samples collected at pristine, post anodic, and post cathodic polarizations in three different supporting electrolytes. In analyzing XRD patterns,  $2\theta$  angles at  $20.78^\circ$  was used as the characteristic peak for  $Ti_4O_7$ . Pristine  $Ti_nO_{2n-1}$  samples in all three cases, as shown in Figure 25, consisted of pure phase  $Ti_4O_7$ , the pattern matched JCPDS (Joint Committee on Powder Diffraction Standards) card no. 00-050-0787 without any notable crystalline impurities. Phase change from the pristine state occurred during the anodic polarization in the  $H_2SO_4$  electrolyte, where a new dominant peak at  $22.80^\circ$  was observed. Observable changes were not identified in the XRD patterns of samples polarized in  $HClO_4$  and  $HCl$  electrolytes. The appearance of new peak at  $22.80^\circ$  can be attributed to  $Ti_6O_{11}$  (JCPDS # 00-050-0788) and/or  $TiOSO_4$  (JCPDS # 00-040-0653), while fitting to the standard patterns yielded similar figures of merit (FOM) (17.2 on  $Ti_6O_{11}$  and 16.1 on  $TiOSO_4$ ). The process of FOM weights involves several factors, such as number of matched peaks and intensity, and a smaller value of FOM represents a more likely fit to the standard card. The peak area ratio ( $PR$ ) of the new dominant peak at  $22.80^\circ$  to the characteristic peak of  $Ti_4O_7$  was used to quantify the variation in crystalline structure in the  $H_2SO_4$  electrolyte, and was calculated as 0.10 at pristine state, when the background intensity (signal noise) at  $22.80^\circ$  position was used for calculation, since a peak was not found at this position. The value of  $PR$  increased to 1.02 after the anodic polarization, decreased to 0.51 and 0.11 after the 1<sup>st</sup> 30 min and 2<sup>nd</sup> 120 min cathodic polarizations, respectively (Figure 25A).

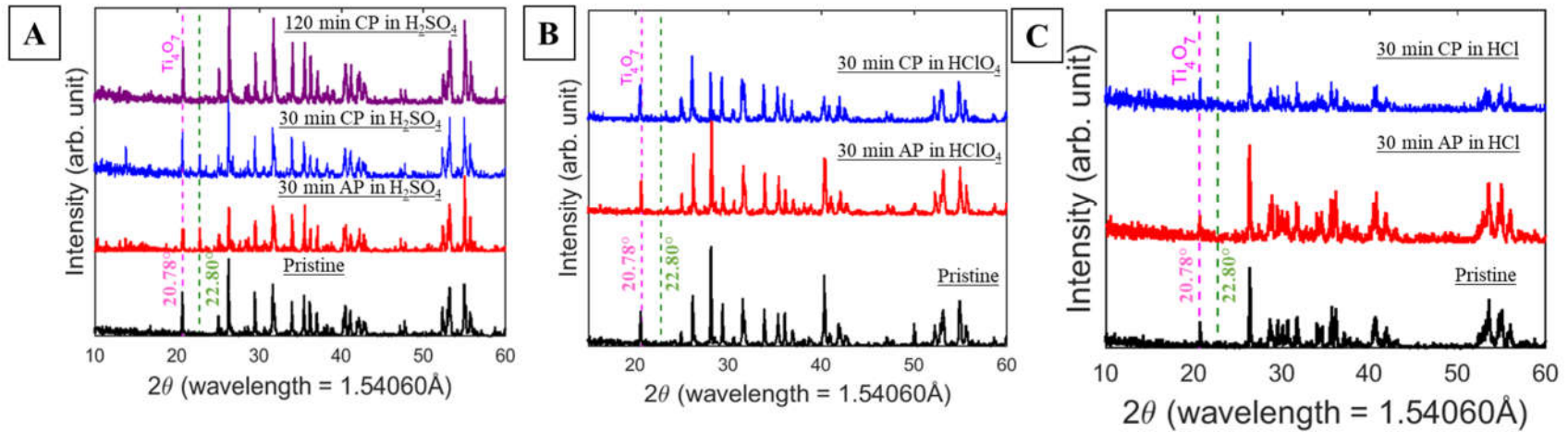


**Figure 25** XRD patterns of the  $\text{Ti}_n\text{O}_{2n-1}$  samples at pristine state and after anodic and cathodic polarizations in (A) 1 M  $\text{H}_2\text{SO}_4$ , (B) 2 M  $\text{HClO}_4$ , and (C) 2 M  $\text{HCl}$  solutions. Characteristic peak of  $\text{Ti}_4\text{O}_7$  is shown as the dashed pink line ( $2\theta = 20.78$ ), and  $2\theta$  angle position at  $22.80^\circ$  is shown as green vertical line. AP and CP stand for anodic polarization and cathodic polarization, respectively.

In the case of a semiconductor, densities of electrons and holes are limited, and therefore, the current flow is often governed by  $N_D$  [303]. As shown in Table XXIX, Appendix D, the value of  $N_D$  was decreased to 2.21% of the pristine state ( $1.79 \times 10^{26} \pm 1.23 \times 10^{23} \text{ cm}^{-3}$ ) after the anodic polarization ( $3.96 \times 10^{24} \pm 4.11 \times 10^{22} \text{ cm}^{-3}$ ), and recovered to 29.9% of the pristine state after the 1<sup>st</sup> cathodic polarization ( $5.35 \times 10^{25} \pm 3.87 \times 10^{22} \text{ cm}^{-3}$ ) and to 52.0% of the pristine state after the 2<sup>nd</sup> cathodic polarization ( $9.31 \times 10^{25} \pm 4.54 \times 10^{23} \text{ cm}^{-3}$ ). The same trend was observed for the  $\rho_f$  of the samples (Table XXX, Appendix D), whose values were  $18.67 \pm 0.020$ ,  $132.70 \pm 0.0040$ ,  $33.94 \pm 0.0010$ , and  $24.17 \pm 0.0023 \text{ } \Omega \text{ cm}$  at pristine, post anodic, 1<sup>st</sup> cathodic, and 2<sup>nd</sup> cathodic polarizations, respectively.

Although changes in crystalline structure were not observed in the diffractograms as a result of anodic and cathodic polarizations in the HClO<sub>4</sub> and HCl electrolytes, variations in both the  $N_D$  and  $\rho_f$  existed. For example, in the HClO<sub>4</sub> electrolyte, as shown in Table XXIX, Appendix D, compared to the pristine state ( $2.34 \times 10^{26} \pm 8.79 \times 10^{22} \text{ cm}^{-3}$ ), the value of  $N_D$  decreased to 6.62% after the anodic polarization ( $1.55 \times 10^{25} \pm 6.29 \times 10^{23} \text{ cm}^{-3}$ ), and then increased to 26.4% after the cathodic polarization ( $6.17 \times 10^{25} \pm 6.33 \times 10^{23} \text{ cm}^{-3}$ ). Meanwhile, Table XXX, Appendix D shows that the value of  $\rho_f$  increased 632% from  $22.72 \pm 0.0020$  to  $143.59 \pm 0.0010 \text{ } \Omega \text{ cm}$  after the anodic polarization, and decreased to  $29.47 \pm 0.0040 \text{ } \Omega \text{ cm}$  after the cathodic reversal. Similar trends in  $N_D$  and  $\rho_f$  were also observed with HCl electrolyte, as shown in Tables XXIX and XXX, Appendix D, the values of  $N_D$  decreased to 27.0 % of the pristine ( $2.80 \times 10^{27} \pm 8.79 \times 10^{23} \text{ cm}^{-3}$ ) after the anodic polarization, and recovered to 54.6 % after the cathodic polarization, furthermore, the values of  $\rho_f$  increased 647% to  $110.89 \pm 0.0031 \text{ } \Omega \text{ cm}$  from the pristine ( $17.13 \pm 0.0010 \text{ } \Omega \text{ cm}$ ), and decreased to  $19.72 \pm 0.0029 \text{ } \Omega \text{ cm}$ . The flat band potentials determined from the Mott-Schottky analysis varied from  $-0.59 \pm 0.017$  to  $-0.84 \pm 0.021 \text{ V}$ , which is comparable to those measured on a N-doped TiO<sub>2</sub> film ( $-0.75$  to  $-0.65 \text{ V}$ ) [132].

All these observations indicated that crystalline structure change was only associated with anodic polarization of Ti<sub>n</sub>O<sub>2n-1</sub> in the H<sub>2</sub>SO<sub>4</sub> electrolyte and can be considered as a reversible process upon cathodic treatment. This change was caused by the electrochemical treatments, since a change in the XRD data was

not observed when the sample was left at the open circuit potential in the H<sub>2</sub>SO<sub>4</sub> electrolyte (see Figure 56, Appendix D). Although changes in crystalline structure were not found in both HClO<sub>4</sub> and HCl electrolytes, changes in  $N_D$  and  $\rho_f$  existed during anodic and cathodic polarizations, which will be discussed later in the text.

#### 6.4.2 Variation in localized and bulk charge transfer kinetics during electrolysis

As discussed above, the changes in the electronic properties, such as  $N_D$  and  $\rho_f$ , occurred during anodic and cathodic polarizations, and in turn, would also affect the electrochemical activity of Ti<sub>n</sub>O<sub>2n-1</sub>, i.e., the charge transfer kinetics at the electrolyte/electrode interface, which can be explained by an electron tunneling mechanism in the space charge layer [304]. At a constant applied anodic potential on the Ti<sub>n</sub>O<sub>2n-1</sub>, which is considered as n-type semiconductor as confirmed by the positive slope shown in the Mott-Schottky plots (see Figure 54, Appendix D), band bending will introduce a space charge layer near the electrode surface, where electrons are depleted [305]. The width of the space charge layer ( $d_{sc}$ ) is strongly affected by and inverse to  $N_D$ . Therefore, a larger  $N_D$  will produce a thinner  $d_{sc}$ , and in turn a higher electron tunneling probability. For example, in H<sub>2</sub>SO<sub>4</sub> electrolyte at 3.20 V applied potential (3.0 V vs SHE, which is suitable for hydroxyl radical production on Ti<sub>n</sub>O<sub>2n-1</sub>) [27,165], the values of  $d_{sc}$  increased from 0.41 nm at the pristine state to 3.24 nm after anodic polarization, and decreased to 0.88 nm after cathodic polarization. It is reported that electron tunneling can only take place when  $d_{sc}$  is less than 1-2 nm [306], which indicates Ti<sub>n</sub>O<sub>2n-1</sub> after anodic polarization was less electrochemically active due to a longer  $d_{sc}$ , and its activity can be partially recovered upon cathodic polarization. Although the  $d_{sc}$  after anodic polarization (3.24 nm) is beyond the electron tunneling width, reactivity for hydroxyl radical formation was still observed, which could be attributed to the heterogeneity of the energy band structure, charge carrier density, local conductivity, electric field induced band bending and electron hopping [305].

In this section, the localized and bulk charge transfer kinetics were examined using SECM and EIS, respectively. In the SECM test, 80 × 80 μm<sup>2</sup> surface images were taken on five well-separated areas, and four approach curves were collected in each area to resolve the local charge transfer kinetics. In discussing

the local kinetics, only one set of surface images at pristine, post anodic, and cathodic polarizations in 1 M H<sub>2</sub>SO<sub>4</sub> electrolyte was discussed as a representative data set, the other images and kinetic data were summarized in the Appendix D.10 – D.13.

The localized and bulk kinetics of the charge transfer reaction were studied using the redox reaction between Ru(NH<sub>3</sub>)<sub>6</sub><sup>3+</sup> and Ru(NH<sub>3</sub>)<sub>6</sub><sup>2+</sup> at the working electrode due to a facile outer sphere electron transfer and electrode fouling was not observed at either the Pt UME or substrate [294]. Figure 26A to 26C show the surface images of mixed kinetics and topography collected in the same area of Ti<sub>n</sub>O<sub>2n-1</sub> electrode at different states, while Figure 26D shows the pure topographic information of this specific area. The oxygen reduction reaction resolved topographic image indicated a  $2.13 \pm 0.17 \mu\text{m}$  surface roughness, and was very comparable to that determined by the surface profilometer ( $2.36 \pm 0.32 \mu\text{m}$ ), which confirmed the robustness of the SECM method for topographic mapping. The topographic images remained almost identical among experiments (See Appendix Figure 63), which suggested the differences in the images (Figure 26A to 26C) should be dominated by the kinetic changes. The normalized averaged currents over the images were calculated as  $1.26 \pm 0.044$ ,  $1.08 \pm 0.0082$ , and  $1.20 \pm 0.023$  at the pristine, post anodic, and cathodic polarizations, respectively. The trend in current change indicated a loss of electrochemical activity at the post anodic polarization, and partial reactivation at the post cathodic polarization, which was in line with the measurements for  $N_D$  and  $\rho_f$ . Localized kinetics were also measured at four well separated spots (point 1 to 4) shown in Figure 26A by the probe approach curves, and the normalized kinetic constants were determined by fitting the equation developed by Lefrou and Cornut for a kinetic controlled system to the data (see fitting details in Appendix D.13 and fitting results in Table XXXIII to XXXV), Appendix D [301]. The kinetics at the post anodic and cathodic polarizations ranged from 43.14 – 65.74% and 69.28 – 93.52% of the pristine values, respectively (Table XXXIII to XXXV, Appendix D).

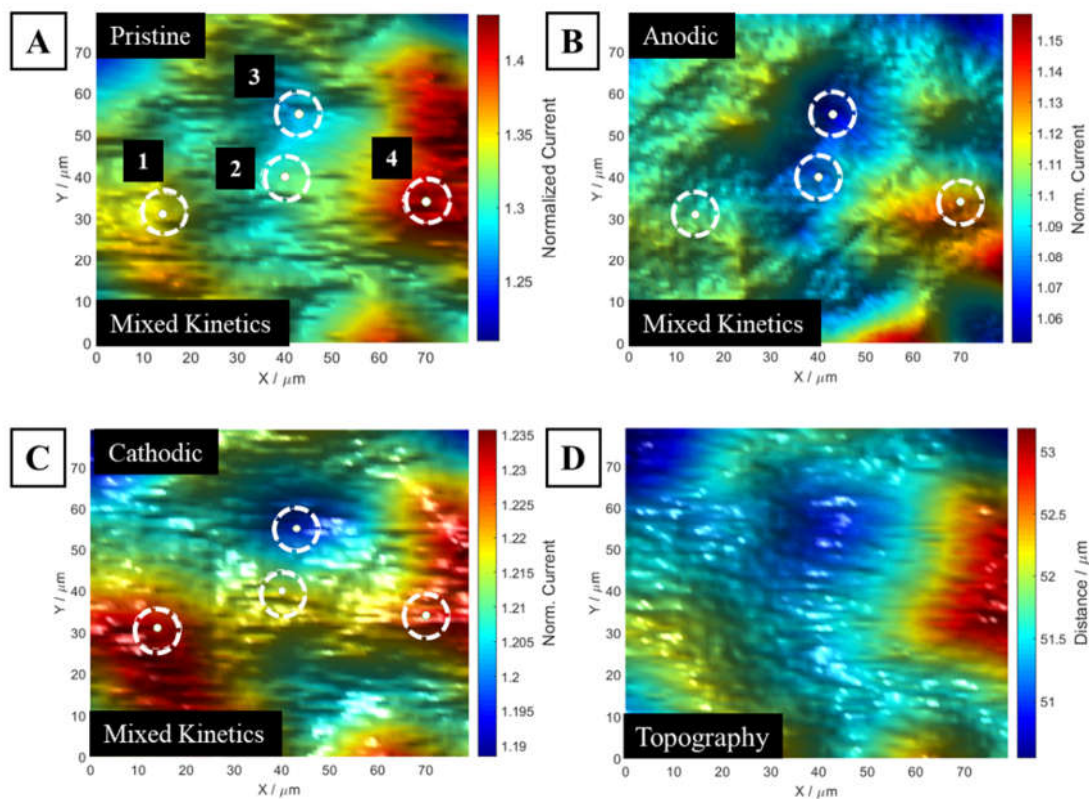


**Figure 26** Surface images collected in the same area at (A) pristine, (B) post anodic polarization in  $\text{H}_2\text{SO}_4$  electrolyte, and (C) post cathodic polarization states in  $\text{H}_2\text{SO}_4$  electrolyte. (D) Topographic mapping of this area. (Dashed circles represent the actual size of UME tip.)

The other images in each electrolyte exhibited similar trends as the one discussed above, i.e., diminished kinetics after anodic polarizations and partial or complete recoveries after cathodic polarizations. Figure 27 summarizes the averaged kinetic changes after anodic and cathodic polarization in the three different electrolytes at all the spots ( $N = 20$ ). In Figure 27A, a greater value indicates a more significant loss of electrochemical activity, and it was clear that, after the anodic polarization, the averaged kinetic

change relative to the pristine was more drastic in the H<sub>2</sub>SO<sub>4</sub> electrolyte ( $34.7 \pm 5.89$  %) compared to the other two, i.e.  $12.5 \pm 5.12$  % in HClO<sub>4</sub> and  $10.8 \pm 4.87$  % in HCl.

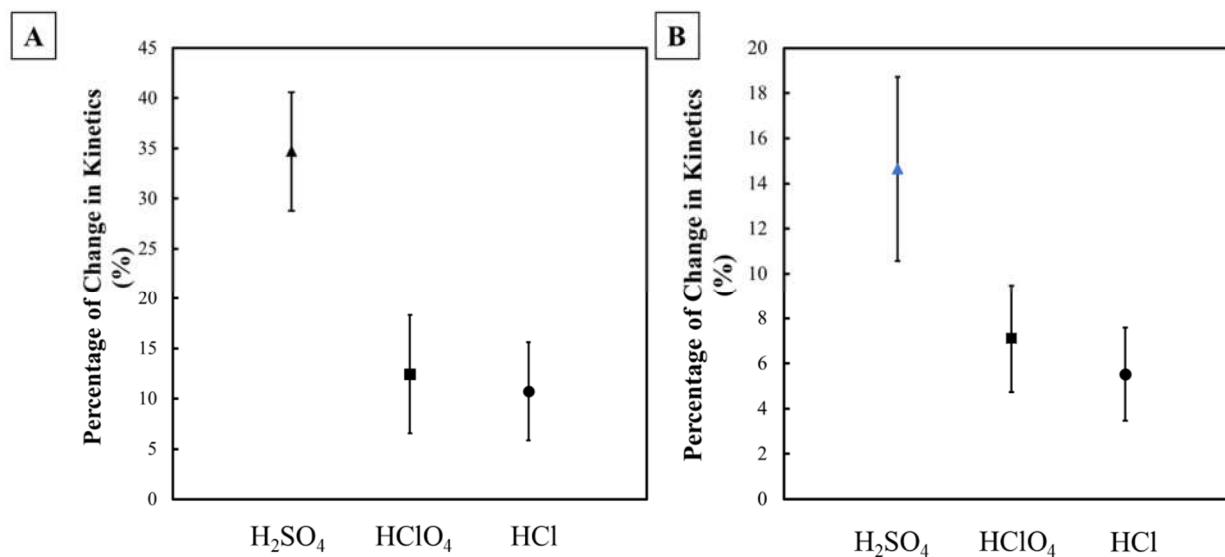


**Figure 27** Averaged kinetic change in 1 M H<sub>2</sub>SO<sub>4</sub> (▲), 2 M HClO<sub>4</sub> (●) and 2 M HCl (■) electrolyte at post (A) anodic and (B) cathodic polarizations. Error bars represent 95% confidence interval.

In terms of surface reactivation shown in Figure 27B, a lower value indicates more recovery in localized kinetics. Compared to the pristine, after the cathodic polarization, the averaged kinetic change in H<sub>2</sub>SO<sub>4</sub>, HClO<sub>4</sub>, and HCl were  $14.7 \pm 4.07$  %,  $7.10 \pm 2.38$  %, and  $5.52 \pm 2.05$  %, respectively. Furthermore, in each of the three electrolytes, more than 50% of interrogated spots were recovered to within 10% kinetic difference compared to the pristine, and it indicated that cathodic polarization was effective in reactivating the passivated Ti<sub>n</sub>O<sub>2n-1</sub>.

These statistics of local interrogations can be used to compare with bulk impedance measurements. The bulk first order kinetic rate constant ( $k$ ) is linearly proportional to the exchange current density ( $i_0$ ), and therefore, inversely proportional to the  $R_{ct}$  ( $k \sim i_0 \sim \frac{1}{R_{ct}}$ ). Table XXXII, Appendix D summarizes the changes in  $R_{ct}$  from the bulk measurements, and compared to the pristine electrodes, the changes in  $k$  were determined as  $65.6 \pm 1.92$  %,  $50.7 \pm 1.30$  %, and  $49.6 \pm 0.663$  % after anodic polarization and  $30.7 \pm 3.61$  %,

$24.4 \pm 3.28$  %, and  $15.3 \pm 0.715$  % after cathodic polarization in  $\text{H}_2\text{SO}_4$ ,  $\text{HClO}_4$ , and  $\text{HCl}$  electrolytes, respectively. Compared to the local kinetic statistics, the bulk measurement exhibited a more drastic decrease in  $k$  after anodic polarization, and less reactivation after cathodic polarization. This difference in local kinetic statistics and  $k$  is probably due to insufficient population of interrogated spots in the SECM experiment, however, the trends of local kinetic statistics is well comparable to that of the bulk measurements, which justifies the robustness of this method.

#### 6.4.3 Implication of Surface Passivation and Reactivation in Energy Technologies

Energy storage is one of the most crucial technologies used in various areas, where electric power can be supplied as needed from rechargeable battery banks. In order to meet the rigorous energy demands, these batteries must have a long cycle life, as well as high energy and power density. From the results of this study, the surface passivation can occur when  $\text{Ti}_n\text{O}_{2n-1}$  is used as electrodes, which is attributed to the formation of passivation film or loss of charge carriers. In many studies,  $\text{Ti}_n\text{O}_{2n-1}$  has been used as a cathode material, such as in Lithium-Sulfur [278], Lead/Acid [151,287], and Zinc-Air [285,286] batteries. Therefore, surface passivation of  $\text{Ti}_n\text{O}_{2n-1}$  mainly occurs during the charging process, and a surface passivated  $\text{Ti}_n\text{O}_{2n-1}$  acts as a barrier to electron flow, which causes capacity loss and poor cycling stability [293]. Due to its reversible nature, during discharging process, surface passivation on  $\text{Ti}_n\text{O}_{2n-1}$  can be gradually reduced by either reintroducing charge carriers or removing the passivation film, however the surface passivation still can cause an electric potential dip immediately after a load is placed on the cell, due to the high resistance of surface passivation [307]. Hence, in many applications where the electric potential dip can be below the minimum operating potential, a pre-condition of the cell to the point where the electric potential is stabilized is necessary.

#### 6.4.4 Implication of surface passivation and regeneration in water treatment

It was shown above that anodic polarization of  $\text{Ti}_n\text{O}_{2n-1}$  caused a decrease in  $N_D$  and increases in  $\rho_f$  and  $R_{cr}$ . At a potential suitable for hydroxyl radical production, analysis of  $d_{sc}$  also indicated lower electron

tunneling probability near the interface of anodically polarized  $Ti_nO_{2n-1}$ , and therefore hydroxyl radical production is expectedly affected by the electrochemical activity of  $Ti_nO_{2n-1}$ . The hydroxyl radical production is the key to operation of EAOPs, due to its ability to react with organic compounds at diffusion limited rates and its fast decay to a harmless product of water [221,222]. In order to examine the influence of electrochemical activity on hydroxyl radical production on the  $Ti_nO_{2n-1}$  electrodes in the electrochemical systems, five samples with different Magnéli phase compositions, as shown in Figure 28A, were synthesized (See *Section 6.3.8* for synthesis method), and in Figure 28B, the values of  $n$  in  $Ti_nO_{2n-1}$  were determined from the TGA data. Hydroxyl radical production rate was examined through the removal of terephthalic acid in a dead-end flow-through reactor, and  $[OH^*]_s$  was reported by converting the removal rate of terephthalic acid using Equation 6-2.

Among these five samples, as shown in Figure 28A and B, Sample 1 possessed a composition of pure  $Ti_4O_7$  and exhibited the highest hydroxyl radical surface concentration ( $2.55 \times 10^{-11} \pm 1.08 \times 10^{-12} \text{ mol m}^{-2}$ ), i.e., the greatest ability to produce hydroxyl radicals. The other samples contained a mixture of higher oxidation state Magnéli phases, and their ability to produce hydroxyl radical decreased with increasing oxidation state (or  $n$  value) (Figure 28B). This result demonstrated the importance of maintaining a high electrochemical activity of  $Ti_nO_{2n-1}$  in water treatment. Given the discussion above, it is suggested that the ability of hydroxyl radical production on an anodically polarized  $Ti_nO_{2n-1}$  should decrease, and can be recovered upon cathodic polarization. Therefore, an operational strategy that periodically reverses the polarity of the electrodes is necessary to maintain optimal performance.

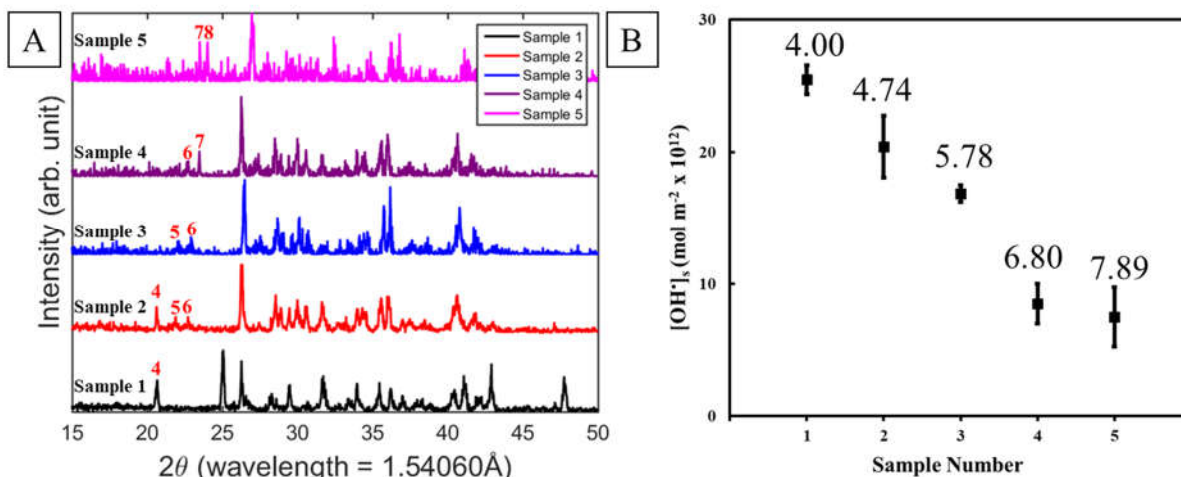


**Figure 28** (A) XRD patterns of different Magnéli phase mixtures, and (B) steady state surface hydroxyl radical concentration on different samples in a dead-end flow-through setup at room temperature. The number on top of each data point in (B) represents the  $n$  in  $Ti_nO_{2n-1}$ . Solution: 0.1 mM terephthalic acid in 1 M  $KH_2PO_4$  (pH 5.8). The solution resistance corrected electric potentials on Sample 1 to 5 are 3.32, 3.29, 3.35, 3.38 and 3.40 V, respectively. Permeate flux on Sample 1 to 5 (LMH): 780, 840, 900, 720, 1080. Transelectrode pressure: 1.03 bar.

#### 6.4.5 Mechanism of loss and regeneration of electrochemical activity in various electrolyte

In both  $HClO_4$  and  $HCl$  electrolytes,  $N_D$ , film conductivity, and charge transfer kinetics decreased after anodic polarization, and increased after cathodic polarization. Phase changes were not found in the electrodes polarized in both electrolytes, and therefore, it suggests that the changes in  $N_D$ , film conductivity and charge transfer kinetics were associated with hydrogen doping level in the  $Ti_nO_{2n-1}$  sample, instead of surface oxidation by radicals and strong oxidants, since  $ClO_4^-$  is considered as an inert electrolyte, and the standard reduction potential for chlorine evolution (1.57 V vs SHE) is much less than that for the sulfate radical formation (2.01 V vs SHE) [269,308]. The pristine samples were synthesized in the hydrogen gas environment at an elevated temperature, hydrogen atoms could be deprotonated and intercalated in the lattice structure, which resulted in free electrons, and in turn, improves the electronic conductivity [309]. During the anodic polarization, a number of donor center  $Ti^{3+}$  sites can be oxidized to  $Ti^{4+}$  within  $Ti_nO_{2n-1}$ , and therefore the excessive charge was removed by  $H^+$  discharge from the system [152]. During the cathodic

polarization,  $\text{Ti}^{4+}$  sites within the lattice were electrochemically reduced to  $\text{Ti}^{3+}$ , with the loss of charge compensated by  $\text{H}^+$  intercalation, and thus the electronic conductivity and charge transfer kinetics were recovered [304,309,310]. It is reported that the proton intercalation can be readily achieved in an acidic media under a negative biased potential, since the high proton concentration of the electrolyte facilitates the intercalation [309].

Contrary to the cases in  $\text{HClO}_4$  and  $\text{HCl}$ ,  $\text{Ti}_n\text{O}_{2n-1}$  sample electrolyzed in the presence of sulfate ions involved phase change. As shown in Figure 25A, the new dominant peak after anodic polarization appeared at  $22.80^\circ$ , which could refer to  $\text{Ti}_6\text{O}_{11}$  and/or  $\text{TiOSO}_4$ . It is generally accepted that oxygen vacancies arrange themselves upon sufficient annealing, and crystal structure collapse to produce crystallographic shear and leads to a local  $\text{Ti}_2\text{O}_3$  corundum structure [311,312]. Therefore, phase change from  $\text{Ti}_4\text{O}_7$  to  $\text{Ti}_6\text{O}_{11}$  is not likely realized by anodic polarization, besides, the activation energy of converting  $\text{Ti}_4\text{O}_7$  to  $\text{Ti}_6\text{O}_{11}$  was estimated at  $64.3 \text{ kJ mol}^{-1}$  by TGA, and the amount of energy provided by the anodic polarization was only  $36.1 \text{ kJ mol}^{-1}$  (20 mA, 2.81 V and 0.5 hour), which was insufficient for crystal structure rearrangement. Therefore, the loss of electrochemical activity of  $\text{Ti}_n\text{O}_{2n-1}$  in the presence of sulfate ion may be attributed to the combination of  $\text{Ti}^{4+}$  and sulfate ion at the surface.

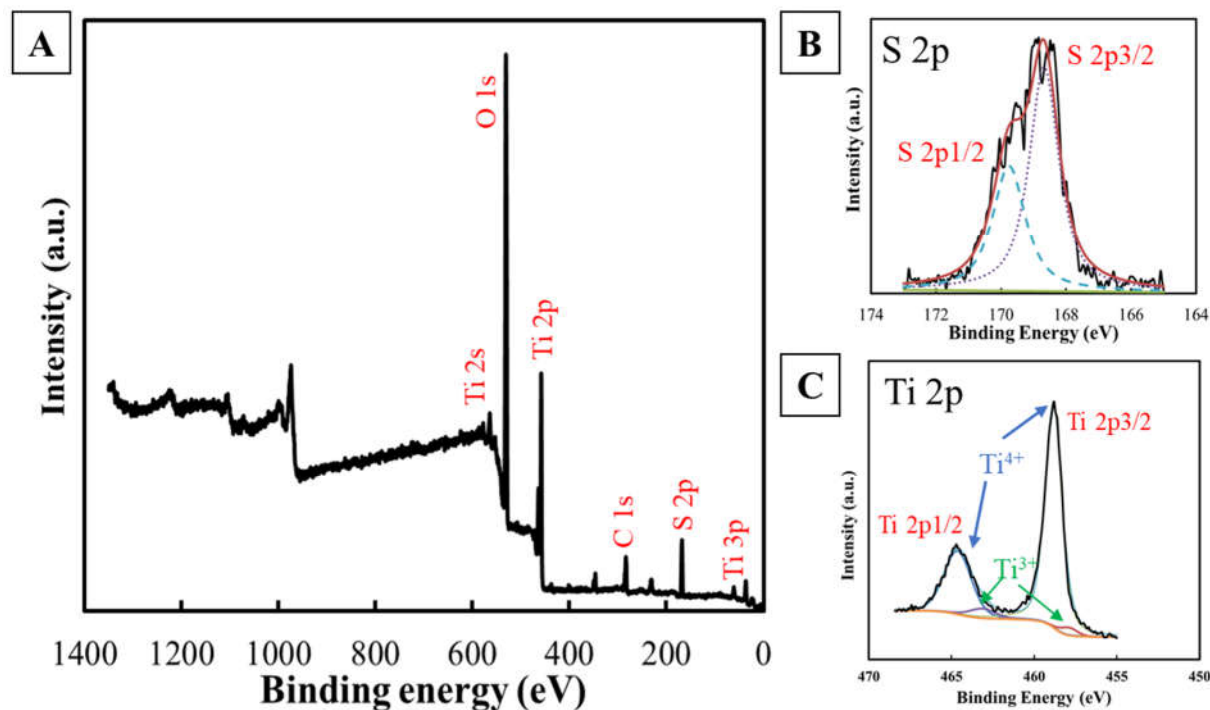


**Figure 29** XPS spectra of  $\text{Ti}_n\text{O}_{2n-1}$  electrode after 30 mins' anodic polarization in 1 M  $\text{H}_2\text{SO}_4$  electrolyte at  $20 \text{ mA cm}^{-2}$ . (A) Full spectrum, (B) S 2p doublet regions, and (C) Ti 2p doublet regions.

XPS confirmed the existence of sulfate, which 9.5% of the atomic percentage, on the sample surface after the anodic polarization ( $20 \text{ mA cm}^{-2}$ ) in 1 M  $\text{H}_2\text{SO}_4$  electrolyte for 30 min as shown in Figure 29A, while 3.5% atomic percentage of surface sulfate was also observed on the control sample, which was left at OCP in 1 M  $\text{H}_2\text{SO}_4$  for 30 min. The surface sulfate on the control sample may be attributed to the sulfate residual after the cleaning, and based on the discussion above, sulfate residual of this extent did not induce a change in the XRD data or was below the XRD detection limit (see Figure 56, Appendix D). The XPS spectra did not need further adjustment, since the C 1s peak was located at 284.5 eV (Figure 29A). As shown in Figure 29A, S 2p peak was observed and Figure 5B exhibited a  $\text{S } 2p_{3/2}-2p_{1/2}$  doublet with 1.1 eV splitting. A unique S 2p doublet related to sulfate species ( $\text{SO}_4^{2-}$ ) with S  $2p_{3/2}$  at 169.0 eV was found, while sulfite with S  $2p_{3/2}$  at 167.0 eV was not present [313]. Figure 29C shows the Ti 2p spectrum, the binding energy peaks at 464.6 and 458.8 eV are associated to  $2p_{1/2}$  and  $2p_{3/2}$  of  $\text{Ti}^{4+}$ . The Ti  $2p_{1/2}$  peak was fitted to

reveal two peak energies at 464.6 and 463.1 eV. The Ti 2p<sub>3/2</sub> can also be resolved into two Gaussian peaks at 468.8 and 457.9 eV, which can be related to the Ti<sup>4+</sup> and Ti<sup>3+</sup>, respectively, meanwhile, the 2p<sub>1/2</sub> binding energy of 464.6 and 463.1 eV can be attributed to Ti<sup>4+</sup> and Ti<sup>3+</sup>, respectively. These resolved peaks are consistent with literature values [314,315]. The above observations suggested that the loss of electronic conductivity and electrochemical activity of Ti<sub>n</sub>O<sub>2n-1</sub> after anodic polarization in H<sub>2</sub>SO<sub>4</sub> electrolyte was due to the formation of surface passivation layer with a major constituent of TiOSO<sub>4</sub>. Furthermore, surface passivation can only occur when a certain surface coverage of sulfate is reached, and therefore, future study is needed to evaluate the sulfate tolerance of Ti<sub>n</sub>O<sub>2n-1</sub>, where the formation of passivation layer can be prevented.

### **6.5 Conclusion**

Maintaining a high electronic conductivity and electrochemical activity is the key to operate the Ti<sub>n</sub>O<sub>2n-1</sub> in electrochemical advanced oxidation processes, visible light photocatalysis and energy conversion devices in order to achieve the best performance. This study found that the mechanism for the loss of electronic conductivity and electrochemical activity in the anodic polarization depends on the type of electrolyte. In both ClO<sub>4</sub><sup>-</sup> and Cl<sup>-</sup> electrolytes, this observation was due to the decrease in the charge carrier density, and in SO<sub>4</sub><sup>2-</sup> electrolyte, a combined effect of charge carrier density and formation of TiOSO<sub>4</sub> was attributed to the surface passivation. However, the electronic conductivity and electrochemical activity can be recovered through cathodic polarization, and thus a regular cathodic reversal is extremely necessary.

### **6.6 Acknowledgements**

Funding for this work was provided by the National Science Foundation (CBET-1159764 and CBET-1453081 (CAREER)). We thank Dr. Berry and his research group for performing two-point probe measurement, Pralay Gayen for performing the XPS measurement, and Songwei Che for the XPS peak

fitting and discussion. Portions of this work were carried out in the Nano Core Facility and Electron Microscopy Service *via* the Research Resources Center at the University of Illinois at Chicago.

## VII. CONCLUDING REMARKS

Work presented in this dissertation focused on mechanistic studies of electrochemical processes on a substoichiometric  $\text{TiO}_2$  ( $\text{Ti}_n\text{O}_{2n-1}$ ) reactive electrochemical membrane (REM) used for water treatment. Research began with an emphasis on the suitability of using a transmission line model (TLM) to study membrane fouling and the development of TLM to spatially characterize various membrane fouling mechanisms on an asymmetric REM. Results from **Chapter 3** showed that the TLM was able to distinguish among layers of the asymmetric REM, such as outer surface, active layer and support layer, by a controllable penetration depth. The penetration depth was inversely related to the sinusoidal signal's frequency, and therefore, different layers of the REM could be resolved by a TLM over a specific range of frequencies. Different fouling mechanisms, such as monolayer adsorption, pore constriction, and intermediate pore blockage, were simulated using TLMs, and studied through Nyquist and Bode phases plots from these simulations. These simulations showed TLMs produced characteristic signatures of membrane fouling at different spatial locations.

The results from **Chapter 3** provided the theoretical framework to characterize REM fouling after experimental fouling and regeneration treatments, which were reported in **Chapter 4**. A  $\text{Ti}_n\text{O}_{2n-1}$  asymmetric UF tubular REM, with a composition of  $\text{Ti}_4\text{O}_7$  and  $\text{Ti}_6\text{O}_{11}$ , was synthesized. REM fouling by humic acid and regeneration performance were evaluated using electrochemical impedance spectroscopy (EIS). The results indicated that (1) REM fouling occurred at all three membrane interfaces; (2) membrane regeneration in a forward wash mode was not able to fully recover membrane flux due to shallow  $\text{OH}^\bullet$  production in the porous matrix, which was regulated by a ohmic potential drop; (3) membrane regeneration in a backwash mode was able to completely recover membrane flux, due to the physical transport of desorbed foulants and intermediates in the direction of higher electrode potential where  $\text{OH}^\bullet$  production prevails, shear force by the backwash flow, and enhanced shear force by electrochemically regenerated gas bubbles and the release of energy by bubble collapse. This chemical free electrochemical regeneration (CFER) strategy was proven efficient and cost effective for 5 consecutive fouling/regeneration cycles. In

addition, polystyrene microspheres, with well-defined size and shape, were used to justify the model developed in **Chapter 3**, produced an intermediate pore blockage fouling mechanism on the REM, and the experimental EIS spectra matched with theoretical prediction in **Chapter 3**.

Hydroxyl radical ( $\text{OH}^\bullet$ ) is the key to operate the electrochemical advanced oxidation processes (EAOPs) and the successful application of CFER to REM regeneration is also associated with  $\text{OH}^\bullet$ . Therefore, identifying and quantifying  $\text{OH}^\bullet$  using appropriate probes in the electrochemical systems are extremely important, which was evaluated in **Chapter 5**. Spin traps and probe molecules are two categories of  $\text{OH}^\bullet$  probes, many studies have showed that spin trap compounds used for  $\text{OH}^\bullet$  detection have anodic peak potentials lower than  $\text{OH}^\bullet$  formation, and therefore they are not appropriate probes in the electrochemical systems. In this study, we examined four commonly used  $\text{OH}^\bullet$  probe molecules for use in EAOPs, and the results showed that coumarin and *p*-chlorobenzoic acid could readily undergo direct electron transfer reaction. The formation of 7-hydroxycoumarin from coumarin oxidation was observed, which was previously considered as an adduct product by reaction with  $\text{OH}^\bullet$ . A non- $\text{OH}^\bullet$  mediated pathway was found in association with 7-hydroxycoumarin formation by density functional theory simulations. Meanwhile, *p*-benzoquinone and terephthalic acid were stable under direct electron transfer reactions, however, *p*-benzoquinone could be easily reduced at the cathode side, and thus a membrane separating the anode and cathode sides is needed. The results of this study indicated that terephthalic acid is the most suitable  $\text{OH}^\bullet$  probe molecule, due to its high redox potential, high resistance to the direct electron transfer, and stability against reduction.

In addition to  $\text{OH}^\bullet$  identification and quantification, maintaining a high  $\text{OH}^\bullet$  production performance and conductivity at  $\text{Ti}_n\text{O}_{2n-1}$  are of great significance in EAOPs and energy technologies. **Chapter 6** examined the surface passivation and reactivation of  $\text{Ti}_n\text{O}_{2n-1}$  in three types of electrolytes (i.e.,  $\text{H}_2\text{SO}_4$ ,  $\text{HClO}_4$ , and  $\text{HCl}$ ). This study showed that gradual loss of conductivity and electrochemical activity was found on  $\text{Ti}_n\text{O}_{2n-1}$  anodically polarized in all three electrolytes, while a passivation layer of  $\text{TiOSO}_4$  was formed on the sample treated in  $\text{H}_2\text{SO}_4$  electrolyte. The mechanism of this observation is due to

decreasing in the hydrogen doping level in HClO<sub>4</sub> and HCl electrolytes, and a combination of a decreased hydrogen doping level and passivation layer formation in the H<sub>2</sub>SO<sub>4</sub> electrolyte. The loss of conductivity and electrochemical activity, as well as the passivation layer were found reversible upon cathodic polarization. Variations in localized kinetic rate constants over the same spots were examined in SECM as a function of anodic and cathodic charge passed, of which results are statistically comparable to the bulk impedance measurements. The effect of conductivity on OH<sup>•</sup> formation kinetics was examined by using different phases of Ti<sub>n</sub>O<sub>2n-1</sub>, and showed a decreasing OH<sup>•</sup> production rate with increasing *n* in the general form Ti<sub>n</sub>O<sub>2n-1</sub>. Therefore, the results of this study indicate that Ti<sub>4</sub>O<sub>7</sub> phase should be maintained to operate at the best performance, and periodic cathodic polarization is important to preserve the electrode's optimal conductivity and electrochemical reactivity.

The results and conclusions presented in this dissertation imply several opportunities for future research. First, the mechanism of the effectiveness of CFER in backwash mode is still unclear, possible reasons are (1) transport of desorbed foulants and intermediates in the direction of higher electric potential where OH<sup>•</sup> can be produced, and (2) the enhanced backwash shear forces from the interaction between the bubbles and adsorbed foulants, and (3) the energy release from the bubble collapse. Studies using electrochemically generated oxygen nanobubbles as cleaning agents both for fouling prevention and foulant removal have been reported on graphite and gold surfaces, the results of both studies showed prominent removals of bovine serum albumin from the electrode surfaces [316,317]. Aeration has been explored to prevent membrane fouling and remove the foulants in membrane bioreactors. However it is often associated with a negative effect on membrane permeability, for example, a low aeration could not effectively remove surface foulants due to weak driving force, whereas a high aeration could result in a severe floc breakage, and the released small size sludge particles lead to dramatic membrane fouling [318]. Therefore, studies are needed to investigate the electrochemical generated hydrogen/oxygen bubbles on REMs to realize fouling prevention and foulant removal, which include bubble quantity, size, and morphology. The formation of hydrogen/oxygen bubbles requires much less electric potential than that of OH<sup>•</sup>, and therefore,

successful application of electrochemically generated bubbles with appropriate amount, size, and morphology to membrane regeneration would significantly reduce the operational cost.

Second, the use of a redox active species for EIS measurements does not allow this method to be used for *in situ* membrane fouling measurement. The future research should explore using EIS measurements in equilibrium with the oxygen evolution reaction so that the use of redox active species can be eliminated. Chen *et al.* and Waraska *et al.* have successfully studied the impedance of Nb doped TiO<sub>2</sub> and Ebonex, a mixture of Ti<sub>4</sub>O<sub>7</sub> and Ti<sub>6</sub>O<sub>11</sub>, disk electrodes using EIS with a dc bias in the oxygen evolution region [152], which suggests the possibility of using this method for the REM. However, studies are needed to explore the potential drop along the pore depth during the oxygen evolution reaction.

Third, as discussed in **Chapter 6**, 3.5% (atomic percentage) residual sulfate was found on the control sample, which was left at open circuit potential condition in 1 M H<sub>2</sub>SO<sub>4</sub> electrolyte, however changes in crystalline structure, conductivity, and electrochemical activity were not observed in XRD, two-point probe method, and EIS measurement, respectively. Therefore, future study is needed to evaluate the sulfate tolerance of Ti<sub>n</sub>O<sub>2n-1</sub> so that the formation of passivation layer can be prevented. In addition, **Chapter 6** indicated that phase change among Ti<sub>n</sub>O<sub>2n-1</sub> was not observed due to insufficient activation energy induced by low electric potential. Therefore, conversion of the crystal structure through anodic polarization is possible under higher potential. Future study is needed to investigate the possibility and reversibility of phase change under a higher anodic potential. Results of this study would be useful in EAOPs operated at high applied potentials, and energy devices with high open circuit potentials.

## APPENDICES

### APPENDIX A

#### A.1 Mass transfer effect on electrochemical impedance spectroscopic measurement using redox active species

In order to avoid the complications of electrode polarization effects and drifting of the OCP, an active redox couple is used during EIS measurements, and a small  $\Delta E$  is superimposed on the OCP of the redox couple. In order to avoid mass transport effects on the EIS measurements, spectra are collected during convective flow of the solution through the REM pores. To determine if concentration gradients will develop in the REM pores, an analysis of reactive mass transport of the redox species under dc conditions is necessary. The time dependent concentration profile of the oxidized redox species is given by Equation A-1.

$$\frac{\partial a}{\partial t} = D \frac{\partial^2 a}{\partial x^2} - u \frac{\partial a}{\partial x} - \frac{2}{nFrC_o^*} \cdot J \quad \text{A-1}$$

where  $a = \frac{C_o(x)}{C_o^*}$ ,  $D$  ( $\text{m}^2 \text{s}^{-1}$ ) is the diffusion coefficient of the oxidant species,  $C_o^*$  (M) is the bulk concentration of the oxidant species,  $C_o(x)$  is the oxidant molar concentration profile with respect to distance from the pore orifice ( $x$  (m)),  $u$  ( $\text{m s}^{-1}$ ) is the volume-averaged pore velocity of the solution,  $n$  is the number of electrons transferred during the redox reaction ( $n = 1$ ),  $r$  (m) is the pore radius,  $J$  ( $\text{A m}^{-2}$ ) is the current density of the redox reaction, and  $F$  ( $\text{C mol}^{-1}$ ) is the Faraday constant. The equation for the potential drop in the pore is given by:

$$\frac{d^2 \eta}{dx^2} = \frac{2\rho}{r} J \quad \text{A-2}$$

where  $\eta$  (V) is the overpotential and  $\rho$  ( $\Omega \text{ m}$ ) is the specific solution resistance.

The current as a function of overpotential is described by Butler-Volmer Equation:

$$J = J_0 \left( \frac{C_O}{C_O^*} e^{b\eta} - \frac{C_R}{C_R^*} e^{-b\eta} \right) \quad \text{A-3}$$

where  $b$  is the transfer coefficient and can be taken as 0.5 for general case,  $C_R(x)$  (M) is the reductant molar concentration profile with respect to distance from the pore orifice,  $C_R^*$  (M) is the bulk concentration of the reductant species and  $J_0$  (A m<sup>-2</sup>) is the exchange current density, which is on the order of magnitude of -2 in the general case.

The concentrations of the oxidant and reductant obey the following relation assuming the same diffusion coefficient:

$$C_O^* + C_R^* = C_O + C_R \quad \text{A-4}$$

Equation A-4 is incorporated into Equation A-3:

$$J = J_0 \left[ a(e^{b\eta} + m e^{-b\eta}) - (m + 1)e^{-b\eta} \right] \quad \text{A-5}$$

where  $m = C_O^*/C_R^*$  and is taken as 1 for equal molarity of the redox active species.

Equation A-1 can be further simplified by neglecting the diffusion term if the Péclet number ( $Pe$ )  $\gg 1$ , which is defined by Equation A-6.

$$Pe = \frac{uL}{D} \quad \text{A-6}$$

where  $L$  (m) is the total length of the pore.

Under steady state conditions, Equation A-2, A-3 and A-5 are solved together while neglecting diffusion and applying the following boundary conditions:

$$@ x = 0, a = 1 \text{ and } \eta = \eta_0 \quad \text{A-7}$$

$$@ x = L, \frac{d\eta}{dx} = 0 \quad \text{A-8}$$

The numerical solution of the coupled ordinary differential equation is obtained using a boundary value problem solver (bvp5c) in MATLAB R2015a. The absolute and relative tolerance are set to 1E-6. The number of mesh points is determined by the solver so as to obtain an accurate numerical solution. The

normalized overpotential decay and concentration gradient were examined under three  $u$  ( $5.6\text{E-}2\text{ m s}^{-1}$ ,  $5.6\text{E-}4\text{ m s}^{-1}$  and  $5.6\text{E-}6\text{ m s}^{-1}$ ) and two  $\eta_0$  (100 mV and 10 mV). Normalized overpotential is calculated by  $\frac{\eta}{\eta_0}$ . The simulation is performed along the normalized pore depth (0 - 1) and accounts for the dual layer structure (pore radius 5.0 nm for 0 - 0.03 (60  $\mu\text{m}$  of total 2.19 mm) and pore radius 1.5  $\mu\text{m}$  for 0.03 - 1).

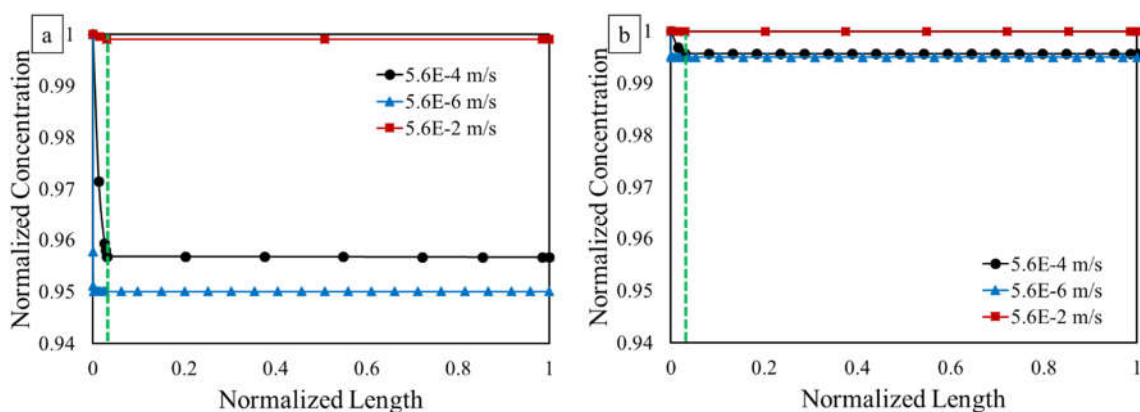


**Figure 30** Normalized concentration of oxidant in the pore at various convection velocities under (a) 100 mV overpotential and (b) 10 mV overpotential. Green dashed line represents the boundary between active and support layers.

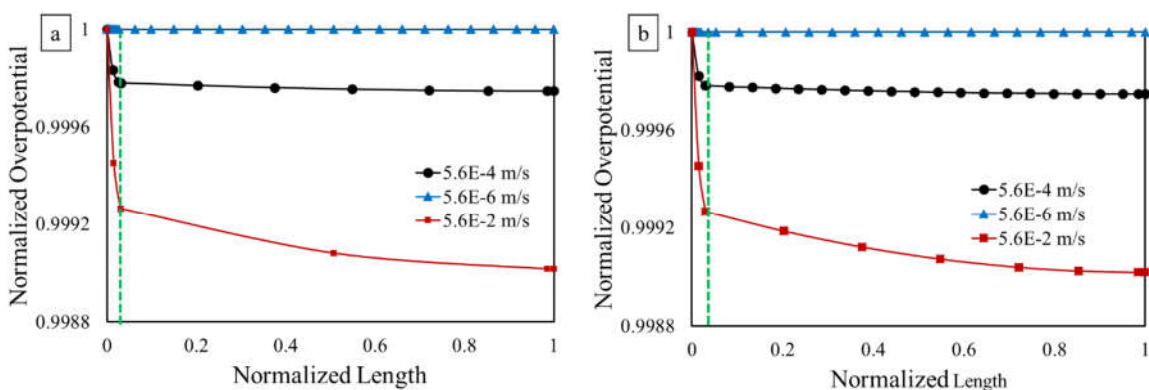


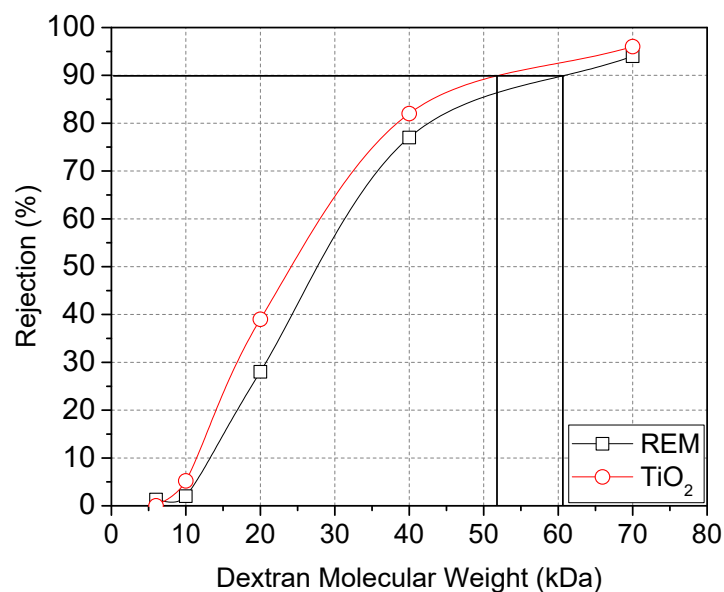
**Figure 31** Normalized overpotential decay in the pore at various convection velocities under (a) 100 mV overpotential and (b) 10 mV overpotential. Green dashed line represents the boundary between active and support layers.

The simulation results are summarized in Figure A-1 and A-2. In Figure A-1 (a) and (b), the concentration of oxidant is sensitive to  $u$  only when  $\eta_0$  is greater than 100 mV. When  $\eta_0$  decreases to 10

mV, the change in concentration of the oxidant is within 1% in all cases, and therefore a concentration gradient is unlikely to develop in the pore. Besides, it is shown that the  $\eta_0$  decay increases with respect to  $u$ , but the overall  $\eta_0$  is not experiencing significant change in all cases as shown in Figure A-2 (a) and (b). The simulation results indicate that EIS measurement does not experience mass transfer limitation and overpotential decay when  $\eta_0$  is restricted to small values ( $< 10$  mV).

**APPENDIX B****B.1 Molecular weight cutoff determination****Table IX** MOLECULAR WEIGHT CUTOFF DETERMINATION OF PRISTINE TiO<sub>2</sub> MEMBRANE AND REM

Molecular Weight (kDa)	Characteristic Wavelength (nm)	Initial Concentration C <sub>0</sub> (wt%)	Rejection (%)		Initial Permeability J <sub>0</sub> (LMH)	
			TiO <sub>2</sub>	REM	TiO <sub>2</sub>	REM
6	269	0.1	0.1	1.3	626.5	2174.1
10 (9 - 11)	271	0.5	5.2	2.1	617.3	2201.9
20 (15 – 25)	275	0.5	39.2	28.3	630.9	2189.7
40	275	1.0	81.9	77.0	622.0	2165.0
70	275	2.5	95.8	94.2	619.7	2231.4

**Figure 32** Molecular weight cutoff determination of a pristine TiO<sub>2</sub> membrane and REM

*B.2 Reproducibility of polystyrene microspheres fouling and regeneration on reactive electrochemical membrane*

Reproducibility of polystyrene microsphere fouling and regeneration on REMs were examined here. The normalized permeate flux results under different operational conditions for anodic treatment and cathodic treatment in backwash mode are shown in Figure B-2 and Figure B-4 respectively. Repeated EIS measurements were presented in Figure B-3 and Figure B-5. Filtration law model calculations of the flux data were tabulated in Table X to XIII. Permeate flux data were normalized to the initial value of each experiment, which is shown in the caption of Figure B-2 and Figure B-4.

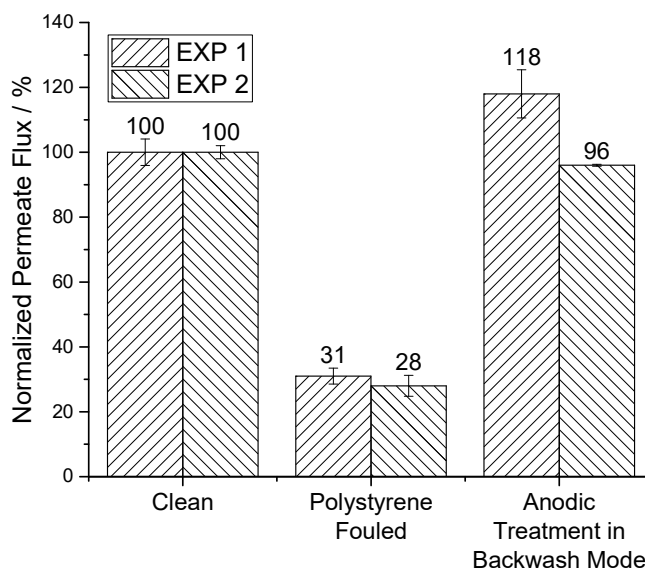


**Figure 33** Reproducibility of polystyrene microspheres fouling and regeneration on REM under anodic CFER in backwash mode, initial flux  $J_0$  (Exp 1) = 2285.6 LMH;  $J_0$  (Exp 2) = 2374.7 LMH.

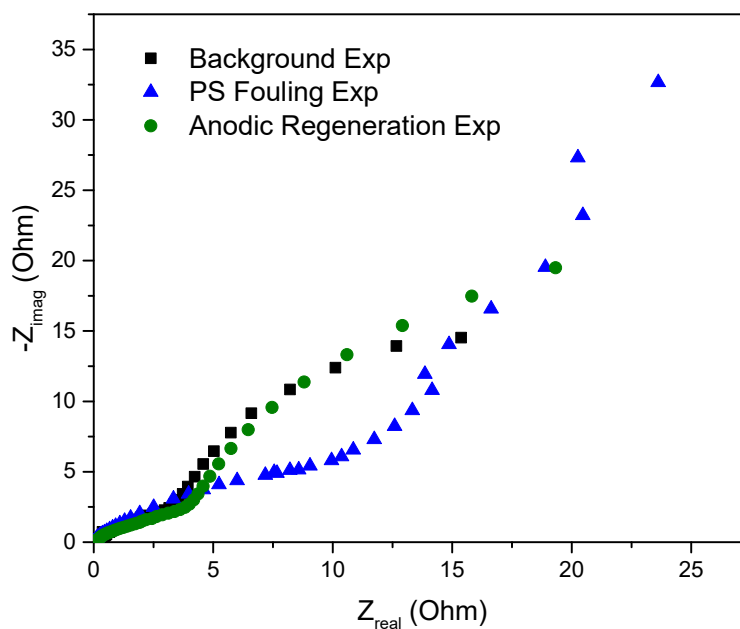


**Figure 34** EIS spectra in repeated anodic CFER in backwash mode of polystyrene fouled membrane (Exp 2).

**Table X** FLUX RECORD ON 1.58  $\mu\text{M}$  POLYSTYRENE FOULING BEFORE ANODIC CFER IN BACKWASH MODE AND FILTRATION MODEL CALCULATION (EXP 1)

dt (min)	dV (mL)	dt/dv	$d^2t/dV^2$	Log(dt/dV)	Log( $d^2t/dV^2$ )
1	98	0.0102			
1	75	0.0133	4.17E-05	-1.88	-4.38
1	62	0.0161	4.51E-05	-1.79	-4.35
1	53	0.0189	5.17E-05	-1.72	-4.29
1	47	0.0213	5.12E-05	-1.67	-4.29
1	42	0.0238	6.03E-05	-1.62	-4.22
1	38	0.0263	6.60E-05	-1.58	-4.18
1	35	0.0286	6.44E-05	-1.54	-4.19
1	32.5	0.0308	6.76E-05	-1.51	-4.17
1	30	0.0333	8.55E-05	-1.48	-4.07

**Table XI** FLUX RECORD ON 1.58  $\mu\text{M}$  POLYSTYRENE FOULING BEFORE ANODIC CFER IN BACKWASH MODE AND FILTRATION MODEL CALCULATION (EXP 2)

dt (min)	dV (mL)	dt/dv	d <sup>2</sup> t/dV <sup>2</sup>	Log(dt/dv)	Log(d <sup>2</sup> t/dV <sup>2</sup> )
1	107	0.0093			
1	85	0.0118	2.85E-05	-1.93	-4.55
1	73	0.0137	2.65E-05	-1.86	-4.58
1	63	0.0159	3.45E-05	-1.80	-4.46
1	52	0.0192	6.46E-05	-1.72	-4.19
1	47	0.0213	4.35E-05	-1.67	-4.36
1	43	0.0233	4.60E-05	-1.63	-4.34
1	39	0.0256	6.12E-05	-1.59	-4.21
1	34	0.0294	1.11E-04	-1.53	-3.96
1	30	0.0333	1.31E-04	-1.48	-3.88

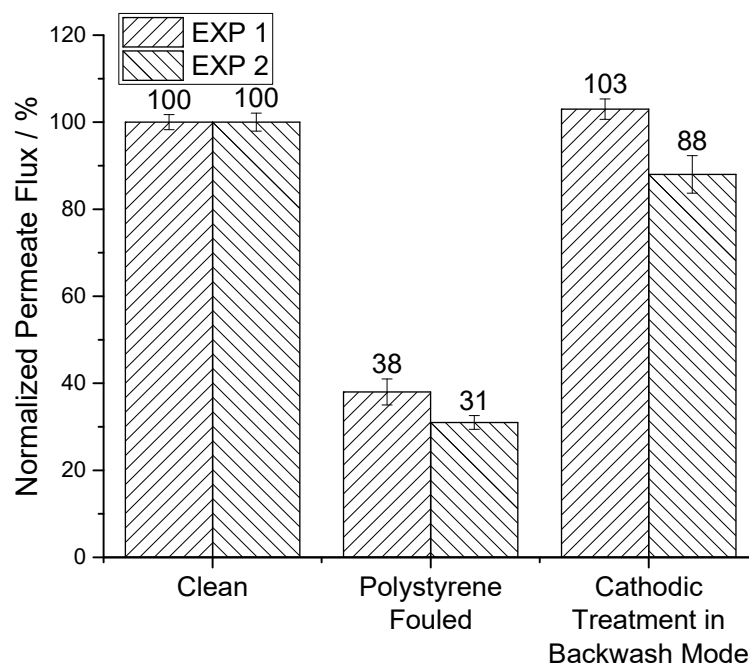


**Figure 35** Reproducibility of polystyrene microspheres fouling and regeneration on REM under cathodic CFER in backwash mode, initial flux  $J_0$  (Exp 1) = 2291.7 LMH;  $J_0$  (Exp 2) = 2390.1 LMH.

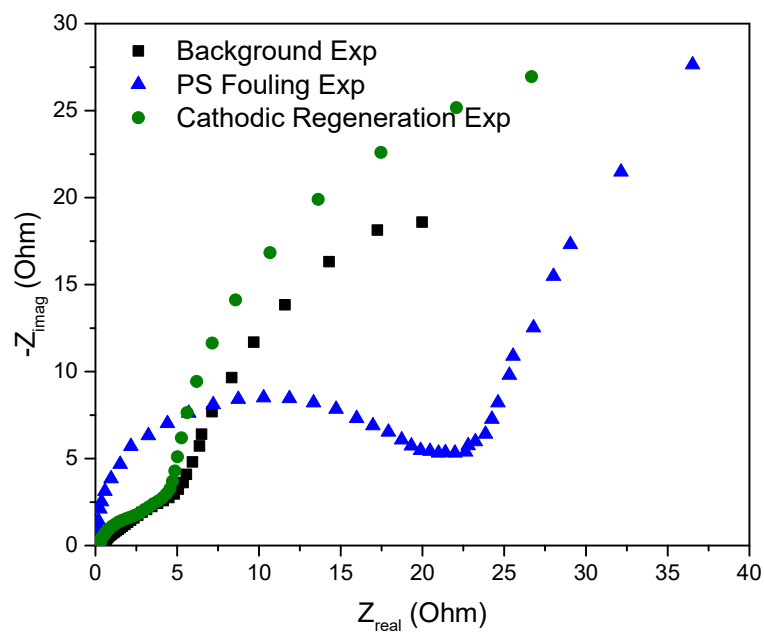


**Figure 36** EIS spectra in repeated cathodic CFER in backwash mode of polystyrene fouled membrane (Exp 2)

**Table XII** FLUX RECORD ON 1.58  $\mu\text{M}$  POLYSTYRENE FOULING BEFORE CATHODIC CFER IN BACKWASH MODE AND FILTRATION MODEL CALCULATION (EXP 1)

dt (min)	dV (mL)	dt/dv	d <sup>2</sup> t/dV <sup>2</sup>	Log(dt/dV)	Log(d <sup>2</sup> t/dV <sup>2</sup> )
1	110	0.0091			
1	90	0.0111	2.24E-05	-1.95	-4.65
1	76	0.0132	2.69E-05	-1.88	-4.57
1	66	0.0152	3.02E-05	-1.82	-4.52
1	58	0.0172	3.60E-05	-1.76	-4.44
1	52	0.0192	3.83E-05	-1.72	-4.42
1	48	0.0208	3.34E-05	-1.68	-4.48
1	46	0.0217	1.97E-05	-1.66	-4.71
1	42	0.0238	4.93E-05	-1.62	-4.31

**Table XIII** FLUX RECORD ON 1.58  $\mu\text{M}$  POLYSTYRENE FOULING BEFORE CATHODIC CFER IN BACKWASH MODE AND FILTRATION MODEL CALCULATION (EXP 2)

<b>dt (min)</b>	<b>dV (mL)</b>	<b>dt/dv</b>	<b>d<sup>2</sup>t/dV<sup>2</sup></b>	<b>Log(dt/dV)</b>	<b>Log(d<sup>2</sup>t/dV<sup>2</sup>)</b>
1	105	0.0095			
1	86	0.0116	2.45E-05	-1.93	-4.61
1	71	0.0141	3.46E-05	-1.85	-4.46
1	60	0.0167	4.30E-05	-1.78	-4.37
1	53	0.0189	4.15E-05	-1.72	-4.38
1	47	0.0213	5.12E-05	-1.67	-4.29
1	42	0.0238	6.03E-05	-1.62	-4.22
1	34	0.0294	1.65E-04	-1.53	-3.78
1	33	0.0303	2.70E-05	-1.52	-4.57

*B.3 Concentrations of active redox species in feed and permeate w/ and w/o electrochemical impedance spectroscopy*

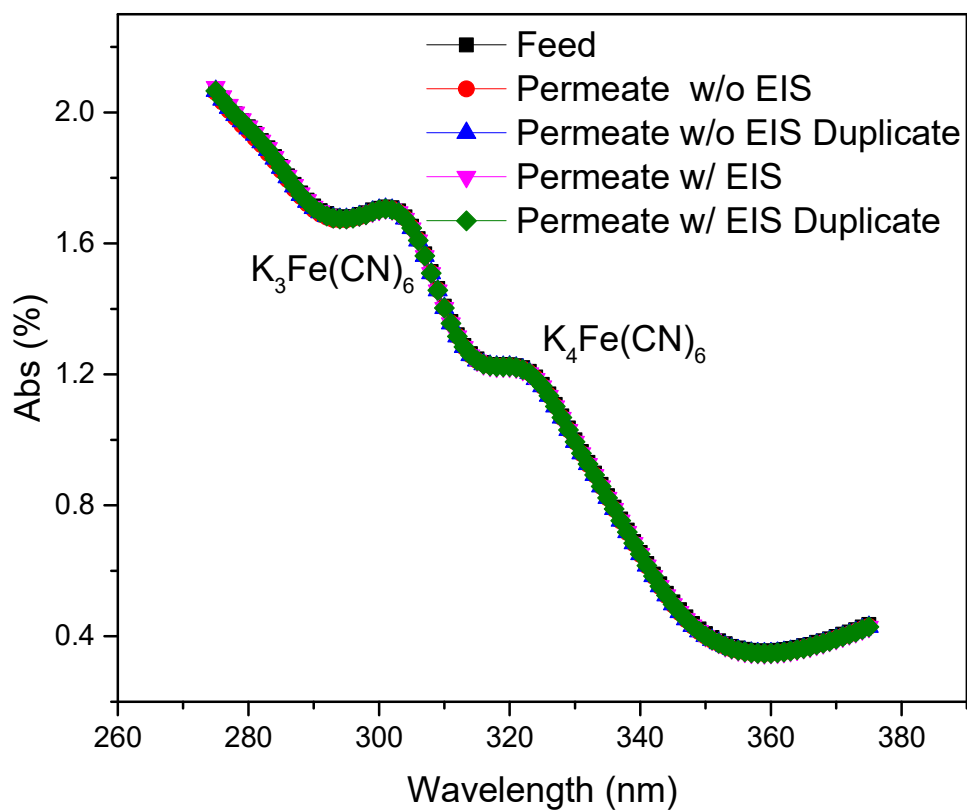


**Figure 37** Concentrations of redox active species during filtration process

*B.4 Complementary fitting parameters of electrochemical impedance spectroscopic spectra*

**Table XIV** COMPLEMENTARY FITTING PARAMETERS TO TABLE XI IN THE MAIN MANUSCRIPT

<b>Parameter</b>	<b>Background</b>	<b>HA Fouling</b>	<b>Anodic CFER</b>
$R_s$	$1.25 \times 10^{-1}$	$1.35 \times 10^{-1}$	$7.48 \times 10^{-1}$
$L$	$9.92 \times 10^{-1}$	$9.95 \times 10^{-1}$	$9.85 \times 10^{-1}$
$\chi^2$	$4.60 \times 10^{-1}$	$4.91 \times 10^{-1}$	$5.12 \times 10^{-1}$
$Z_B$	$7.12 \times 10^{-7}$	$5.93 \times 10^{-7}$	$2.06 \times 10^{-7}$

**Table XV** COMPLEMENTARY FITTING PARAMETERS TO TABLE XII IN THE MAIN MANUSCRIPT

<b>Parameter</b>	<b>Background</b>	<b>HA Fouling</b>	<b>Anodic CFER w/ Backwash</b>
$R_s$	$3.83 \times 10^{-1}$	$8.59 \times 10^{-1}$	$3.28 \times 10^{-1}$
$L$	$9.06 \times 10^{-1}$	$9.05 \times 10^{-1}$	$9.01 \times 10^{-1}$
$\chi^2$	$3.42 \times 10^{-1}$	$5.25 \times 10^{-1}$	$3.02 \times 10^{-1}$
$Z_B$	$1.00 \times 10^{-6}$	$1.17 \times 10^{-8}$	$3.36 \times 10^{-7}$

**Table XVI** COMPLEMENTARY FITTING PARAMETERS TO TABLE XIII IN THE MAIN MANUSCRIPT

<b>Parameter</b>	<b>Background</b>	<b>HA Fouling</b>	<b>2<sup>nd</sup> Backwash</b>
$R_s$	$5.87 \times 10^{-1}$	$2.35 \times 10^{-1}$	$4.50 \times 10^{-1}$
$L$	$9.45 \times 10^{-1}$	$9.51 \times 10^{-1}$	$9.44 \times 10^{-1}$
$\chi^2$	$7.65 \times 10^{-1}$	$7.91 \times 10^{-1}$	$7.12 \times 10^{-1}$
$Z_B$	$8.37 \times 10^{-8}$	$7.40 \times 10^{-7}$	$6.70 \times 10^{-7}$

**Table XVII** COMPLEMENTARY FITTING PARAMETERS TO TABLE XIV IN THE MAIN MANUSCRIPT

<b>Parameter</b>	<b>Background</b>	<b>HA Fouling</b>	<b>Cathodic CFER w/ Backwash</b>
$R_s$	$5.09 \times 10^{-1}$	$8.63 \times 10^{-1}$	$3.74 \times 10^{-1}$
$L$	$9.40 \times 10^0$	$9.42 \times 10^{-1}$	$9.41 \times 10^{-1}$
$\chi^2$	$6.53 \times 10^{-1}$	$6.32 \times 10^{-1}$	$4.61 \times 10^{-1}$
$Z_B$	$7.49 \times 10^{-7}$	$1.09 \times 10^{-8}$	$7.04 \times 10^{-7}$

**Table XVIII** COMPLEMENTARY FITTING PARAMETERS TO TABLE XIV IN THE MAIN MANUSCRIPT

<b>Parameter</b>	<b>Background</b>	<b>HA Fouling</b>	<b>Anodic CFER w/ Backwash</b>
$R_s$	$1.08 \times 10^{-1}$	$1.02 \times 10^{-1}$	$9.77 \times 10^{-1}$
$L$	$9.18 \times 10^{-1}$	$9.20 \times 10^{-1}$	$9.19 \times 10^{-1}$
$\chi^2$	$3.66 \times 10^{-1}$	$3.64 \times 10^{-1}$	$4.65 \times 10^{-1}$
$Z_B$	$6.08 \times 10^{-7}$	$9.12 \times 10^{-7}$	$3.68 \times 10^{-7}$

### B.5 Electrochemical impedance spectroscopic spectra fit and error estimate calculation

Gamry Echem Analyst software (Version 6.23) was used to fit the TLM to EIS data and for examination of EIS data by Kramers-Kronig. The simplex method was adopted as the algorithm to fit the highly nonlinear data based on a minimization of the sum squared errors (SSE). The fitting results are reported along with error estimates calculated at the 95% confidence interval using the relationship shown in Equation B-1 [152] and were calculated in MATLAB 2015a.

$$SSE_{95\%}[S] = SSE[\hat{S}]\left(1 + \frac{P}{N_{set} - P}F[P, N_{set} - P]\right) \quad \text{B-1}$$

*SSE* is defined in Equation B-2:

$$SSE = \sum_{\text{all frequencies}} [(Z_{data,re} - Z_{fit,re})^2 + (Z_{data,im} - Z_{fit,im})^2] \quad \text{B-2}$$

where  $N_{set}$  is the number of data points in the frequency range ( $N_{set} = 132$ ),  $P$  is the number of adjustable parameters ( $P = 14$ ),  $F[P, N_{set} - P]$  is equal to 0.46 and is the statistical  $F$  distribution at the specified degrees of freedom ( $N_{set} - P = 118$ ) and confidence interval (95%),  $\hat{S}$  is the returned optimal fitted parameter set, and  $S$  is the optimal parameter set with one parameter changed to make the resulting *SSE* within  $SSE_{95\%}$ .

### B.6 Potential drop along membrane pore

The potential distribution was modeled in a cylindrical pore of diameter  $r$  and length  $l$  according to the analytical solution presented by Lasia [319]. The model also assumed that the resistance of the electrode material is negligible, and electroactive species are present in high concentration to avoid concentration polarization. The analytical solution for modeling the potential distribution along the membrane pore is shown as follows:

$$\tanh\left(\frac{b\eta}{4}\right) = \tanh\left(\frac{b\eta_0}{4}\right)\exp(-\sqrt{2Bb}\bar{x}L) \quad \text{B-3}$$

$$b = 0.5f \quad \text{B-4}$$

$$f = \frac{F}{RT} \quad \text{B-5}$$

$$B = \frac{2\rho j_0}{r} \quad \text{B-6}$$

where  $\eta$  is overpotential (V),  $\eta_0$  is initial overpotential (V),  $x$  is the dimensionless length along the membrane pore,  $L$  is length of the pore (cm),  $F$  is Faraday constant (96485 C mol<sup>-1</sup>),  $R$  is gas constant (8.314 J mol<sup>-1</sup> K<sup>-1</sup>),  $T$  is temperature (298.15 K),  $\rho$  is the specific solution resistance (8.3  $\Omega$  cm for 100mM NaClO<sub>4</sub>) and  $r$  is the radius of membrane pore (cm).

The potential distribution shown in Figure B-5 is the simulation result of assuming that only water oxidation was taking place on the REM surface. The potential at the pore entrance, formal potential for water oxidation in the 100mM NaClO<sub>4</sub> (pH 5.95) electrolyte, and the exchange current density need to be determined before the simulation is realized in Matlab 2015a.

#### B.6.1 Potential at pore entrance

The anodic potential at the pore entrance of the REM is given by:

$$E_{anodic} = E_{measured} - i R_{solution} \quad \text{B-7}$$

where  $E_{measured}$  is the potential measured between the anode and reference electrode (4.52 V / saturated Ag/AgCl) (V),  $i$  is the applied current (0.8 A), and  $R_{solution}$  is the solution resistance (Ohm). The  $R_{solution}$  value was the real part of the impedance at high frequency in EIS measurements, where the imaginary part of the impedance is zero. In 100mM NaClO<sub>4</sub>, the  $R_{solution}$  is 0.4 Ohm.

### B.6.2 Formal potential of water oxidation

The formal potential  $E'_0$  at standard state conditions is 1.23 V/SHE [197]. The formal potential of water oxidation in 100mM NaClO<sub>4</sub> electrolytic solution (pH 5.95) was corrected by the Nernst equation:

$$E_0 = E'_0 + \frac{RT}{nF} \ln[H^+]^4 [P_{O_2}] \quad \text{B-8}$$

which yields the value of formal potential to be 0.87V / SHE assuming oxygen evolution reaction is in equilibrium with oxygen bubbles.

### B.6.3 Exchange current density

The exchange current was determined by Tafel plot. The data were acquired in cross flow filtration model using Linear Scan Voltammetry to scan a potential range from 3.1 to 3.4V SHE. Figure B-7 shows the linear fit of the Tafel plot.

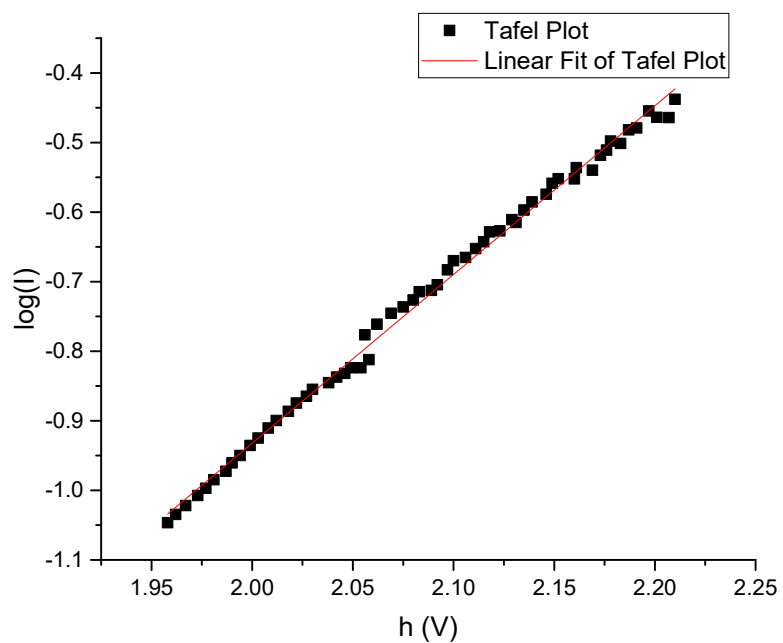


**Figure 38** Tafel plot and its linear fit; Fit equation:  $\log(i) = 2.43\eta - 5.78$ ; R-square = 0.9956

The exchange current  $i_0$  is obtained by extrapolating to an overpotential of zero. In this case, it's  $1.66 \times 10^{-6}$  A. Considering the internal diameter of 5.54 mm and length 100 mm, the exchange current density is  $9.53 \times 10^{-8}$  A  $\text{cm}^{-2}$ .

*B.7 Electrochemical impedance spectroscopic data in multi-cycle test*

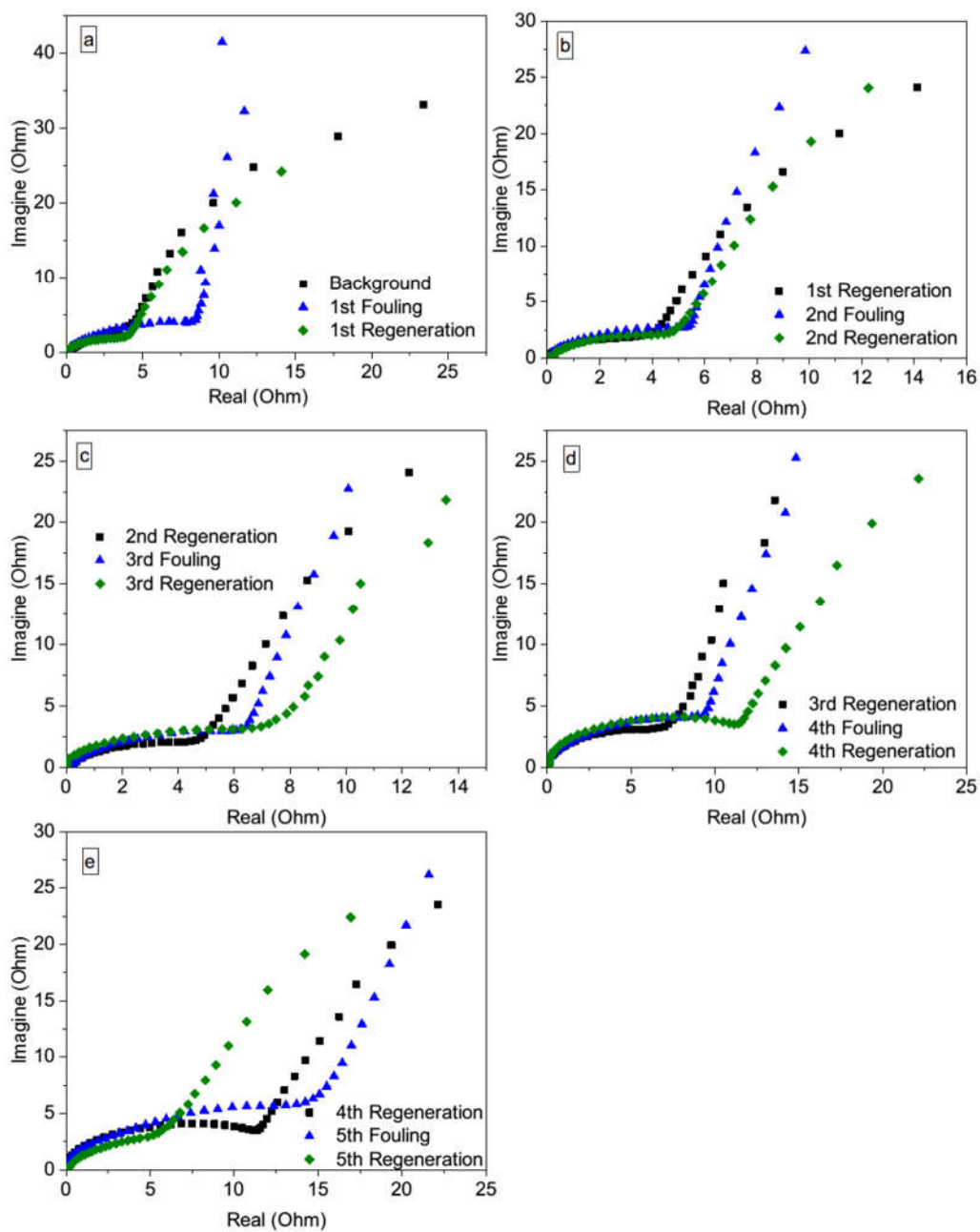


**Figure 39** EIS spectra in multi-cycle test of anodic regeneration of humic acid fouled REM in backwash mode, and (a)- (e) represent Cycle 1 - 5.

**Table XIX** MODEL PARAMETERS, CALCULATED DOUBLE LAYER CAPACITANCES AND ELECTRO-ACTIVE SURFACE AREAS UNDER BACKGROUND, 150MG L<sup>-1</sup> HA FOULING AND ANODIC CFER IN BACKWASH MODE IN LONGEVITY TEST (UNIT: R, R<sub>s</sub>, X<sub>1</sub>, X<sub>2</sub> AND Z<sub>B</sub> (OHM), Y (F S<sup>A-1</sup>), CDL (F), A (CM<sup>2</sup>))

Parameter	BG	1st F	1st R	2nd F	2nd R	3rd F	3rd R	4th F	4th R	5th F	5th R	
R <sub>s</sub>	2.91×10 <sup>-1</sup>	6.24×10 <sup>-1</sup>	3.60×10 <sup>-1</sup>	4.72×10 <sup>-1</sup>	1.12×10 <sup>-1</sup>	8.14×10 <sup>-1</sup>	4.31×10 <sup>-1</sup>	5.64×10 <sup>-1</sup>	1.26×10 <sup>-1</sup>	3.08×10 <sup>-1</sup>	2.47×10 <sup>-1</sup>	
L	9.91×10 <sup>-1</sup>	9.87×10 <sup>-1</sup>	9.93×10 <sup>-1</sup>	9.79×10 <sup>-1</sup>	9.92×10 <sup>-1</sup>	9.78×10 <sup>-1</sup>	9.95×10 <sup>-1</sup>	9.88×10 <sup>-1</sup>	9.93×10 <sup>-1</sup>	9.95×10 <sup>-1</sup>	9.91×10 <sup>-1</sup>	
χ <sub>1</sub>	9.00×10 <sup>0</sup>	1.16×10 <sup>1</sup>	1.06×10 <sup>1</sup>	1.91×10 <sup>1</sup>	8.89×10 <sup>0</sup>	1.05×10 <sup>1</sup>	1.11×10 <sup>1</sup>	1.17×10 <sup>1</sup>	1.09×10 <sup>1</sup>	1.29×10 <sup>1</sup>	9.33×10 <sup>0</sup>	
χ <sub>2</sub>	5.72×10 <sup>-1</sup>	6.41×10 <sup>-1</sup>	5.39×10 <sup>-1</sup>	5.92×10 <sup>-1</sup>	6.30×10 <sup>-1</sup>	6.00×10 <sup>-1</sup>	5.97×10 <sup>-1</sup>	5.72×10 <sup>-1</sup>	5.99×10 <sup>-1</sup>	5.66×10 <sup>-1</sup>	6.79×10 <sup>-1</sup>	
Z <sub>B</sub>	4.06×10 <sup>-7</sup>	4.96×10 <sup>-7</sup>	4.93×10 <sup>-7</sup>	4.36×10 <sup>-7</sup>	7.35×10 <sup>-7</sup>	7.96×10 <sup>-7</sup>	3.93×10 <sup>-7</sup>	9.59×10 <sup>-7</sup>	7.13×10 <sup>-7</sup>	9.97×10 <sup>-7</sup>	8.54×10 <sup>-7</sup>	
Outer Surface	R <sub>ct,out</sub>	5.00×10 <sup>1</sup>	8.26×10 <sup>2</sup>	6.45×10 <sup>1</sup>	4.78×10 <sup>2</sup>	1.00×10 <sup>2</sup>	9.14×10 <sup>2</sup>	1.23×10 <sup>2</sup>	6.00×10 <sup>2</sup>	6.16×10 <sup>3</sup>	1.29×10 <sup>3</sup>	4.25×10 <sup>1</sup>
	Y <sub>0,out</sub>	8.12×10 <sup>-2</sup>	2.06×10 <sup>-2</sup>	7.00×10 <sup>-2</sup>	3.19×10 <sup>-2</sup>	5.01×10 <sup>-2</sup>	1.26×10 <sup>-2</sup>	3.80×10 <sup>-2</sup>	2.80×10 <sup>-2</sup>	8.28×10 <sup>-3</sup>	9.66×10 <sup>-3</sup>	8.32×10 <sup>-2</sup>
	α	8.63×10 <sup>-1</sup>	7.37×10 <sup>-1</sup>	7.00×10 <sup>-1</sup>	7.80×10 <sup>-1</sup>	7.00×10 <sup>-1</sup>	8.12×10 <sup>-1</sup>	7.53×10 <sup>-1</sup>	7.10×10 <sup>-1</sup>	8.48×10 <sup>-1</sup>	8.07×10 <sup>-1</sup>	9.36×10 <sup>-1</sup>
Active Layer	R <sub>ct,active</sub>	1.83×10 <sup>-2</sup>	3.42×10 <sup>2</sup>	2.08×10 <sup>0</sup>	7.20×10 <sup>2</sup>	1.59×10 <sup>0</sup>	7.14×10 <sup>2</sup>	8.34×10 <sup>2</sup>	4.65×10 <sup>3</sup>	9.31×10 <sup>0</sup>	5.10×10 <sup>2</sup>	1.00×10 <sup>0</sup>
	Y <sub>0,active</sub>	1.99×10 <sup>-1</sup>	6.81×10 <sup>-3</sup>	5.01×10 <sup>-2</sup>	4.96×10 <sup>-3</sup>	5.00×10 <sup>-2</sup>	4.65×10 <sup>-3</sup>	3.94×10 <sup>-3</sup>	8.05×10 <sup>-4</sup>	1.71×10 <sup>-2</sup>	5.99×10 <sup>-3</sup>	1.80×10 <sup>-1</sup>
	α	7.82×10 <sup>-1</sup>	8.19×10 <sup>-1</sup>	7.02×10 <sup>-1</sup>	9.63×10 <sup>-1</sup>	9.51×10 <sup>-1</sup>	9.42×10 <sup>-1</sup>	7.73×10 <sup>-1</sup>	7.06×10 <sup>-1</sup>	7.01×10 <sup>-1</sup>	8.43×10 <sup>-1</sup>	8.20×10 <sup>-1</sup>
Support Layer	R <sub>ct,sup</sub>	2.82×10 <sup>-1</sup>	1.66×10 <sup>5</sup>	7.60×10 <sup>1</sup>	6.57×10 <sup>2</sup>	1.45×10 <sup>2</sup>	3.33×10 <sup>4</sup>	2.30×10 <sup>2</sup>	1.40×10 <sup>3</sup>	4.43×10 <sup>2</sup>	1.32×10 <sup>4</sup>	9.88×10 <sup>1</sup>
	Y <sub>0,sup</sub>	8.94×10 <sup>-1</sup>	3.99×10 <sup>-1</sup>	6.00×10 <sup>-1</sup>	5.04×10 <sup>-1</sup>	5.52×10 <sup>-1</sup>	4.34×10 <sup>-1</sup>	5.37×10 <sup>-1</sup>	4.72×10 <sup>-1</sup>	5.91×10 <sup>-1</sup>	4.58×10 <sup>-1</sup>	5.91×10 <sup>-1</sup>
	α	7.42×10 <sup>-1</sup>	9.89×10 <sup>-1</sup>	9.85×10 <sup>-1</sup>	9.39×10 <sup>-1</sup>	9.18×10 <sup>-1</sup>	9.10×10 <sup>-1</sup>	8.49×10 <sup>-1</sup>	8.89×10 <sup>-1</sup>	9.00×10 <sup>-1</sup>	9.06×10 <sup>-1</sup>	9.15×10 <sup>-1</sup>
Parameter	BG	1st F	1st R	2nd F	2nd R	3rd F	3rd R	4th F	4th R	5th F	5th R	
Outer Surface	C <sub>dl,out</sub>	7.53×10 <sup>-2</sup>	1.23×10 <sup>-2</sup>	6.63×10 <sup>-2</sup>	2.04×10 <sup>-2</sup>	4.63×10 <sup>-2</sup>	7.31×10 <sup>-3</sup>	2.68×10 <sup>-2</sup>	1.76×10 <sup>-2</sup>	5.75×10 <sup>-3</sup>	5.85×10 <sup>-3</sup>	8.39×10 <sup>-2</sup>
	A <sub>out</sub>	1.25×10 <sup>3</sup>	2.05×10 <sup>2</sup>	1.10×10 <sup>3</sup>	3.41×10 <sup>2</sup>	7.72×10 <sup>2</sup>	1.22×10 <sup>2</sup>	4.46×10 <sup>2</sup>	2.93×10 <sup>2</sup>	9.58×10 <sup>1</sup>	9.75×10 <sup>1</sup>	1.40×10 <sup>3</sup>
Active Layer	C <sub>dl,active</sub>	4.16×10 <sup>-2</sup>	3.85×10 <sup>-3</sup>	1.82×10 <sup>-2</sup>	4.35×10 <sup>-3</sup>	4.37×10 <sup>-2</sup>	3.79×10 <sup>-3</sup>	1.51×10 <sup>-3</sup>	1.15×10 <sup>-4</sup>	6.41×10 <sup>-3</sup>	3.70×10 <sup>-3</sup>	1.22×10 <sup>-1</sup>
	A <sub>active</sub>	6.93×10 <sup>2</sup>	6.42×10 <sup>1</sup>	3.03×10 <sup>2</sup>	7.25×10 <sup>1</sup>	7.28×10 <sup>2</sup>	6.31×10 <sup>1</sup>	2.52×10 <sup>1</sup>	1.91×10 <sup>0</sup>	1.07×10 <sup>2</sup>	6.17×10 <sup>1</sup>	2.03×10 <sup>3</sup>
Support Layer	C <sub>dl,sup</sub>	5.48×10 <sup>-1</sup>	4.06×10 <sup>-1</sup>	6.20×10 <sup>-1</sup>	5.45×10 <sup>-1</sup>	6.77×10 <sup>-1</sup>	4.87×10 <sup>-1</sup>	7.17×10 <sup>-1</sup>	5.84×10 <sup>-1</sup>	7.55×10 <sup>-1</sup>	5.52×10 <sup>-1</sup>	7.31×10 <sup>-1</sup>
	A <sub>sup</sub>	9.13×10 <sup>3</sup>	6.77×10 <sup>3</sup>	1.03×10 <sup>4</sup>	9.08×10 <sup>3</sup>	1.13×10 <sup>4</sup>	8.12×10 <sup>3</sup>	1.19×10 <sup>4</sup>	9.73×10 <sup>3</sup>	1.26×10 <sup>4</sup>	9.19×10 <sup>3</sup>	1.22×10 <sup>4</sup>

### B.8 *Zeta-potential of polystyrene microspheres in different pH*

A solution of 0.001 wt% polystyrene microspheres with a mean diameter of 1.58  $\mu\text{m}$  was prepared in 100mM  $\text{NaClO}_4$  electrolyte. The solution pH was adjusted by adding  $\text{HClO}_4$  and  $\text{NaOH}$ .

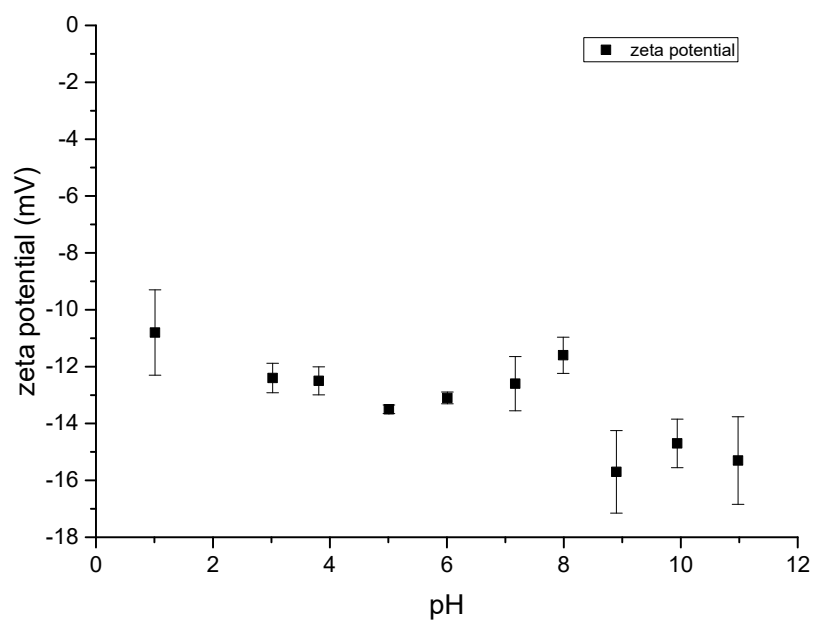


**Figure 40** zeta-potential of polystyrene microspheres in pH range 1 to 11

*B.9 Concentration decay of polystyrene microspheres in the feed solution during filtration experiment*

The microsphere concentration profiles accurately fit a 1<sup>st</sup> order removal rate model, which is consistent with a continuously stirred tank reactor mass balance model that assumes complete removal of the microspheres during filtration and 100% recycle of the permeate solution.

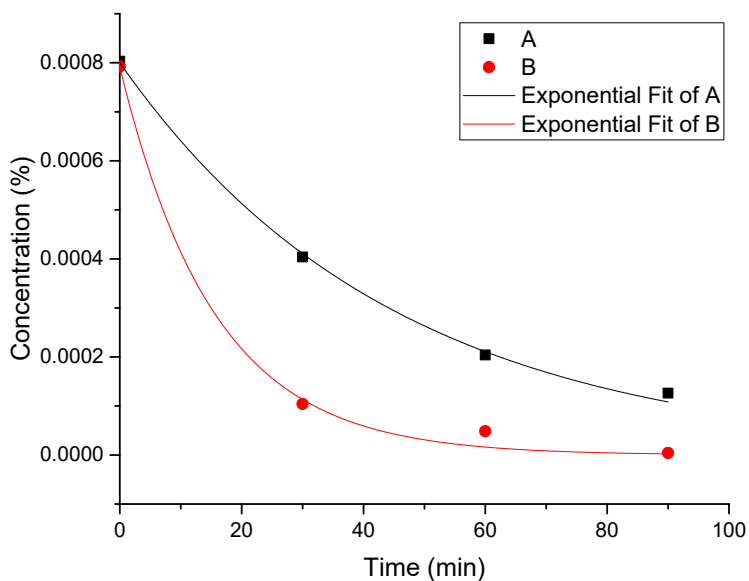


**Figure 41** Change in polystyrene concentration in feed solution during fouling experiment; A: the fouling experiment before cathodic CFER with backwash; B: the fouling experiment before anodic CFER with backwash; fit equation:  $C_A = C_{A0} \cdot \exp(k \cdot t)$ ;  $R^2$  after the exponential fit A:0.99765, B: 0.99591

### B.10 Backwash control experiment using ionic solution

Here presents the permeate flux results in backwash control experiment using 100 mM NaClO<sub>4</sub> solution without an applied current.

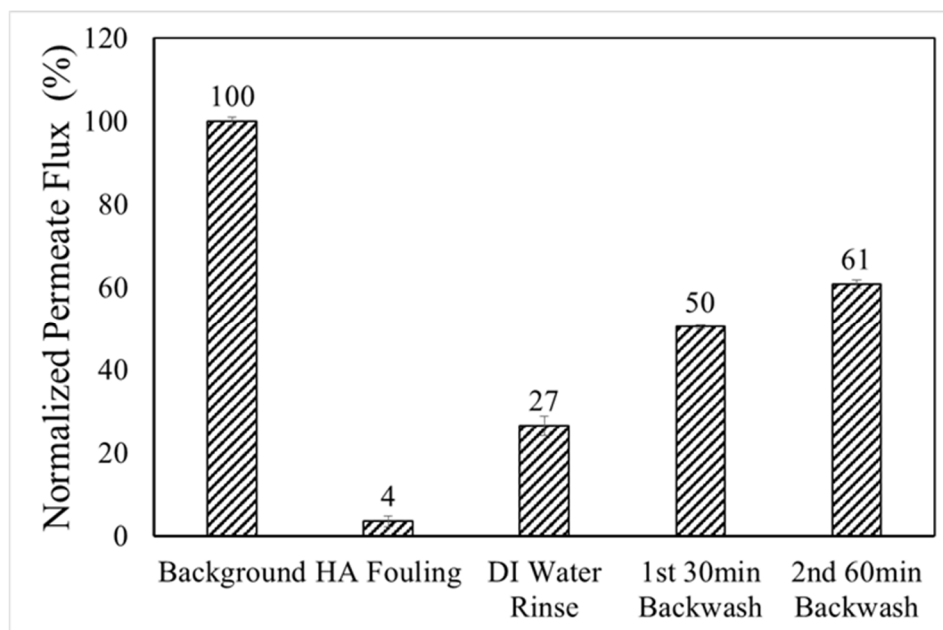


**Figure 42** Normalized permeate flux  $\bar{J}$  under different operation conditions for backwash regeneration of 150 mg L<sup>-1</sup> HA fouled REM; (Backwash conditions: 100 mM NaClO<sub>4</sub> and 40 mbar vacuum); initial membrane flux  $J_0 = 1295.1$  LMH bar<sup>-1</sup>.

**APPENDIX C***C.1. Literature summary of hydroxyl radical probes***Table XX** LITERATURE SUMMARY OF HYDROXYL RADICAL PROBES USED IN THE ELECTROCHEMICAL OXIDATION PROCESS

Probe molecule	Electrode	Electrolyte	Applied E or I	Ref.	
salicylic acid	PbO <sub>2</sub>	0.1 M KH <sub>2</sub> PO <sub>4</sub> & NaOH (pH=7.4)	1.60 V vs SHE	[82]	
	BDD	0.05 M Na <sub>2</sub> SO <sub>4</sub> (pH=3.0)	33 mA cm <sup>-2</sup>	[25]	
		1 M HClO <sub>4</sub>	0.4 – 4 mA cm <sup>-2</sup>	[90]	
benzoic acid	BDD	0.5 M HClO <sub>4</sub>	1.5 A		
DMPO	BDD	1 M HClO <sub>4</sub>	0.1 mA cm <sup>-2</sup>	[90]	
	F-doped PbO <sub>2</sub>	2 g L <sup>-1</sup> Na <sub>2</sub> SO <sub>4</sub>	7.5 V cell potential	[89]	
		50 mM Na <sub>2</sub> SO <sub>4</sub>	25 mA cm <sup>-2</sup>	[91]	
	$\gamma$ -Bi <sub>2</sub> MoO <sub>6</sub>	0.1 M Na <sub>2</sub> SO <sub>4</sub>	3.05 V vs SHE	[86]	
coumarin	BDD	1 M H <sub>2</sub> SO <sub>4</sub>	2.6 V vs SHE	[105]	
		0.2 M H <sub>2</sub> SO <sub>4</sub>	15, 30 and 60 mA	[81]	
		0.12 M HClO <sub>4</sub>	2.0 V vs SHE	[107]	
		0.12 M H <sub>2</sub> SO <sub>4</sub>	1.8 V vs SHE		
		0.12 M HNO <sub>3</sub>	1.6 V vs SHE		
		0.12 M HCl	1.6 V vs SHE		
		0.1 M NaClO <sub>4</sub>	2.64 V vs SHE	[28]	
	Ti <sub>4</sub> O <sub>7</sub> graphite	1.0 M H <sub>2</sub> SO <sub>4</sub>	10 – 20 mA	[100]	
	terephthalic acid	Ti <sub>4</sub> O <sub>7</sub>	0.1 M NaClO <sub>4</sub>	3.14 V vs SHE	[28]
	1,4-benzoquinone	graphite	1.0 M H <sub>2</sub> SO <sub>4</sub>	10 – 20 mA	[100]
Ti <sub>4</sub> O <sub>7</sub> (Ebonex)		0.1 M NaClO <sub>4</sub>	3.0 V vs SHE	[27]	
Ti <sub>4</sub> O <sub>7</sub> (Ebonex)		0.05 M Na <sub>2</sub> SO <sub>4</sub>	40 mA	[123]	
Sb-doped SnO <sub>2</sub>		0.1 g L <sup>-1</sup> 1,4-benzoquinone	0.2 A cm <sup>-2</sup>	[124]	
Fe-PbO <sub>2</sub> /Ti		1.8 M NaOAc / 1.0 M HOAc (pH=5.0)	100 mA	[253]	
RNO	PbO <sub>2</sub>	0.2 M phosphate buffer (pH=7.1)	5 mA cm <sup>-2</sup>	[135]	
	BDD	0.2 M phosphate buffer (pH=7.1)	33 – 100 mA cm <sup>-2</sup>	[137]	
indigotrisulfonate	cobalt coated PbO <sub>2</sub>	0.001 M Na <sub>2</sub> SO <sub>4</sub>	0 – 50 mA cm <sup>-2</sup>	[126]	
<i>p</i> -chlorobenzoic acid	cobalt coated PbO <sub>2</sub>	0.001 M Na <sub>2</sub> SO <sub>4</sub>	0 – 50 mA cm <sup>-2</sup>	[126]	
	BDD	0.2 M phosphate buffer (pH=7.1)	100 mA cm <sup>-2</sup>	[127]	
	Ti/RuO <sub>2</sub>				
	Ti/IrO <sub>2</sub>				
	Ti/Pt-IrO <sub>2</sub> Pt				

**Table XXI** LITERATURE SUMMARY OF HYDROXYL RADICAL PROBES USED IN THE ELECTROCHEMICAL FENTON PROCESS

Probe molecule	Electrode	Electrolyte	Applied E or I	Ref.
DMPO	porous graphite	1 mM FeCl <sub>3</sub> , 1.02 mM EDTA and 10 mM H <sub>2</sub> O <sub>2</sub>	0.5 V (cell potential)	[92]
terephthalic acid	PbO <sub>2</sub> coated SnO <sub>2</sub>	50 mM Na <sub>2</sub> B <sub>4</sub> O <sub>7</sub> & NaOH (pH=11.3)	-0.403 V vs SHE	[120]
	Pt/Co coated graphene	100 mM NaOH	-0.8 – 0.2 V vs SHE cycling scan	[121]
1,4 - Dioxane	RuO <sub>2</sub> coated Ti	NaCl and FeCl <sub>3</sub> [Cl <sup>-</sup> ] = 281 mM, [Fe <sup>3+</sup> ] = 0.5 - 4.0 mM	0 – 30 mA cm <sup>-2</sup>	[139]

**Table XXII** LITERATURE SUMMARY OF HYDROXYL RADICAL PROBES USED IN THE FENTON PROCESS

Probe Molecule	Solution	Ref.
salicylic acid	100 µg mL <sup>-1</sup> H <sub>2</sub> O <sub>2</sub> (pH 3.0) and 10 µg mL <sup>-1</sup> Fe <sup>2+</sup>	[112]
terephthalic acid (+2Na)	2.5 - 30 µM H <sub>2</sub> O <sub>2</sub> and 50 µM Fe <sup>2+</sup>	[122]
DMPO	0.199 M H <sub>2</sub> O <sub>2</sub> , 25 µM Fe <sup>2+</sup> , 100 µM EDTA	[93]
	0.6% H <sub>2</sub> O <sub>2</sub> , 50 µM KH <sub>2</sub> PO <sub>4</sub> (pH=7.4), 1 mM DETAPAC	[94]
	0.06% H <sub>2</sub> O <sub>2</sub> (UV photolysis)	[95]
	10 mM H <sub>2</sub> O <sub>2</sub> , 0.5 mM Cr(V)	
benzoic acid	1.1 M H <sub>2</sub> O <sub>2</sub> with 9.2 mM Co <sup>2+</sup>	[109]
	0.2 -1.0 mM H <sub>2</sub> O <sub>2</sub> and 0.2 - 0.53 mM Fe <sup>2+</sup>	[110]
	iron plus ascorbate driven Fenton	[111]
DMSO	200 µM H <sub>2</sub> O <sub>2</sub> , 1 mM FeSO <sub>4</sub>	[97]
	250 µM H <sub>2</sub> O <sub>2</sub> , 1mM FeSO <sub>4</sub>	[96]
	0.1 M H <sub>2</sub> O <sub>2</sub> and 1 mM Fe <sup>2+</sup> in EDTA	[98]
1-propanol	0.2 -1.0 mM H <sub>2</sub> O <sub>2</sub> and 0.2 - 0.53 mM Fe <sup>2+</sup>	
methylene blue dye	3mM H <sub>2</sub> O <sub>2</sub> and 0.15 mM Fe <sup>2+</sup>	[140]
<i>p</i> -chlorobenzoic acid	0.15 or 0.6 mM H <sub>2</sub> O <sub>2</sub> (UV)	[320]

**Table XXIII** LITERATURE SUMMARY OF HYDROXYL RADICAL PROBES USED IN THE PHOTOCATALYTIC PROCESS

Probe molecule	Catalyst	Solution	Ref.	
coumarin	TiO <sub>2</sub> film	1 mM coumarin in DI	[103]	
	TiO <sub>2</sub> single crystal	0.1 mM Na <sub>2</sub> SO <sub>4</sub>	[104]	
	TiO <sub>2</sub> nanoparticle	1 mM coumarin in DI	[102]	
	ZnO nanoparticle			
	WO <sub>3</sub> nanoparticle			
	CdS nanoparticle			
	Bi <sub>2</sub> WO <sub>4</sub> nanoparticle			
	BiOCl nanoparticle			
	TiO <sub>2</sub> nanoparticle	0.1 mM coumarin in DI	[101]	
luminol	TiO <sub>2</sub> nanoparticle	10 mM NaOH	[113]	
terephthalic acid	TiO <sub>2</sub> film	2 mM NaOH	[103]	
	TiO <sub>2</sub> single crystal	0.1 M Na <sub>2</sub> SO <sub>4</sub>	[114]	
	TiO <sub>2</sub> nanoparticle	10 mM NaOH	[113]	
		1 M NaOH	[117]	
		50 mg L <sup>-1</sup> terephthalic acid (pH=10)	[118]	
		Various pH solution by mixing NaOH and H <sub>2</sub> SO <sub>4</sub>	[119]	
		C-doped TiO <sub>2</sub> nanoparticle	2 mM NaOH	[115]
		Sm-doped TiO <sub>2</sub> nanoparticle	2 mM NaOH	[116]
	ZnO nanoparticle	Various pH solution by mixing NaOH and H <sub>2</sub> SO <sub>4</sub>	[119]	
<i>p</i> -chlorobenzoic acid	TiO <sub>2</sub> film	450 µg L <sup>-1</sup> <i>p</i> -CBA in DI	[128]	
	TiO <sub>2</sub> nanoparticle	1.92 µM <i>p</i> -CBA in DI	[129]	
	SWCNT-COOH	2 µM <i>p</i> -CBA in DI	[130]	
	N-doped TiO <sub>2</sub> nanorod	1.92 µM <i>p</i> -CBA in DI	[131]	
	N-doped TiO <sub>2</sub> nanoparticle	1.92 µM <i>p</i> -CBA in DI	[132]	
	Ag coated TiO <sub>2</sub> thin film	1.92 µM <i>p</i> -CBA in DI	[51,133]	
DMPO	TiO <sub>2</sub> nanoparticle	10 mM DMPO in DI	[87]	
		20 mM DMPO in DI	[88]	
CTPO	TiO <sub>2</sub> nanoparticle	0.8 mM CTPO in DI		
CTMPO	TiO <sub>2</sub> nanoparticle	0.8 mM CTMPO	[87]	
TEMPOL	TiO <sub>2</sub> nanoparticle	0.8 mM TEMPOL		
PBN	TiO <sub>2</sub> nanoparticle	0.1 M PBN in 5 mM KH <sub>2</sub> PO <sub>4</sub>	[99]	
4-POBN	TiO <sub>2</sub> nanoparticle	0.1 M POBN in 5 mM KH <sub>2</sub> PO <sub>4</sub>		
DMSO	N/A	UV photolysis of unbuffered H <sub>2</sub> O <sub>2</sub>	[96]	
3-carboxyproxyl	TiO <sub>2</sub> nanoparticle	0.8 mM 3-carboxyproxyl	[138]	

**Note:** **DMPO** – 5,5-dimethyl-1-pyrroline-N-oxide, **RNO** – *p*-nitrosodimethylaniline, **DMSO** – dimethyl sulphoxide, **CTPO** – 3-carboxyl-2,2,5,5-tetramethyl-1-pyrrolidine-1-oxyl, **CTMPO** – 4-carboxyl-2,2,6,6-tetramethylpiperidine-1-oxyl, **TEMPOL** – 4-hydroxyl-2,2,6,6-tetramethylpiperidine-1-oxyl, **PBN** – alpha-phenyl-N-tert-butyl nitron, **4-POBN** – alpha-(4-pyridyl N-oxide) N-tert-butyl nitron

### C.2 *Anodic peak potentials for selected compounds*

**Table XXIV** ANODIC PEAK POTENTIALS FOR SELECTED COMPOUNDS

<b>Molecule</b>	<b>Anodic Peak E (V / SHE)</b>	<b>Note</b>	<b>Ref.</b>
Salicylic Acid	1.20 V	On Au electrode	[321]
Luminol	0.75 V	On glassy carbon electrode	[322]
1,4-dioxane	2.40 V	On BDD	[80]
1-propanol	-0.05 V	On Pb electrode	[323]
Methylene Blue	0.09 V	On carbon fiber electrode	[324]

### C.3 *Details of linear sweep voltammetry simulation*

Linear sweep voltammetry mathematical modeling was performed numerically, using Matlab 2015b, on a one-step and one-electron process by solving a set of parabolic partial differential equations (PDE) with appropriate boundary conditions, as described by Gavaghan and Bond [325]. Briefly, forward and central finite difference methods were used to approximate the time and spatial derivatives, respectively. Bulk concentrations for reactant and product were assumed far from the electrode surface (semi-infinite boundary condition), and first order Butler-Volmer kinetics governed reaction at the electrode surface. Convergence and stability of the PDE solution were satisfied by maintaining  $\left(\Delta t \leq \frac{1\Delta x^2}{2D}\right)$  [326]. The curve fitting was achieved by minimizing the sum of squared errors by varying the values of formal potential ( $E^0$ ), first order heterogeneous kinetic rate constant ( $k^0$ ), and electron transfer coefficient ( $\alpha$ ).

C.4. System schematic for voltammetry and bulk oxidation experiments

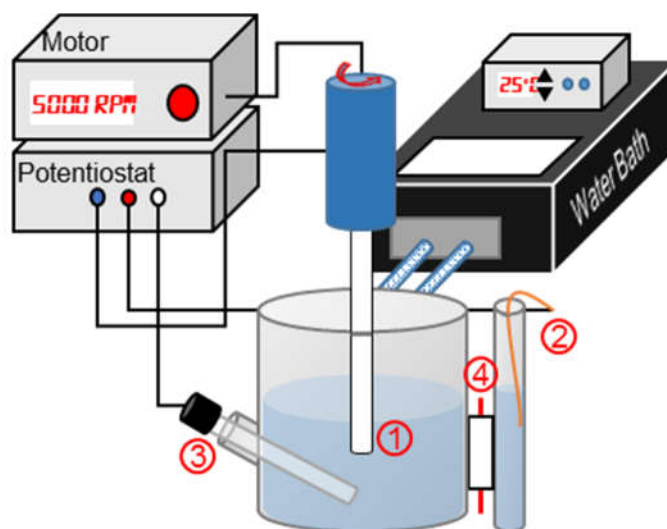


**Figure 43** System schematic for voltammetry and bulk oxidation experiments. ① working electrode, ② counter electrode, ③ reference electrode, and ④ Nafion membrane.

*C.5 Diffusion coefficients and mass transfer rate constants***Table XXV** DIFFUSION COEFFICIENTS AND MASS TRANSFER RATE CONSTANTS OF COU, TA, AND *p*-BQ AT 25 °C

<b>Compound</b>	<b>Diffusion Coefficient/ m<sup>2</sup> s<sup>-1</sup></b>	<b>Mass Transfer Rate Constant/ m s<sup>-1</sup></b>
COU	$9.5 \times 10^{-10}$ [165]	$1.26 \times 10^{-4}$
TA	$1.0 \times 10^{-9}$ [327]	$1.30 \times 10^{-4}$
<i>p</i> -BQ	$2.7 \times 10^{-9}$ [270]	$2.53 \times 10^{-4}$

C.6 Linear sweep voltammetry of terephthalic acid and *p*-benzoquinone

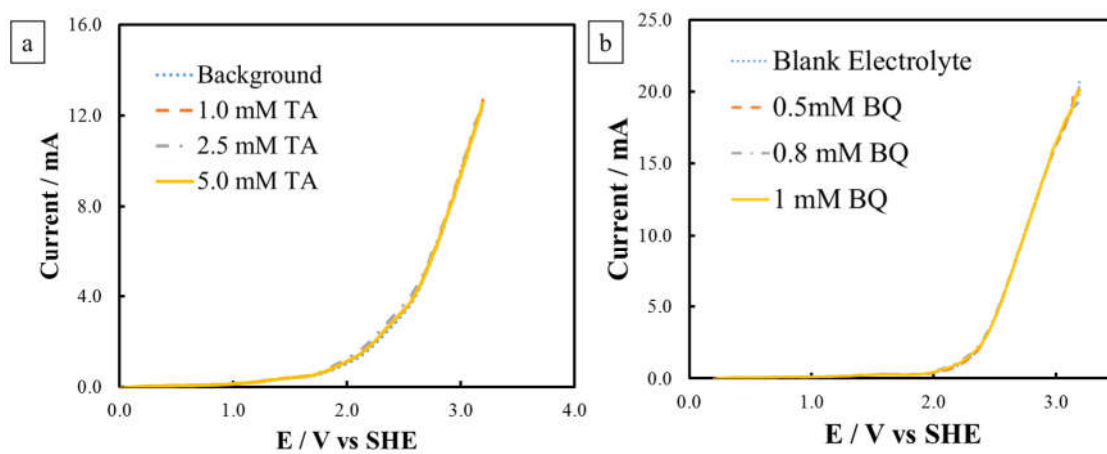


**Figure 44.** LSV on BDD of (a) TA and (b) *p*-BQ with different concentrations. Temperature: 25°C and electrolyte: 1.0 M  $\text{KH}_2\text{PO}_4$  (pH adjusted to 6.37 with NaOH for TA LSV, and pH 5.8 for BQ LSV).

C.7 Linear sweep voltammetry of coumarin, *p*-chlorobenzoic acid and terephthalic acid on a platinum electrode

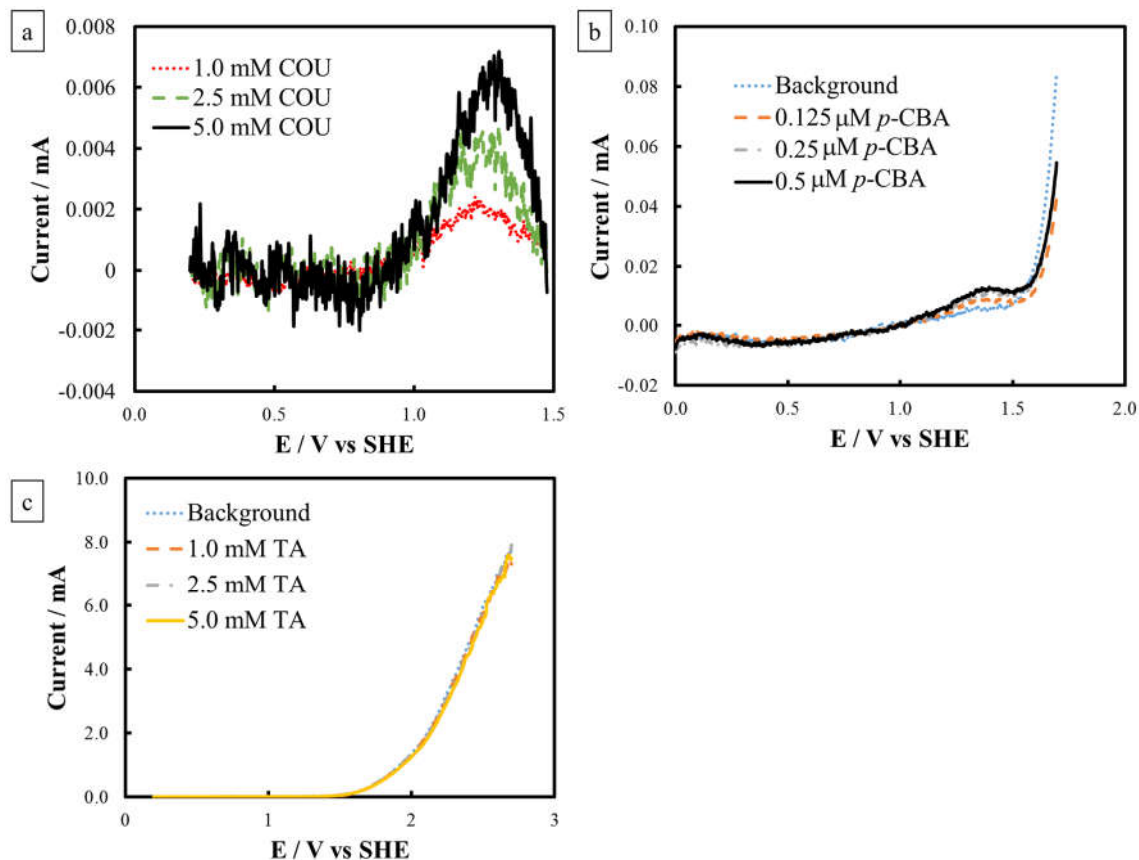


**Figure 45** LSV on Pt of (a) COU (background subtracted), (b) *p*-CBA, and (c) TA with different concentrations on a platinum disk electrode (surface area 0.03 cm<sup>2</sup>). Temperature: 25°C. Electrolyte: 1 M KH<sub>2</sub>PO<sub>4</sub> (pH 5.8) for COU LSV, 0.1 M HClO<sub>4</sub> (pH 1.0) for *p*-CBA LSV, and 1 M KH<sub>2</sub>PO<sub>4</sub> (pH adjusted to 6.37 with NaOH) for TA LSV.

C.8 *Cyclic voltammetry of coumarin*

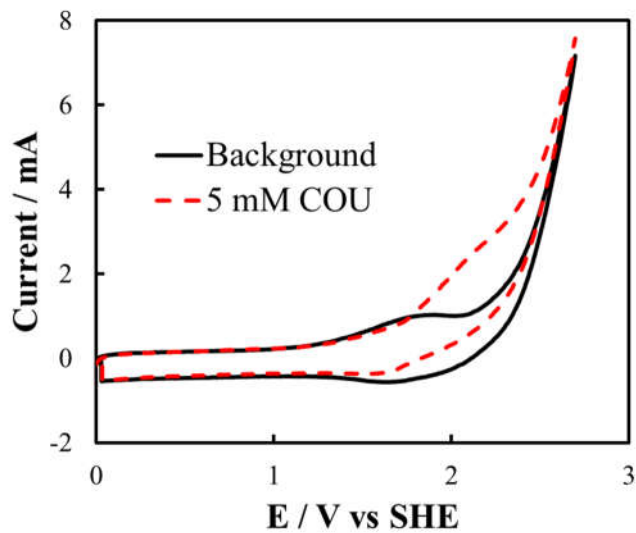


**Figure 46** CV on BDD of 5 mM COU (red dashed line) in 1.0 M  $\text{K}_2\text{HPO}_4$  electrolyte (background, black solid line). Temperature: 25°C and electrolyte: 1.0 M  $\text{KH}_2\text{PO}_4$  (pH 5.8).

C.9 Reaction rate constants and mass transfer rate constants for bulk oxidation

**Table XXVI** REACTION RATE CONSTANTS ( $K_s$ ) AND MASS TRANSFER RATE CONSTANTS ( $K_m$ ) FOR BULK OXIDATION OF COU, TA, AND *p*-BQ AT DIFFERENT TEMPERATURES AND 3.0 V/SHE.

Compound	T / °C	$k_s / \text{m s}^{-1}$	$k_m / \text{m s}^{-1}$
COU	15	$1.03 \times 10^{-5} \pm 1.25 \times 10^{-6}$	$1.05 \times 10^{-4}$
	25	$1.41 \times 10^{-5} \pm 8.97 \times 10^{-7}$	$1.26 \times 10^{-4}$
	35	$1.61 \times 10^{-5} \pm 3.07 \times 10^{-7}$	$1.49 \times 10^{-4}$
TA	25	$1.64 \times 10^{-4} \pm 1.24 \times 10^{-5}$	$1.30 \times 10^{-4}$
	35	$1.84 \times 10^{-4} \pm 6.97 \times 10^{-6}$	$1.54 \times 10^{-4}$
	45	$2.05 \times 10^{-4} \pm 1.17 \times 10^{-6}$	$1.78 \times 10^{-4}$
<i>p</i> -BQ	25	$1.15 \times 10^{-4} \pm 1.19 \times 10^{-6}$	$2.53 \times 10^{-4}$
	30	$1.20 \times 10^{-4} \pm 1.22 \times 10^{-6}$	$2.75 \times 10^{-4}$
	35	$1.28 \times 10^{-4} \pm 2.11 \times 10^{-6}$	$2.98 \times 10^{-4}$
	45	$1.38 \times 10^{-4} \pm 1.30 \times 10^{-6}$	$3.46 \times 10^{-4}$

C.10 Coumarin oxidation experiment under various temperatures at 1.7 V vs standard hydrogen electrode

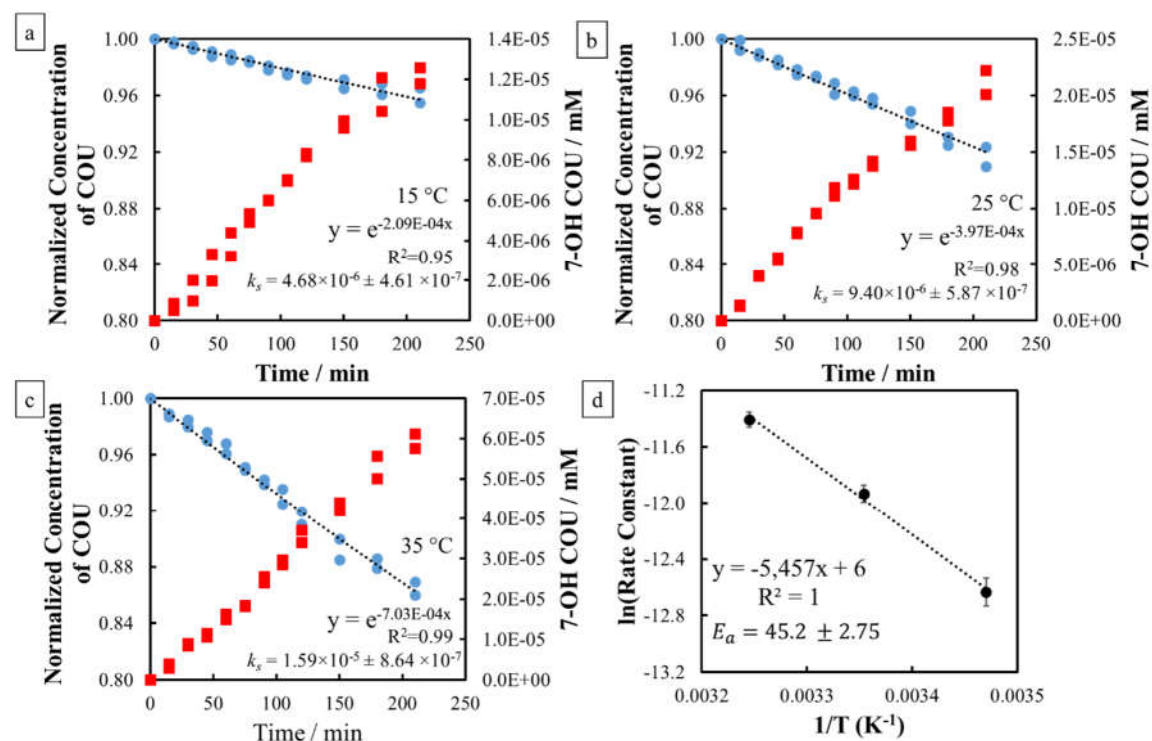


**Figure 47** Bulk oxidation on BDD of 1 mM COU at 1.7 V/SHE and a temperature of (a) 15 °C, (b) 25 °C, and (c) 35 °C, respectively. (d) Arrhenius plot for the oxidation of COU at 1.7 V/SHE. ● and ■ represent reactant (COU) and product (7-OH COU), respectively. Experiments were performed in duplicate, and the 1<sup>st</sup> order reaction rate was fitted to both data sets simultaneously (dashed line). Electrolyte: 100 mM KH<sub>2</sub>PO<sub>4</sub> (pH 4.5).

*C.11 Terephthalic acid oxidation experiments under different temperatures at 3.0 V vs standard hydrogen electrode*

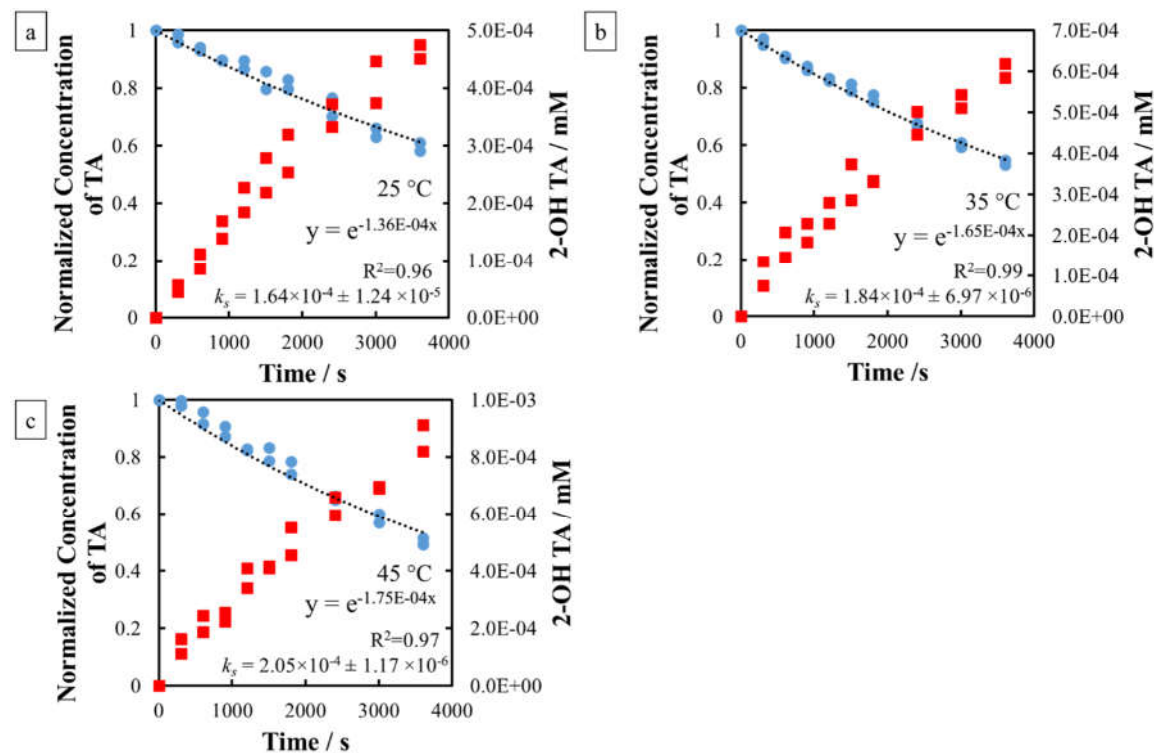


**Figure 48** Bulk oxidation on BDD of 0.1 mM TA at 3.0 V/SHE and a temperature of (a) 15 °C, (b) 25 °C, and (c) 35 °C, respectively. ● and ■ represent reactant (TA) and product (2-OH TA), respectively. Experiments were performed in duplicate, and the 1<sup>st</sup> order reaction rate was fitted to both data sets simultaneously (dashed line). Electrolyte: 100 mM KH<sub>2</sub>PO<sub>4</sub> (pH 4.5).

C.12 *p*-benzoquinone oxidation experiments under different temperatures at 3.0 V vs standard hydrogen electrode

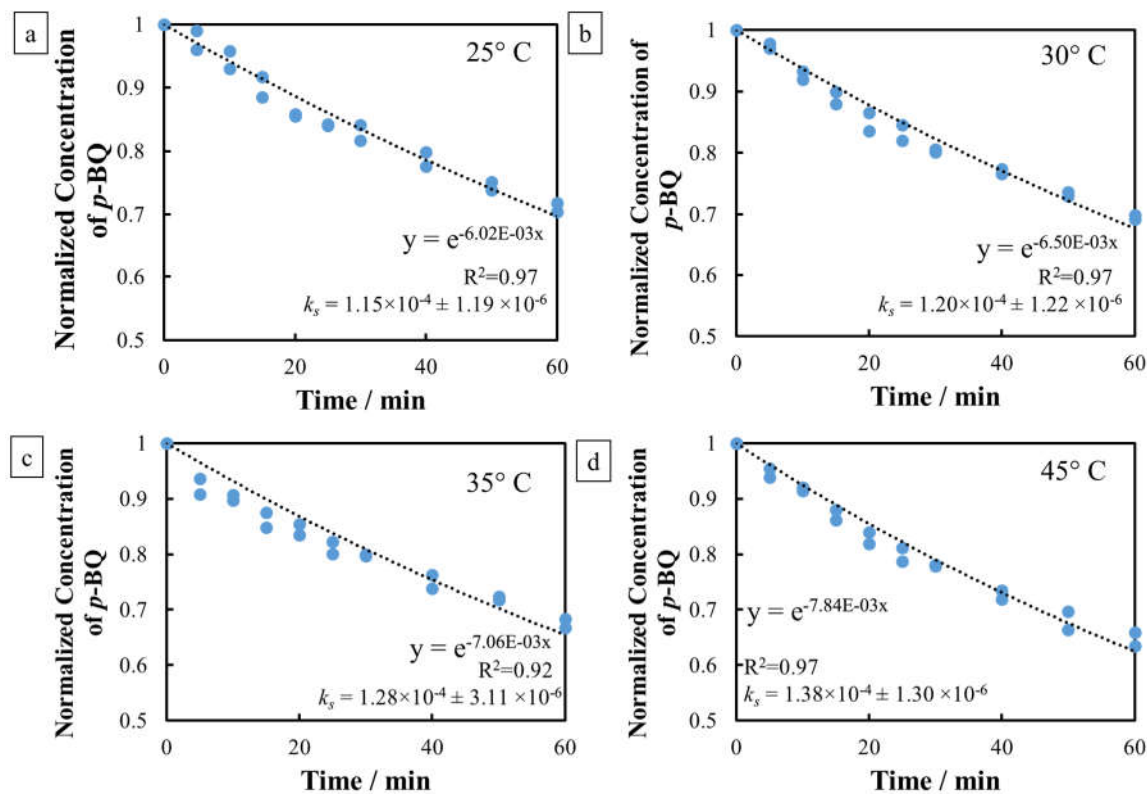


**Figure 49** Bulk oxidation on BDD of 1 mM *p*-BQ at 3.0 V/SHE and a temperature of (a) 25 °C, (b) 35 °C, (c) 35 °C, and (d) 45 °C, respectively in a H-cell jacketed glass reactor. Experiments were performed in duplicate, and the 1<sup>st</sup> order reaction rate was fitted to both data sets simultaneously (dashed line). Electrolyte: 100 mM KH<sub>2</sub>PO<sub>4</sub> (pH 4.5).

C.13 Theoretical  $E^0$  and  $\lambda_f$  values determined by density functional theory methods

**Table XXVII** THEORETICAL VALUES DETERMINED BY DFT METHODS AND USED TO DETERMINE  $E_A$  VERSUS POTENTIAL PROFILES.

Compound	$E^0$ (V/SHE)	$\lambda_f$ (kJ mol <sup>-1</sup> )
RNO	0.84	48.2
COU	2.04	9.77
<i>p</i> -CBA	2.48	19.9
BA	2.55	10.7
TA	2.76	13.6
<i>p</i> -BQ	3.21	13.6

C.14 Theoretical parameters determined for the reaction of probe molecules by the Forrester-Hepburn mechanism

**Table XXVIII** THEORETICAL PARAMETERS DETERMINED FOR THE REACTION OF PROBE MOLECULES BY THE FORRESTER-HEPBURN MECHANISM.

Reaction	$\Delta_r G^0$	$E_a$	$E^0$	$\lambda_f$
	(kJ mol <sup>-1</sup> )	(kJ mol <sup>-1</sup> )	(V/SHE)	(kJ mol <sup>-1</sup> )
COU + OH <sup>-</sup> → COU-OH <sup>-</sup>	118	130	--	--
COU-OH <sup>-</sup> → COU-OH + e <sup>-</sup>	--	--	-0.23	13.4
TA + OH <sup>-</sup> → TA-OH <sup>-</sup>	111	123	--	--
TA-OH <sup>-</sup> → TA-OH + e <sup>-</sup>	--	--	-0.05	11.9
<i>p</i> -BQ + OH <sup>-</sup> → <i>p</i> -BQ-OH <sup>-</sup>	14.9	42.1	--	--
<i>p</i> -BQ-OH <sup>-</sup> → <i>p</i> -BQ-OH + e <sup>-</sup>	--	--	1.22	14.9
<i>p</i> -CBA + OH <sup>-</sup> → <i>p</i> -HBA + Cl <sup>-</sup>	-146	125	--	--

C.15 Transition state structures

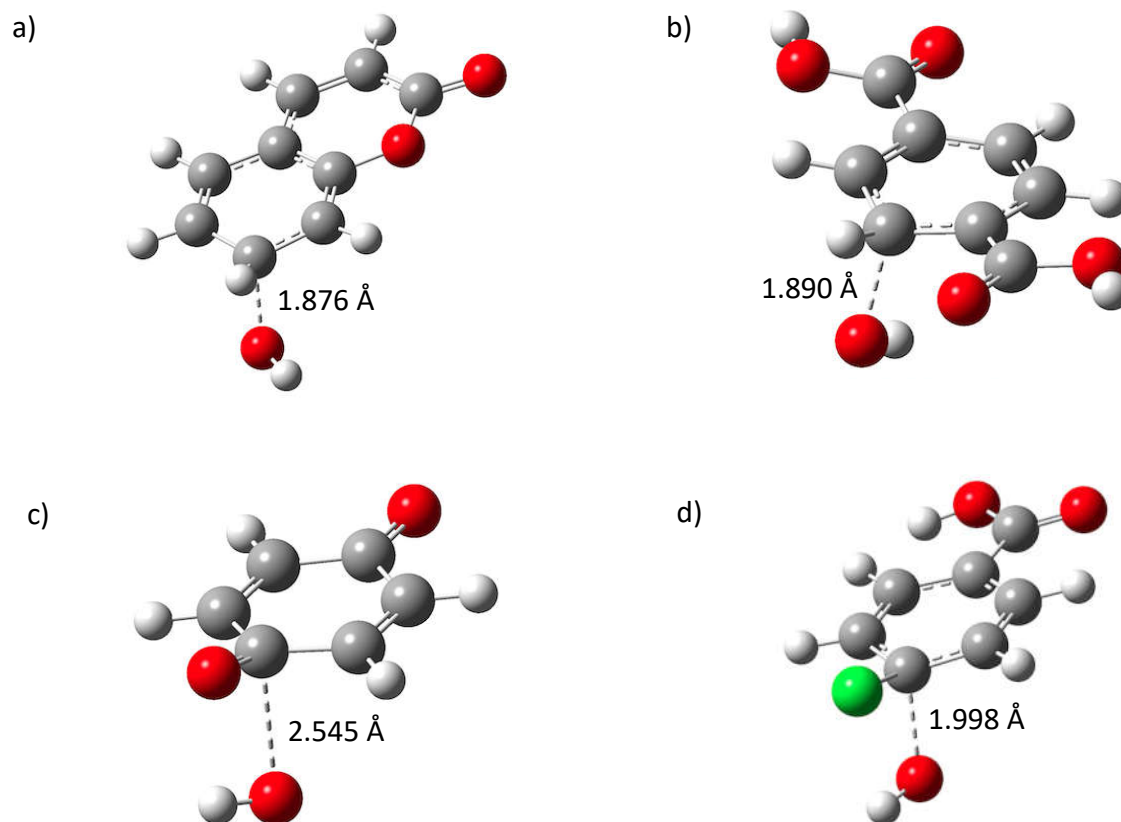


**Figure 50** Transition state structures for nucleophilic attack of  $\text{OH}^-$  on: a) COU; b) TA; c) *p*-BQ; d) *p*-CBA.

## **APPENDIX D**

### **D.1 Accurate positioning on $Ti_nO_{2n-1}$ electrode and laser marking**

To study the local kinetics in different electrode states, 5 random and well separated marker points were picked from the electrode surface, and a circular area of 80-micron diameter was studied using each marker point as the center of the circle. To accurately position the UME to the same spots of interest among different experiments, a triangulation scheme was adopted, which determines the location of the marker point by creating triangles to it from three anchor points. Briefly, the relative distances of one marker point to the three anchor points were recorded in the first experiment, and a new coordinate of that specific point in later experiments can be found by satisfying these relative distances in a Matlab 2016a script, which can be found in the *Appendix D.2*.

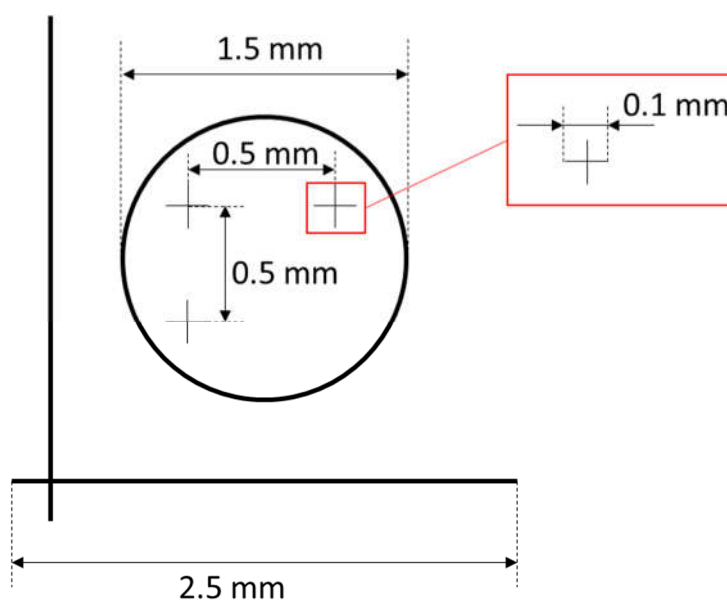


**Figure 51** Laser marking pattern sketch

These three anchor points, as shown in Figure 51, were created on the electrode using a TYKMA electrox laser marking system (Model, EMS300) with 30% laser power, 15 repeated times and 200.0 mm s<sup>-1</sup> traveling speed. The marked pattern, as shown in Figure 58, was examined by using a nano-contour GT-K optical profilometer (Bruker, Billerica, Massachusetts), and it was confirmed that the laser at this configuration was able to make a trench with a 40 μm depth determined by the profilometer. A comparison of the images collected by the profilometer and SECM was shown in Appendix D.9.

## D.2 Matlab script for triangulation positioning

### D.2.1 Calculation of relative distance from the coordinate of any spot in the interrogated area to three anchors

```
clear
clc
```

Write the coordinates for the three anchors determined from the SECM experiment

```
anchor = [148 288; % Anchor A
          632 272; % Anchor B
          236 628]; % Anchor C
```

Write the central coordinate for the interrogated area

```
position = [504 420];

distance = get_distance(position, anchor);
```

```
function dis = get_distance( pos, anchor)
    dis_1 = pdist2(pos, anchor(1,:), 'euclidean');
    dis_2 = pdist2(pos, anchor(2,:), 'euclidean');
    dis_3 = pdist2(pos, anchor(3,:), 'euclidean');

    dis = [dis_1; dis_2; dis_3];
end
```

### D.2.2 Calculation of new coordinates of specific spot by new anchor coordinates and relative distances

```
clear  
clc
```

Write the coordinates for the three anchors

```
tri_A = [148, 288];  
tri_B = [632, 272];  
tri_C = [236, 628];
```

Write the relative distances from a point to all three anchors

```
dis_A = 389.00;  
dis_B = 273.64;  
dis_C = 225.21;
```

Reorganize the coordinates

```
triangle = [tri_A; tri_B; tri_C];  
distance = [dis_A; dis_B; dis_C];  
point_location = [0,0];
```

Send for calculation

```
real_location = get_location(point_location, triangle, distance);  
  
pos_x = [tri_A(1), tri_B(1), tri_C(1), real_location(1)];  
pos_y = [tri_A(2), tri_B(2), tri_C(2), real_location(2)];  
sz = [10, 10, 10, 50];  
scatter(pos_x, pos_y, sz);
```

```
function new_position = get_location( pos, triangle, distance )
```

```
new_position = fminsearch(@err_func, pos);
```

```
function err = err_func(pos)
```

```
dis_1 = pdist2(pos, triangle(1,:), 'euclidean');
```

```
dis_2 = pdist2(pos, triangle(2,:), 'euclidean');
```

```
dis_3 = pdist2(pos, triangle(3,:), 'euclidean');
```

```
dis = [dis_1; dis_2; dis_3];
```

```
err = norm(dis - distance);
```

```
end
```

```
end
```

*D.3 Cyclic voltammetry on scanning electrochemical microscope ultramicroelectrode in 5 mM*

*Ru(NH<sub>3</sub>)<sub>6</sub>Cl<sub>3</sub> and 100 mM KCl*

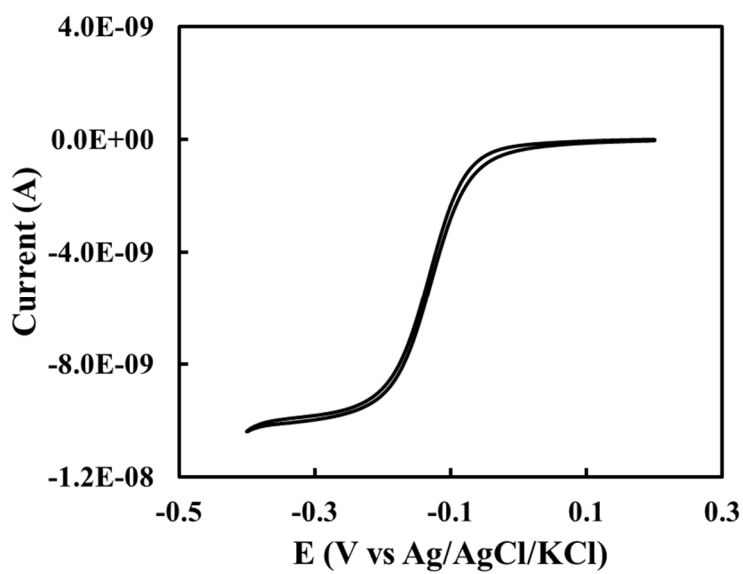


**Figure 52** Cyclic voltammetry on UME in 5 mM Ru(NH<sub>3</sub>)<sub>6</sub>Cl<sub>3</sub> and 100 mM KCl

#### *D.4 Justification of topographic mapping using oxygen reduction reaction on $Ti_nO_{2n-1}$*

The probe approach curve from the bulk solution to the unbiased  $Ti_nO_{2n-1}$  (open circuit potential 0.32 V vs SHE) substrate exhibited negative feedback, indicating that the unbiased substrate is not electrochemical active to oxygen reduction reaction. Cyclic voltammetry (CV) results, as shown in the Figure 53, also showed that the potential required to drive oxygen reduction reaction at  $Ti_nO_{2n-1}$  substrate is -1.20 V, so that the unbiased substrate (0.32 V vs SHE) would have little impact on the tip current when it was held at oxygen reduction potential.

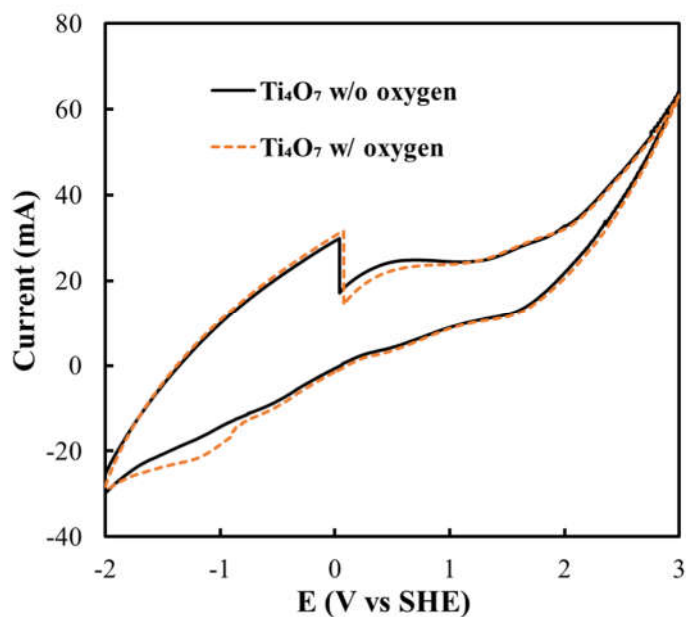


**Figure 53** CV of  $Ti_nO_{2n-1}$  electrode in 1 M  $NaClO_4$  aerated solution (solid black line) and argon purged solution (dashed orange line)

D.5 Charge carrier density and flat band potential by Mott-Schottky method

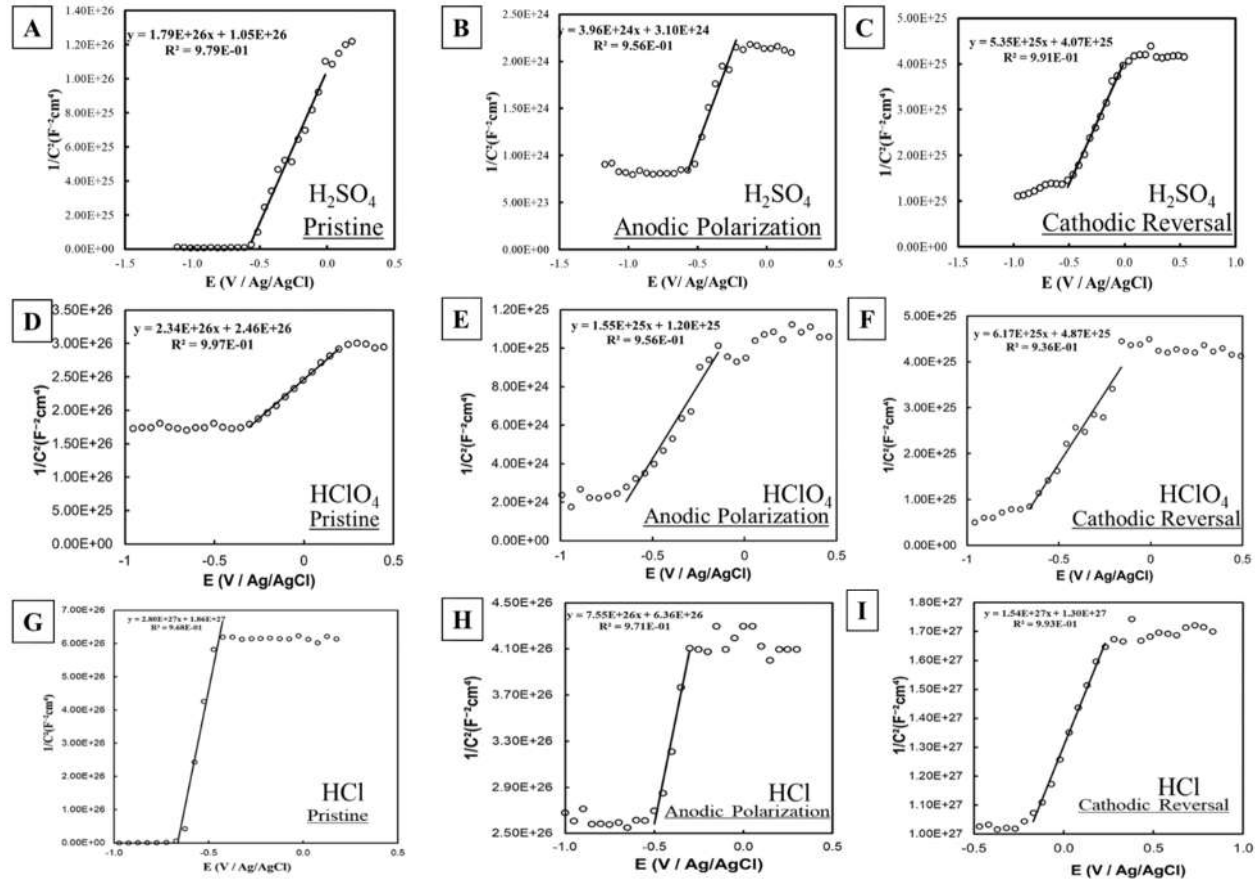


**Figure 54** Summary of Mott Schottky results of  $Ti_nO_{2n-1}$  at different states in (A)-(C) 1 M  $H_2SO_4$ , (D)-(F) 2 M  $HClO_4$ , and (G)-(I) 2 M  $HCl$  electrolytes. Hollow symbols and solid lines represent experimental and simulation data, respectively

**Table XXIX** SUMMARY OF CHARGE CARRIER DENSITY ( $N_D$ ) OF  $Ti_NO_{2N-1}$  AT DIFFERENT STATES. ERRORS REPRESENT 95% CONFIDENCE INTERVAL.

State	$N_D / \text{cm}^{-3}$		
	$H_2SO_4$	$HClO_4$	$HCl$
<b>Pristine</b>	$1.79 \times 10^{26} \pm 1.23 \times 10^{23}$ (1.00)	$2.34 \times 10^{26} \pm 8.79 \times 10^{22}$ (1.00)	$2.80 \times 10^{27} \pm 8.47 \times 10^{23}$ (1.00)
<b>Anodic Polarization</b>	$3.96 \times 10^{24} \pm 4.11 \times 10^{22}$ (0.022)	$1.55 \times 10^{25} \pm 6.29 \times 10^{23}$ (0.066)	$7.55 \times 10^{26} \pm 5.34 \times 10^{24}$ (0.27)
<b>Cathodic Reversal</b>	$5.35 \times 10^{25} \pm 3.87 \times 10^{22}$ (0.30)	$6.17 \times 10^{25} \pm 6.33 \times 10^{23}$ (0.26)	$1.54 \times 10^{27} \pm 6.89 \times 10^{23}$ (0.55)

**Table XXX** SUMMARY OF FLAT BAND POTENTIAL ( $E_{FB}$ ) OF  $Ti_NO_{2N-1}$  AT DIFFERENT STATES. ERRORS REPRESENT 95% CONFIDENCE INTERVAL.

State	$E_{fb} / V$		
	$H_2SO_4$	$HClO_4$	$HCl$
<b>Pristine</b>	$-0.59 \pm 0.017$	$-0.81 \pm 0.007$	$-0.66 \pm 0.012$
<b>Anodic Polarization</b>	$-0.75 \pm 0.034$	$-0.78 \pm 0.041$	$-0.84 \pm 0.021$
<b>Cathodic Reversal</b>	$-0.76 \pm 0.009$	$-0.79 \pm 0.049$	$-0.84 \pm 0.008$

D.6 *Film resistivity by two-point probe method*

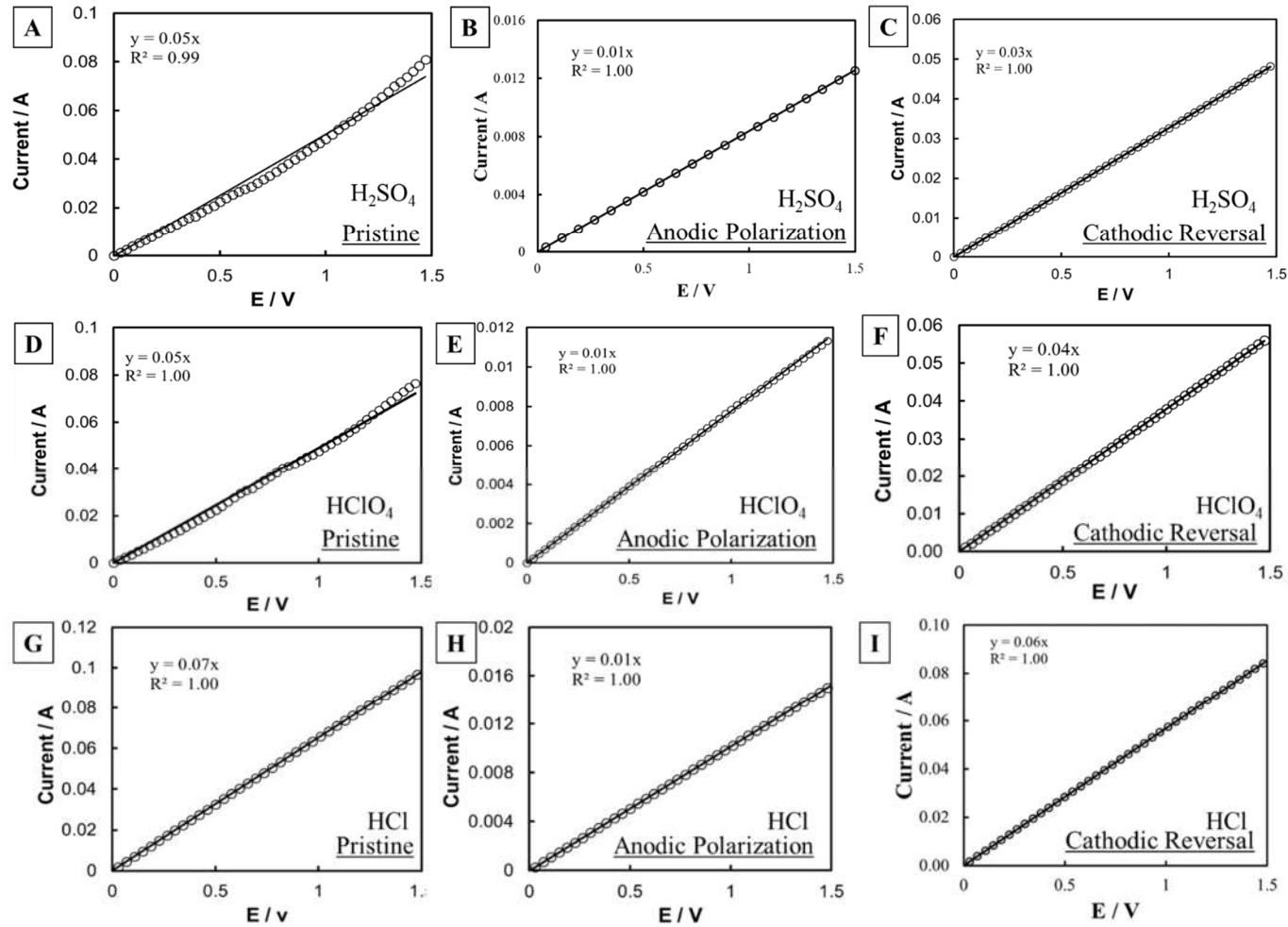


**Figure 55** Summary of film resistivities of  $\text{Ti}_n\text{O}_{2n-1}$  at different states in (A)-(C) 1 M  $\text{H}_2\text{SO}_4$ , (D)-(F) 2 M  $\text{HClO}_4$ , and (G)-(I) 2 M  $\text{HCl}$  electrolytes. Hollow symbols and solid lines represent experimental and simulation data, respectively.

**Table XXXI** SUMMARY OF FILM RESISTIVITIES OF  $Ti_NO_{2N-1}$  AT DIFFERENT STATES. ERRORS REPRESENT 95% CONFIDENCE INTERVAL.

State	Resistivity / $\Omega$ cm		
	$H_2SO_4$	$HClO_4$	$HCl$
<b>Pristine</b>	18.67±0.020 (1.00)	22.72±0.002 (1.00)	17.13±0.001 (1.00)
<b>Anodic Polarization</b>	132.70±0.004 (7.11)	143.59±0.001 (6.32)	110.89±0.003 (6.47)
<b>Cathodic Reversal</b>	33.94 ±0.001 (1.82)	29.47±0.004 (1.30)	19.72±0.003 (1.15)

D.7 XRD patterns of control samples at open circuit potential in various electrolytes

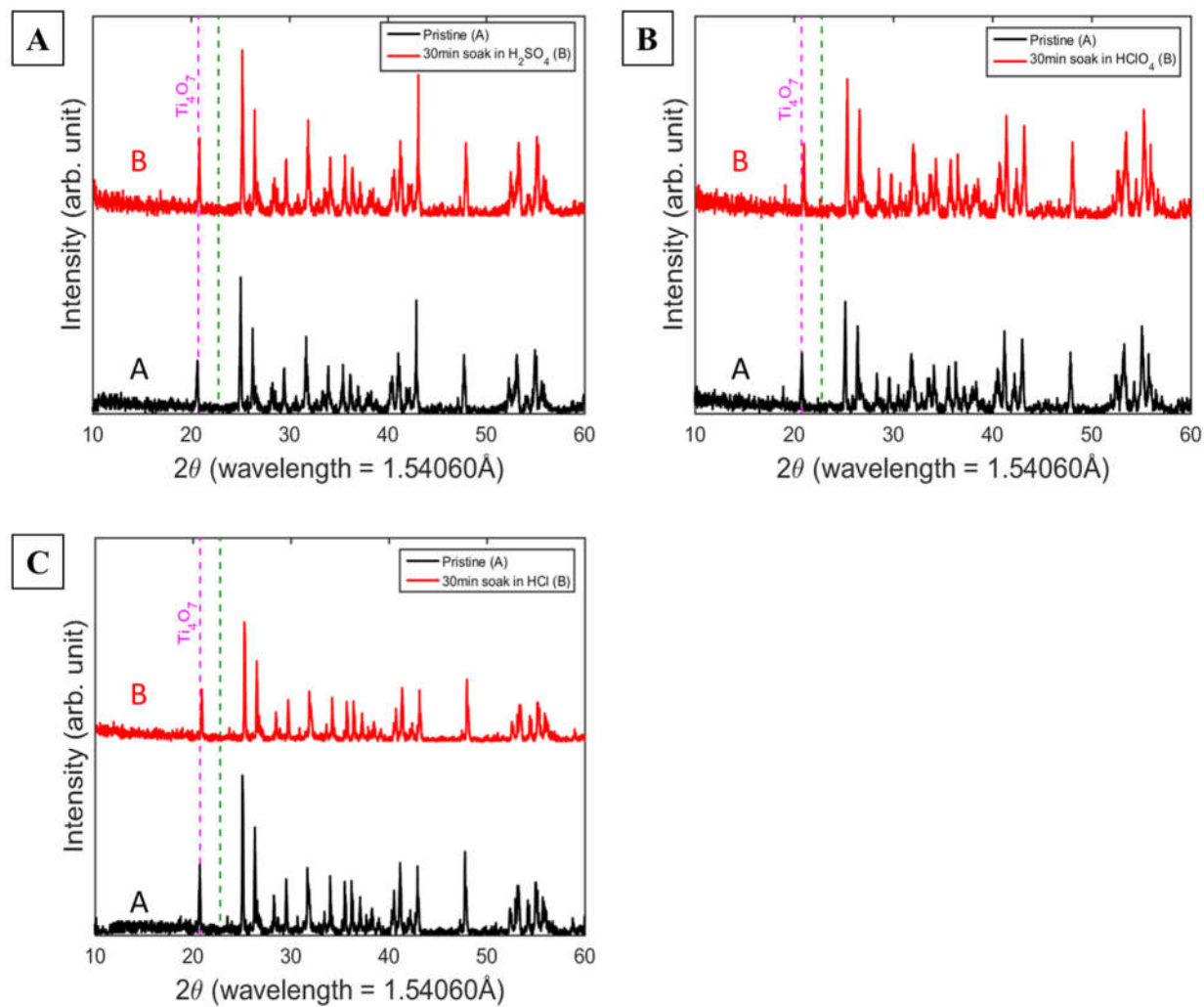


**Figure 56** XRD patterns of control samples at open circuit potential in (A) 1 M  $\text{H}_2\text{SO}_4$ , (B) 2 M  $\text{HClO}_4$ , and (C) 2 M  $\text{HCl}$ .

D.8 Electrochemical impedance spectroscopy of  $Ti_nO_{2n-1}$  at different states

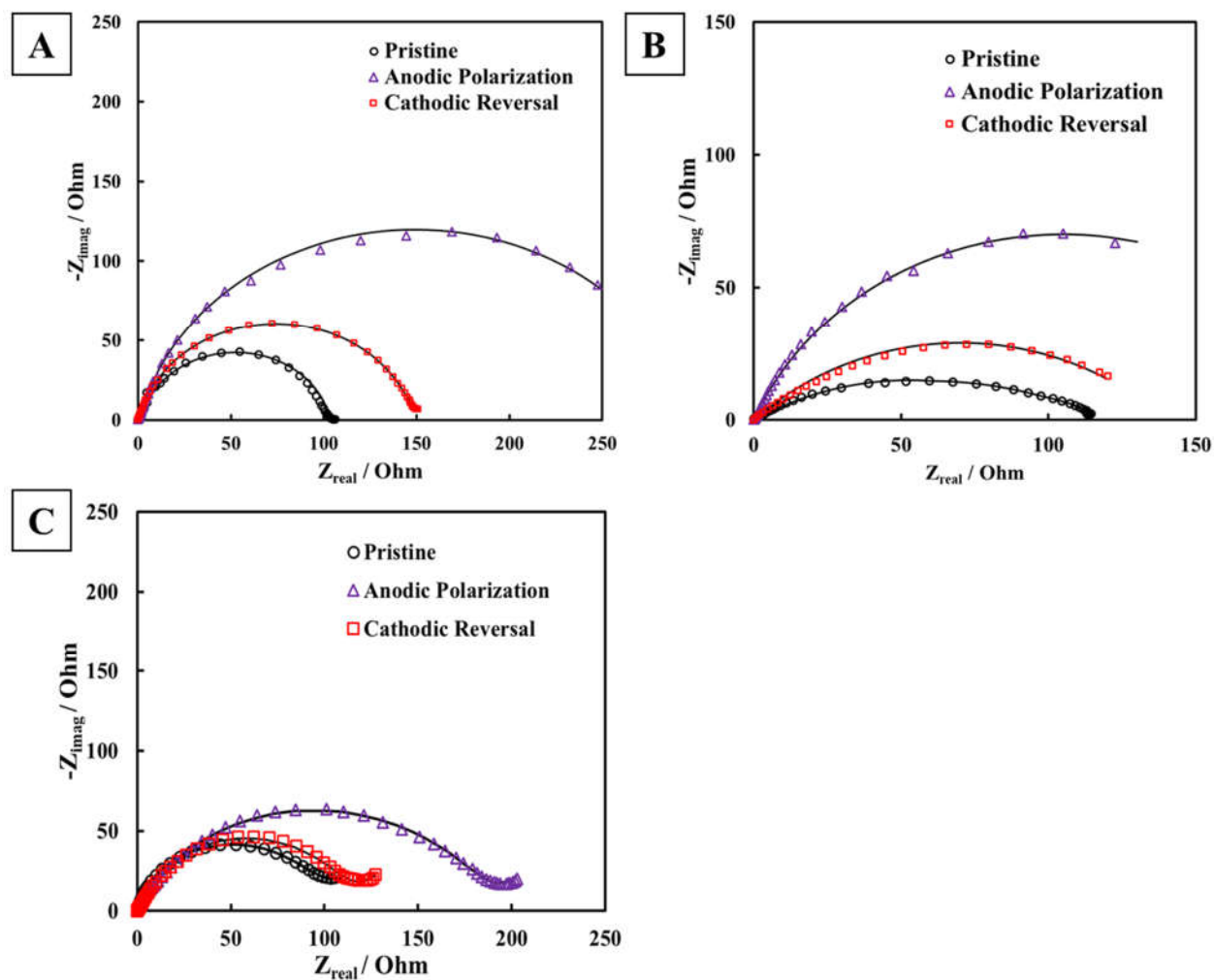


**Figure 57** Electrochemical impedance spectroscopy of  $Ti_nO_{2n-1}$  at different states in (A) 1 M  $H_2SO_4$ , (B) 2 M  $HClO_4$ , and (C) 2 M  $HCl$ . Hollow symbols and solid lines represent experimental and simulation data, respectively.

**Table XXXII** SUMMARY OF CHARGE TRANSFER RESISTANCES ( $R_{CT}$ ) OF  $Ti_NO_{2N-1}$  AT DIFFERENT STATES. ERRORS REPRESENT 95% CONFIDENCE INTERVAL

State	$R_{ct} / \Omega$		
	$H_2SO_4$	$HClO_4$	$HCl$
<b>Pristine</b>	$101.96 \pm 5.15$ (1.00)	$105.43 \pm 2.22$ (1.00)	$95.01 \pm 0.21$ (1.00)
<b>Anodic Polarization</b>	$296.14 \pm 1.58$ (2.90)	$214.62 \pm 1.15$ (2.04)	$188.39 \pm 2.06$ (1.98)
<b>Cathodic Reversal</b>	$147.04 \pm 0.22$ (1.44)	$139.61 \pm 3.13$ (1.32)	$112.22 \pm 0.70$ (1.18)

*D.9 Laser marked pattern examined by profilometer and scanning electrochemical microscope*

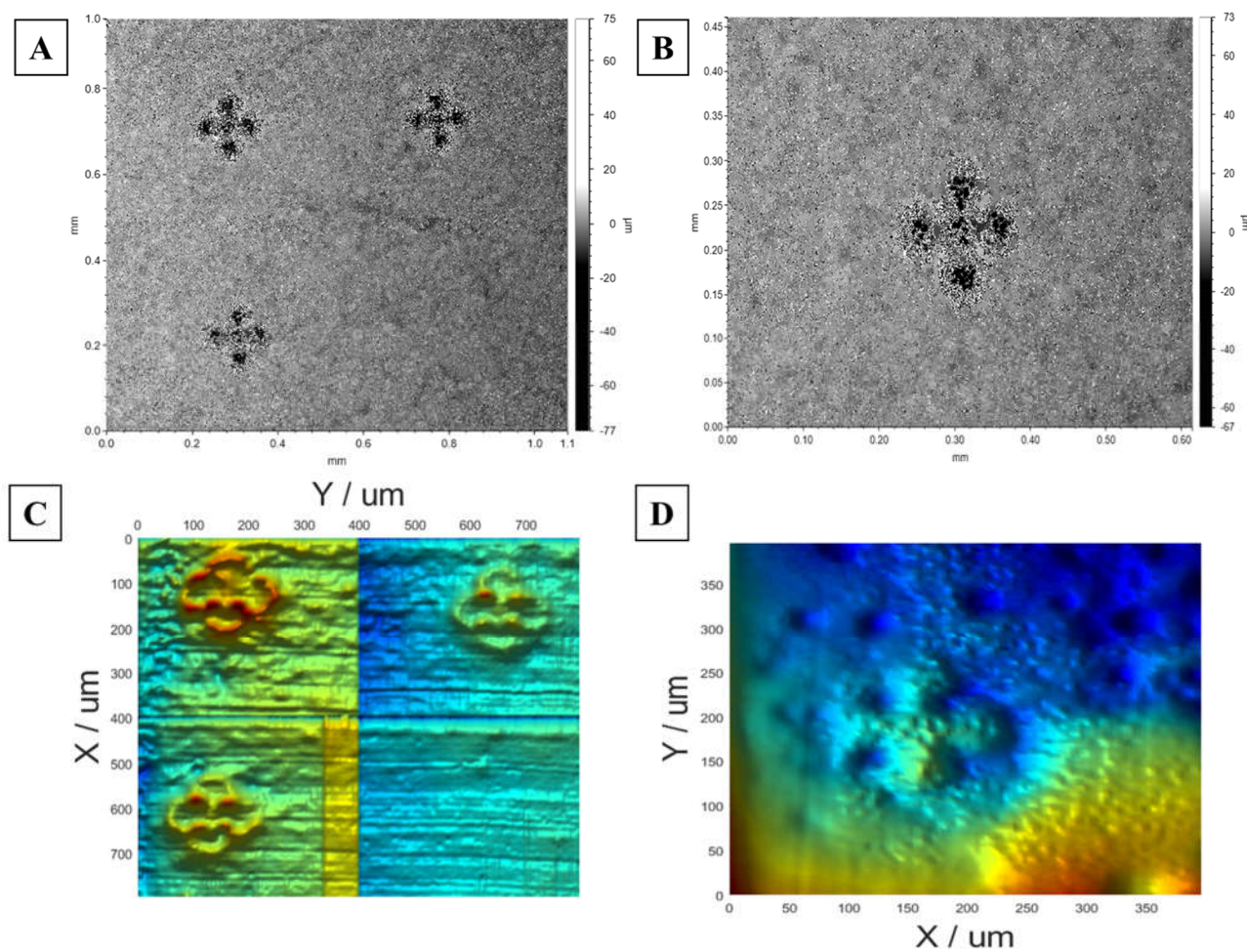


**Figure 58** Laser marked patterns shown in (A) overview by profilometer, (B) single view by profilometer, (C) overview by SECM ( $\text{Ru}(\text{NH}_3)_6\text{Cl}_3$  redox reaction), (D) single view by SECM (oxygen reduction reaction)

*D.10 Scanning electrochemical microscope imaging and kinetics for sample treated in 1 M H<sub>2</sub>SO<sub>4</sub> electrolyte*

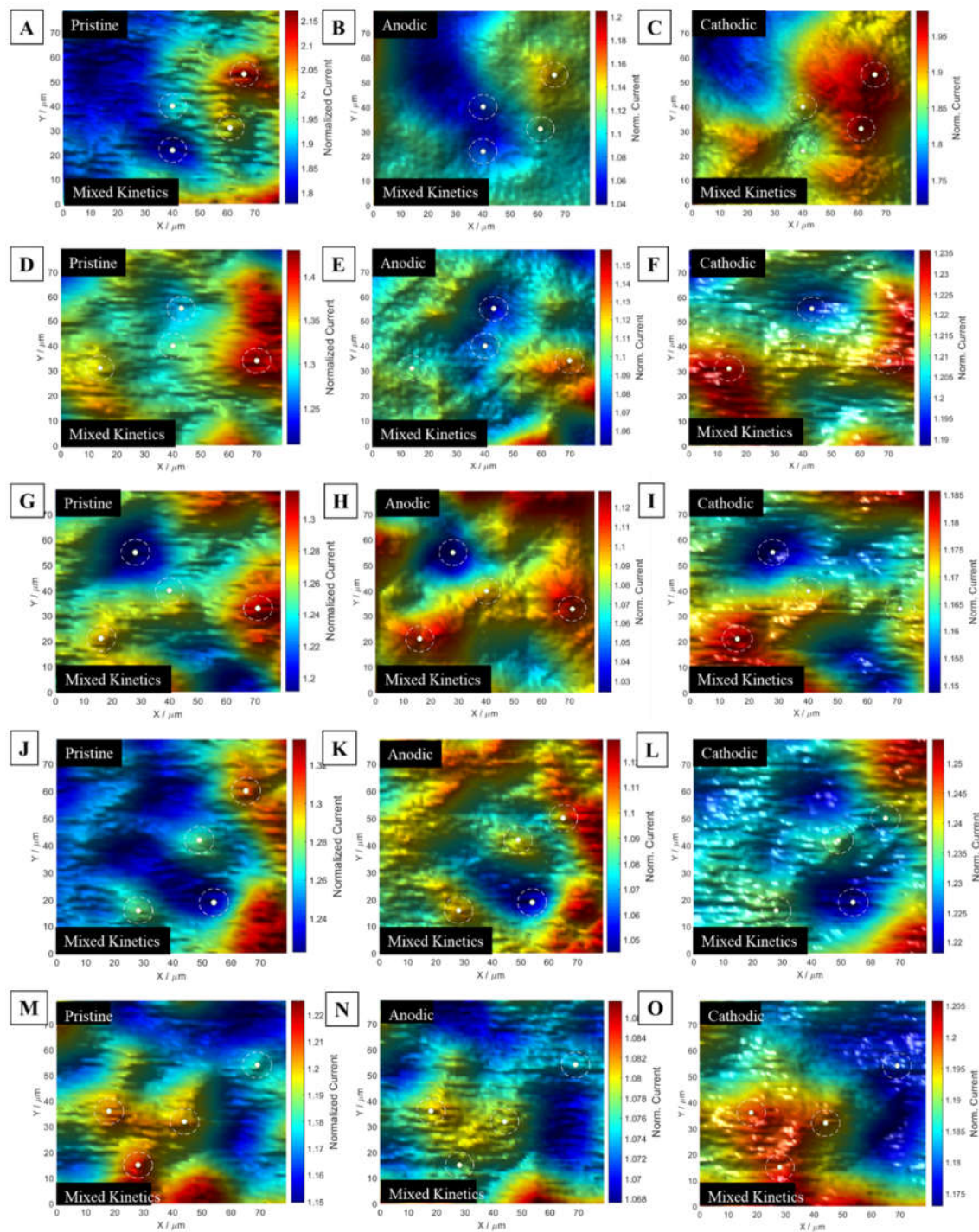


**Figure 59** SECM Images of Ti<sub>n</sub>O<sub>2n-1</sub> at different states in 1 M H<sub>2</sub>SO<sub>4</sub> electrolyte at (A)-(C) area 1, (D)-(F) area 2, (G)-(I) area 3, (J)-(L) area 4, and (M)-(O) area 5.

*D.11 Scanning electrochemical microscope imaging and kinetics for sample treated in 2 M HClO<sub>4</sub> electrolyte*

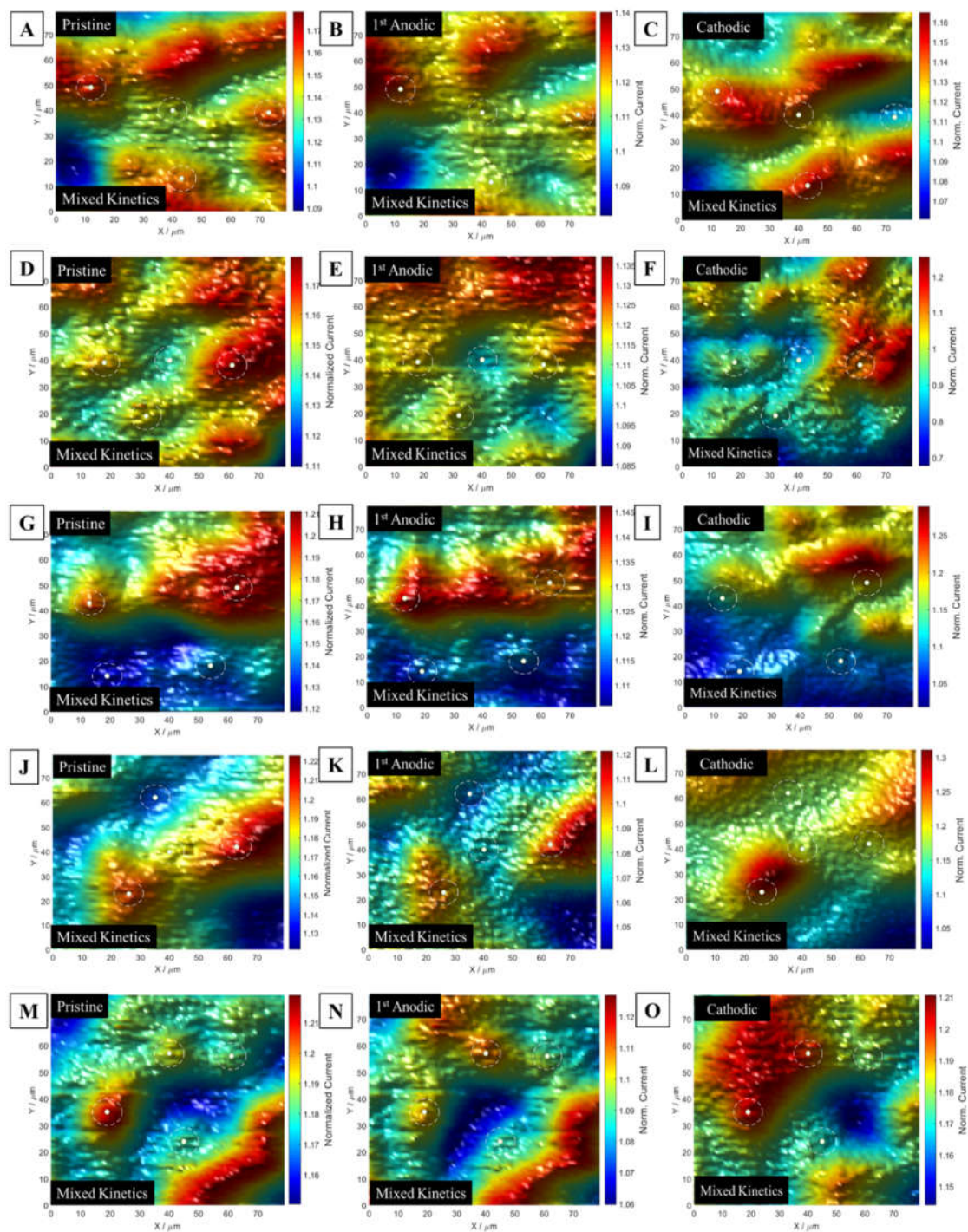


**Figure 60** SECM Images of  $Ti_nO_{2n-1}$  at different states in 2 M  $HClO_4$  electrolyte at (A)-(C) area 1, (D)-(F) area 2, (G)-(I) area 3, (J)-(L) area 4, and (M)-(O) area 5.

*D.12 Scanning electrochemical microscope imaging and kinetics for sample treated in 2 M HCl electrolyte*

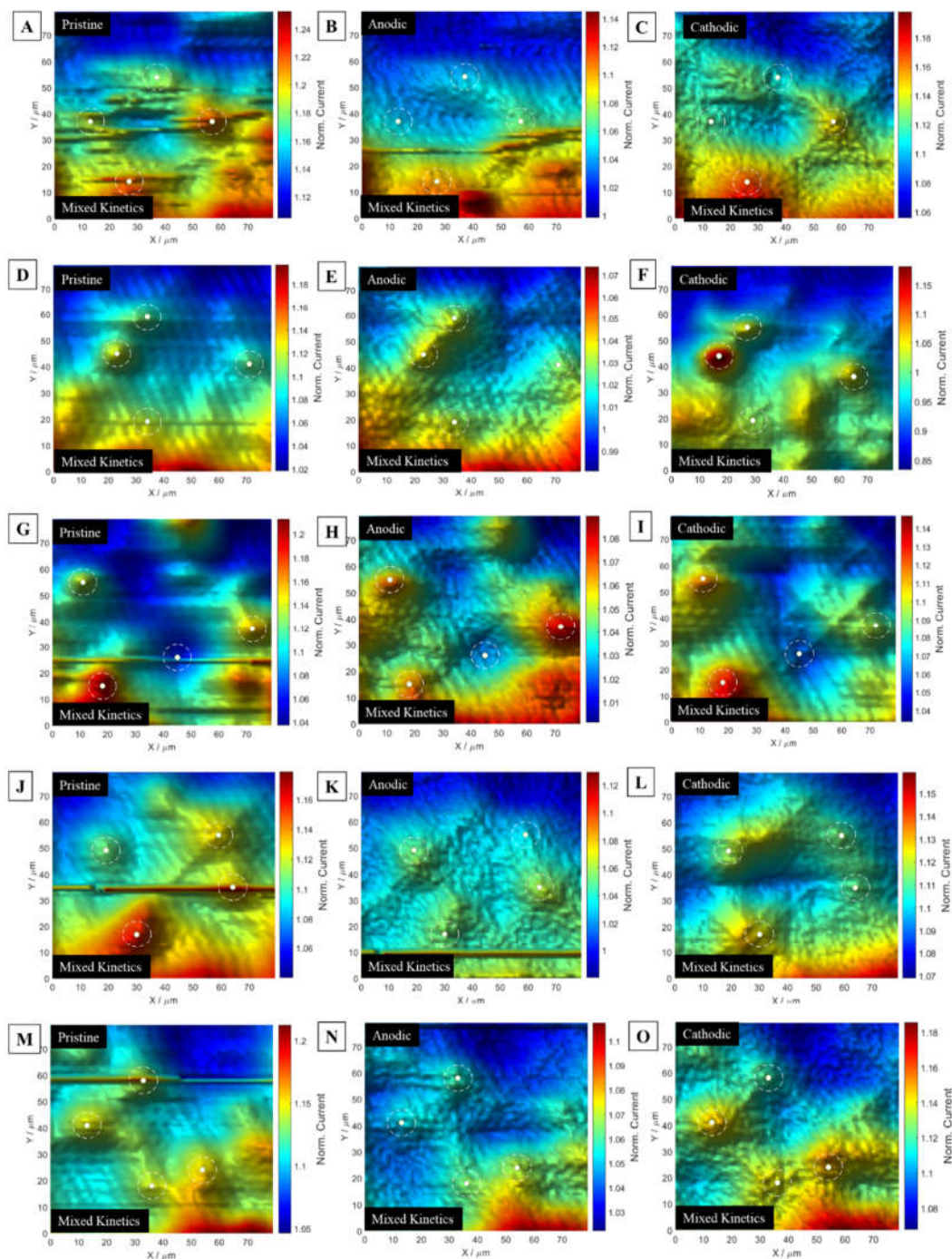


**Figure 61** SECM Images of  $\text{Ti}_n\text{O}_{2n-1}$  at different states in 2 M HCl electrolyte at (A)-(C) area 1, (D)-(F) area 2, (G)-(I) area 3, (J)-(L) area 4, and (M)-(O) area 5.

D.13 Simulation of probe approach curve to resolve localized kinetics and summary of normalized first order kinetic constants

In order to compare the localized kinetics, the probe approach curves are collected at the same spot at the pristine, post anodic and cathodic polarizations. The localized normalized first order irreversible kinetics ( $k = \frac{k_1}{Da}$ ) are obtained by fitting the probe approach curves into the Equation D-1 to D-5.

$$\bar{I}_T(L, RG, k) = \bar{I}_T^{cond} \left( L + \frac{1}{k}, RG \right) \quad D-1$$

$$+ \frac{\bar{I}_T^{ins}(L, RG) - 1}{(1 + 2.47RG^{0.31}Lk)(1 + L^{0.006RG+0.113k^{-0.0236RG+0.91})}$$

$$\bar{I}_T^{cond} = \alpha(RG) + \frac{1}{\beta(RG)} \frac{\pi}{4ArcTanL} + (1 - \alpha(RG) - \frac{1}{2\beta(RG)}) \frac{2}{\pi} ArcTanL \quad D-2$$

$$\bar{I}_T^{ins} = \left[ \frac{2.08}{RG^{0.358}} \left( L - \frac{0.145}{RG} \right) + 1.585 \right] \times \left[ \frac{2.08}{RG^{0.358}} (L + 0.0023RG) + 1.57 + \frac{\ln RG}{L} + \frac{2}{\pi RG} \ln \left( 1 + \frac{\pi RG}{2L} \right) \right]^{-1} \quad D-3$$

$$\alpha = \ln 2 + \ln 2 \left( 1 - \frac{2}{\pi} ArcCos \frac{1}{RG} \right) - \ln 2 \left[ 1 - \left( \frac{2}{\pi} ArcCos \frac{1}{RG} \right)^2 \right] \quad D-4$$

$$\beta = 1 + 0.639 \left( 1 - \frac{2}{\pi} ArcCos \frac{1}{RG} \right) - 0.186 \left[ 1 - \left( \frac{2}{\pi} ArcCos \frac{1}{RG} \right)^2 \right] \quad D-5$$

where RG is the glass ratio of UME, L is the distance between the UME tip and substrate normalized by the tip radius (5  $\mu\text{m}$  in this study).

A Matlab script is written to realize the above fitting, and the fitted normalized first order kinetic constant is reported with 95% confidence interval.

```

clear;
clc;
format long
global RG Len
exp_data = importdata('PATH_OF_THE_DATA_HERE');
Len = exp_data.data(:, 1);
i = exp_data.data(:, 2);
i_inf = max(abs(exp_data.data(:,2)));

% normalize experiment data
Len = max(Len) - Len;
i = abs(i / i_inf);

RG = 2.97;
fit_ini = 1;

[final_fit, resnorm, residual, exitflag, output, lambda, j] =
lsqcurvefit(@kinetic_control, fit_ini, Len, i);
conf = nlparci(final_fit,residual,'jacobian',j);

fit_data = kinetic_control(final_fit, Len);
Len = max(Len) - Len;
s = size(Len, 1);
intv = floor(linspace(1, s - 2, 40));

plot(Len, i, Len(intv), fit_data(intv),'o')
xlabel('Normalized Traveling Distance', 'FontSize',18)
ylabel('Normalized Current', 'FontSize',18)
set(gca, 'fontsize',14)
myLegend = legend('Experiment','Simulation', 'Location','northwest');
myLegend.FontSize = 14;

result = [final_fit, conf];

```

```

function current = kinetic_control(lambda, L )
global RG

rg = RG;

left = positive_feedback(L + 1 / lambda, rg);

right = (negative_feedback(L, rg) - 1) ./ ((1 + 2.47 * rg ^ 0.31 * L *
lambda) .* (1 + L .^ (0.006 * rg + 0.113) * lambda ^ (-0.0236 * rg +
0.91)));

current = (left + right);

end

```

```

function current = positive_feedback( l, rg )

current = alpha(rg) + pi ./ (4 * beta(rg) * atan(l)) + (1 - alpha(rg)
- 1 / (2 * beta(rg))) * 2 * atan(l) / pi;

end

```

```

function current = negative_feedback( l, rg )

up = (2.08 / rg ^ 0.358 * ( 1 - 0.145 / rg) + 1.585);
down = 2.08 / rg ^ 0.358 * (1 + 0.0023 * rg) + 1.57 + log(rg) ./ 1 + 2
/ (pi * rg) * log(1 + pi * rg / 2 ./ l);

current = up ./ down;

```

```
end
```

```
function result = alpha( rg )
```

```
result = log(2) + log(2) * (1 - 2 / pi * acos(1 / rg)) - log(2) * ( 1  
- (2 / pi * acos(1 / rg))^2);
```

```
end
```

```
function result = beta( rg )
```

```
result = 1 + 0.639 * (1 - 2 / pi * acos(1 / rg)) - 0.186 * (1 - (2 /  
pi * acos( 1 / rg))^2);
```

```
end
```

For example, probe approach curves, as shown in Figure D-13B, were collected at point 1 in Figure D-13A, at the pristine, post anodic and cathodic polarizations of  $\text{Ti}_n\text{O}_{2n-1}$ . The fitting of these curves to Equation D1 – D5 yielded the normalized first order kinetic constant  $1.22 \pm 0.0085$ ,  $1.04 \pm 0.0083$ , and  $1.23 \pm 0.0013$ .

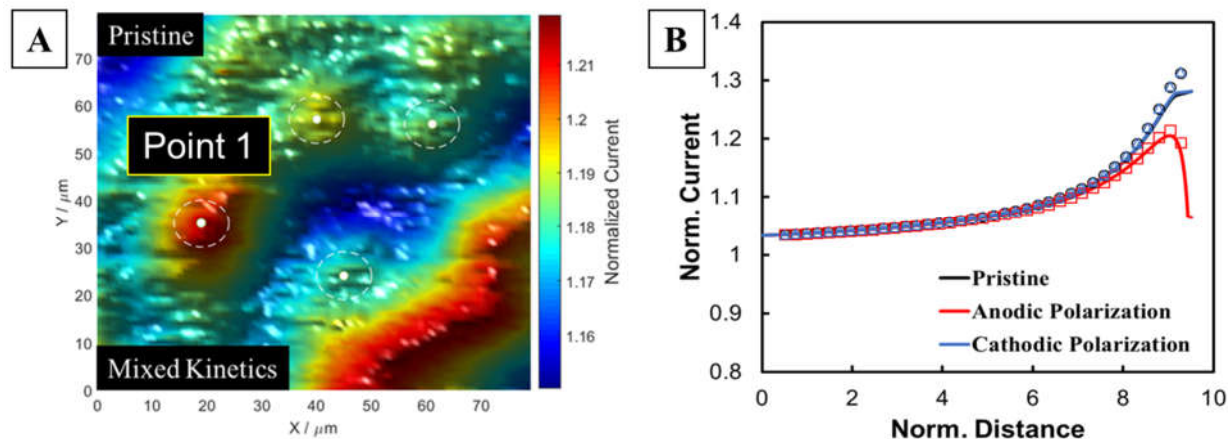


**Figure 62** (A) Image collected in 5 mM  $\text{Ru}(\text{NH}_3)_6\text{Cl}_3$  in 100 mM KCl by SECM, and (B) probe approach curve collected at point 1 at pristine, post anodic and cathodic polarizations. Solid lines and hollow points represent experimental data and simulation, respectively.

**Table XXXIII** SUMMARY OF NORMALIZED FIRST ORDER KINETIC CONSTANTS OF  $\text{Ti}_N\text{O}_{2N-1}$  TREATED IN 1 M  $\text{H}_2\text{SO}_4$  ELECTROLYTE

Area	Spot	$\text{H}_2\text{SO}_4$		
		Pristine	Anodic	Cathodic
1	40,22	1.22±0.0034	0.67±0.0021	1.17±0.0027
	40,40	1.53±0.0013	0.71±0.0011	1.49±0.0020
	61,31	1.45±0.012	0.77±0.019	1.51±0.013
	66,53	1.66±0.0019	1.22±0.010	1.51±0.0084
2	14,31	1.36±0.018	0.79±0.014	1.21±0.0018
	40,40	1.53±0.011	0.66±0.0017	1.06±0.016
	43,55	1.08±0.0075	0.71±0.0069	1.01±0.0075
	70,34	1.62±0.0072	0.89±0.0039	1.19±0.0074
3	16,21	1.29±0.013	0.89±0.019	1.01±0.012
	28,55	1.22±0.0083	0.67±0.0092	0.88±0.016
	40,40	1.57±0.012	0.75±0.0090	1.12±0.0035
	71,33	1.45±0.013	0.94±0.014	0.99±0.015
4	28,16	1.36±0.0080	0.98±0.0050	1.23±0.013
	49,42	1.62±0.0034	1.31±0.0076	1.49±0.0091
	54,19	0.97±0.0075	0.82±0.018	0.99±0.0059
	65,50	1.36±0.014	1.20±0.0053	1.27±0.017
5	18,36	1.29±0.0068	1.01±0.013	1.35±0.0097
	28,15	1.11±0.0050	0.86±0.0070	1.09±0.0077
	44,32	1.66±0.010	1.01±0.019	1.30±0.013
	69,54	0.93±0.0043	0.72±0.015	0.80±0.012

**Table XXXIV** SUMMARY OF NORMALIZED FIRST ORDER KINETIC CONSTANTS OF  $Ti_NO_{2N-1}$  TREATED IN 2 M  $HClO_4$  ELECTROLYTE

Area	Spot	$HClO_4$		
		Pristine	Anodic	Cathodic
1	12,49	1.32±0.0013	1.30±0.0067	1.33±0.024
	40,40	1.02±0.0017	0.95±0.0046	1.25±0.025
	43,13	1.36±0.0097	1.01±0.0017	1.33±0.0086
	79,39	1.30±0.0067	1.22±0.0052	0.87±0.016
2	18,39	1.17±0.0053	1.15±0.0023	1.06±0.010
	32,19	1.12±0.014	1.01±0.012	0.94±0.0093
	40,40	0.97±0.0066	0.81±0.015	0.67±0.0065
	61,38	1.08±0.017	0.83±0.0043	1.32±0.0060
3	1.24	1.24±0.0097	1.20±0.0070	1.19±0.019
	0.97	0.97±0.015	0.94±0.0084	0.87±0.011
	1.15	1.15±0.0088	1.09±0.0018	1.21±0.0082
	1.29	1.29±0.017	0.99±0.0010	1.41±0.0043
4	26,23	1.11±0.010	1.02±0.0027	1.16±0.0021
	35,62	0.79±0.0048	0.75±0.019	0.77±0.0084
	40,40	0.65±0.015	0.33±0.017	0.51±0.017
	63,42	1.32±0.0058	1.27±0.013	1.11±0.017
5	19,35	1.22±0.0085	1.04±0.0083	1.23±0.0013
	40,57	1.02±0.011	0.99±0.012	1.22±0.012
	45,24	1.66±0.016	1.57±0.019	1.64±0.0026
	61,56	1.02±0.0056	0.88±0.0039	1.10±0.0076

**Table XXXV** SUMMARY OF NORMALIZED FIRST ORDER KINETIC CONSTANTS OF  $TiN_{0.2N-1}$  TREATED IN 2 M HCL ELECTROLYTE

Area	Spot	HCl		
		Pristine	Anodic	Cathodic
1	26, 14	1.45±0.0095	1.31±0.0025	1.45±0.0074
	57, 37	1.62±0.0004	1.44±0.0004	1.65±0.015
	13, 37	1.36±0.0009	1.25±0.0018	1.30±0.011
	37, 54	1.05±0.0026	0.61±0.0050	0.97±0.018
2	23, 45	2.09±0.0023	1.79±0.0043	1.97±0.012
	34, 19	1.05±0.0086	0.48±0.0040	0.83±0.0030
	34, 59	1.66±0.0072	1.47±0.0031	1.72±0.0030
	71, 41	1.29±0.0001	1.10±0.0051	1.26±0.0081
3	18, 15	1.66±0.0014	1.44±0.0098	1.61±0.0097
	11, 55	1.11±0.0057	0.98±0.0017	0.99±0.015
	45, 26	0.79±0.0051	0.59±0.0015	0.66±0.0071
	72, 37	1.24±0.0027	0.96±0.0035	1.26±0.0074
4	64, 35	1.40±0.0081	1.28±0.0019	1.31±0.0033
	30, 17	1.40±0.0006	1.33±0.0098	1.43±0.011
	19, 49	1.22±0.0058	1.08±0.0078	1.17±0.0064
	59, 55	1.05±0.0005	0.66±0.0063	1.06±0.0032
5	33, 58	1.66±0.0035	1.42±0.0018	1.66±0.0064
	36, 18	1.48±0.0067	1.33±0.0052	1.39±0.013
	54, 24	1.48±0.0037	1.45±0.0100	1.31±0.020
	13, 41	1.48±0.0053	0.79±0.0020	1.25±0.013

*D.14 Topographic imaging by oxygen reduction reaction in scanning electrochemical microscope*

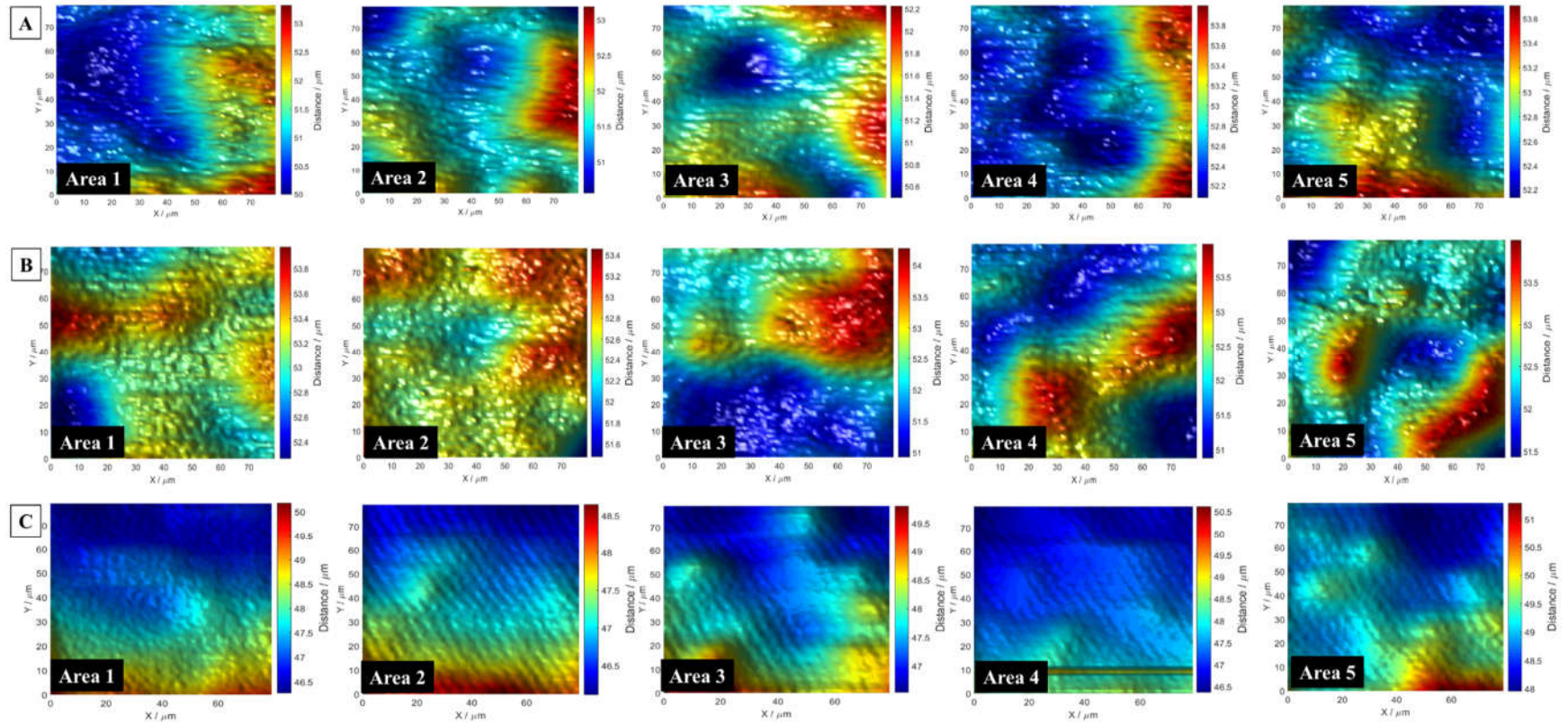


**Figure 63** Topographic images collected by oxygen reduction reaction in SECM for  $\text{Ti}_n\text{O}_{2n-1}$  samples studied in (A)  $\text{H}_2\text{SO}_4$ , (B)  $\text{HClO}_4$ , and (C)  $\text{HCl}$  cases.

D.15 *Thermogravimetric Analysis*

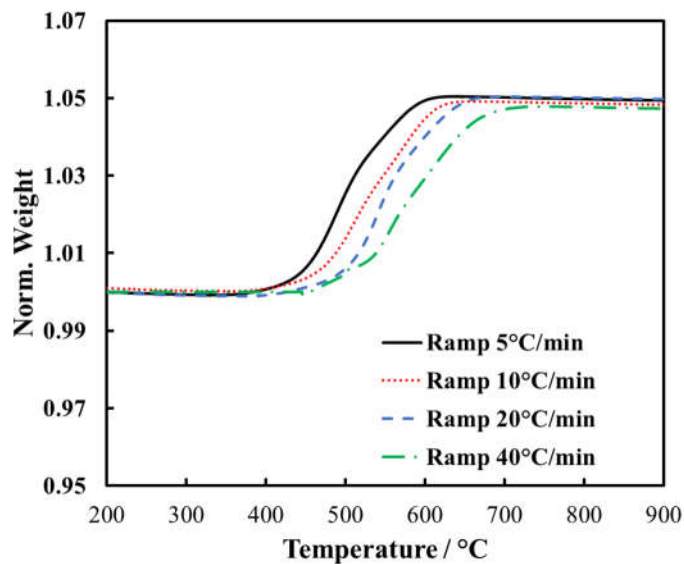


**Figure 64** Thermogravimetric analysis results of  $\text{Ti}_n\text{O}_{2n-1}$  in air at different temperature ramps

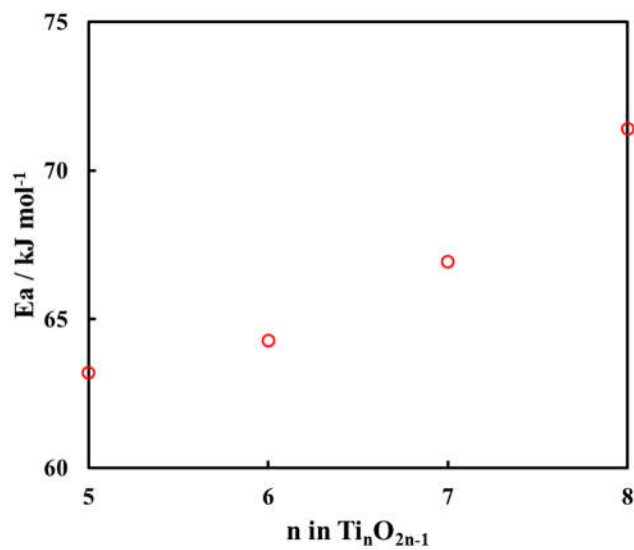


**Figure 65** Activation energy required for the conversion from  $\text{Ti}_4\text{O}_7$  to  $\text{Ti}_n\text{O}_{2n-1}$  ( $n > 4$ )

*D.16 Atomic concentration of surface composition on  $Ti_nO_{2n-1}$  treated with and without applied potential in 1 M  $H_2SO_4$  electrolyte for 30 min*

**Table XXXVI** ATOMIC CONCENTRATION OF SURFACE COMPOSITION ON  $Ti_nO_{2n-1}$  TREATED WITH AND WITHOUT APPLIED POTENTIAL IN 1 M  $H_2SO_4$  ELECTROLYTE FOR 30 MIN

	Without Applied Potential	With Applied Potential
<b>O 1s</b>	70.95	68.42
<b>Ti 2p</b>	25.43	22.3
<b>S 2p</b>	3.55	9.57

**APPENDIX E**

This Agreement between Yin Jing ("You") and Elsevier ("Elsevier") consists of your license details and the terms and conditions provided by Elsevier and Copyright Clearance Center.

License Number	4158291018412
License date	Jul 29, 2017
Licensed Content Publisher	Elsevier
Licensed Content Publication	Journal of Membrane Science
Licensed Content Title	Electrochemical impedance spectroscopy study of membrane fouling characterization at a conductive sub-stoichiometric TiO <sub>2</sub> reactive electrochemical membrane: Transmission line model development
Licensed Content Author	Yin Jing, Brian P. Chaplin
Licensed Content Date	Aug 1, 2016
Licensed Content Volume	511
Licensed Content Issue	n/a
Licensed Content Pages	12
Start Page	238
End Page	249
Type of Use	reuse in a thesis/dissertation
Intended publisher of new work	other
Portion	full article
Format	electronic
Are you the author of this Elsevier article?	Yes
Will you be translating?	No
Title of your thesis/dissertation	MECHANISTIC STUDY OF ELECTROCHEMICAL PROCESSES ON A POROUS MAGNÉLI PHASE ELECTRODE
Expected completion date	Aug 2017
Estimated size (number of pages)	238
Requestor Location	Yin Jing 810 S Clinton Street  CHICAGO, IL 60607 United States Attn: Yin Jing
Publisher Tax ID	98-0397604
Total	0.00 USD

This Agreement between Yin Jing ("You") and Elsevier ("Elsevier") consists of your license details and the terms and conditions provided by Elsevier and Copyright Clearance Center.

License Number	4158290893379
License date	Jul 29, 2017
Licensed Content Publisher	Elsevier
Licensed Content Publication	Journal of Membrane Science
Licensed Content Title	Electrochemical impedance spectroscopy study of membrane fouling and electrochemical regeneration at a sub-stoichiometric TiO <sub>2</sub> reactive electrochemical membrane
Licensed Content Author	Yin Jing, Lun Guo, Brian P. Chaplin
Licensed Content Date	Jul 15, 2016
Licensed Content Volume	510
Licensed Content Issue	n/a
Licensed Content Pages	14
Start Page	510
End Page	523
Type of Use	reuse in a thesis/dissertation
Intended publisher of new work	other
Portion	full article
Format	electronic
Are you the author of this Elsevier article?	Yes
Will you be translating?	No
Title of your thesis/dissertation	MECHANISTIC STUDY OF ELECTROCHEMICAL PROCESSES ON A POROUS MAGNÉLI PHASE ELECTRODE
Expected completion date	Aug 2017
Estimated size (number of pages)	238
Requestor Location	Yin Jing 810 S Clinton Street  CHICAGO, IL 60607 United States Attn: Yin Jing
Publisher Tax ID	98-0397604
Total	0.00 USD



**Title:** Mechanistic Study of the Validity of Using Hydroxyl Radical Probes To Characterize Electrochemical Advanced Oxidation Processes

**Author:** Yin Jing, Brian P. Chaplin

**Publication:** Environmental Science & Technology

**Publisher:** American Chemical Society

**Date:** Feb 1, 2017

Copyright © 2017, American Chemical Society

Logged in as:

Yin Jing

Account #:  
3001178096

[LOGOUT](#)

### PERMISSION/LICENSE IS GRANTED FOR YOUR ORDER AT NO CHARGE

This type of permission/license, instead of the standard Terms & Conditions, is sent to you because no fee is being charged for your order. Please note the following:

- Permission is granted for your request in both print and electronic formats, and translations.
- If figures and/or tables were requested, they may be adapted or used in part.
- Please print this page for your records and send a copy of it to your publisher/graduate school.
- Appropriate credit for the requested material should be given as follows: "Reprinted (adapted) with permission from (COMPLETE REFERENCE CITATION). Copyright (YEAR) American Chemical Society." Insert appropriate information in place of the capitalized words.
- One-time permission is granted only for the use specified in your request. No additional uses are granted (such as derivative works or other editions). For any other uses, please submit a new request.

## CITED LITERATURE

- [1] C.J. Vörösmarty, P. Green, J. Salisbury, R.B. Lammers, Global Water Resources: Vulnerability from Climate Change and Population Growth, Science (80-. ). 289 (2000).
- [2] S. Zaman, S. Yeasmin, Y. Inatsu, C. Ananchaipattana, M.L. Bari, Low-cost sustainable technologies for the production of clean drinking water — a review, J. Environ. Prot. (Irvine., Calif), 5 (2014) 42–53.
- [3] M. LeChevallier, K. Au, Water treatment and pathogen control, 2004.
- [4] T. Leiknes, The effect of coupling coagulation and flocculation with membrane filtration in water treatment: A review, J. Environ. Sci. 21 (2009) 8–12.
- [5] A. Matilainen, M. Vepsäläinen, M. Sillanpää, Natural organic matter removal by coagulation during drinking water treatment: a review, Adv. Colloid. (2010).
- [6] J. Edzwald, Coagulation in drinking water treatment: particles, organics and coagulants, Water Sci. Technol. (1993).
- [7] J.C. Crittenden, R.R. Trussell, D.W. Hand, K.J. Howe, G. Tchobanoglous, MWH's Water Treatment: Principles and Design, John Wiley & Sons, 2012.
- [8] N. Tzoupanos, A. Zouboulis, Coagulation-flocculation processes in water/wastewater treatment: the application of new generation of chemical reagents, 6th IASME/WSEAS Int. (2008).
- [9] N. Porcelli, S. Judd, Chemical cleaning of potable water membranes: A review, Sep. Purif. Technol. 71 (2010) 137–143.
- [10] Q. Li, M. Elimelech, Organic fouling and chemical cleaning of nanofiltration membranes: measurements and mechanisms., Environ. Sci. Technol. 38 (2004) 4683–93.
- [11] A. Lim, Membrane fouling and cleaning in microfiltration of activated sludge wastewater, J. Memb. Sci. 216 (2003) 279–290.
- [12] Y. Ye, P. Le Clech, V. Chen, A.G. Fane, Evolution of fouling during crossflow filtration of model EPS solutions, J. Memb. Sci. 264 (2005) 190–199.
- [13] J.K. Dunnick, R.L. Melnick, Assessment of the Carcinogenic Potential of Chlorinated Water: Experimental Studies of Chlorine, Chloramine, and Trihalomethanes, JNCI J. Natl. Cancer Inst. 85 (1993) 817–822.
- [14] F. Pacheco-Torgal, S. Jalali, Nanotechnology: Advantages and drawbacks in the field of construction and building materials, Constr. Build. Mater. 25 (2011) 582–590.
- [15] L.Y.C. Leong, J. Kuo, C.-C. Tang, Disinfection of Wastewater Effluent - Comparison of Alternative Technologies, 1st ed., Water Environment Research Foundation, 2008.
- [16] B. Kasprzyk-Hordern, M. Ziółek, J. Nawrocki, Catalytic ozonation and methods of enhancing molecular ozone reactions in water treatment, Appl. Catal. B Environ. 46 (2003) 639–669.

- [17] F. Fiessinger, Y. Richard, A. Montiel, P. Musquere, Advantages and disadvantages of chemical oxidation and disinfection by ozone and chlorine dioxide, Stud. Environ. Sci. 12 (1981) 245–261.
- [18] H. Wenzel, H. Larsen, J. Clauson-Kaas, Weighing environmental advantages and disadvantages of advanced wastewater treatment of micro-pollutants using environmental life cycle assessment, Water Sci. (2008).
- [19] B.P. Chaplin, Critical review of electrochemical advanced oxidation processes for water treatment applications., Environ. Sci. Process. Impacts. 1 (2014) 1182–1203.
- [20] S. Garcia-Segura, E. Brillas, Mineralization of the recalcitrant oxalic and oxamic acids by electrochemical advanced oxidation processes using a boron-doped diamond anode., Water Res. 45 (2011) 2975–84.
- [21] I. Tröster, I., Recent developments in production and application of DiaChem®-electrodes for wastewater treatment, New Diam. Front. Carbon Technol. 12 (2002) 89–97.
- [22] I. Tröster, M. Fryda, D. Herrmann, L. Schäfer, W. Hänni, A. Perret, M. Blaschke, A. Kraft, M. Stadelmann, Electrochemical advanced oxidation process for water treatment using DiaChem® electrodes, Diam. Relat. Mater. 11 (2002) 640–645.
- [23] J. Boudreau, D. Bejan, S. Li, N.J. Bunce, Competition between Electrochemical Advanced Oxidation and Electrochemical Hypochlorination of Sulfamethoxazole at a Boron-Doped Diamond Anode, Ind. Eng. Chem. Res. 49 (2010) 2537–2542.
- [24] A. Kraft, M. Stadelmann, M. Blaschke, Anodic oxidation with doped diamond electrodes: a new advanced oxidation process, J. Hazard. Mater. 103 (2003) 247–261.
- [25] E. Guinea, C. Arias, P.L. Cabot, J.A. Garrido, R.M. Rodríguez, F. Centellas, E. Brillas, Mineralization of salicylic acid in acidic aqueous medium by electrochemical advanced oxidation processes using platinum and boron-doped diamond as anode and cathodically generated hydrogen peroxide., Water Res. 42 (2008) 499–511.
- [26] M. Pimentel, N. Oturan, M. Dezotti, M.A. Oturan, Phenol degradation by advanced electrochemical oxidation process electro-Fenton using a carbon felt cathode, Appl. Catal. B Environ. 83 (2008) 140–149.
- [27] A.M. Zaky, B.P. Chaplin, Porous substoichiometric TiO<sub>2</sub> anodes as reactive electrochemical membranes for water treatment., Environ. Sci. Technol. 47 (2013) 6554–63.
- [28] L. Guo, Y. Jing, B.P. Chaplin, Development and Characterization of Ultrafiltration TiO<sub>2</sub> Magnéli Phase Reactive Electrochemical Membranes, Environ. Sci. Technol. 50 (2016) 1428–1436.
- [29] M.C. Santos, Y.A. Elabd, Y. Jing, B.P. Chaplin, L. Fang, Highly porous Ti<sub>4</sub>O<sub>7</sub> reactive electrochemical water filtration membranes fabricated *via* electrospinning/electrospraying, AIChE J. 62 (2016) 508–524.
- [30] A. Salahi, M. Abbasi, T. Mohammadi, Permeate flux decline during UF of oily wastewater: Experimental and modeling, Desalination. 251 (2010) 153–160.
- [31] J.M. Kavanagh, S. Hussain, T.C. Chilcott, H.G.L. Coster, Fouling of reverse osmosis membranes

- using electrical impedance spectroscopy: Measurements and simulations, Desalination, 236 (2009) 187–193.
- [32] M. Taniguchi, J.E. Kilduff, G. Belfort, Modes of Natural Organic Matter Fouling during Ultrafiltration, Environ. Sci. Technol. 37 (2003) 1676–1683.
- [33] A. Antony, J.H. Low, S. Gray, A.E. Childress, P. Le-Clech, G. Leslie, Scale formation and control in high pressure membrane water treatment systems: A review, J. Memb. Sci. 383 (2011) 1–16.
- [34] E.M.V. Hoek, J. Allred, T. Knoell, B.-H. Jeong, Modeling the effects of fouling on full-scale reverse osmosis processes, J. Memb. Sci. 314 (2008) 33–49.
- [35] a. W. Zularisam, a. F. Ismail, R. Salim, Behaviours of natural organic matter in membrane filtration for surface water treatment — a review, Desalination, 194 (2006) 211–231.
- [36] J.C. Chen, Q. Li, M. Elimelech, *In situ* monitoring techniques for concentration polarization and fouling phenomena in membrane filtration., Adv. Colloid Interface Sci. 107 (2004) 83–108.
- [37] T. Thorsen, Concentration polarisation by natural organic matter (NOM) in NF and UF, J. Memb. Sci. 233 (2004) 79–91.
- [38] N. Hilal, O.O. Ogunbiyi, N.J. Miles, R. Nigmatullin, Methods Employed for Control of Fouling in MF and UF Membranes: A Comprehensive Review, Sep. Sci. Technol. 40 (2005) 1957–2005.
- [39] Y. Kaiya, Y. Itoh, K. Fujita, S. Takizawa, Study on fouling materials in the membrane treatment process for potable water, Desalination, 106 (1996) 71–77.
- [40] S. Peldszus, C. Hallé, R.H. Peiris, M. Hamouda, X. Jin, R.L. Legge, H. Budman, C. Moresoli, P.M. Huck, Reversible and irreversible low-pressure membrane foulants in drinking water treatment: Identification by principal component analysis of fluorescence EEM and mitigation by biofiltration pretreatment, Water Res. 45 (2011) 5161–5170.
- [41] C. Duclos-Orsello, W. Li, C.C. Ho, A three mechanism model to describe fouling of microfiltration membranes, J. Memb. Sci. 280 (2006) 856–866.
- [42] J. Cho, G. Amy, J. Pellegrino, Membrane filtration of natural organic matter: factors and mechanisms affecting rejection and flux decline with charged ultrafiltration (UF) membrane, J. Memb. Sci. 164 (2000) 89–110.
- [43] W. Yuan, A. Kocic, A.L. Zydney, Analysis of humic acid fouling during microfiltration using a pore blockage–cake filtration model, J. Memb. Sci. 198 (2002) 51–62.
- [44] W. Yuan, A.L. Zydney, Humic acid fouling during microfiltration, J. Memb. Sci. 157 (1999) 1–12.
- [45] K. Katsoufidou, S.G. Yiantsios, a. J. Karabelas, A study of ultrafiltration membrane fouling by humic acids and flux recovery by backwashing: Experiments and modeling, J. Memb. Sci. 266 (2005) 40–50.
- [46] K. Ruohomäki, M. Nyström, Fouling of ceramic capillary filters in vacuum filtration of humic acid, Filtr. Sep. 37 (2000) 51–57.

- [47] K.J. Jim, A.G. Fane, C.J.D. Fell, D.C. Joy, Fouling mechanisms of membranes during protein ultrafiltration, *J. Memb. Sci.* 68 (1992) 79–91.
- [48] H.Y. Ng, T.W. Tan, S.L. Ong, Membrane Fouling of Submerged Membrane Bioreactors: Impact of Mean Cell Residence Time and the Contributing Factors, *Environ. Sci. Technol.* 40 (2006) 2706–2713.
- [49] B.J. James, Y. Jing, X. Dong Chen, Membrane fouling during filtration of milk—a microstructural study, *J. Food Eng.* 60 (2003) 431–437.
- [50] M. Herzberg, M. Elimelech, Biofouling of reverse osmosis membranes: Role of biofilm-enhanced osmotic pressure, *J. Memb. Sci.* 295 (2007) 11–20.
- [51] D. Wu, H. You, D. Jin, X. Li, Enhanced inactivation of *Escherichia coli* with Ag-coated TiO<sub>2</sub> thin film under UV-C irradiation, *J. Photochem. Photobiol. A Chem.* 217 (2011) 177–183.
- [52] S. Robinson, S.Z. Abdullah, P. Bérubé, L.-C. Pierre, Ageing of Membranes For Water Treatment: Linking Changes to Performance, *J. Memb. Sci.* 503 (2015) 177–187.
- [53] M.. Purkait, S. DasGupta, S. De, Resistance in series model for micellar enhanced ultrafiltration of eosin dye, *J. Colloid Interface Sci.* 270 (2004) 496–506.
- [54] P. Rai, C. Rai, G. Majumdar, S. DasGupta, Resistance in series model for ultrafiltration of mosambi (*Citrus sinensis* (L.) Osbeck) juice in a stirred continuous mode, *J. Membr.* (2006).
- [55] H. Choi, K. Zhang, D.D. Dionysiou, D.B. Oerther, G.A. Sorial, Influence of cross-flow velocity on membrane performance during filtration of biological suspension, *J. Memb. Sci.* 248 (2005) 189–199.
- [56] J. HERMIA, Constant Pressure Blocking Filtration Law Application to Powder-Law Non-Newtonian Fluid, *Trans. Inst. Chem. Eng.* 60 (1982) 183–187.
- [57] Y. Ye, P. Le Clech, V. Chen, A.G. Fane, B. Jefferson, Fouling mechanisms of alginate solutions as model extracellular polymeric substances, *Desalination.* 175 (2005) 7–20.
- [58] J. Li, D.K. Hallbauer, R.D. Sanderson, Direct monitoring of membrane fouling and cleaning during ultrafiltration using a non-invasive ultrasonic technique, *J. Memb. Sci.* 215 (2003) 33–52.
- [59] J. Li, R.D. Sanderson, E.P. Jacobs, Non-invasive visualization of the fouling of microfiltration membranes by ultrasonic time-domain reflectometry, *J. Memb. Sci.* 201 (2002) 17–29.
- [60] A. Lasia, Modeling of impedance of porous electrodes, *Model. Numer. Simulations.* 43 (2009) 67–137.
- [61] H.G.L. Coster, K.J. Kim, K. Dahlan, J.R. Smith, C.J.D. Fell, Characterisation of ultrafiltration membranes by impedance spectroscopy. I. Determination of the separate electrical parameters and porosity of the skin and sublayers, *J. Memb. Sci.* 66 (1992) 19–26.
- [62] H.G.L. Coster, T.C. Chilcott, A.C.F. Coster, Impedance spectroscopy of interfaces, membranes and ultrastructures, *Bioelectrochemistry Bioenerg.* 40 (1996) 79–98.
- [63] T.C. Chilcott, M. Chan, L. Gaedt, L. Gaedt, T.C. Chilcott, T.C. Chilcott, M. Chan, M. Chan, T.

- Nantawisarakul, T. Nantawisarakul, a G. Fane, a G. Fane, Electrical impedance spectroscopy characterisation of conducting membranes: I. Theory, J. Memb. Sci. 195 (2002) 153–167.
- [64] A. Antony, T. Chilcott, H. Coster, G. Leslie, *In situ* structural and functional characterization of reverse osmosis membranes using electrical impedance spectroscopy, J. Memb. Sci. 425–426 (2013) 89–97.
- [65] Y. Gao, W. Li, W.C.L. Lay, H.G.L. Coster, A.G. Fane, C.Y. Tang, Characterization of forward osmosis membranes by electrochemical impedance spectroscopy, Desalination. 312 (2013) 45–51.
- [66] Y. Xu, M. Wang, Z. Ma, C. Gao, Electrochemical impedance spectroscopy analysis of sulfonated polyethersulfone nanofiltration membrane, Desalination. 271 (2011) 29–33.
- [67] S. Bannwarth, M. Darestani, H. Coster, M. Wessling, Characterization of hollow fiber membranes by impedance spectroscopy, J. Memb. Sci. 473 (2015) 318–326.
- [68] S. Bannwarth, T. Trieu, C. Oberschelp, M. Wessling, On-line monitoring of cake layer structure during fouling on porous membranes by *in situ* electrical impedance analysis, J. Memb. Sci. 503 (2016) 188–198.
- [69] Richard W. Baker, Membrane Technology and Applications, 2nd Edition, Membr. Technol. Appl. (2004).
- [70] K. Katsoufidou, S.G. Yiantsios, a. J. Karabelas, Experimental study of ultrafiltration membrane fouling by sodium alginate and flux recovery by backwashing, J. Memb. Sci. 300 (2007) 137–146.
- [71] A. V. Dudchenko, J. Rolf, K. Russell, W. Duan, D. Jassby, Organic fouling inhibition on electrically conducting carbon nanotube–polyvinyl alcohol composite ultrafiltration membranes, J. Memb. Sci. 468 (2014) 1–10.
- [72] K.S. Kim, K.H. Lee, K. Cho, C.E. Park, Surface modification of polysulfone ultrafiltration membrane by oxygen plasma treatment, J. Memb. Sci. 199 (2002) 135–145.
- [73] A. Nabe, Surface modification of polysulfone ultrafiltration membranes and fouling by BSA solutions, J. Memb. Sci. 133 (1997) 57–72.
- [74] G. Gao, Q. Zhang, Z. Hao, C.D. Vecitis, Carbon nanotube membrane stack for flow-through sequential regenerative electro-Fenton, Environ. Sci. Technol. 49 (2015) 2375–2383.
- [75] Q. Zhang, C.D. Vecitis, Conductive CNT-PVDF membrane for capacitive organic fouling reduction, J. Memb. Sci. 459 (2014) 143–156.
- [76] Y. Liu, H. Liu, Z. Zhou, T. Wang, C.N. Ong, C.D. Vecitis, Degradation of the Common Aqueous Antibiotic Tetracycline using a Carbon Nanotube Electrochemical Filter., Environ. Sci. Technol. 49 (2015) 7974–80.
- [77] N. Rabaaoui, M.S. Allagui, Anodic oxidation of salicylic acid on BDD electrode: Variable effects and mechanisms of degradation, J. Hazard. Mater. 243 (2012) 187–192.
- [78] J.-F. Zhi, H.-B. Wang, T. Nakashima, T.N. Rao, A. Fujishima, Electrochemical incineration of organic pollutants on boron-doped diamond electrode. Evidence for direct electrochemical

- oxidation pathway, J. Phys. Chem. B. 107 (2003) 13389–13395.
- [79] O. Azizi, D. Hubler, G. Schrader, J. Farrell, B.P. Chaplin, Mechanism of perchlorate formation on boron-doped diamond film anodes, Environ. Sci. Technol. 45 (2011) 10582–10590.
- [80] J. Iniesta, Electrochemical oxidation of phenol at boron-doped diamond electrode, Electrochim. Acta. 46 (2001) 3573–3578.
- [81] D. Bejan, E. Guinea, N.J. Bunce, On the nature of the hydroxyl radicals produced at boron-doped diamond and Ebonex® anodes, Electrochim. Acta. 69 (2012) 275–281.
- [82] S. Ai, Q. Wang, H. Li, L. Jin, Study on production of free hydroxyl radical and its reaction with salicylic acid at lead dioxide electrode, J. Electroanal. Chem. 578 (2005) 223–229.
- [83] N. Belhadj Tahar, Mechanistic Aspects of Phenol Electrochemical Degradation by Oxidation on a Ta/PbO<sub>2</sub> Anode, J. Electrochem. Soc. 145 (1998) 3427.
- [84] R. Kötzt, S. Stucki, B. Carcer, Electrochemical waste water treatment using high overvoltage anodes. Part I: Physical and electrochemical properties of SnO<sub>2</sub> anodes, J. Appl. Electrochem. 21 (1991) 14–20.
- [85] C. Comninellis, C. Pulgarin, Electrochemical oxidation of phenol for wastewater treatment using SnO<sub>2</sub>, anodes, J. Appl. Electrochem. 23 (1993) 108–112.
- [86] X. Zhao, J. Qu, H. Liu, C. Hu, Photoelectrocatalytic degradation of triazine-containing azo dyes at gamma-Bi<sub>2</sub>MoO<sub>6</sub> film electrode under visible light irradiation (lambda > 420 nm), Environ. Sci. Technol. 41 (2007) 6802–7.
- [87] Y. Nosaka, S. Komori, K. Yawata, T. Hirakawa, A.Y. Nosaka, Photocatalytic ·OH radical formation in TiO<sub>2</sub> aqueous suspension studied by several detection methods, Phys. Chem. Chem. Phys. 5 (2003) 4731–4735.
- [88] K.W. Kim, E.H. Lee, Y.J. Kim, M.H. Lee, K.H. Kim, D.W. Shin, A relation between the non-stoichiometry and hydroxyl radical generated at photocatalytic TiO<sub>2</sub> on 4CP decomposition, J. Photochem. Photobiol. A Chem. 159 (2003) 301–310.
- [89] Y. Cong, Z. Wu, Y. Li, Hydroxyl radical electrochemically generated with water as the complete atom source and its environmental application, Chinese Sci. Bull. 52 (2007) 1432–1435.
- [90] B. Marselli, J. Garcia-Gomez, P.-A. Michaud, M. a. Rodrigo, C. Comninellis, Electrogeneration of Hydroxyl Radicals on Boron-Doped Diamond Electrodes, J. Electrochem. Soc. 150 (2003) D79.
- [91] J. Cao, H. Zhao, F. Cao, J. Zhang, C. Cao, Electrocatalytic degradation of 4-chlorophenol on F-doped PbO<sub>2</sub> anodes, Electrochim. Acta. 54 (2009) 2595–2602.
- [92] U. Jurva, H. V. Wikström, A.P. Bruins, Electrochemically assisted Fenton reaction: Reaction of hydroxyl radicals with xenobiotics followed by on-line analysis with high-performance liquid chromatography/tandem mass spectrometry, Rapid Commun. Mass Spectrom. 16 (2002) 1934–1940.
- [93] J. Moore, J.-J.J. Yin, L.L. Yu, Novel fluorometric assay for hydroxyl radical scavenging capacity

- (HOSC) estimation., J. Agric. Food Chem. 54 (2006) 617–626.
- [94] E. Finkelstein, G.M. Rosen, E.J. Rauckman, Spin trapping. Kinetics of the reaction of superoxide and hydroxyl radicals with nitrones, J. Am. Chem. Soc. 102 (1980) 4994–4999.
- [95] S. Rafat Husain, J. Cillard, P. Cillard, Hydroxyl radical scavenging activity of flavonoids, Phytochemistry. 26 (1987) 2489–2491.
- [96] M.G. Steiner, C.F. Babbs, Quantitation of the hydroxyl radical by reaction with dimethyl sulfoxide, Arch. Biochem. Biophys. 278 (1990) 478–481.
- [97] S. Fukui, Y. Hanasaki, S. Ogawa, High-performance liquid chromatographic determination of methanesulphonic acid as a method for the determination of hydroxyl radicals, J. Chromatogr. A. 630 (1993) 187–193.
- [98] X.-F. Yang, X.-Q. Guo, Study of nitroxide-linked naphthalene as a fluorescence probe for hydroxyl radicals, Anal. Chim. Acta. 434 (2001) 169–177.
- [99] C.D. Jaeger, A.J. Bard, Spin trapping and electron spin resonance detection of radical intermediates in the photodecomposition of water at titanium dioxide particulate systems, J. Phys. Chem. 83 (1979) 3146–3152.
- [100] M. Rueffer, D. Bejan, N.J.N. Bunce, Graphite: An active or an inactive anode?, Electrochim. Acta. 56 (2011) 2246–2253.
- [101] H. Czili, A. Horváth, Applicability of coumarin for detecting and measuring hydroxyl radicals generated by photoexcitation of TiO<sub>2</sub> nanoparticles, Appl. Catal. B Environ. 81 (2008) 295–302.
- [102] Q. Xiang, J. Yu, P.K. Wong, Quantitative characterization of hydroxyl radicals produced by various photocatalysts., J. Colloid Interface Sci. 357 (2011) 163–7.
- [103] K. Ishibashi, A. Fujishima, T. Watanabe, K. Hashimoto, Detection of active oxidative species in TiO<sub>2</sub> photocatalysis using the fluorescence technique, Electrochem. Commun. 2 (2000) 207–210.
- [104] Y. Nakabayashi, Y. Nosaka, OH Radical Formation at Distinct Faces of Rutile TiO<sub>2</sub> Crystal in the Procedure of Photoelectrochemical Water Oxidation, J. Phys. Chem. C. 117 (2013) 23832–23839.
- [105] M. Komatsu, T. Rao, A. Fujishima, Detection of Hydroxyl Radicals Formed on an Anodically Polarized Diamond Electrode Surface in Aqueous Media, Chem. Lett. 32 (2003) 396–397.
- [106] N. Ohguri, A. Nosaka, Y. Nosaka, Detection of OH radicals as the effect of Pt particles in the membrane of polymer electrolyte fuel cells, J. Power Sources. 195 (2010) 4647–4652.
- [107] M. Salazar-Gastélum, S. Lin, Electrochemical and Spectrometric Studies for the Determination of the Mechanism of Oxygen Evolution Reaction, J. Electrochem. Soc. 163 (2016) G37–G43.
- [108] F. Montilla, P. Michaud, E. Morallón, J. Vázquez, C. Comninellis, Electrochemical oxidation of benzoic acid at boron-doped diamond electrodes, Electrochim. Acta. 47 (2002) 3509–3513.
- [109] B. Ou, M. Hampsch-Woodill, J. Flanagan, E.K. Deemer, R.L. Prior, D. Huang, Novel Fluorometric Assay for Hydroxyl Radical Prevention Capacity Using Fluorescein as the Probe, J. Agric. Food Chem. 50 (2002) 2772–2777.

- [110] M.E. Lindsey, M.A. Tarr, Quantitation of hydroxyl radical during Fenton oxidation following a single addition of iron and peroxide, Chemosphere. 41 (2000) 409–417.
- [111] F. Regoli, G.W. Winston, P. Radicals, H. Radi-, G.W.T.A. Phar-, Quantification of Total Oxidant Scavenging Capacity of Antioxidants for Peroxynitrite, Peroxyl Radicals, and Hydroxyl Radicals, Reactions. 105 (1999) 96–105.
- [112] J.-F.J. Jen, M.M.-F. Leu, T.C. Yang, Determination of hydroxyl radicals in an advanced oxidation process with salicylic acid trapping and liquid chromatography, J. Chromatogr. A. 796 (1998) 283–288.
- [113] T. Hirakawa, Y. Nosaka, Properties of  $O_2^{\cdot-}$  and  $OH^{\cdot}$  Formed in  $TiO_2$  Aqueous Suspensions by Photocatalytic Reaction and the Influence of  $H_2O_2$  and Some Ions, Langmuir. 18 (2002) 3247–3254.
- [114] Y. Nakabayashi, Y. Nosaka, The pH dependence of OH radical formation in photo-electrochemical water oxidation with rutile  $TiO_2$  single crystals., Phys. Chem. Chem. Phys. 17 (2015) 30570–6.
- [115] Q. Xiao, L. Ouyang, Photocatalytic activity and hydroxyl radical formation of carbon-doped  $TiO_2$  nanocrystalline: Effect of calcination temperature, Chem. Eng. J. 148 (2009) 248–253.
- [116] Q. Xiao, Z. Si, J. Zhang, C. Xiao, X. Tan, Photoinduced hydroxyl radical and photocatalytic activity of samarium-doped  $TiO_2$  nanocrystalline., J. Hazard. Mater. 150 (2008) 62–7.
- [117] J.M. SAV Eremia, D Chevalier-Lucia, GL Radu, Optimization of hydroxyl radical formation using  $TiO_2$  as photocatalyst by response surface methodology, Talanta. 77 (2008) 858–862.
- [118] R. Thiruvenkatachari, T.O. Kwon, J.C. Jun, S. Balaji, M. Matheswaran, I.S. Moon, Application of several advanced oxidation processes for the destruction of terephthalic acid (TPA)., J. Hazard. Mater. 142 (2007) 308–14.
- [119] A. Shafaei, M. Nikazar, M. Arami, Photocatalytic degradation of terephthalic acid using titania and zinc oxide photocatalysts: Comparative study, Desalination. 252 (2010) 8–16.
- [120] J. Liu, G. Lager, P. Tacchini, H.H. Girault, Generation of OH radicals at palladium oxide nanoparticle modified electrodes, and scavenging by fluorescent probes and antioxidants, J. Electroanal. Chem. 619–620 (2008) 131–136.
- [121] Q. Yue, K. Zhang, X. Chen, L. Wang, J. Zhao, J. Liu, J. Jia, Generation of OH radicals in oxygen reduction reaction at Pt-Co nanoparticles supported on graphene in alkaline solutions., Chem. Commun. (Camb). 46 (2010) 3369–71.
- [122] L. Linxiang, Y. Abe, Y. Nagasawa, R. Kudo, N. Usui, K. Imai, T. Mashino, M. Mochizuki, N. Miyata, An HPLC assay of hydroxyl radicals by the hydroxylation reaction of terephthalic acid., Biomed. Chromatogr. 18 (2004) 470–4.
- [123] D. Bejan, J.D. Malcolm, L. Morrison, N.J. Bunce, Mechanistic investigation of the conductive ceramic Ebonex® as an anode material, Electrochim. Acta. 54 (2009) 5548–5556.
- [124] L.L. Houk, S.K. Johnson, J. Feng, R.S. Houk, D.C. Johnson, Electrochemical incineration of

- benzoquinone in aqueous media using a quaternary metal oxide electrode in the absence of a soluble supporting electrolyte, J. Appl. Electrochem. 28 (1998) 1167–1177.
- [125] J. Feng, L. Houk, D. Johnson, S. Lowery, Electrocatalysis of Anodic Oxygen-Transfer Reactions: The Electrochemical Incineration of Benzoquinone, Journal of the Electrochemical Society (1995).
- [126] J. Kim, G. V. Korshin, Generation of Hydroxyl Radicals and Ozone in a Flow-through Electrochemical Reactor, Ozone Sci. Eng. 30 (2008) 113–119.
- [127] J. Jeong, C. Kim, J. Yoon, The effect of electrode material on the generation of oxidants and microbial inactivation in the electrochemical disinfection processes, Water Res. 43 (2009) 895–901.
- [128] W. Han, P. Zhang, W. Zhu, J. Yin, L. Li, Photocatalysis of p-chlorobenzoic acid in aqueous solution under irradiation of 254 nm and 185 nm UV light, Water Res. 38 (2004) 4197–4203.
- [129] M. Cho, H. Chung, W. Choi, J. Yoon, Linear correlation between inactivation of E. coli and OH radical concentration in TiO<sub>2</sub> photocatalytic disinfection, Water Res. 38 (2004) 1069–1077.
- [130] C.-Y. Chen, C.T. Jafvert, Photoreactivity of carboxylated single-walled carbon nanotubes in sunlight: reactive oxygen species production in water., Environ. Sci. Technol. 44 (2010) 6674–9.
- [131] M. Lee, H.J. Yun, S. Yu, J. Yi, Enhancement in photocatalytic oxygen evolution *via* water oxidation under visible light on nitrogen-doped TiO<sub>2</sub> nanorods with dominant reactive {102} facets, Catal. Commun. 43 (2014) 11–15.
- [132] H.J. Yun, D.M. Lee, S. Yu, J. Yoon, H.J. Park, J. Yi, Effect of valence band energy on the photocatalytic performance of N-doped TiO<sub>2</sub> for the production of O<sub>2</sub> *via* the oxidation of water by visible light, J. Mol. Catal. A Chem. 378 (2013) 221–226.
- [133] D. Wu, H. You, R. Zhang, C. Chen, D.J. Lee, Inactivation of Amphidinium sp. in ballast waters using UV/Ag-TiO<sub>2</sub>+O<sub>3</sub> advanced oxidation treatment, Bioresour. Technol. 102 (2011) 9838–9842.
- [134] J. Muff, L.R. Bennedsen, E.G. Søgaaard, Study of electrochemical bleaching of p-nitrosodimethylaniline and its role as hydroxyl radical probe compound, J. Appl. Electrochem. 41 (2011) 599–607.
- [135] R. Amadelli, A. De Battisti, D. V. Girenko, S. V. Kovalyov, A.B. Velichenko, Electrochemical oxidation of trans-3,4-dihydroxycinnamic acid at PbO<sub>2</sub> electrodes: Direct electrolysis and ozone mediated reactions compared, Electrochim. Acta. 46 (2000) 341–347.
- [136] J. Muff, L. Bennedsen, E. Søgaaard, Detailed parameter study on the mechanisms in electrochemical oxidation of p-nitrosodimethylaniline in chloride electrolyte, 2nd European Conference on Environmental Applications of Advanced Oxidation Processes (2009).
- [137] J. Jeong, J.E.E.Y. Kim, The Role of Reactive Oxygen Species in the Electrochemical Inactivation of Microorganisms, Environ. Sci. Technol. 40 (2006) 6117–6122.
- [138] P.F. Schwarz, N.J. Turro, S.H. Bossmann, A.M. Braun, A.-M.A.A. Wahab, H. Dürr, A New Method To Determine the Generation of Hydroxyl Radicals in Illuminated TiO<sub>2</sub> Suspensions, J.

- Phys. Chem. B. 101 (1997) 7127–7134.
- [139] N. Kishimoto, E. Sugimura, Feasibility of an electrochemically assisted Fenton method using  $\text{Fe}^{2+}/\text{HOCl}$  system as an advanced oxidation process., Water Sci. Technol. 62 (2010) 2321–9.
- [140] A.Y. Satoh, J.E. Trosko, Methylene Blue Dye Test for Rapid Qualitative Detection of Hydroxyl Radicals Formed in a Fenton's Reaction Aqueous Solution, Environ. Sci. Technol. 41 (2007) 2881–2887.
- [141] G. Wang, Y. Yang, D. Han, Y. Li, Oxygen defective metal oxides for energy conversion and storage, Nano Today. 13 (2017) 23–39.
- [142] G. Wang, H. Wang, Y. Ling, Y. Tang, X. Yang, R.C. Fitzmorris, C. Wang, J.Z. Zhang, Y. Li, Hydrogen-treated  $\text{TiO}_2$  nanowire arrays for photoelectrochemical water splitting, Nano Lett. 11 (2011) 3026–3033.
- [143] X. Pan, M.-Q. Yang, X. Fu, N. Zhang, Y.-J. Xu, Defective  $\text{TiO}_2$  with oxygen vacancies: synthesis, properties and photocatalytic applications., Nanoscale. 5 (2013) 3601–14.
- [144] L. Liborio, G. Mallia, N. Harrison, Electronic structure of the  $\text{Ti}_4\text{O}_7$  Magnéli phase, Phys. Rev. B - Condens. Matter Mater. Phys. 79 (2009) 1–9.
- [145] J. Smith, F. Walsh, R. Clarke, Electrodes based on Magnéli phase titanium oxides: the properties and applications of Ebonex® materials, J. Appl. Electrochem. 28 (1998).
- [146] S. Harada, K. Tanaka, H. Inui, Thermoelectric properties and crystallographic shear structures in titanium oxides of the Magnéli phases, J. Appl. Phys. 108 (2010).
- [147] D.S. Jeong, R. Thomas, R.S. Katiyar, J.F. Scott, H. Kohlstedt, A. Petraru, C.S. Hwang, Emerging memories: resistive switching mechanisms and current status, Reports Prog. Phys. 75 (2012) 76502.
- [148] K. Szot, M. Rogala, W. Speier, Z. Klusek, A. Besmehn, R. Waser,  $\text{TiO}_2$  —a prototypical memristive material, Nanotechnology. 22 (2011) 254001.
- [149] J. Kwon, A.A. Sharma, J.A. Bain, Y.N. Picard, M. Skowronski, Oxygen vacancy creation, drift, and aggregation in  $\text{TiO}_2$ -based resistive switches at low temperature and voltage, Adv. Funct. Mater. 25 (2015) 2876–2883.
- [150] M. Toyoda, T. Yano, B. Tryba, S. Mozia, Preparation of carbon-coated Magnéli phases  $\text{Ti}_n\text{O}_{2n-1}$  and their photocatalytic activity under visible light, Appl. Catal. B Environ. 88 (2009) 160–164.
- [151] W. Kao, P. Patel, S.L. Haberichter, Formation Enhancement of a Lead Acid Battery Positive Plate by Barium Metaplumbate and Ebonex®, J. Electrochem. Soc. 144 (1997) 1907.
- [152] C.C. Waraksa, G. Chen, D.D. Macdonald, T.E. Mallouk, C.C. Waraksa, H. Cho, D.D. Macdonald, T.E. Mallouka, EIS Studies of Porous Oxygen Electrodes with Discrete Particles, J. Electrochem. Soc. 150 (2003) E423.
- [153] S. El-Sherif, D. Bejan, N.J. Bunce, Electrochemical oxidation of sulfide ion in synthetic sour brines using periodic polarity reversal at Ebonex® electrodes, Can. J. Chem. 88 (2010) 928–936.

- [154] V. Mavrov, E. Bélières, Reduction of water consumption and wastewater quantities in the food industry by water recycling using membrane processes, Desalination. (2000).
- [155] G. Daufin, J. Escudier, H. Carrere, Recent and emerging applications of membrane processes in the food and dairy industry, Food Bioprod. Process. (2001).
- [156] C. Blöcher, M. Noronha, L. Fünfroeken, Recycling of spent process water in the food industry by an integrated process of biological treatment and membrane separation, Desalination. (2002).
- [157] S. Lee, A. Burt, Microfiltration of recombinant yeast cells using a rotating disk dynamic filtration system, Biotechnol. Bioeng. (1995).
- [158] C. Parnham, R. Davis, Protein recovery from cell debris using rotary and tangential crossflow microfiltration, Biotechnol. Bioeng. (1995).
- [159] J. Vogel, K. Kroner, Controlled shear filtration: a novel technique for animal cell separation, Biotechnol. Bioeng. (1999).
- [160] M. Clever, F. Jordt, R. Knauf, N. Rübiger, M. Rüdibusch, R. Hilker-Scheibel, Process water production from river water by ultrafiltration and reverse osmosis, Desalination. 131 (2000) 325–336.
- [161] K.J. Howe, M.M. Clark, Fouling of Microfiltration and Ultrafiltration Membranes by Natural Waters, Environ. Sci. Technol. 36 (2002) 3571–3576.
- [162] V. Coşofreţ, R. Buck, Phenothiazine drug poly (vinyl chloride) matrix membrane electrodes and their use in pharmaceutical analysis, Analyst. (1984).
- [163] T. Urase, C. Kagawa, T. Kikuta, Factors affecting removal of pharmaceutical substances and estrogens in membrane separation bioreactors, Desalination. (2005).
- [164] K. Kimura, H. Hara, Y. Watanabe, Removal of pharmaceutical compounds by submerged membrane bioreactors (MBRs), Desalination. (2005).
- [165] A.M. Zaky, B.P. Chaplin, Mechanism of *p*-Substituted Phenol Oxidation at a Ti<sub>4</sub>O<sub>7</sub> Reactive Electrochemical Membrane, Environ. Sci. Technol. 48 (2014) 5857–67.
- [166] Y. Jing, L. Guo, B.P. Chaplin, Electrochemical impedance spectroscopy study of membrane fouling and electrochemical regeneration at a sub-stoichiometric TiO<sub>2</sub> reactive electrochemical membrane, J. Memb. Sci. 510 (2016) 510–523.
- [167] A. Lasia, Electrochemical impedance spectroscopy and its applications, 2002.
- [168] F. Fabregat-Santiago, G. Garcia-Belmonte, J. Bisquert, A. Zaban, P. Salvador, Decoupling of transport, charge storage, and interfacial charge transfer in the nanocrystalline TiO<sub>2</sub>/electrolyte system by impedance methods, J. Phys. Chem. B. 106 (2002) 334–339.
- [169] H. SONG, J. JANG, J. KIM, S. OH, Electrochemical porosimetry: Deconvolution of distribution functions, Electrochem. Commun. 8 (2006) 1191–1196.
- [170] J.R. Park, D.D. Macdonald, Impedance studies of the growth of porous magnetite films on carbon steel in high temperature aqueous systems, Corros. Sci. 23 (1983) 295–315.

- [171] J. Bisquert, Influence of the boundaries in the impedance of porous film electrodes, Phys. Chem. Chem. Phys. (2000).
- [172] P. Aimar, M. Meireles, V. Sanchez, A contribution to the translation of retention curves into pore size distributions for sieving membranes, J. Memb. Sci. 54 (1990) 321–338.
- [173] J. Ren, Z. Li, F.-S. Wong, A new method for the prediction of pore size distribution and MWCO of ultrafiltration membranes, J. Memb. Sci. 279 (2006) 558–569.
- [174] A.K. Ghosh, E.M.V. Hoek, Impacts of support membrane structure and chemistry on polyamide–polysulfone interfacial composite membranes, J. Memb. Sci. 336 (2009) 140–148.
- [175] U. Rammelt, G. Reinhard, On the applicability of a constant phase element (CPE) to the estimation of roughness of solid metal electrodes, Electrochim. Acta. 35 (1990) 1045–1049.
- [176] M. Orazem, B. Tribollet, Electrochemical impedance spectroscopy, 2011.
- [177] G.J. Brug, A.L.G. van den Eeden, M. Sluyters-Rehbach, J.H. Sluyters, The analysis of electrode impedances complicated by the presence of a constant phase element, J. Electroanal. Chem. Interfacial Electrochem. 176 (1984) 275–295.
- [178] S. Levine, A.L. Smith, Theory of the differential capacity of the oxide/aqueous electrolyte interface, Discuss. Faraday Soc. 52 (1971) 290.
- [179] A. Lasia, Porous electrodes in the presence of a concentration gradient, J. Electroanal. Chem. 428 (1997) 155–164.
- [180] L. Valek, Impedance Spectroscopy Characterization Of the Electrodeposited Ni-15Mo Catalyst Designed for the HER in Acid Solution: Modified Porous Model, J. New Mater. Electrochem. Syst. (2006).
- [181] D.D. Macdonald, Reflections on the history of electrochemical impedance spectroscopy, Electrochim. Acta. 51 (2006) 1376–1388.
- [182] G. Reinhard, U. Rammelt, K. Rammelt, Analysis of impedance spectra on corroding metals, Corros. Sci. 26 (1986) 109–120.
- [183] A.M. Zayed, A.A. Sagues, Corrosion at surface damage on an epoxy-coated reinforcing steel, Corros. Sci. 30 (1990) 1025–1044.
- [184] T. Hong, Y.H. Sun, W.P. Jepson, Study on corrosion inhibitor in large pipelines under multiphase flow using EIS, Corros. Sci. 44 (2002) 101–112.
- [185] P.R. Bueno, E.R. Leite, Nanostructured Li Ion Insertion Electrodes. 1. Discussion on Fast Transport and Short Path for Ion Diffusion, J. Phys. Chem. B. 107 (2003) 8868–8877.
- [186] S.W. Donne, J.H. Kennedy, Transmission Line Modeling of the Manganese Dioxide Electrode in Concentrated KOH Electrolytes, J. Appl. Electrochem. 34 (2004) 477–486.
- [187] M.E. Suss, T.F. Baumann, M. a. Worsley, K. a. Rose, T.F. Jaramillo, M. Stadermann, J.G. Santiago, Impedance-based study of capacitive porous carbon electrodes with hierarchical and bimodal porosity, J. Power Sources. 241 (2013) 266–273.

- [188] W.R. Bowen, J.S. Welfoot, Modelling the performance of membrane nanofiltration—critical assessment and model development, Chem. Eng. Sci. 57 (2002) 1121–1137.
- [189] K. Kant, C. Priest, J. Shapter, D. Losic, The influence of nanopore dimensions on the electrochemical properties of nanopore arrays studied by impedance spectroscopy, Sensors. (2014).
- [190] C. Ho, A. Zydney, A Combined Pore Blockage and Cake Filtration Model for Protein Fouling during Microfiltration., J. Colloid Interface Sci. 232 (2000) 389–399.
- [191] D. Grier, Comparison of Inland Waterways and Surface Freight Modes, TR News, Transp. Res. Board. 221 (2002) 17.
- [192] EPA, Emission Facts: Average Carbon Dioxide Emissions Resulting from Gasoline and Diesel Fuel, (2005) 3.
- [193] W. Duan, A. Dudchenko, E. Mende, Electrochemical mineral scale prevention and removal on electrically conducting carbon nanotube–polyamide reverse osmosis membranes, Environ. Sci. Process. Impacts. (2014).
- [194] R. Hashaikeh, B. Lalia, N. Hilal, Novel in-situ membrane cleaning using periodic electrolysis, US Pat. App. 14/169,764. (2014).
- [195] A. Kapałka, G. Fóti, C. Comninellis, The importance of electrode material in environmental electrochemistry. Formation and reactivity of free hydroxyl radicals on boron-doped diamond electrodes, Electrochim. Acta. 54 (2009) 2018–2023.
- [196] X. Sun, J. Wu, Z. Chen, X. Su, B.J. Hinds, Fouling characteristics and electrochemical recovery of carbon nanotube membranes, Adv. Funct. Mater. 23 (2013) 1500–1506.
- [197] M.M. Saleh, Simulation of oxygen evolution reaction at porous anode from flowing electrolytes, J. Solid State Electrochem. 11 (2007) 811–820.
- [198] A. Bard, L. Faulkner, Electrochemical methods: fundamentals and applications, 2nd Editio, Wiley, 2000.
- [199] R.R. Miller-Folk, R.E. Nofle, D. Pletcher, Electron transfer reactions at Ebonex ceramic electrodes, J. Electroanal. Chem. Interfacial Electrochem. 274 (1989) 257–261.
- [200] R.J. Pollock, J.F. Houlihan, A.N. Bain, B.S. Coryea, Electrochemical properties of a new electrode material,  $Ti_4O_7$ , Mater. Res. Bull. 19 (1984) 17–24.
- [201] P.C.S. Hayfield, Development of a New Material: Monolithic  $Ti_4O_7$  Ebonex Ceramic, Royal Society of Chemistry, 2002.
- [202] D. Kearney, D. Bejan, N. Bunce, The use of Ebonex electrodes for the electrochemical removal of nitrate ion from water, Can. J. Chem. 674 (2012) 666–674.
- [203] F.C. Walsh, R.G. a. Wills, The continuing development of Magnéli phase titanium sub-oxides and Ebonex® electrodes, Electrochim. Acta. 55 (2010) 6342–6351.
- [204] Y. Jing, B.P. Chaplin, Electrochemical impedance spectroscopy study of membrane fouling

- characterization at a conductive sub-stoichiometric TiO<sub>2</sub> reactive electrochemical membrane: Transmission line model development, J. Memb. Sci. 511 (2016) 238–249.
- [205] P. Webb, An introduction to the physical characterization of materials by mercury intrusion porosimetry with emphasis on reduction and presentation of experimental data, Micromeritics Instrum. Corp, Norcross. (2001).
- [206] C. Combe, E. Molis, P. Lucas, R. Riley, M. Clark, The effect of CA membrane properties on adsorptive fouling by humic acid, J. Memb. Sci. 154 (1999) 73–87.
- [207] M. Nyström, K. Ruohomäki, L. Kaipia, Humic acid as a fouling agent in filtration, Desalination. 106 (1996) 79–87.
- [208] R.L. Wershaw, A new model for humic materials and their interactions with hydrophobic organic chemicals in soil-water or sediment-water systems, J. Contam. Hydrol. 1 (1986) 29–45.
- [209] J. V. Goldstone, M.J. Pullin, S. Bertilsson, B.M. Voelker, Reactions of Hydroxyl Radical with Humic Substances: Bleaching, Mineralization, and Production of Bioavailable Carbon Substrates, Environ. Sci. Technol. 36 (2002) 364–372.
- [210] L. Antropov, Theoretical Electrochemistry., (1977).
- [211] J. Wiszniowski, D. Robert, Photocatalytic decomposition of humic acids on TiO<sub>2</sub>: Part I: Discussion of adsorption and mechanism, J. Photochem. Photobiol. A Chem. 152 (2002) 267–273.
- [212] S.D. Faust, O.M. Aly, Chemistry of water treatment. Second edition., (1998).
- [213] Z.. Cui, S. Chang, A.. Fane, The use of gas bubbling to enhance membrane processes, J. Memb. Sci. 221 (2003) 1–35.
- [214] J. Li, Ultrasonic cleaning of nylon microfiltration membranes fouled by Kraft paper mill effluent, J. Memb. Sci. 205 (2002) 247–257.
- [215] C. Mansfield, B. Depro, V. Perry, The Chlorine Industry: A Profile, 2000.
- [216] J. Markestah, K. Renolds, D. Larsen, Sodium Hydroxide (NaOH) Practicality Study, 2010.
- [217] L. Machlin, A. Bendich, Free radical tissue damage: protective role of antioxidant nutrients, FASEB J. 1 (1987) 441–445.
- [218] J.M. Kesselman, O. Weres, N.S. Lewis, M.R. Hoffmann, Electrochemical Production of Hydroxyl Radical at Polycrystalline Nb-Doped TiO<sub>2</sub> Electrodes and Estimation of the Partitioning between Hydroxyl Radical and Direct Hole Oxidation Pathways, J. Phys. Chem. B. 101 (1997) 2637–2643.
- [219] V.M. Mishin, P.E. Thomas, Characterization of hydroxyl radical formation by microsomal enzymes using a water-soluble trap, terephthalate., Biochem. Pharmacol. 68 (2004) 747–52.
- [220] C. Feng, N. Sugiura, S. Shimada, T. Maekawa, Development of a high performance electrochemical wastewater treatment system, J. Hazard. Mater. 103 (2003) 65–78.
- [221] G. V. Buxton, C.L. Greenstock, W.P. Helman, A.B. Ross, Critical review of rate constants for reactions of hydrated electrons, hydrogen atoms and hydroxyl radicals ( $\cdot\text{OH}/\cdot\text{O}^-$  in aqueous

- solution, J. Phys. Chem. Ref. Data. 17 (1988) 513.
- [222] W. Pryor, Oxy-radicals and related species: their formation, lifetimes, and reactions, Annu. Rev. Physiol. 48 (1986) 657–667.
- [223] G. Louit, S. Foley, J. Cabillic, H. Coffigny, F. Taran, A. Valleix, J.P. Renault, S. Pin, The reaction of coumarin with the OH radical revisited: hydroxylation product analysis determined by fluorescence and chromatography, Radiat. Phys. Chem. 72 (2005) 119–124.
- [224] P. Trogadas, J. Parrondo, V. Ramani, Degradation Mitigation in Polymer Electrolyte Membranes Using Cerium Oxide as a Regenerative Free-Radical Scavenger, Electrochem. Solid-State Lett. 11 (2008) B113.
- [225] C. Perrot, L. Gonon, M. Bardet, C. Marestin, A. Pierre-Bayle, G. Gebel, Degradation of a sulfonated aryl ether ketone model compound in oxidative media (sPAEK), Polymer (Guildf). 50 (2009) 1671–1681.
- [226] M. Gummalla, V. V. Atrazhev, D. Condit, N. Cipollini, T. Madden, N.Y. Kuzminykh, D. Weiss, S.F. Burlatsky, Degradation of Polymer-Electrolyte Membranes in Fuel Cells, J. Electrochem. Soc. 157 (2010) B1542.
- [227] H. Li, K. Tsay, H. Wang, J. Shen, S. Wu, J. Zhang, N. Jia, S. Wessel, R. Abouatallah, N. Joos, J. Schrooten, Durability of PEM fuel cell cathode in the presence of  $\text{Fe}^{3+}$  and  $\text{Al}^{3+}$ , J. Power Sources. 195 (2010) 8089–8093.
- [228] V. Atrazhev, E. Timokhina, S.F. Burlatsky, V. Sultanov, T. Madden, M. Gummalla, Direct Mechanism of OH Radicals Formation in PEM Fuel Cells, ECS Trans. 6 (2008) 69–74.
- [229] R. Borup, J. Meyers, B. Pivovar, Y.S. Kim, R. Mukundan, N. Garland, D. Myers, M. Wilson, F. Garzon, D. Wood, and P. Zelenay, Scientific aspects of polymer electrolyte fuel cell durability and degradation, Chem. Rev. 107 (2007) 3904–3951.
- [230] A. Collier, H. Wang, X. Zi Yuan, J. Zhang, D.P. Wilkinson, Degradation of polymer electrolyte membranes, Int. J. Hydrogen Energy. 31 (2006) 1838–1854.
- [231] S. Hommura, K. Kawahara, T. Shimohira, Y. Teraoka, Development of a method for clarifying the perfluorosulfonated membrane degradation mechanism in a fuel cell environment., J. Electrochem. Soc. 155 (2007) A29–A33.
- [232] S. Maurya, S. Shin, M. Kim, S. Yun, S. Moon, Stability of composite anion exchange membranes with various functional groups and their performance for energy conversion, J. Memb. Sci. 443 (2013) 28–35.
- [233] D. Chen, S. Wang, M. Xiao, D. Han, Y. Meng, Sulfonated poly (fluorenyl ether ketone) membrane with embedded silica rich layer and enhanced proton selectivity for vanadium redox flow battery, J. Power Sources. 195 (2010) 7701–7708.
- [234] G.L. Newton, J.R. Milligan, Fluorescence detection of hydroxyl radicals, Radiat. Phys. Chem. 75 (2006) 473–478.
- [235] J. Méndez-Díaz, M. Sánchez-Polo, J. Rivera-Utrilla, S. Canonica, U. Von Gunten, Advanced

- oxidation of the surfactant SDBS by means of hydroxyl and sulphate radicals, Chem. Eng. J. 163 (2010) 300–306.
- [236] I. Arslan-Alaton, A review of the effects of dye-assisting chemicals on advanced oxidation of reactive dyes in wastewater, Color. Technol. 119 (2003) 345–353.
- [237] M.R. Hoffmann, S.T. Martin, W.Y. Choi, D.W. Bahnemann, Environmental Applications of Semiconductor Photocatalysis, Chem. Rev. 95 (1995) 69–96.
- [238] B. Aguilera-Venegas, H. Speisky, Identification of the transition state for fast reactions: The trapping of hydroxyl and methyl radicals by DMPO - A DFT approach, J. Mol. Graph. Model. 52 (2014) 57–70.
- [239] S. Bhattacharjee, M.N. Khan, H. Chandra, M.C.R. Symons, Radical cations from nitron spin-traps: reaction with water to give OH adducts, J. Chem. Soc. Perkin Trans. 2. (1996) 2631.
- [240] K.D. Sugden, K.E. Wetterhahn, Reaction of Chromium ( V ) with the EPR Spin Traps 5 , 5-Dimethylpyrroline N -Oxide and Phenyl-N-tert-butyl nitron Resulting in Direct Oxidation, Inorg. Chem. (1996) 651–657.
- [241] J.G. Roberts, M.A. Voinov, A.C. Schmidt, T.I. Smirnova, L.A. Sombers, The Hydroxyl Radical is a Critical Intermediate in the Voltammetric Detection of Hydrogen Peroxide, J. Am. Chem. Soc. 138 (2016) 2516–2519.
- [242] F. a Villamena, C.M. Hadad, J.L. Zweier, Theoretical study of the spin trapping of hydroxyl radical by cyclic nitrones: a density functional theory approach., J. Am. Chem. Soc. 126 (2004) 1816–1829.
- [243] A.R. Forrester, S.P. Hepburn, Spin traps. A cautionary note, J. Chem. Soc. C Org. (1971) 701.
- [244] H. Chandra, M.C.R. Symons, Hydration of spin-trap cations as a source of hydroxyl adducts, J. Chem. Soc. Chem. Commun. 16 (1986) 1301–1302.
- [245] L. Ebersson, Formation of Hydroxyl Spin Adducts *via* Nucleophilic Addition—Oxidation to 5, 5-Dimethyl-1-pyrroline N-Oxide, Acta Chem. Scand. 53 (1999) 584–593.
- [246] V. Cerri, C. Frejaville, F. Vila, A. Allouche, Synthesis, redox behavior and spin-trap properties of 2, 6-di-tert-butyl nitrosobenzene (DTBN), J. Org. Chem. 54 (1989) 1447–1450.
- [247] F. Leinisch, K. Ranguelova, E.F. Derose, J. Jiang, R.P. Mason, Evaluation of the Forrester-Hepburn mechanism as an artifact source in ESR spin-trapping, Chem. Res. Toxicol. 24 (2011) 2217–2226.
- [248] F. Leinisch, J. Jiang, E.F. Derose, V. V. Khramtsov, R.P. Mason, Investigation of spin-trapping artifacts formed by the Forrester-Hepburn mechanism, Free Radic. Biol. Med. 65 (2013) 1497–1505.
- [249] K. Ranguelova, R.P. Mason, The fidelity of spin trapping with DMPO in biological systems, Magn. Reson. Chem. 49 (2011) 152–158.
- [250] G.L.G. McIntire, H.H.N. Blount, H.H.J. Stronks, R. V. Shetty, E.G. Janzen, Spin trapping in

- electrochemistry. 2. Aqueous and nonaqueous electrochemical characterizations of spin traps, J. Phys. Chem. 84 (1980) 916–921.
- [251] P.M. Hanna, W. Chamulitrat, P. Mason, Z. Health, P.O. Box, A. Hagi, M. Nishi, A. Murakami, When are metal ion-dependent hydroxyl and alkoxy radical adducts of 5,5-dimethyl-1-pyrroline N-oxide artifacts?, Arch. Biochem. Biophys. 296 (1992) 640–644.
- [252] S.E. Page, W.A. Arnold, K. McNeill, Terephthalate as a probe for photochemically generated hydroxyl radical, J. Environ. Monit. 12 (2010) 1658.
- [253] J. Feng, Electrocatalysis of Anodic Oxygen-Transfer Reactions: The Electrochemical Incineration of Benzoquinone, J. Electrochem. Soc. 142 (1995) 3626.
- [254] M. Nien Shuchmann, E. Bothe, von S. Justus, C. von Sonntag, Reaction of OH radicals with benzoquinone in aqueous solutions. A pulse radiolysis study, Spectrum. 0 (1998) 791–796.
- [255] M. Anbar, D. Meyerstein, P. Neta, Reactivity of aromatic compounds toward hydroxyl radicals, J. Phys. Chem. 70 (1966) 2660–2662.
- [256] A. Donaghue, B.P. Chaplin, Effect of select organic compounds on perchlorate formation at boron-doped diamond film anodes., Environ. Sci. Technol. 47 (2013) 12391–9.
- [257] T. Al-Shemmeri, Engineering Fluid Mechanics, Bookboon, 2012.
- [258] M. Frisch, G. Trucks, H. Schlegel, G. Scuseria, M. Robb, J. Cheeseman, G. Scalmani, V. Barone, B. Mennucci, G. Petersson, Gaussian09, (2009).
- [259] C.W. Bauschlicher, H. Partridge, A modification of the Gaussian-2 approach using density functional theory, J. Chem. Phys. 105 (1995) 1788.
- [260] A. V Marenich, C.J. Cramer, D.G. Truhlar, Universal solvation model based on solute electron density and on a continuum model of the solvent defined by the bulk dielectric constant and atomic surface tensions, J. Phys. Chem. B. 113 (2009) 6378–6396.
- [261] C.P. Kelly, C.J. Cramer, D.G. Truhlar, Aqueous solvation free energies of ions and ion-water clusters based on an accurate value for the absolute aqueous solvation free energy of the proton, J. Phys. Chem. B. 110 (2006) 16066–16081.
- [262] M.D. Tissandier, K.A. Cowen, W.Y. Feng, E. Gundlach, M.H. Cohen, A.D. Earhart, J. V. Coe, T.R. Tuttle, The proton's absolute aqueous enthalpy and Gibbs free energy of solvation from cluster-ion solvation data, J. Phys. Chem. A. 102 (1998) 7787–7794.
- [263] C.P. Kelly, C.J. Cramer, D.G. Truhlar, Single-ion solvation free energies and the normal hydrogen electrode potential in methanol, acetonitrile, and dimethyl sulfoxide, J. Phys. Chem. B. 111 (2007) 408–422.
- [264] V. Vaissier, P. Barnes, J. Kirkpatrick, J. Nelson, Influence of polar medium on the reorganization energy of charge transfer between dyes in a dye sensitized film., Phys. Chem. Chem. Phys. 15 (2013) 4804–14.
- [265] C. Peng, H. Bernhard Schlegel, Combining Synchronous Transit and Quasi-Newton Methods to

- Find Transition States, Isr. J. Chem. 33 (1993) 449–454.
- [266] C.Y. Peng, P.Y. Ayala, H.B. Schlegel, M.J. Frisch, Using redundant internal coordinates to optimize equilibrium geometries and transition states, J. Comput. Chem. 17 (1996) 49–56.
- [267] S. de Visser, The accuracy of density functional theory calculations in biocatalysis, J. Proteomics Enzymol. (2013).
- [268] A.H. Shah, W. Zaid, A. Shah, U.A. Rana, H. Hussain, M.N. Ashiq, R. Qureshi, A. Badshah, M.A. Zia, H.-B. Kraatz, pH Dependent Electrochemical Characterization, Computational Studies and Evaluation of Thermodynamic, Kinetic and Analytical Parameters of Two Phenazines, J. Electrochem. Soc. 162 (2014) H115–H123.
- [269] G. Chen, Electrochemical technologies in wastewater treatment, Sep. Purif. Technol. 38 (2004) 11–41.
- [270] A. Bard, M. Mirkin, Scanning Electrochemical Microscopy, CRC Press, Inc., 2012.
- [271] J.M. Smith, Chemical engineering kinetics, No. TP149 S58, 1981.
- [272] B. Chaplin, D. Hubler, J. Farrell, Understanding anodic wear at boron doped diamond film electrodes, Electrochim. Acta. 89 (2013) 122–131.
- [273] N. Ohguri, A. Nosaka, Y. Nosaka, Detection of OH radicals formed at PEFC electrodes by means of a fluorescence probe, Electrochem. Solid-State Lett. 12 (2009) B94–B96.
- [274] A. Brunmark, Formation of electronically excited states during the interaction of p-benzoquinone with hydrogen peroxide, J. Biolumin. Chemilumin. 4 (1989) 219–225.
- [275] J.F. Bunnett, R.E. Zahler, Aromatic Nucleophilic Substitution Reactions., Chem. Rev. 49 (1951) 273–412.
- [276] C.M. Oliveira, A.C.S. Ferreira, V. De Freitas, A.M.S. Silva, Oxidation mechanisms occurring in wines, Food Res. Int. 44 (2011) 1115–1126.
- [277] A.A. Kutyrev, Nucleophilic reactions of quinones, Tetrahedron. 47 (1991) 8043–8065.
- [278] X. Tao, J. Wang, Z. Ying, Q. Cai, G. Zheng, Y. Gan, H. Huang, Y. Xia, C. Liang, W. Zhang, Y. Cui, Strong Sulfur Binding with Conducting Magnéli-Phase, Nano Lett. 14 (2014) 5288–5294.
- [279] M.V. Ganduglia-Pirovano, A. Hofmann, J. Sauer, Oxygen vacancies in transition metal and rare earth oxides: Current state of understanding and remaining challenges, Surf. Sci. Rep. 62 (2007) 219–270.
- [280] G. Lu, a Linsebigler, J.T. Yates,  $Ti^{3+}$  Defect Sites on  $TiO_2(110)$ : Production and Chemical Detection of Active Sites, J. Phys. Chem. 98 (1994) 11733–11738.
- [281] A.F. Arif, R. Balgis, T. Ogi, F. Iskandar, A. Kinoshita, K. Nakamura, K. Okuyama, Highly conductive nano-sized Magnéli phases titanium oxide ( $TiO_x$ ), Sci. Rep. 7 (2017) 3646.
- [282] M. Abbate, R. Potze, G.A. Sawatzky, C. Schlenker, H.J. Lin, L.H. Tjeng, C.T. Chen, D. Teehan, T.S. Turner, Changes in the electronic structure of  $Ti_4O_7$  across the semiconductor-semiconductor-

- metal transitions, Phys. Rev. B. 51 (1995) 10150–10153.
- [283] O. Scialdone, A. Galia, G. Filardo, Electrochemical incineration of 1,2-dichloroethane: Effect of the electrode material, Electrochim. Acta. 53 (2008) 7220–7225.
- [284] R. Zhu, Y. Liu, J. Ye, X. Zhang, Magnéli phase  $\text{Ti}_4\text{O}_7$  powder from carbothermal reduction method: Formation, conductivity and optical properties, J. Mater. Sci. Mater. Electron. 24 (2013) 4853–4856.
- [285] X. Li, A.L. Zhu, W. Qu, H. Wang, R. Hui, L. Zhang, J. Zhang, Magnéli phase  $\text{Ti}_4\text{O}_7$  electrode for oxygen reduction reaction and its implication for zinc-air rechargeable batteries, Electrochim. Acta. 55 (2010) 5891–5898.
- [286] C. Tang, D. Zhou, S. Fang, L. Yang, Effects of  $\text{Ti}_4\text{O}_7$  on Secondary Alkaline Zinc Anode, J. Electrochem. Soc. 159 (2012) A1796–A1800.
- [287] K. Ellis, A. Hill, J. Hill, A. Loyns, T. Partington, The performance of Ebonex® electrodes in bipolar lead-acid batteries, J. Power Sources. 136 (2004) 366–371.
- [288] A. Padilha, H. Raebiger, A. Rocha, G. Dalpian, Charge storage in oxygen deficient phases of  $\text{TiO}_2$ : defect Physics without defects, Sci. Rep. (2016).
- [289] C. Yao, F. Li, X. Li, D. Xia, Fiber-like nanostructured  $\text{Ti}_4\text{O}_7$  used as durable fuel cell catalyst support in oxygen reduction catalysis, J. Mater. Chem. 22 (2012) 16560.
- [290] D. Rajkumar, K. Palanivelu, Electrochemical treatment of industrial wastewater., J. Hazard. Mater. 113 (2004) 123–9.
- [291] T. Ioroi, Z. Siroma, N. Fujiwara, S. Yamazaki, K. Yasuda, Sub-stoichiometric titanium oxide-supported platinum electrocatalyst for polymer electrolyte fuel cells, Electrochem. Commun. 7 (2005) 183–188.
- [292] K. Senevirathne, R. Hui, S. Campbell, S. Ye, J. Zhang, Electrocatalytic activity and durability of  $\text{Pt}/\text{NbO}_2$  and  $\text{Pt}/\text{Ti}_4\text{O}_7$  nanofibers for PEM fuel cell oxygen reduction reaction, Electrochim. Acta. 59 (2012) 538–547.
- [293] Z. Liu, P. Mukherjee, Mesoscale Elucidation of Surface Passivation in the Li–Sulfur Battery Cathode, ACS Appl. Mater. Interfaces. (2017).
- [294] A.K. Neufeld, A.P. O’Mullane, Effect of the mediator in feedback mode-based SECM interrogation of indium tin-oxide and boron-doped diamond electrodes, J. Solid State Electrochem. 10 (2006) 808–816.
- [295] N. Wilson, S. Clewes, M. Newton, P. Unwin, J. Macpherson, Impact of grain-dependent boron uptake on the electrochemical and electrical properties of boron doped polycrystalline diamond electrodes, J. Phys. Chem. B. 110 (2006) 5639.
- [296] K.B. Holt, A.J. Bard, Y. Show, G.M. Swain, Scanning electrochemical microscopy and conductive probe atomic force microscopy studies of hydrogen-terminated boron-doped diamond electrodes with different doping levels, J. Phys. Chem. B. 108 (2004) 15117–15127.

- [297] M.C. Granger, M. Witek, J. Xu, J. Wang, M. Hupert, A. Hanks, M.D. Koppang, J.E. Butler, G. Lucazeau, M. Mermoux, J.W. Strojek, G.M. Swain, Standard electrochemical behavior of high-quality, boron-doped polycrystalline diamond thin-film electrodes, Anal. Chem. 72 (2000) 3793–3804.
- [298] S. Amemiya, A.J. Bard, F.-R.F. Fan, M. V. Mirkin, P.R. Unwin, Scanning Electrochemical Microscopy, Annu. Rev. Anal. Chem. 1 (2008) 95–131.
- [299] C.G. Zoski, Review—Advances in Scanning Electrochemical Microscopy (SECM), J. Electrochem. Soc. 163 (2016) H3088–H3100.
- [300] C. Wei, A. Bard, M. Mirkin, Scanning electrochemical microscopy. 31. Application of SECM to the study of charge transfer processes at the liquid/liquid interface, J. Phys. Chem. (1995).
- [301] C. Lefrou, R. Cornut, Analytical expressions for quantitative scanning electrochemical microscopy (SECM), ChemPhysChem. 11 (2010) 547–556.
- [302] Y. Jing, B.P. Chaplin, A Mechanistic Study of the Validity of Using Hydroxyl Radical Probes to Characterize Electrochemical Advanced Oxidation Processes, Environ. Sci. Technol. 51 (2017) 2355–2365.
- [303] C. Zoski, Handbook of Electrochemistry, Elsevier, 2006.
- [304] Y. Yang, M.R. Hoffmann, Synthesis and Stabilization of Blue-Black TiO<sub>2</sub> Nanotube Arrays for Electrochemical Oxidant Generation and Wastewater Treatment, Environ. Sci. Technol. 50 (2016) 11888–11894.
- [305] Z. Zhang, J.T. Yates, Band bending in semiconductors: Chemical and physical consequences at surfaces and interfaces, Chem. Rev. 112 (2012) 5520–5551.
- [306] H. Lüth, Solid Surfaces, Interfaces and Thin Films, Sixth, Springer International Publishing, Cham, 2015.
- [307] C. Tran, J. Kafle, X. Yang, D. Qu, Increased discharge capacity of a Li-air activated carbon cathode produced by preventing carbon surface passivation, Carbon N. Y. (2011).
- [308] Z. Qiang, J.-H. Chang, C.-P. Huang, Electrochemical generation of hydrogen peroxide from dissolved oxygen in acidic solutions, Water Res. 36 (2002) 85–94.
- [309] F. Fabregat-santiago, E.M. Barea, J. Bisquert, G.K. Mor, K. Shankar, C. a Grimes, High Carrier Density and Capacitance in TiO<sub>2</sub> Nanotube Arrays Induced by Electrochemical Doping High Carrier Density and Capacitance in TiO<sub>2</sub> Nanotube Arrays Induced by Electrochemical Doping, J. Am. Chem. Soc. 130 (2008) 11312–11316.
- [310] H. Wu, D. Li, X. Zhu, C. Yang, D. Liu, X. Chen, Y. Song, L. Lu, High-performance and renewable supercapacitors based on TiO<sub>2</sub> nanotube array electrodes treated by an electrochemical doping approach, Electrochim. Acta. 116 (2014) 129–136.
- [311] L. Liborio, N. Harrison, Thermodynamics of oxygen defective Magnéli phases in rutile: A first-principles study, Phys. Rev. B - Condens. Matter Mater. Phys. 77 (2008) 1–10.

- [312] H. Nörenberg, G.A.D. Briggs, Surface structure of the most oxygen deficient Magnéli phase – an STM study of  $\text{Ti}_4\text{O}_7$ , Surf. Sci. 402–404 (1998) 738–741.
- [313] N. Andreu, D. Flahaut, R. Dedryvère, M. Minvielle, H. Martinez, D. Gonbeau, XPS Investigation of Surface Reactivity of Electrode Materials: Effect of the Transition Metal, ACS Appl. Mater. Interfaces. 7 (2015) 6629–6636.
- [314] S. Pan, X. Liu, M. Guo, S. fung Yu, H. Huang, Engineering the intermediate band states in amorphous  $\text{Ti}^{3+}$ -doped  $\text{TiO}_2$  for hybrid dye-sensitized solar cell applications, J. Mater. (2015).
- [315] P. Geng, G. Chen, Magnéli  $\text{Ti}_4\text{O}_7$  modified ceramic membrane for electrically-assisted filtration with antifouling property, J. Memb. Sci. 498 (2016) 302–314.
- [316] G. Liu, Z. Wu, V.S.J. Craig, Cleaning of Protein-Coated Surfaces Using Nanobubbles: An Investigation Using a Quartz Crystal Microbalance, J. Phys. Chem. C. 112 (2008) 16748–16753.
- [317] Z. Wu, H. Chen, Y. Dong, H. Mao, J. Sun, S. Chen, V.S.J. Craig, J. Hu, Cleaning using nanobubbles: Defouling by electrochemical generation of bubbles, J. Colloid Interface Sci. 328 (2008) 10–14.
- [318] F. Meng, F. Yang, B. Shi, H. Zhang, A comprehensive study on membrane fouling in submerged membrane bioreactors operated under different aeration intensities, Sep. Purif. Technol. 59 (2008) 91–100.
- [319] A. Lasia, Impedance of porous electrodes, J. Electroanal. Chem. 397 (1995) 27–33.
- [320] Y. Zhang, Y. Zhang, L. Zhou, C. Tan, Inactivation of bacillus subtilis spores using various combinations of ultraviolet treatment with addition of hydrogen peroxide, Photochem. Photobiol. 90 (2014) 609–614.
- [321] J. Colucci, V. Montalvo, R. Hernandez, C. Pouillet, Electrochemical oxidation potential of photocatalyst reducing agents, Electrochim. Acta. 44 (1999) 2507–2514.
- [322] S.M. Chen, K.C. Lin, The electrocatalytic properties of biological molecules using polymerized luminol film-modified electrodes, J. Electroanal. Chem. 523 (2002) 93–105.
- [323] D. Wang, J. Liu, Z. Wu, J. Zhang, Y. Su, Z. Liu, C. Xu, Electrooxidation of methanol, ethanol and 1-propanol on pd electrode in alkaline medium, Int. J. Electrochem. Sci. 4 (2009) 1672–1678.
- [324] H. Ju, J. Zhou, C. Cai, H. Chen, The electrochemical behavior of methylene blue at a microcylinder carbon fiber electrode, Electroanalysis. 7 (1995) 1165–1170.
- [325] D.J. Gavaghan, A.M. Bond, A complete numerical simulation of the techniques of alternating current linear sweep and cyclic voltammetry: analysis of a reversible process by conventional and fast Fourier transform methods, J. Electroanal. Chem. 480 (2000) 133–149.
- [326] B. Carnahan, L. Herbert A., W. James O., Applied numerical methods, Krieger Pub Co, 1969.
- [327] M. Saran, K.H. Summer, Assaying for hydroxyl radicals: Hydroxylated terephthalate is a superior fluorescence marker than hydroxylated benzoate, Free Radic. Res. 31 (2009) 429–436.

## VITA

### Yin Jing

(937)760-8609

yjing6@uic.edu

### Work Experience

#### Research Assistant

University of Illinois at Chicago – Chicago, IL – May 2014 to Present

I worked as a research assistant in Prof. Brian P. Chaplin's lab at UIC. During this period, I have,

- Successfully developed the membrane fouling theory using electrochemical impedance spectroscopy, and applied to study the fouling and defouling behavior on a substoichiometric TiO<sub>2</sub> reactive electrochemical membrane;
- Developed a chemical free electrochemical regeneration scheme to recover the membrane with excellent flux recovery and extremely low cost;
- Investigated the validity of several hydroxyl radical probes used in the electrochemical advanced oxidation processes;
- Developed the methodology of ion transport through a polycarbonate track etched membrane using scanning electrochemical microscopy on both the experimental and theoretical bases;
- Developed the methodology of local resolution of kinetic variation on the passivation study of a substoichiometric TiO<sub>2</sub> electrode.

#### ABET Accreditation Assistant

University of Illinois at Chicago – Chicago, IL – August 2013 to May 2014

I worked to assist the accreditation of STEM ABET of chemical engineering department at UIC in 2013 under Prof. Ludwig Nitsche. My responsibilities included organizing student performance data, communicating with professors and lecturers to collect the supportive document and building the certificate website.

#### Teaching Assistant

University of Illinois at Chicago – Chicago, IL – August 2012 to May 2013

I worked as a teaching assistant for CHE 210 (Material and Energy Balances) and CHE 512 (Microhydrodynamics, Diffusion and Membrane Transport), and my responsibilities were grading students' homework and quizzes, holding office hours, as well as leading the discussion class once in a week for CHE 210.

University of Dayton – Dayton, OH – August 2010 to May 2012

I worked as a teaching assistant for CME 311 (Chemical Engineering Thermodynamics) and CME 365 (Separation Techniques), and was responsible to grade students' homework and organize the lecturer's class notes.

---

### Education

- **Ph.D. in Chemical Engineering**

University of Illinois at Chicago – Chicago, IL

August 2012 to August 2017 (Expected)

- **Master's in Chemical Engineering**  
University of Dayton – Dayton, OH  
August 2010 to July 2012
  - **Bachelor's in Chemical Engineering**  
Shenyang University of Chemical Technology – Shenyang, Liaoning  
September 2005 to June 2009
- 

## Skills

Electrochemical Characterization Instrument, Membrane Characterization Techniques, Numerical Simulations and Computer Programming

---

## Patent

- Chaplin, B. P.; Guo, L.; **Jing, Y.**; Nayak, S. 2016. Ultrafiltration  $\text{TiO}_2$  Magnéli phase reactive electrochemical membranes. U.S. Patent Application 15/365,252, filed on Nov. 30<sup>th</sup>, 2016. Patent Pending
- 

## Publications

- **Jing, Y.**; Chaplin, B. P. *A Mechanistic Study of the Validity of Using Hydroxyl Radical Probes to Characterize Electrochemical Advanced Oxidation Processes.* **Environ. Sci. Technol.** 2017, 51 (4), 2355–2365.
  - **Jing, Y.**; Guo, L.; Chaplin, B. P. *Electrochemical impedance spectroscopy study of membrane fouling and electrochemical regeneration at a sub-stoichiometric  $\text{TiO}_2$  reactive electrochemical membrane.* **J. Memb. Sci.** 2016, 510, 510–523.
  - **Jing, Y.**; Chaplin, B. P. *Electrochemical impedance spectroscopy study of membrane fouling characterization at a conductive sub-stoichiometric  $\text{TiO}_2$  reactive electrochemical membrane: Transmission line model development.* **J. Memb. Sci.** 2016, 511, 238–249.
  - Guo, L.; **Jing, Y.**; Chaplin, B. P. *Development and Characterization of Ultrafiltration  $\text{TiO}_2$  Magnéli Phase Reactive Electrochemical Membranes.* **Environ. Sci. Technol.** 2016, 50 (3), 1428–1436.
  - Santos, M. C.; Elabd, Y. A.; **Jing, Y.**; Chaplin, B. P.; Fang, L. *Highly porous  $\text{Ti}_4\text{O}_7$  reactive electrochemical water filtration membranes fabricated via electrospinning/electrospraying.* **AIChE J.** 2016, 62 (2), 508–524.
- 

## Presentations

- **Y. Jing,** B.P. Chaplin, “Mechanisms of organic compound fouling on a sub-stoichiometric titanium dioxide reactive electrochemical membrane,” Oral Presentation: **2014 ACS 248th National Meeting**, San Francisco, CA, Aug. 10th, 2014;

- **Y. Jing**, L. Guo, B.P. Chaplin, “Electrochemical Impedance Spectroscopy Study of Reactive Electrochemical Membrane Fouling and Development of a New Regeneration Scheme,” Poster Presentation: *2015 North American Membrane Society*, Boston, MA, May 21st, 2015;
- **Y. Jing**, L. Guo, B.P. Chaplin, “Electrochemical Impedance Spectroscopy Study of Membrane Fouling Characterization at a Conductive Sub-Stoichiometric TiO<sub>2</sub> Reactive Electrochemical Membrane,” Oral Presentation: *2016 AIChE Midwest Regional Conference*, Chicago, IL, Mar. 4, 2016;
- **Y. Jing**, L. Guo, B.P. Chaplin, “Electrochemical Impedance Spectroscopy Study of Membrane Fouling Characterization at a Conductive Sub-Stoichiometric TiO<sub>2</sub> Reactive Electrochemical Membrane,” Oral Presentation: *2016 ACS 251st National Meeting*, San Diego, CA, Mar. 17, 2016;
- **Y. Jing**, B.P. Chaplin, “Membrane Fouling and Electrochemical Regeneration at a Sub-Stoichiometric TiO<sub>2</sub> Reactive Electrochemical Membrane,” Oral Presentation: *2016 AIChE Annual Meeting*, San Francisco, CA, Nov. 17, 2016